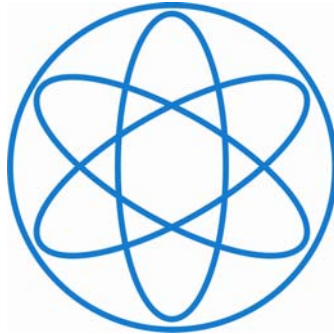


# PHYSIK – DEPARTMENT

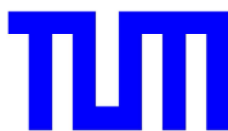


Influence of the alloying element cobalt on the  
key properties of ferromagnetic shape memory  
Ni-Mn-Ga single crystals

Dissertation

von

Katharina Rolfs



TECHNISCHE UNIVERSITÄT  
MÜNCHEN

TECHNISCHE UNIVERSITÄT MÜNCHEN  
Lehrstuhl für Experimentalphysik IV

# Influence of the alloying element cobalt on the key properties of ferromagnetic shape memory Ni-Mn-Ga single crystals

Katharina Rolfs

Vollständiger Abdruck der von der Fakultät für Physik der Technischen  
Universität München zur Erlangung des akademischen Grades eines  
Doktors der Naturwissenschaften (Dr. rer. Nat.)  
genehmigten Dissertation.

Vorsitzender: Univ.-Prof. Dr. H. Friedrich

Prüfer der Dissertation:

1. Univ.-Prof. Dr. W. Petry
2. Univ.-Prof. Dr. P. Böni

Die Dissertation wurde am 30.11.2010 bei der Technischen  
Universität München eingereicht und durch die Fakultät für  
Physik am 09.03.2011 angenommen.

# CONTENTS

---

<b>ZUSAMMENFASSUNG</b> .....	<b>III</b>
<b>SUMMARY</b> .....	<b>V</b>
<b>CHAPTER 1 - INTRODUCTION</b> .....	<b>1</b>
<b>CHAPTER 2 - THEORETICAL BACKGROUND</b> .....	<b>5</b>
2.1 HEUSLER ALLOYS .....	6
2.2 MARTENSITE TRANSFORMATION.....	8
2.3 SHAPE MEMORY EFFECT .....	12
2.3.1 <i>One-Way-Effect</i> .....	13
2.3.2 <i>Two-Way-Effect</i> .....	14
2.3.3 <i>Superelasticity</i> .....	15
2.3.4 <i>Magnetic Shape Memory Effect</i> .....	16
2.4 MAGNETOCALORIC EFFECT .....	18
2.4.1 <i>Direct Measurement</i> .....	21
2.4.2 <i>Indirect Measuremet</i> .....	22
2.5 THE Ni-Mn-Ga-SYSTEM – AN OVERVIEW .....	23
2.5.1 <i>Thermal Properties</i> .....	23
2.5.2 <i>Structural Properties</i> .....	25
2.5.3 <i>Magnetic Properties</i> .....	27
<b>CHAPTER 3 - EXPERIMENTAL TECHNIQUES</b> .....	<b>29</b>
3.1 OPTICAL ANALYSIS .....	30
3.1.1 <i>Scanning Electron Microscopy</i> .....	30
3.2 ENERGY DISPERSIVE X-RAY SPECTROSCOPY.....	30
3.3 DIFFERENTIAL SCANNING CALORIMETRY .....	32
3.4 STRUCTURAL ANALYSIS .....	32
3.4.1 <i>Reciprocal Space</i> .....	32
3.4.2 <i>Laue – Equation</i> .....	33
3.4.3 <i>Bragg Formalism</i> .....	35
3.4.4 <i>Ewald Sphere</i> .....	36
3.4.5 <i>Neutron Diffraction</i> .....	37
3.4.6 <i>X-Ray Diffraction</i> .....	42
3.5 VIBRATING SAMPLE MAGNETOMETER.....	43
3.6 STRESS-STRAIN - MEASUREMENTS .....	45
<b>CHAPTER 4 – SAMPLE PREPARATION</b> .....	<b>47</b>
4.1 WHY SINGLE CRYSTALLINE MATERIALS? .....	48
4.2 CRYSTAL GROWTH – TECHNIQUE .....	49
4.2.1 <i>Bridgman – Technique</i> .....	49
4.2.2 <i>Slag Remelting and Encapsulation (SLARE) – Technique</i> .....	50
4.3 PREPARATION OF Ni-Mn-Ga-Co – SINGLE CRYSTALS .....	51
4.3.1 <i>Slag building Flux melting agent</i> .....	52
4.3.2 <i>Growth Process</i> .....	54

4.3.3 Postgrowth Treatment of the Crystals .....	54
4.3.4 Composition of the Ni-Mn-Ga-Co crystals .....	55
4.4 TRAINING OF SINGLE CRYSTALS .....	56
<b>CHAPTER 5 – RESULTS.....</b>	<b>57</b>
5.1 COMPOSITION OF THE SAMPLES .....	58
5.2 PHASE TRANSFORMATION TEMPERATURES.....	60
5.2.1 Structural and magnetic phase transformation .....	61
5.3 STRUCTURAL PROPERTIES .....	68
5.3.1 Neutron Diffraction .....	68
5.3.2 X-Ray Diffraction .....	76
5.4 MECHANICAL PROPERTIES .....	79
5.4.1 Crystal rod No.1 “Ni <sub>44.0</sub> Mn <sub>30.0</sub> Ga <sub>20.0</sub> Co <sub>6.0</sub> ” .....	79
5.4.2 Crystal rod No.2 “Ni <sub>44.6</sub> Mn <sub>30.7</sub> Ga <sub>19.3</sub> Co <sub>5.4</sub> ” .....	87
5.4.3 Crystal rod No.3 “Ni <sub>45.0</sub> Mn <sub>31.0</sub> Ga <sub>19.2</sub> Co <sub>4.8</sub> ” .....	88
5.4.4 Crystal rod No.4 “Ni <sub>48.8</sub> Mn <sub>28.6</sub> Ga <sub>21.4</sub> Co <sub>1.2</sub> ” .....	89
5.4.5 Crystal rod No.5 “Ni <sub>49.2</sub> Mn <sub>28.4</sub> Ga <sub>21.6</sub> Co <sub>0.8</sub> ” .....	90
5.5 MAGNETIC PROPERTIES.....	93
5.5.1 M vs T - measurements .....	94
5.5.2 M vs H - Measurements.....	100
5.5.3 Magnetocaloric Effect .....	101
<b>CHAPTER 6 – DISCUSSION .....</b>	<b>105</b>
6.1 INFLUENCE OF COBALT ON PHASE TRANSFORMATION TEMPERATURES.....	106
6.1.1 Structural phase transformation temperatures .....	106
6.1.2 Magnetic phase transformation temperatures.....	111
6.2 STRUCTURAL PARAMETERS OF Ni-Mn-Ga-Co OF DIFFERENT COMPOSITIONS.....	113
6.2.1 Influence of Cobalt and Manganese.....	113
6.2.2 Influence of ballmilling .....	115
6.3 STRESS AND STRAIN BEHAVIOUR .....	117
6.3.1 General Aspects.....	117
6.3.2 Twinning mechanism in non modulated tetragonal samples .....	120
6.3.3 Twinning mechanism in non modulated orthorhombic samples.....	121
6.3.4 Twinning mechanism in modulated tetragonal samples.....	124
6.4 MAGNETIC PROPERTIES .....	125
<b>CHAPTER 7 – CONCLUSIONS AND PERSPECTIVES .....</b>	<b>129</b>
<b>ACKNOWLEDGEMENT.....</b>	<b>133</b>
<b>BIBLIOGRAPHY .....</b>	<b>134</b>
<b>APPENDIX A .....</b>	<b>140</b>
<b>APPENDIX B.....</b>	<b>143</b>
<b>APPENDIX C.....</b>	<b>145</b>
CRYSTAL ROD NO.2 “Ni <sub>44.6</sub> Mn <sub>30.7</sub> Ga <sub>19.3</sub> Co <sub>5.4</sub> ” .....	145
CRYSTAL ROD NO.3 “Ni <sub>45.0</sub> Mn <sub>31.0</sub> Ga <sub>19.2</sub> Co <sub>4.8</sub> ” .....	147
CRYSTAL ROD NO.4 “Ni <sub>48.8</sub> Mn <sub>28.6</sub> Ga <sub>21.4</sub> Co <sub>1.2</sub> ” .....	149
CRYSTAL ROD NO.5 “Ni <sub>49.2</sub> Mn <sub>28.4</sub> Ga <sub>21.6</sub> Co <sub>0.8</sub> ” .....	151
<b>ERKLÄRUNG .....</b>	<b>153</b>

# ZUSAMMENFASSUNG

---

Die vorliegende Arbeit untersucht den Einfluss des ferromagnetischen Übergangsmetalls Kobalt auf die thermischen, strukturellen, mechanischen und auch magnetischen Eigenschaften der ferromagnetischen Formgedächtnislegierung Ni-Mn-Ga. Magnetische Formgedächtnislegierungen haben zum einen die Eigenschaft in der Tieftemperaturphase (Martensit - Phase) induzierte plastische Verformungen durch Temperaturerhöhungen über den strukturellen Phasenübergang (Martensit - Temperatur) rückgängig zu machen. Durch erneutes Abkühlen aus der Hochtemperaturphase (Austenit - Phase) in die martensitische Phase liegt das Material anschließend makroskopisch wieder im Ausgangszustand vor. Zum anderen kann in diesen Legierungen durch mechanischen Druck oder aber durch Anlegen eines Magnetfeldes in der Martensit - Phase eine Dehnung von mehreren Prozent induziert werden. Die letztere Eigenschaft beruht auf einer niedrigen Zwillingsgrenzspannung im Material, die durch ein ausreichend starkes Magnetfeld überwunden werden kann und zu einer Neuorientierung der magnetisch weichen und im Fall von Ni-Mn-Ga der kristallographisch kürzesten Achse führt. Die Dehnung kann durch eine Richtungsänderung des Magnetfeldes um  $90^\circ$  ebenfalls rückgängig gemacht werden kann. Dieser Effekt eröffnet neue Möglichkeiten in der Sensoren- und Aktorenkonstruktion, da die Ansprechzeiten sehr viel schneller sind als beim thermischen Formgedächtniseffekt und die induzierten Dehnungen sehr viel höher liegen als zum Beispiel bei Piezokeramiken. Jedoch kann dieses Phänomen nur in ferromagnetischen Martensit-Phasen bestimmter (modulierter) Strukturen beobachtet werden, so dass die Anwendungen bis heute auf einen Temperaturbereich kaum höher als Raumtemperatur und bestimmter Zusammensetzungen der Legierungen beschränkt sind. Für bestimmte Anwendungen, wie zum Beispiel in Motoren müssen aber Arbeitstemperaturen über  $100^\circ\text{C}$  möglich sein. Ni-Mn-Ga ist dabei eines der erfolgsversprechenden Materialsysteme. Sowohl der Martensit-Übergang als auch die Curie-Temperatur konnten bei gleichzeitig niedriger Zwillingsgrenzspannung im Martensiten auf über  $70^\circ\text{C}$  erhöht werden. Allerdings zeigt Ni-Mn-Ga in der notwendigen modulierten Struktur eine Sprödigkeit, die Langzeitanwendungen unterbindet.

Um die oben erwähnten Nachteile des Materialsystems Ni-Mn-Ga zu überwinden, wurde ein Teil des Nickels (0.8 at-% bis 6 at-%) durch Kobalt ersetzt, wodurch eine Erhöhung der Curie-Temperatur sowie der Duktilität erreicht werden sollte. Durch die gleichzeitige Erhöhung des Mangan/Gallium - Verhältnisses sollte die Martensit - Temperatur ebenfalls in einen höheren Temperaturbereich verschoben werden.

Da bis heute nur in einkristallinen Materialien die theoretisch maximale Dehnung gemessen wurde und die Sprödigkeit des Materials durch Korngrenzen im Polykristall erhöht werden kann, wurden für diese Arbeit Einkristalle verschiedener Zusammensetzung mithilfe einer abgeänderten Bridgman - Methode (Slag-Remelting and Encapsulation (SLARE) Technik) gezüchtet. Diese spezielle Methode erhöht die Wahrscheinlichkeit einer erfolgreichen Einkristallzucht mit abschätzbarer Zusammensetzung (trotz des großen Dampfdrucks des Mangans). Sechs verschiedene Einkristalle von mehreren Zentimetern Länge, einem ungefähren Durchmesser von 1.5cm und abnehmendem Kobalt-Gehalt sowie angepasstem Mn/Ga - Verhältnis konnten so erfolgreich gezüchtet werden.

Da die thermischen, strukturellen und damit auch mechanischen und magnetischen Eigenschaften eine starke Abhängigkeit von der Zusammensetzung zeigen, wurde von den aus den einkristallinen Stäben herauspräparierten und oberflächenbehandelten Proben die Zusammensetzung mittels energiedispersiver Röntgenspektroskopie ermittelt. Diese Messungen zeigten deutlich, dass die angewendete SLARE Methode zur Züchtung einen größeren Verlust an Mangan erfolgreich verhindert, jedoch einen gewissen Konzentrationsgradienten von Mangan und Gallium entlang der Wachstumsachse nicht vollständig vermeiden kann.

Der strukturelle und magnetische Phasenübergang in diesen Proben wurde anschließend mittels dynamischer Differenz Kalometrie bestimmt. Es zeigte sich, dass das zulegierte Kobalt einen Einfluss auf beide Phasenübergangstemperaturen hat, da beide im Vergleich zu Ni-Mn-Ga mit gleichem Mn/Ga - Verhältnis, bzw. e/a - Verhältnis bei höheren Temperaturen von bis zu 160°C liegen. Durch nachfolgende Neutronendiffraktionsmessungen an den Vierkreisinstrumenten D9 und D10 (Institut Laue Langevin) an einer Einkristallprobe im Austeniten konnte gezeigt werden, dass sich das Kobalt hauptsächlich auf den Nickel-Plätzen im kubischen Gitter verteilt und zu einem kleinen Teil auch auf den Mangan - Plätzen liegt, wodurch die Erhöhung beider Übergangstemperaturen erklärt wird.

Durch Neutronendiffraktion an Proben verschiedener Zusammensetzung konnte zudem der Einfluss des Kobalts auf die Martensit - Struktur verifiziert werden. Es zeigt sich, dass im selben Mn/Ga - Bereich bzw. e/a - Bereich, in dem Ni-Mn-Ga eine modulierte Struktur zeigt, Ni-Mn-Ga-Co zwei verschiedene nicht-modulierte Strukturen zeigt. Zum einen die in Ni-Mn-Ga anderer Zusammensetzung tetragonal nicht-modulierte Struktur, die Zwillingsgrenzspannungen und Dehnung ähnlich denen in Ni-Mn-Ga zeigt, zum anderen eine orthorhombische nicht-modulierte Struktur, die in Ni-Mn-Ga bislang unbekannt ist. Das Spannungs - Dehnungs - Verhalten der Proben der letzteren Struktur zeigen daher einen anderen Zwillingsmechanismus, der als „Double twinning“ bezeichnet werden kann und Ähnlichkeiten mit dem Mechanismus in moduliertem orthorhombischen Ni-Mn-Ga während der Deformation hat. Beide Strukturen zeigten jedoch eine Zwillingsgrenzspannung, die zu hoch ist, um durch ein Magnetfeld überwunden werden zu können. Mit abnehmendem Kobalt-Gehalt in den Proben konnte eine Erniedrigung der Zwillingsgrenzspannung beobachtet werden, wobei das Kobalt jedoch eine Modulation in der Struktur zu verhindern scheint. In Proben mit 0.8 at-% Kobalt wurde letztendlich auch die modulierte tetragonal Martensit - Struktur gefunden, die mit einer Zwillingsgrenzspannung unter 2MPa den magnetischen Formgedächtniseffekt aufwies und in Langzeitmessungen die theoretisch maximale Dehnung zeigte.

An einigen Proben mit höherem Kobalt-Gehalt von 6at-% und 5.4 at-% wurden außerdem magnetokalorische Messungen durchgeführt, die wie Ni-Mn-Ga eine hohe magnetische Entropieänderung am strukturellen Phasenübergang zeigten. Teilweise wurden die Werte, gemessen in Ni-Mn-Ga, übertroffen. Im Gegensatz zu Ni-Mn-Ga handelt es sich in Ni-Mn-Ga-Co allerdings um den inversen magnetokalorischen Effekt, das heisst, dass die Magnetisierung der ferromagnetischen austenitischen Phase durch das Kobalt in einem Feld bis zu 10T immer noch höher ist als in der martensitischen Phase von Ni-Mn-Ga-Co.

Die für die Arbeit durchgeführten Messungen und Analysen zeigen, dass Kobalt, selbst in kleinen Konzentrationen, tatsächlich einen signifikanten Einfluss auf die charakteristischen Eigenschaften von Ni-Mn-Ga hat.

# SUMMARY

---

The studies presented here, investigate the influence of alloying the ferromagnetic transition metal cobalt on the thermal, structural, mechanical and magnetic properties of the ferromagnetic shape memory alloy Ni-Mn-Ga. Magnetic shape memory alloys are able to recover a plastic deformation, induced in the low temperature phase (Martensite - phase) by increasing the temperature above its structural phase transition temperature (Martensite temperature). Cooling the sample below the martensite temperature again results in the same macroscopic state as before the deformation. Furthermore these alloys show a strain of several percent by an uniaxial deformation by either a mechanical stress or an applied magnetic field. The latter property is based on a twinning stress in the material, which is low enough to be overcome by a magnetic field forces. Thereby the magnetic soft axis (in the case of Ni-Mn-Ga the short crystallographic axis) orientates towards the magnetic field, resulting in the strain mentioned above. A change of the field direction by  $90^\circ$  results in the recovery of the shape. This effect enables the development of new sensors and actuators, since the response time is faster than of the thermal shape memory effect and the induced strain is larger than of actuator materials such as piezo ceramics. However the strain can be induced only in the ferromagnetic martensite with a particular (modulated) structure. That limits the use to a temperature range around room temperature impeding certain applications, e.g. in engines, requiring working temperatures above  $100^\circ\text{C}$ . A very promising material system is therefore Ni-Mn-Ga. Showing a low twinning stress, the martensite and Curie - temperature were shifted to temperatures above  $70^\circ\text{C}$ . An important challenge to be overcome is the brittleness of the system in the modulated martensites, making long term application impossible.

For solving the mentioned problems of Ni-Mn-Ga, nickel was replaced by different amounts of cobalt (0.8 at-% to 6 at-%) to shift the Curie-temperature to higher values as well as to reach a higher ductility. The simultaneous increase of the Mn/Ga - ratio should increase the martensite temperature at the same time.

Since the brittleness is increased by grain boundaries in polycrystalline samples and a theoretical maximum strain was only determined in single crystalline material, for the presented work single crystals of different stoichiometry were grown. For the growth a Bridgman like technique, called "Slag remelting and Encapsulation (SLARE) technique" was used. This method avoids the uncontrolled loss of elements with a high vapour pressure and increases the probability of a successful single crystal growth with a length of several centimetres and a diameter of approximately 1.5cm. This method enabled the growth of six single crystalline rods with different cobalt content and adapted Mn/Ga - ratio.

Due to the strong dependence of the thermal, structural and therefore the mechanical and magnetic properties on the composition, the composition of all specimens cut out of the single crystalline rods was determined by energy dispersive X-ray spectroscopy. The measurements verified the prevention of a high loss of manganese during the growth process. However a

certain concentration gradient of manganese and gallium along the growth axis cannot be fully suppressed.

The subsequent determination of the structural and magnetic phase transition temperatures by differential scanning calorimetry showed that cobalt alloyed Ni-Mn-Ga has higher martensite and Curie – temperatures than Ni-Mn-Ga with a comparable Mn/Ga – and e/a – ratio. In Ni-Mn-Ga alloyed with 6 at-% cobalt, both phase transition temperatures were increased up to 160°C. Neutron diffraction performed on the hot neutron four circle diffractometers D9 and D10 (Institut Laue Langevin) on single crystalline Ni-Mn-Ga-Co in the austenite phase verified that cobalt distributes mainly on the nickel places, but partly also on the manganese places, explaining the increase of the structural and magnetic phase transition temperature.

Neutron diffraction on samples of different composition was additionally performed to investigate the influence of cobalt on the martensite structure. It was determined that Ni-Mn-Ga alloyed with cobalt, but with the same Mn/Ga or e/a – ratio as Ni-Mn-Ga with a modulated martensite structure, show different structures. One structure found is the well known non-modulated tetragonal structure of Ni-Mn-Ga from other composition ranges, which also shows equal twinning stress and strain values. The other structure found in Ni-Mn-Ga-Co is a non-modulated orthorhombic structure with different stress – strain – behaviour, explainable by the so called double twinning mechanism, similar to the mechanism in modulated orthorhombic Ni-Mn-Ga. Both structures show a twinning stress too high to be overcome by a magnetic field. With the decrease of the amount of cobalt, a decrease of the twinning stress was observed. However the cobalt seems to impede a modulated structure. In the samples with 0.8 at-% cobalt the modulated tetragonal structure was finally observed, which shows a twinning stress below 2MPa and hence the magnetic shape memory effect. In long-term measurements the maximum theoretical strain was measured.

For some of the single crystals with a higher cobalt content of 6 at-% and 5.4 at-% the magnetocaloric properties were investigated. The samples showed a high magnetic entropy change at the structural phase transition even with higher values compared to Ni-Mn-Ga. However the determined effect is the inverse magnetocaloric effect with a higher magnetization in the austenite state than in the martensite state, which seems to be stabilized by the cobalt even for high magnetic fields of up to 10T.

The measurements and analysis performed for this work show, that even small amounts of cobalt result in a significant change of the key properties of Ni-Mn-Ga.

# CHAPTER 1 - INTRODUCTION

---

Over the last years the research interest in materials which exhibit the magnetic shape memory effect (MSME) has increased constantly. Since these alloys show a magnetic field induced strain a magnitude higher than magnetostrictive materials, the possibilities in building up actuators and sensors has widened. However the commercial use of magnetic shape memory alloys (MSMAs) in actuating devices demands the application of such materials at low magnetic fields (less than 0.3T) and mechanical stress respectively (less than 2MPa) in combination with high operational temperatures. This requires high mobility of the twin boundaries and high phase-transition-temperatures from a modulated martensite to the austenitic phase. For applications within combustion engines for example the industry demands temperatures of up to 140°C, which has not yet been reached. One of the most prominent and promising magnetic shape memory alloys is Ni-Mn-Ga. Beside the magnetic shape memory effect, this alloy also shows interesting magnetic properties, resulting in the giant magnetocaloric effect.

The aim of the project is to expand the operational temperature range whilst reducing the twinning stress and advancing the crystal's lifetime, hence, Ni-Mn-Ga was alloyed with cobalt. This is based on focused alloy design as well as sample preparation and the subsequent characterization of the alloy's crystallographic and mechanical properties. Since the magnetocaloric effect in Ni-Mn-Ga gives also rise to application in the field of cooling, samples with a higher cobalt content were taken to determine the effect and the influence of cobalt on the magnetic properties.

An introduction to the theoretical fundamentals is presented in chapter 2, giving an overview of the key properties of magnetic shape memory alloys such as martensite transformations in general (subsection 2.2) and the shape memory effect (subsection 2.3), also the magnetocaloric effect is explained in detail in subsection 2.4.

The different experimental techniques used for the investigation of the properties are illustrated in chapter 3.

To cope with the insufficiency of the Bridgman technique for single crystal growth, the Slag – Remelting – and – Encapsulation – method (SLARE), developed at the Helmholtz Centre Berlin for Materials and Energy, was used for reliable and repeatable preparation of homogeneous single crystalline samples of known composition and low porosity. The technique and the chosen compositions are explained in detail in chapter 4, which also shows the after growth treatment and preparation of the small specimen for the experiments performed on the samples.

Chapter 5 presents a summary of the results of the different measurements, starting with the influence of the composition change in the samples (shown in subsection 5.1) on the structural and magnetic phase transformation temperatures in subsection 5.2. Also the structural and mechanical properties of the chosen samples, as well as the magnetic shape memory effect in samples with a lower cobalt content are presented in subsections 5.3 and 5.4, respectively. The last subsection 5.5 of this chapter is about the magnetic properties and therefore about the magnetocaloric effect of samples with higher amounts of cobalt.

The following chapter 6 pulls together the results presented in the previous chapter, starting with the correlation between the phase transformation temperatures and the stoichiometry of the material (subsection 6.1). The potential influence of the stoichiometry on the structural properties is discussed in the subsequent subsection 6.2 and leads directly to the relation between the structure and the stress-strain-behaviour of the specimens. Subsequent the

magnetic properties will be discussed in correlation to the stoichiometry of the particular samples.

The last chapter gives a short summary and conclusions of the before discussed results and also shows the potential of the material as well as possible new questions to be solved due to the properties found in these specimens.



# CHAPTER 2 - THEORETICAL BACKGROUND

---

## 2.1 HEUSLER ALLOYS

Heusler alloys first became of interest when Friedrich Heusler discovered that Mn-Cu produces a ferromagnetic alloy if it is alloyed with Sn, Al, As, Sb, Bi or B [1], even though none of the elements are ferromagnetic themselves.

In 1934 Bradley and Rodgers developed a correlation between the composition, the chemical order and the magnetic properties of the Cu-Mn-Al – system [2]. Therefore  $\text{Cu}_2\text{MnAl}$  became a kind of prototype for Heusler alloys, which are now defined as ternary intermetallic compounds, which exhibit the  $L2_1$ -structure (see Figure 2.1.1) at the stoichiometric composition  $X_2YZ$ .

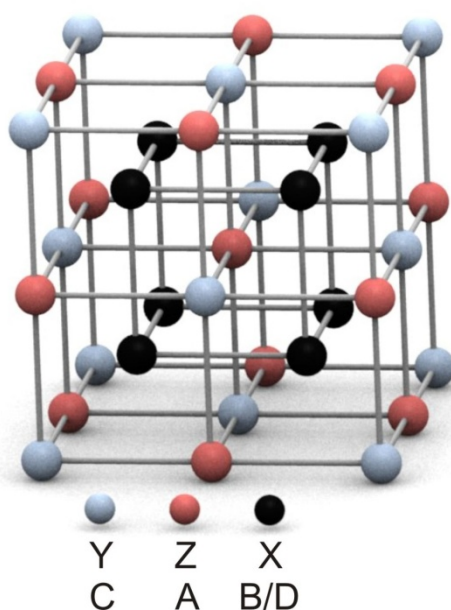


Figure 2.1.1: The stoichiometric Heusler alloy with the  $L2_1$  structure with a spacegroup  $Fm-3m$ . The  $L2_1$  can be described with four interpenetrating fcc-sublattices.

The unit cell of the  $L2_1$ -structure consists of four interpenetrating fcc - sublattices A, B, C, D with their origins at  $(0,0,0)$ ,  $(\frac{1}{4} \frac{1}{4} \frac{1}{4})$ ,  $(\frac{1}{2} \frac{1}{2} \frac{1}{2})$  and  $(\frac{3}{4} \frac{3}{4} \frac{3}{4})$ . This unitcell belongs to the spacegroup  $Fm-3m$ , where the A and C sites exhibit a point symmetry  $m\bar{3}m$  and the B and sites have the point symmetry  $4\bar{3}m$ . In table 2.1.1 examples of elements occupying certain sublattices are given [3].

When combining the Elements X, Y and Z, there is an innumerable way of distributing the elements amongst the four sublattices leading to symmetry, which is lower than present in the  $L2_1$  structure. However Heusler alloys usually exhibit a certain temperature, where the atoms order in the sublattices. This ordering temperature is highly dependent on the elements and also the composition of the Heusler system. Above the specific temperature, Y and Z are randomly distributed over the sublattices A and C, hence the alloys show a B2 structure in the high temperature range. Alloys which contain elements from the 3B group like Al or In form the B2

structure in preference to the  $L2_1$ , where the ordering temperature lies above the melting point of the material [4].

Some Heusler alloys show however a two stage disorder-order transition. Besides the transformation from the B2 structure to the  $L2_1$  structure, these material systems have a second transformation from the A2 lattice to a B2 structure at higher temperature before the melting point. The A2 structure shows a higher disorder than the B2 structure, where all atoms are randomly distributed in a bcc lattice. The A2 structure has been reported in Cu-Al-Mn [5] and Ni-Mn-Al [6], where the order disorder transformation has been verified by DSC, XRD and phonon dispersion [7] in the latter system.

<b>X</b>	<b>Y</b>	<b>Z</b>
Ni, Co, Pt, Ru, Pd	Mn, Ti, Zr, V, Ta	Ga, Al, In, As, Sb
Cu, Fe, Rh, Ir, Au	Hf, Cr, Gd, Tb, Yb	Sn, Ge, Pb, Bi, Tl

Table 2.1.1: Examples of elements which form the Heusler structure and their preferred occupancy

For stoichiometric Heusler alloys  $X_2YZ$  Johnston and Hall proposed a single disordering parameter  $\alpha$  to describe certain types of preferential disorder [5]. In the specific case of  $L2_1$  structure  $\alpha$  is defined as the fraction of either Y or Z atoms not positioned on the correct site. This partial occupation of Y and Z atoms on each other's sublattices results in the  $L2_1$ -B2 type disorder. For alloys showing an ordering temperature below the melting point, thermal treatment influences the  $L2_1$ /B2 ratio strongly.

The chemical order of the Heusler alloys affects the transformation temperatures as well as the magnetic structure and the magnitude of the magnetic moment. In a B2 structure for example the interatomic distances are smaller than in the  $L2_1$  structure and therefore an antiferromagnetic ordering becomes energetically more favourable [6].

The thermal, structural and also magnetic properties of the systems can change significantly not only by heat treatment, but also by changing the composition of the Heusler alloys. Up to now a lot of Heusler-Systems have been investigated and their structural and magnetic properties have been determined in detail. In the course of those investigations several interesting magnetic properties have been found, like the magnetoresistance, the giant magnetocaloric and also the magnetic shape memory effect.

These effects are related to the combination of magnetic and structural properties of the Heusler alloys. At lower temperatures several Heusler compounds, e.g.  $Ni_2MnGa$ ,  $Co_2MnAl$  etc., undergo a martensite transformation from a highly symmetric cubic austenite to a low symmetry martensite phase. Unlike the disorder-order transformation, which involves the diffusion of atoms, the martensite transformation is induced by a nondiffusional co-operative movement of the atoms in the crystal (see section 2.2).

If the Heusler alloys are ferromagnetic in the martensite phase, they can exhibit the magnetic shape memory effect (see section 2.3). In these alloys, an external magnetic field can induce large strains when applied in the martensite state. Therefore magnetic shape memory alloys are

promising smart materials for future technological applications in the field of sensors and actuators

The magnetocaloric effect (MCE) found in Heusler alloys has its origin in the martensite phase transformation that modifies the exchange interactions due to the change in the lattice parameters (see section 2.4). For samples with compositions close to  $\text{Ni}_2\text{MnGa}$  and other Heusler alloys, like Mn-As-Sb, a giant MCE has been reported [8-10]. Applying a magnetic field adiabatically at the martensite phase transformation causes the sample to cool. This feature is regarded as promising for the development of economical and ecological refrigerants.

## 2.2 MARTENSITE TRANSFORMATION

Martensite transformations belong to the class of diffusionless solid state phase transformations. During such a phase change the atoms move less than the interatomic distances and retain their relative relationships. This implies that the low temperature product phase must have the same composition as the high temperature parent phase. The transformation was first discovered in quenched steel, where the high temperature fcc-structure changes to a bct-structure [11]. In honour of Adolph Martens, the low temperature product phase was named martensite, which gives also the name for this type of phase transformation. The high temperature phase is called austenite, named after William Chandler Roberts-Austen, an English metallurgist at the end of the 19<sup>th</sup> century.

During the last decades martensite transformations were also found in several other materials such as superconductors [12,13], zirconia [14,15] and Heusler alloys [16,17]. Diffusionless solid state phase transformations are also called displacive transformations. The change from the austenite to the martensite structure can be described by homogeneous lattice-distortive strain and shuffling (see Figure 2.2.1).

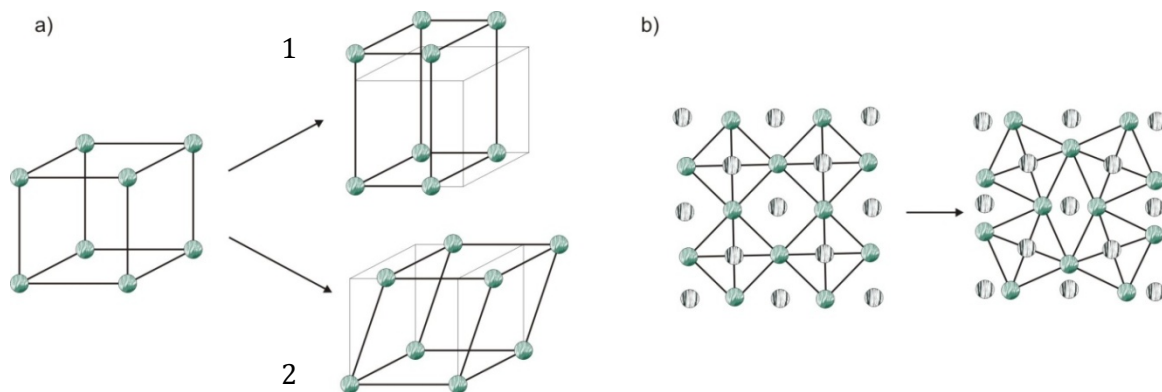


Figure 2.2.1: a: Examples for lattice-distortive deformations of a cubic system. (1) a dilatation along one axis, while a second one contracts, which leads to a tetragonal lattice. (2) due to a shear along (001) a monoclinic system is created. b: Example of shuffle displacement: the anti-clockwise rotation of one atom group (green) around the other (white) results in a change of symmetry.

The lattice-distortive deformation is associated with a volume and a shear dominant shape change causing elastic strains in the parent phase and gives rise to elastic strain energy stored within the sample. During the phase transformation an interface between the austenite and the martensite phase is created, generating an additional interfacial energy  $\gamma$ . The plane of contact is invariant and is called habit plane, where all vectors remain constant in their direction and length during the transformation.

Shuffling also induces an interface and therefore interfacial energy but does not cause elastic strains. It is defined as the relative displacements of the various atomic sublattices and thus the change of the symmetry or structure of the crystal.

Due to the volume change and strain energy appearing within the martensite transformation, this transformation is characterized by heterogeneous nucleation and the growth of martensite seeds. The starting points for an austenite to martensite transformation are defects in the lattice, grain boundaries in a polycrystalline sample, as well as the surface of the sample. The martensite phase usually appears as thin plates or needles and laths in the austenite phase (see Figure 2.2.2). These plates lie on distinct crystallographic planes in the austenite phase.



Figure 2.2.2: Schematic of the formation of the martensite plates. The growth of the plates is interrupted at grain boundaries (black lines within the squares), other martensite areas (grey shaded areas) and the surface of the sample.

The martensite transformation is also associated with a change of the symmetry. Usually, the high temperature phase exhibits a higher symmetry than the martensite phase. The coordinated movement of the atoms results in a lattice variant deformation explained in detail by Bain [18]. The macroscopic shape change accords to shear along the invariant habitus plane. Due to the shape change a high distortion of the austenite and therefore a high internal strain occurs during the martensite transformation. This is compensated by a lattice invariant shear within the built martensite areas. The invariant shear can either result in deformation voids, cleavage planes or twinning. The first two processes result in a plastic deformation and are irreversible. However the development of a twinned structure is elastic and therefore reversible. In this process the lattice is mirrored on a certain plane of the lattice (see Figure 2.2.3).

The full transformation shape change, induced locally, spreads gradually over the whole sample within a small temperature interval. The martensite phase starts to form at the Martensite start temperature  $M_S$  and is complete below the Martensite finish temperature  $M_f$ , below which further cooling does not increase the volume fraction of the martensite phase (see Figure 2.2.5). The reverse transformation starts at the so called Austenite start temperature  $A_S$  and finishes at the Austenite finish temperature  $A_f$ .

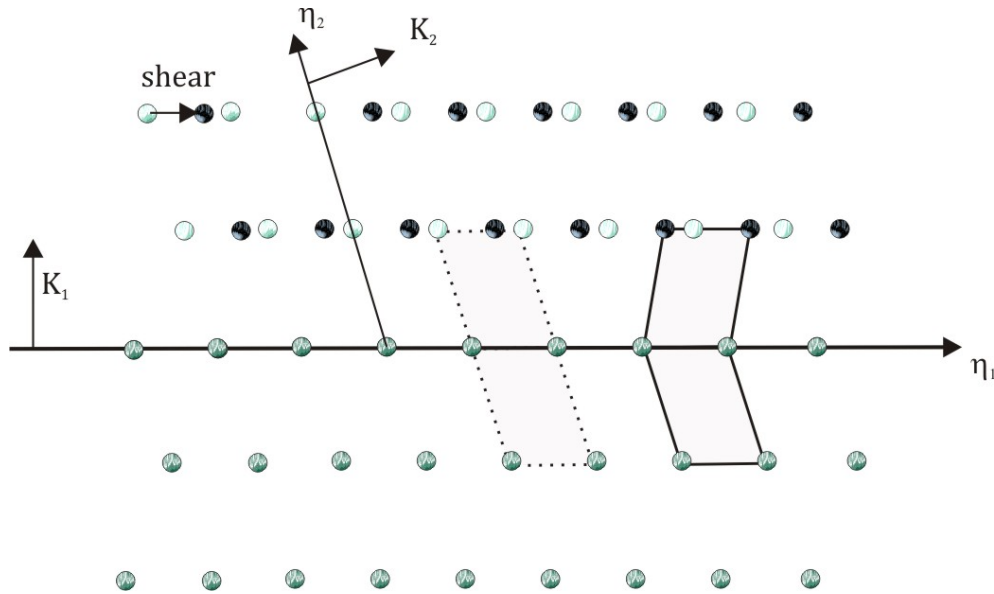


Figure 2.2.3: Schematic of a twinned martensite resulting from an invariant shear during the martensite transformation to compensate the variant lattice deformation. The green circles indicate the lattice points before the shear, the black circles show the position of the lattice points after the shear. The dashed line illustrate two unit cells before the twinning, the solid lines show the unit cell existing after the twinning. The twin plane normal is parallel to  $K_1$  and the direction of the shear is parallel to  $\eta_1$ , while  $K_2$  and  $\eta_2$  indicate the normal and an undistorted vector of the previous plane.

Like for all phase transformations, the free energy of the system determines, if the martensite transformation is thermodynamically possible. The transformation has to result in an overall reduction of the Gibbs free energy  $G$  of the system.

$$G = H - T \cdot S$$

H:enthalpy; S: entropy [1]

Plotting the Free Gibbs Energy, of the austenite  $G^A$  and the Free Gibbs Enthalpy of the martensite phase  $G^M$  versus the temperature, results in two subtended curves with the negative slopes  $S^A$  and  $S^M$  (see Figure 2.2.4).

The phase which shows a lower Gibbs enthalpy at a given temperature is the thermodynamic more stable phase. At the intersection the martensite and austenite phase are in a thermodynamic equilibrium. The formation of a martensite nucleus in the parent phase creates interfacial and elastic energies and requires a definite amount of energy  $\Delta G^{A \rightarrow M}$ , thus the austenite does not transform to the martensite at  $T_{eq}$  but at a certain undercooling  $\Delta T = M_s - T_{eq}$ .  $\Delta G^{A \rightarrow M}$  is therefore the critical chemical driving force, composed of the chemical Gibbs energy  $G_c$  and the strain energy  $E_e$ . The undercooling and superheating (the reverse transformation to the austenite at  $\Delta T = A_s - T_{eq}$ ) necessary to overcome the chemical driving force varies for different alloys and even compositions. Due to undercooling and superheating respectively, the martensite transformation shows a thermal hysteresis.

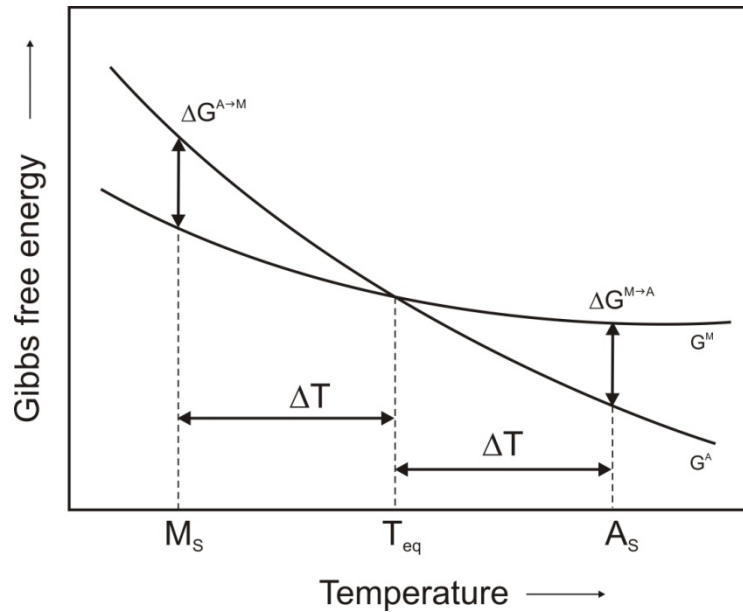


Figure 2.2.4: Schematic of the free Gibbs energy as a function of the temperature for the austenite and martensite phase.  $\Delta G^{A \rightarrow M}$  and  $\Delta G^{M \rightarrow A}$  is the driving force needed for the nucleation of the martensite and austenite, respectively.

To obtain the equilibrium temperature  $T_{eq}$  of different systems, the following equation can be used:

$$T_{eq} = \frac{(A_S + A_F)/2 + (M_S + M_F)/2}{2}$$

[2]

The Austenite and Martensite start ( $A_S$  and  $M_S$ ) as well as the finish temperatures ( $A_F$  and  $M_F$ ) are determined by the Onset-method. Therefore the intersection of the tangents of the cooling and heating graph and the tangents of the part where only martensite and austenite, respectively are present are taken (see Figure 2.2.5).

The thermal hysteresis does not depend on the chemical Gibbs energy  $G_C$ , but is highly influenced by the strain energy  $E_e$ , which contains the internal friction resulting from the movement of the interface between the austenite and martensite phase and also the amount of lattice defects. The more defects a sample contains, the broader the thermal hysteresis becomes. The minimum of the width is given by the defects formed due to the incapability of the austenite and martensite phase, which cannot be avoided during the martensite transformation.

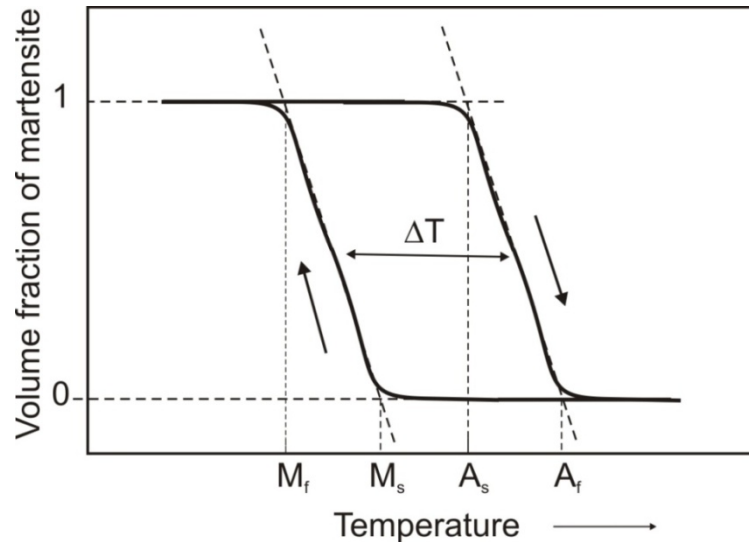


Figure 2.2.5: Variation of the volume fraction of the martensite phase as a function of temperature.

If the temperature for the nucleation of the martensite is reached, the martensite volume fraction can increase either isothermally or athermally. In isothermal martensites, the transformation progresses with time at a constant temperature, whereas the athermal type transforms with decreasing temperature. The isothermal martensite growth is caused by autocatalytic nucleation and a fast growth of several martensite plates (about 10-30 vol%) within the austenite. The athermal martensite grows in a thermoelastic mode by the formation of thin parallel sided plates or wedge shaped pairs of plates. This martensite forms progressively by sustained decrease of the temperature below  $M_s$  and shrinks and disappears by heating above  $A_s$ . During the thermoelastic growth the transformation front and the matrix are in a thermodynamic equilibrium, thus the energy of the shape deformation of the martensite is stored elastically in the sample. The change of the temperature results in a displacement of the equilibrium and therefore in a growth or shrinkage of the martensite. This transformation is reversible. By heating the sample into the austenite, the sample returns to the original high temperature arrangement. This is the reason why the shape memory effect only appears in thermoelastic alloys.

## 2.3 SHAPE MEMORY EFFECT

The shape memory effect is based on the reversible structural phase transformation between two crystal structures, the thermoelastic martensite phase transformation [19]. Specific materials, deformed below a critical temperature, “remember” and go back to their original shape by heating them over the phase transformation temperature.

The effect can be induced either by temperature or stress. Figure 2.3.1 shows a simplified mechanism of the thermal induced shape memory effect. By decreasing the temperature below  $M_s$ , the higher symmetric (mostly cubic in shape memory alloys) austenite starts due to lattice invariant deformation and shuffling to transform into a twinned martensite. Below the

Martensite finish temperature  $M_f$  the crystal consists of martensite variants only. In cubic systems there are 24 equivalent shear systems thus the shape memory alloy has 24 martensite variants. However the martensite consists only of variants which minimize the distortion by so called self accommodation. Therefore no shape change besides the surface relief appears.

Due to the highly mobile twin boundaries between the variants the martensite can be easily deformed by external mechanical stress  $\sigma$ . This results in a detwinning and a reorientation of the variants which show the highest strain along the stress direction.

The deformed martensite stays in this shape even after releasing the mechanical stress. By heating the sample above the Austenite start temperature  $A_s$  the martensite transforms back to high temperature phase with the original crystal orientation. By cooling the sample below  $M_f$  a second time can result either in a self accommodated martensite again or in the deformed martensite depending on the mechanism [20].

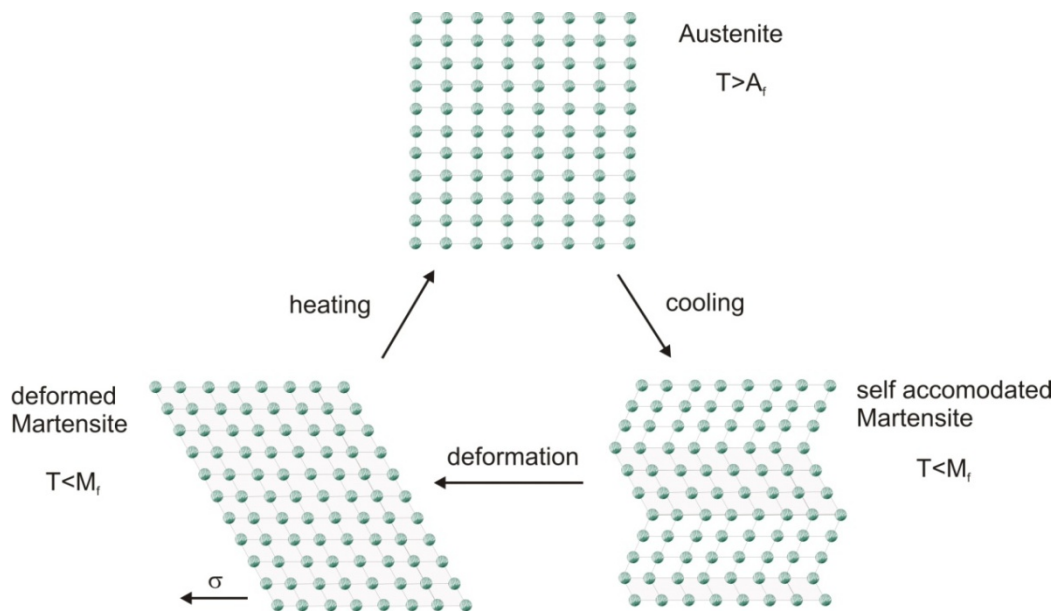


Figure 2.3.1: The principle of the thermal shape memory effect in materials induced by temperature change

### 2.3.1 ONE-WAY-EFFECT

At temperatures below  $M_f$  the martensite shows a special behaviour when applying external stress  $\sigma$ . By applying an increasing external stress on a sample in the martensite phase, the sample passes an elastic range and undergoes a pseudoplastic deformation (see Figure 2.3.2), where the sample deforms due to the reorientation of the martensite variants. This range in a stress-strain-diagram is called the martensite plateau and shows an increasing strain at a constant stress. Up to the point where the single variant state is reached, the sample shows the

conventional elastic deformation before the plastic deformation is reached and results in crack formation. The stress-strain diagram shown here does not contain the plastic deformation.

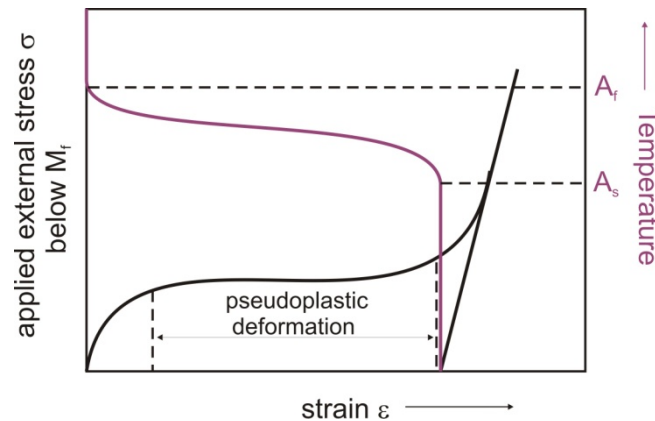


Figure 2.3.2: Strain behaviour of a shape memory alloy as a function of applied external stress (black) and as a function of Temperature (green) when heating a deformed martensite sample above  $A_f$

If the external stress is removed before the sample reaches the plastic deformation, the strain stays constant until the sample is heated above the Austenite start temperature  $A_s$ . The sample returns to the original austenite shape. In the case of the one-way-effect, repeated cooling below the Martensite finish temperature results in the self accommodated martensite and therefore does not undergo a macroscopic shape change again. The maximum strain which can be reached due to heating a deformed martensite is given by the crystallographic properties of the austenite and martensite. Depending on the ratio of the length of the axes in the martensite and austenite, strains of up to 10% have been reported up to now [21,22].

## 2.3.2 TWO-WAY-EFFECT

If the martensite transformation goes along with macroscopic shape change by heating and cooling, the effect is known as the two-way-effect. By cooling the sample below the Martensite start temperature only certain martensite variants are formed and a self accommodation in the martensite cannot take place.

In order to establish the two-way-effect in a sample, thermomechanical training is used. A repeated external applied stress into the plastic deformation range leads to a specific defect structure. Because of the artificially created defects, the subsequent heating of the sample into the austenite structure, results in an austenite different from the original austenite. By subsequent cooling below the Martensite start temperature  $M_s$ , only martensite variants favourable to the defect structure are formed. This results in a transformation from the austenite to a deformed martensite.

However the intrinsic stress in the sample is much smaller than an external stress applicable. Up to now, maximum strains of 5% have been reported [23], which are much smaller than the strain reachable in the one-way-effect. Hence a combination of the one-way-effect and an

external counteracting force is used. The counteracting force, e.g. a spring force, is big enough to deform the martensite within the transformation pseudoplastically.

Beside these two thermal shape memory effects, the one-way- and two-way-shape memory effect, ferromagnetic shape memory alloys can show other interesting properties like superelasticity [24] and the magnetic shape memory effect. Alloys showing these properties can reach a magnetic field induced strain of up to 10%.

### 2.3.3 SUPERELASTICITY

The martensite phase transformation can be passed also by the isothermal application of a mechanical stress in the austenite phase. Up to a defined external stress, the shape memory alloy in the austenite state shows an elastic deformation. By increasing the external stress the material starts to create stress induced martensite, whereby the variants, with an orientation yielding and minimizing the stress are favourably built. Due to the phase transformation from the austenite to the stress induced martensite, a high strain of up to 8% can be reached [25]. The further increase of the mechanical stress above this pseudoelastic range results in a second range of elastic deformation, followed by plastic deformation and cracking of the sample.

The release of the mechanical stress, after the second range of elastic deformation is reached, leads to a strong decrease of the strain, due to the elastic behaviour and simultaneous phase transformation from the martensite back to the austenite. If the reverse phase transformation is not complete and therefore the original structure not fully recovered, the effect is named pseudoelasticity. Only if the original full austenite structure is reached by stress release, the effect is called superelasticity (see Figure 2.3.3). Above the Austenite finish temperature  $A_F$ , the release of stress always results in a full shape recovery, since the martensite phase becomes unstable.

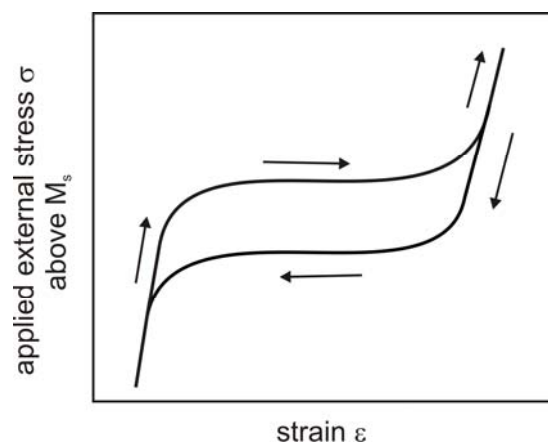


Figure 2.3.3: Stress-strain-diagram of a superelastic material. Applying an external mechanical stress leads to an elastic deformation followed by a pseudoplastic plateau, due to the phase transformation from the austenite to the stress induced martensite, and a second elastic deformation range. The release of the stress results in a full shape recovery

The necessary stress for creating a martensite above  $M_s$  increases with an increasing martensite temperature and can reach values where the plastic deformation becomes energetically more favourable. Above a specific temperature  $M_d$ , the stress strain behaviour of the shape memory alloys becomes equal to conventional alloys, since no stress induced martensite can be made. Therefore the austenite shows a linear-elastic deformation only, which recovers completely when the external stress is released. However, the austenite can be plastically deformed by the application of a high external mechanical stress due to the development or movement of dislocations.

---

### 2.3.4 MAGNETIC SHAPE MEMORY EFFECT

---

The magnetic shape memory effect (MSME) is a unique property of certain alloys exhibited in the ferromagnetic martensite phase. These materials show a large reversible shape change by inducing a stress, like a mechanical force or a magnetic field. The original shape can be restored when applying the mechanical or magnetic stress  $90^\circ$  to the first direction.

The MSME was first found in Dy single crystals showing a reversible magnetically induced strain of 3.4% in a magnetic field of 10T at 4.2K [26]. Further investigations led to the assumption, that twinning, the movement of twin boundaries in particular, is the origin of the shape change and the driving force is the lowering in magnetostatic and magnetocrystalline anisotropy energies. However, the detailed mechanism is still being discussed.

With the assumption, that the MSM material has only two twin variants, a simplified model of the effect is given in Figure 2.3.4. Materials only show the magnetic shape memory effect if the Curie temperature is well above the martensite phase transformation. Due to that pre-condition, the martensite variants are spontaneously magnetized even in the absence of an external magnetic field. The variants have different crystallographic and magnetic orientation. In the absence of a magnetic field, the magnetic moments are aligned along the easy axis of magnetization.

By applying a magnetic field perpendicular to the easy axis of one of the variants, the magnetic moments start to rotate towards the direction of the magnetic field. Three competing mechanisms exist in MSMA to achieve this alignment. Two of them, the magnetization vector rotation and the magnetic domain wall motion are common for ferromagnetic materials, whereas the reorientation of the martensite variants in a magnetic field only appears in magnetic shape memory alloys.

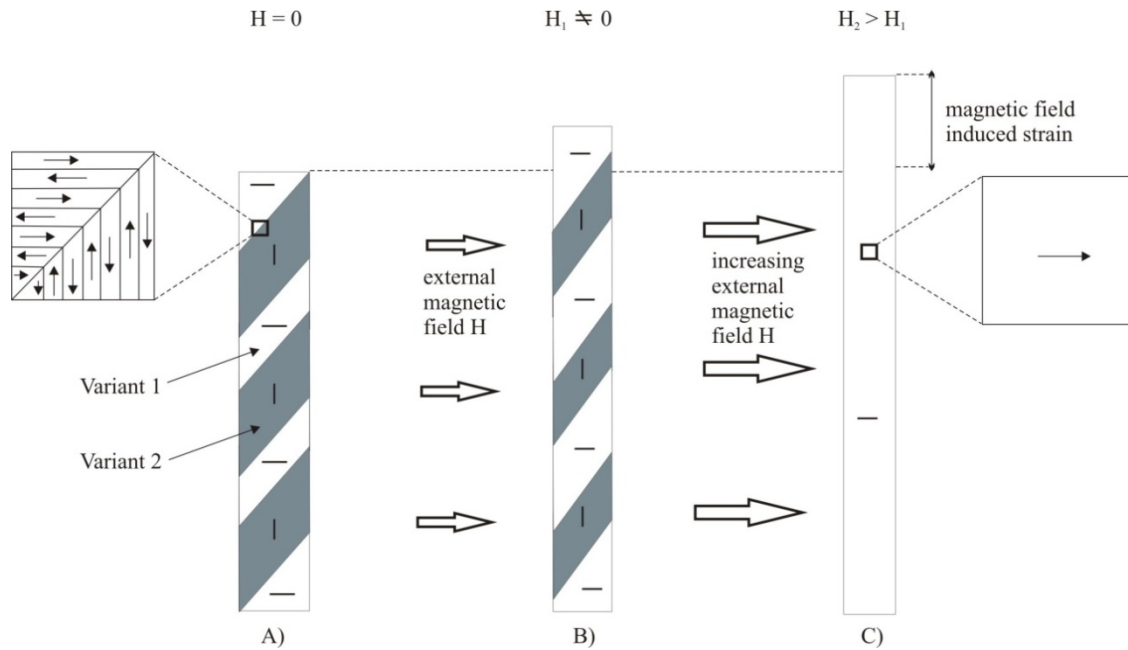


Figure 2.3.4: Schematic diagram of the field induced strain in a ferromagnetic shape memory alloy. A) The sample without an external field below the martensite phase transformation. The martensite variants show different structural orientation and therefore different directions of the easy axis (indicated by the black bars). The inset shows the sample on a micro-scale and the arrangement of the magnetic domains within the variants at the twin boundary. B) Due to the application of the magnetic field the volume fraction of variant 1 with the favourable direction of the easy axis increases in expense of variant 2. C) By increasing the magnetic field domain wall motion, rotation of the magnetization vectors and the reorientation of the martensite variants towards the direction of the external applied magnetic field, a single variant and single domain (see inset) state of the sample is reached, resulting in a macroscopic shape change.

The ferromagnetic variants exhibit magnetic domains, separated by  $180^\circ$  domain walls [27]. These regions of uniform magnetization minimize the magnetostatic energy of the system. In each of the domains the magnetization vectors are aligned along the easy axis of the particular variant (indicated by the arrows in Figure 2.3.4) pointing in either the positive or negative coordination direction. If no external field is applied, both domains are equal in size within one variant and no macroscopic magnetization can be determined. By applying an external magnetic field towards one of the directions of the magnetizations vector of domains, the volume fraction of the domain with the favourable direction of the magnetization vector increases until the saturation magnetization where the variant only consists out of one magnetic domain.

If the magnetic field is applied perpendicular to the magnetization vectors in both domains, both of them start to rotate towards the direction of the applied magnetic field. This rotation requires work against the magnetocrystalline anisotropy energy. This creates a pressure  $\Delta M \cdot H$  due to the Zeeman Energy difference on the twin boundaries. In a material with high magnetocrystalline anisotropy, the magnetic moments within the variants where the easy axis is perpendicular to the direction of the external magnetic field cannot rotate towards the field direction. However if the twin boundaries are mobile enough, the material reduces the Zeeman energy by the movement of the twin boundaries. Regions with twins in the favourable orientation grow in expense of other twin variants, which results in the determined macroscopic strain.

Heczko [28] has shown that the twin reorientation is possible in a saturating magnetic field if the following condition is fulfilled:

$$\frac{K_u}{\varepsilon_0} \geq \sigma_{tw} + \sigma_{bias} \quad [3]$$

Whereat  $K_u$  is the magnetic anisotropy,  $\varepsilon_0$  the theoretical strain,  $\sigma_{tw}$  the twinning stress of the material and  $\sigma_{bias}$  as the bias stress.

With increasing temperature, the magnetic anisotropy of martensite FSMAs increases [29]. The theoretical maximum strain  $\varepsilon_0$ , which can be reached by a magnetic field, depends on the lattice parameters of the material. Considering, that the sample changes from one single variant state to another, the magnetic field induced strain (MFIS) can be calculated by the following equation, whereas  $c$  is the shortest axis and  $a$  the longest axis of the unit cell:

$$\varepsilon_0 = 1 - \frac{c}{a} \quad [4]$$

If the temperature of the sample approaches the martensite phase transformation temperature, the lattice parameters become similar to each other. As a result the maximum theoretical strain  $\varepsilon_0$  decreases with increasing temperature. The twinning stress  $\sigma_{tw}$  which has to be overcome for the movement of the twin boundaries is also a function of temperature and decreases with increasing temperature. Furthermore it is highly influenced by the structure, the quality and the treatment of the material. It was shown, that a self-accommodated tetragonal martensite structure shows a lower magnetic anisotropy than a single variant martensite with the same structure, which leads to a smaller magnetic shape memory effect [30]. To reach a single variant state in a martensite sample, thermo-mechanical training is necessary, which will be presented in section 3.2.

## 2.4 MAGNETOCALORIC EFFECT

By applying a homogenous magnetic field on a thermally insulated solid, a temperature change of the solid can be determined. This property was discovered 1881 in pure iron by Warburg [31]. The origin of this so called magnetocaloric effect has been explained by Debye and Giauque in 1923 independently [32,33]. In addition they suggested the first practical use of the effect, the adiabatic demagnetization to reach temperatures lower than of liquid helium, which had been the lowest experimental reachable temperature at the time. Recently there has been a great interest in using the MCE as an environment-friendly technology for refrigeration within a large temperature range [34-36].

The magnetocaloric effect has its origin in the coupling of the spin system of the solid and the applied external magnetic field  $H$ , resulting in a change of the magnetic contribution to the entropy of the system. The value of the entropy of a ferromagnetic solid at constant pressure depends on the temperature  $T$  as well as the applied external magnetic field  $H$  and consists of an electronic  $S_{el}$ , a lattice  $S_{lat}$  and a magnetic  $S_m$  part.

$$S(H, T) = S_{el}(T) + S_{lat}(T) + S_m(T, H) \quad [5]$$

Applying an external magnetic field  $H$  isothermally to a ferromagnetic solid leads to the alignment of the magnetic spin system towards the direction of the magnetic field (see Figure 2.4.1). Due to the decrease of the magnetic contribution in this process a decrease of the total entropy can be observed, which is defined as

$$\Delta S_m = S(T_0, H_0) - S(T_0, H_1) \quad [6]$$

By applying the external magnetic field  $H$  adiabatically the magnetic entropy decreases, but the total entropy has to remain constant.

$$S_0(T_0, H_0) = S(T_1, H_1) \quad [7]$$

Therefore the electronic  $S_{el}$  and the lattice part  $S_{lat}$  have to compensate the change of the magnetic entropy  $S_m$ .

$$\Delta S_m = \Delta S_{el} + \Delta S_{lat} \quad [8]$$

The change of the lattice entropy can lead for example to a change of the lattice vibration and therefore induces a temperature change of the solid.

$$\Delta T_{ad}(T) = T_2 - T_1 \quad [9]$$

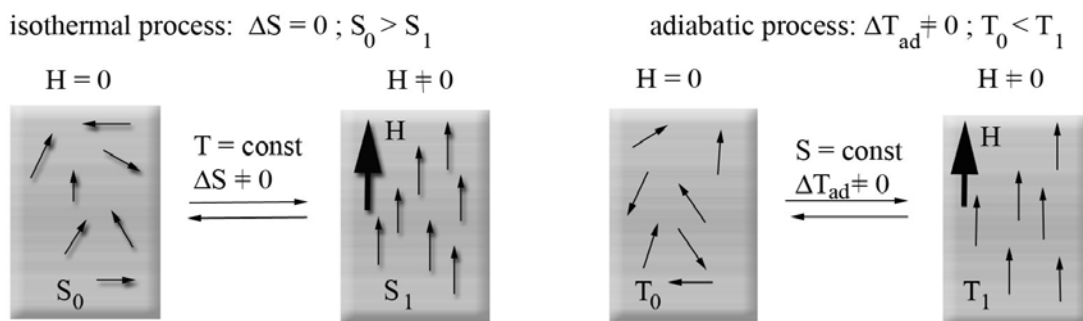


Figure 2.4.1: Schematic of the two processes taking place when a magnetic field is applied or removed from a magnetic system. The isothermal process goes along with an entropy change when changing the magnetic field and the adiabatic process, where the variation in field results in a temperature change of the sample.

This adiabatic temperature change  $\Delta T_{ad}(T)$  can be visualized as the isentropic difference of the corresponding functions of the entropy  $S(T,H)$  (see Figure 2.4.2)

Both the adiabatic temperature change  $\Delta T_{ad}(T)$  and the isothermal magnetic entropy change  $\Delta S_M$  values are characteristic for the magnetocaloric effect and are functions of the initial temperature  $T_0$  and the change of the external magnetic field  $\Delta H$ . The correlation of these two characteristic values, the adiabatic temperature change  $\Delta T_{ad}(T)$  and the magnetic entropy change  $\Delta S_M$ , with the magnetic field  $H$ , the magnetization  $M$  of the sample and the temperature  $T$  is given by the following Maxwell equation.

$$\left(\frac{\partial S(T, H)}{\partial H}\right)_T = \left(\frac{\partial M(T, H)}{\partial T}\right)_H \quad [10]$$

Considering that the electronic and the lattice part of the entropy are not affected by a magnetic field change, the change of the magnetic entropy for an isothermal and isobaric process can be calculated with the change of the magnetization by integrating equation 10.

$$\Delta S_m(T, \Delta H) = - \int_{H_1}^{H_2} \left(\frac{\partial M(T, H)}{\partial T}\right)_H dH \quad [11]$$

With the following two equations (eq.12 and eq.13), taking into account the heat capacity  $C_H$ ,

$$\left(\frac{\partial T}{\partial H}\right)_S = - \left(\frac{\partial S}{\partial H}\right)_T \left(\frac{\partial T}{\partial S}\right)_H \quad [12]$$

$$C_H = T \left(\frac{\partial S}{\partial T}\right)_H \quad [13]$$

the infinitesimal adiabatic temperature change can be calculated by using equation 14:

$$dT_{ad} = - \left(\frac{T}{C(T, H)}\right)_H \left(\frac{\partial M(T, H)}{\partial T}\right)_H dH \quad [14]$$

By integrating this equation the second characteristic value of the magnetocaloric effect, the adiabatic temperature change, can be quantified.

$$\Delta T_{ad}(T, \Delta H) = - \int_{H_1}^{H_2} \left(\frac{T}{C(T, H)}\right)_H \left(\frac{\partial M(T, H)}{\partial T}\right)_H dH \quad [15]$$

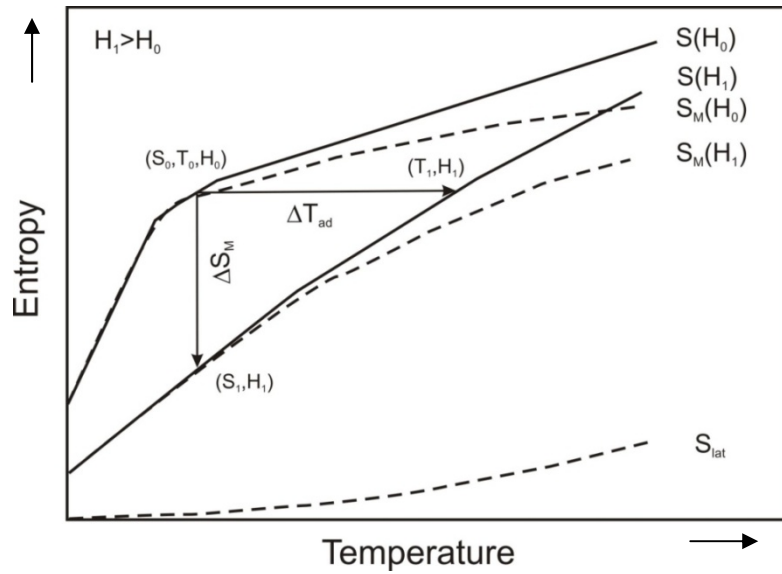


Figure 2.4.2: Schematic of the characteristic values (entropy  $S$ , lattice entropy  $S_{lat}$  and magnetic entropy  $S_M$ ) in two different magnetic fields, of the magnetocaloric effect, showing the isothermal and adiabatic process, which takes place when the magnetic field in a sample changes.

For ferromagnetic and paramagnetic solids some predictions for the MCE can be made using equation 11 and 15.

With the assumption that the magnetization of simple ferromagnets and paramagnets decreases with increasing temperature equation 15 has a negative second term  $(\partial M(T, H)/\partial T)_H < 0$ . By increasing the magnetic field, applied to a ferromagnet, the magnetic entropy decreases and can lead to an increase of the sample's temperature.

Furthermore simple ferromagnets show the maximum of  $(\partial M(T, H)/\partial T)_H$  at the Curie-temperature  $T_c$  and therefore a peak in the magnetic entropy change at this magnetic phase transformation.

Since  $(\partial M(T, H)/\partial T)_H$  is small in paramagnets the adiabatic temperature change increases only at temperatures close to absolute zero.

In order to quantify the magnetocaloric effect of materials, two different approaches are applicable (direct and indirect measurement) and will be explained in the following subsections.

## 2.4.1 DIRECT MEASUREMENT

The direct measurement of the MCE includes the determination of the initial temperature  $T_0$  and the temperature  $T_1$  of the sample, whereas the applied magnetic field changes from an initial value  $H_0$  to the final value  $H_1$ .

Therefore the adiabatic temperature change is given by the temperature change of the sample due to the change of the magnetic field:

$$\Delta T_{ad}(T_0, H_1 - H_0) = T_1 - T_0 \quad [16]$$

In order to measure the temperature change, a fast changing magnetic field is needed. The sample can be either moved out of a constant magnetic field or is fixed and the applied magnetic field is changing fast enough. In the latter case pulsed magnets can be used and MCE measurements in the range of 0 to 40T have been reported. When moving the sample and the magnetic field, respectively, permanent or superconducting magnets are used. In that case the magnetic field strength goes usually up to 10T.

Depending on the error in thermometry and the setting of the magnetic field and furthermore the insulation of the sample during the measurement, the accuracy of this technique can be claimed to be within 5 to 10%. Besides this relatively large uncertainty, another disadvantage is the missing information about the magnetic entropy change. Only the adiabatic temperature can be determined.

## 2.4.2 INDIRECT MEASUREMENT

The indirect experimental technique leads to the determination of both standard values of the MCE of a sample by using heat capacity measurements and the magnetic entropy change by using magnetization measurements. For the determination of the magnetic entropy change, the magnetization has to be measured depending on the change in temperature and the magnetic field and using equation 11. Here the uncertainty is given by the accuracy of the magnetic moments measurement and the accuracy of setting the magnetic field and temperature. Furthermore the uncertainty increases due to the replacement of  $\partial M$ ,  $\partial T$  and  $\partial H$  with  $\Delta M$ ,  $\Delta T$  and  $\Delta H$ . All these effects lead to an uncertainty of 3 to 10% in the values for the magnetic entropy change.

By determining the heat capacity at constant pressure and magnetic field as a function of temperature,  $C(T)_{p,H}$ , the adiabatic temperature change can be calculated using eq. 14, while the magnetic entropy change of a solid sample can be evaluated by the following equations:

$$S(T)_{H=0} = \int_0^T \frac{C(T)_{p,H=0}}{T} dT + S_0 \quad [17]$$

$$S(T)_{H \neq 0} = \int_0^T \frac{C(T)_{p,H}}{T} dT + S_{0,H} \quad [18]$$

Where  $S_0$  and  $S_{0,T}$  are the zero temperature entropies, which are equal in a condensed system [37]. However, these equations cannot be used in the case of a first order phase transformation,

since the entropy curves exhibit a discontinuity due to the entropy change of the transformation. To evaluate the discontinuity, the enthalpy of the transformation has to be determined in order to correct the entropy curve [38]. The uncertainty in the magnetic entropy change and the adiabatic temperature change strongly depend on the accuracy of the heat capacity measurements.

---

## 2.5 THE NI-MN-GA-SYSTEM – AN OVERVIEW

---

As already mentioned in section 2.1, the number of Heusler alloys is immense. Besides the alkali metals, the alkaline earths and the non-metallic elements, Heusler alloys can be built out of the combinations of the main group and B-group elements as well as the rare earth elements.

However Ni<sub>2</sub>MnGa is the only stoichiometric Heusler alloy, which is ferromagnetic and shows a martensite phase transformation, which was first described by P.J. Webster in 1984 [39]. In 1996 Ullakko et al determined a reversible magnetic field induced strain of 0.2% in the martensite phase of Ni-Mn-Ga single crystals [40]. Furthermore they verified a shift of the martensite temperature of up to 2°C in a magnetic field of 10T [41]. Wang *et al* suggested and established therefore the two way shape memory effect (see section 2.3) in this material [42].

---

### 2.5.1 THERMAL PROPERTIES

---

Like in all Heusler alloys, the thermal, structural and magnetic properties of the Ni-Mn-Ga – system highly depend on the composition. Jin *et al* showed by empirical mapping the influence of the change in composition on the Curie- and martensite temperature [43]. It was shown, that Ni-Mn-Ga exhibits a relatively stable magnetic phase transformation temperature over a large composition range (see Figure 2.5.1).

Starting from the stoichiometric compound and increasing the Ni-content about 5% replacing manganese for example leads to a decrease of the magnetic phase transformation of less than 20°C as well as the increase of manganese about 8% keeping the nickel-content constant, also results in a decrease of 20°C only.

However, the martensite temperature is strongly affected by the change of composition. Since Heusler alloys belong to the Hume-Rothery-alloys, their physical properties, like the crystal structure and the phase transformation temperature are a function of the valence electron concentration per atom  $e/a$ .

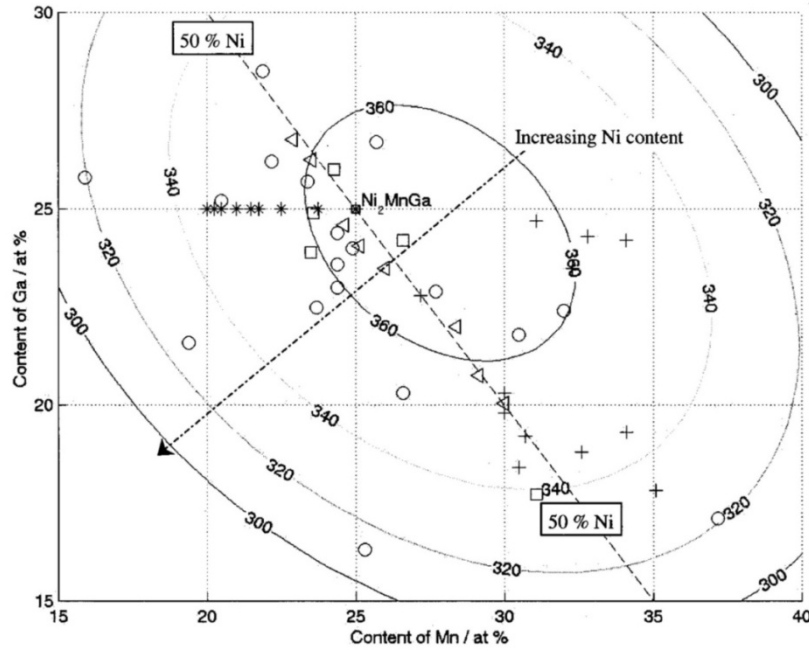


Figure 2.5.1: Contour view (taken from [43]) of the Curie temperature of Ni-Mn-Ga with superimposed second order two polynomial fitting curves including the experimental data of (o) Chernenko and (□) for single crystals [44,45], (+) Murray [46], (\*) Vasil'ev [47] and (Δ) Ullakko [48].

This can be calculated by using equation 19 taking into account, that nickel has 10 valence electrons ( $4s^23d^8$ ), manganese 7 ( $4s^23d^5$ ) and gallium 3 ( $4s^24p^1$ ) valence electrons. The concentration  $c$  of the elements is given in at-%.

$$e/a = \frac{10 \cdot c^{Ni} + 7 \cdot c^{Mn} + 3 \cdot c^{Ga}}{c^{Ni} + c^{Mn} + c^{Ga}} \quad [19]$$

The concentration of the valence electrons and the martensite temperature  $T_M$  of the Ni-Mn-Ga system show a linear correlation. Therefore the martensite temperature can be calculated using following equation taken from [43]

$$T_M = 702.5 \cdot (e/a) - 5067K \quad [20]$$

Comparing the calculated values with experimental data from Chernenko [45] and Richards [49] the equation 20 shows a good agreement (see Figure 2.5.2). From this relation it can be seen, that the increase of the nickel content replacing either manganese or gallium leads to an increase of  $T_M$ , whereas the replacement of nickel by manganese results in a decrease of  $T_M$ . Substituting gallium by manganese leads to an increase of the martensite temperature, while the increase of gallium replacing nickel or manganese always goes along with a decrease of  $T_M$ .

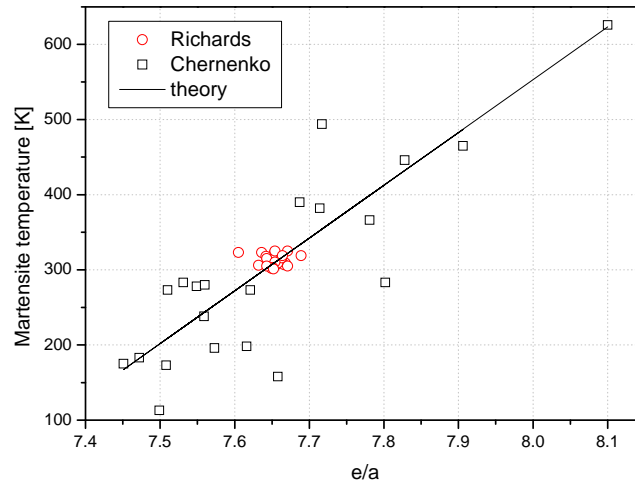


Figure 2.5.2: Martensite temperatures of Ni-Mn-Ga as a function of  $e/a$ . The black line shows a linear fit to the empirical values of the martensite temperatures calculated with eq. 20. The experimental data were taken from (□) Chernenko[45] and (○) Richards [49].

## 2.5.2 STRUCTURAL PROPERTIES

In 2000 Murray reached a magnetic field induced strain of 6% in an offstoichiometric  $\text{Ni}_{49.8}\text{Mn}_{28.5}\text{Ga}_{21.7}$ -single crystal at room temperature with a compressive stress of approximately 0.34MPa in a magnetic field of about 400 mT [50]. The crystal structure of alloys showing this 6% strain was verified as a tetragonal lattice with a five layered shuffling type modulation (see Figure 2.5.3 e, taken from [51]) and a  $c/a$  ratio  $< 1$  [52]. As explained in section 2.3, the maximum strain reachable in a MSM alloy is a function of the lattice parameters. Sozinov *et al* determined a MFIS of 9.5% in a  $\text{Ni}_{48.8}\text{Mn}_{29.7}\text{Ga}_{21.5}$  – single crystal at room temperature by applying a magnetic field of 1.05 T [53]. The sample showed an orthorhombic structure with a seven layer modulation along the  $(100)[\bar{1}\bar{1}0]_P$  system and a  $c/a$  ratio  $> 1$ . The maximal twinning strain  $\varepsilon_0$  reachable in this sample was 10.66%.

The crystal structures of Ni-Mn-Ga alloys have been extensively studied with various techniques like neutron and x-ray diffraction as well as TEM. The austenite phase in the stoichiometric  $\text{Ni}_2\text{MnGa}$  has been verified as the well known cubic  $L2_1$  Heusler structure (see Figure 2.1.1). In dependence of the composition different martensite phases of lower symmetry have been determined in this material.

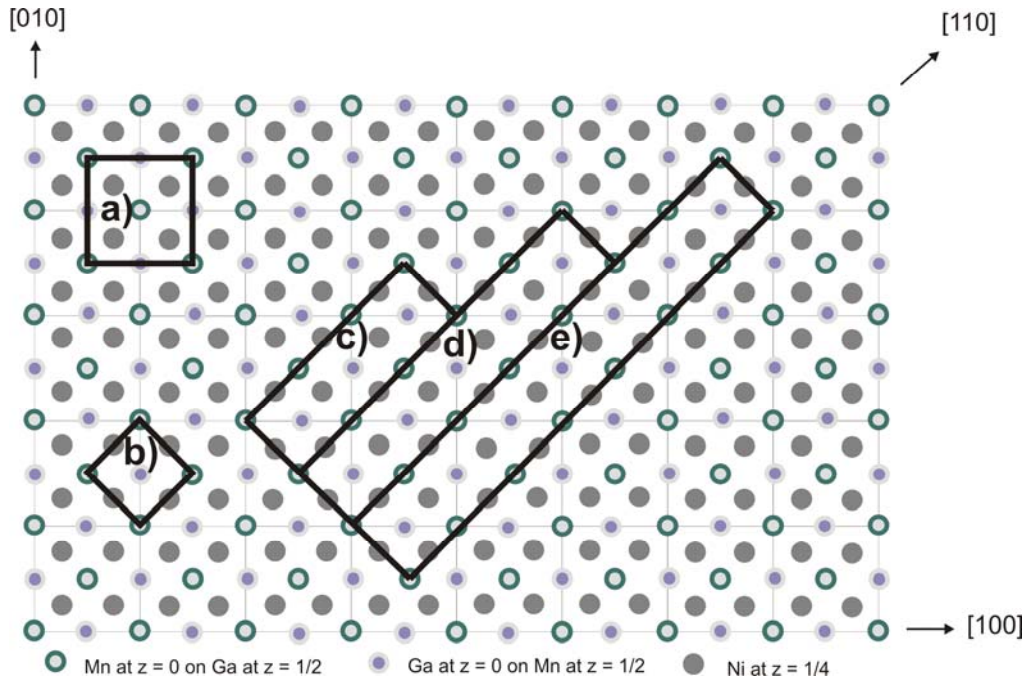


Figure 2.5.3: Projection in (001) plane of the  $L2_1$  -  $Ni_2MnGa$  - structure. The black squares show the austenite and different martensitic phases with the  $c$  axes of the cells perpendicular to the projection: (a) the  $L2_1$  unit cell, (b) the body centred tetragonal unit cell, (c) the premartensite 3-layered modulated super cell, (d) the 5-layered modulated super cell and (e) the martensite 7-layered modulated super cell

It has been shown, that, during the martensite phase transformation, Ni-Mn-Ga can undergo a contraction along one of the  $\langle 100 \rangle$  directions of the cubic phase. This tetragonal distortion of the parent phase leads to a strong deformation of the unit cell ( $c/a \approx 0.94$ ). Furthermore the martensite lattice shows a periodic shuffling along the  $(110)[\bar{1}\bar{1}0]_P$  system, whereby the modulation period is five (110) planes. In general Ni-Mn-Ga samples with that so called 5M martensite structure show a twinning stress  $\sigma_{tw}$ , which is low enough and a magnetic anisotropy, which is high enough, to induce a strain by applying a magnetic field [54,55].

By increasing the manganese/gallium ratio of the Ni-Mn-Ga-system (see Figure 2.5.4), a body centered monoclinic structure with seven (110) planes can be determined in the martensite. The structure is very close to an orthorhombic structure with the space group  $I2/m$  and a  $c/a$  ratio  $>1$  (see Figure 2.5.3 d) [56]. The maximum strain reachable in this structure lies around 10%. Like in the 5M - structure samples, the twinning stress  $\sigma_{tw}$  in 7M - samples is usually very small, which makes the magnetic shape memory effect possible [53, 57].

Another structure with a  $c/a$  ratio  $> 1$  has been found in Ni-Mn-Ga with a relatively high martensite transformation temperature and therefore a high  $e/a$  ratio. The structure has been verified as a body centered tetragonal  $L1_0$  structure without modulations, belonging to the space group  $I4/mmm$  (see Figure 2.5.3 b) [58]. Although the theoretical strain is about 20%, samples with that martensite structure receive less attention because of their high twinning stress, which makes a magnetic field induced strain impossible [59].

Beside these three “main structures”, Ni-Mn-Ga can exhibit several other more complicated modulated structures. Structures like the 8M structure have been found as an intermediate

phase cooling  $\text{Ni}_{50}\text{Mn}_{26.6}\text{Ga}_{23.4}$  from the cubic  $L2_1$  structure to the tetragonal non modulated (NM) structure [60].

Another precursor (intermediate) phase was found in  $\text{Ni}_2\text{MnGa}$  and Ni-Mn-Ga with an e/a ratio smaller than 7.6 having a well separated martensite and Curie temperature. The phase shows an orthorhombic [61] structure with threefold modulation along the (110) planes of the parent cubic phase.

For industrial applications e.g. in sensors or in actuators, based on the magnetic shape memory effect, the material which is used has to have a very low twinning stress in order to apply magnetic fields. Up to now, this property has been found only in martensite Ni-Mn-Ga exhibiting a 5M and 7M structure, respectively, which limits the composition range usable for this kind of application. Another limit is set by the requirements of the temperature range (see Figure 2.5.4). Depending on the application, the material has to show the MSM effect up to 140°C like in combustion engines. Such a high martensite phase transformation combined with a small twinning stress has yet to be reached.

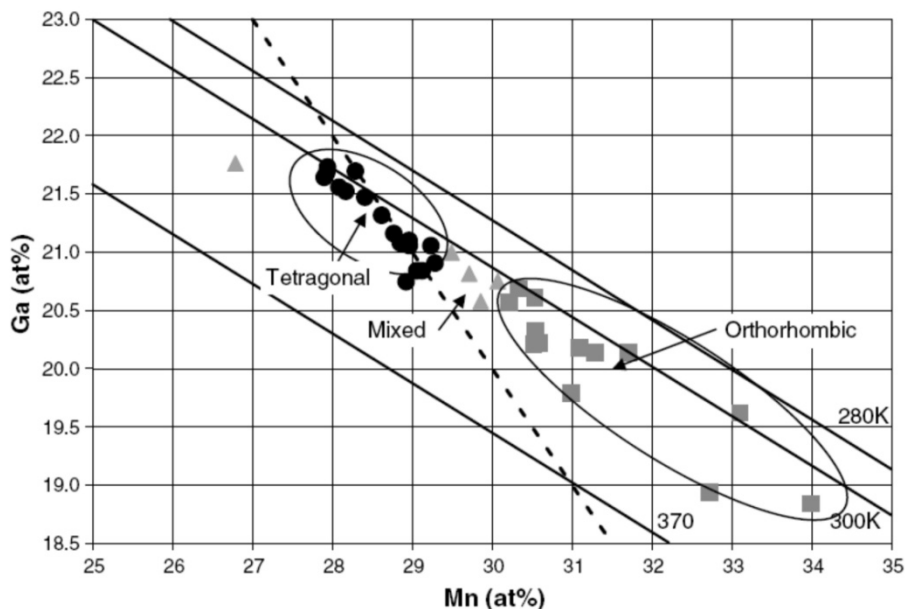


Figure 2.5.4: Structures of several Ni-Mn-Ga samples [49] as a function of the gallium and manganese content. The black lines indicate the martensite temperature, the dashed line shows compositions with 50% nickel. The black circles (●) represent compositions with a 5M structure, the grey squares (■) display compositions exhibiting a 7M structure. The triangles (▲) indicate the compositions, which show mixed phases of 5M and 7M structures.

### 2.5.3 MAGNETIC PROPERTIES

As mentioned in section 2.1, the magnetic properties of Heusler alloys are strongly influenced by the composition. In the  $L2_1$  phase,  $\text{Ni}_2\text{MnGa}$  has a magnetic moment of  $4.17 \mu_B$ , whereby the

main contribution to the magnetic moment comes from the manganese ( $3.86 \mu_B$ ) and only a small contribution of  $\approx 0.3 \mu_B$  from nickel. Therefore, the change of the manganese content results in a change of the magnetic properties, whereas, the change of the nickel content, while keeping the manganese content constant, has a much smaller effects on the magnetic properties. Jiang *et al* showed, that the excess of manganese leads to a strong decrease of the total magnetic moment of Ni-Mn-Ga [62]. In stoichiometric  $\text{Ni}_2\text{MnGa}$ , the manganese atoms interact indirectly via the gallium atoms, while in samples with manganese excess, the direct coupling of the manganese atoms leads to a local antiferromagnetic ordering in the  $L1_0$  structure.

In 2001 Hu *et al* determined a large magnetic field induced entropy change of  $18 \text{ J/kgK}$  at  $5 \text{ T}$  in  $\text{Ni}_{52.6}\text{Mn}_{23.1}\text{Ga}_{24.3}$  at the martensite phase transformation [63]. Cherechukin *et al* showed, that the saturation magnetization and the magnetocaloric effect in Ni-Mn-Ga depends on the composition [64]. With a decreasing manganese content, the saturation magnetization decreases as well as the magnetic field induced entropy change. Furthermore they have shown, that the entropy change on the first order structural phase transformation is much bigger than at the second order magnetic phase transformation. In 2007 Ingale *et al* have determined, that Ni-Mn-Ga with coincides structural and magnetic phase transformation show the highest magnetocaloric effect [65] (see Figure 2.5.5)

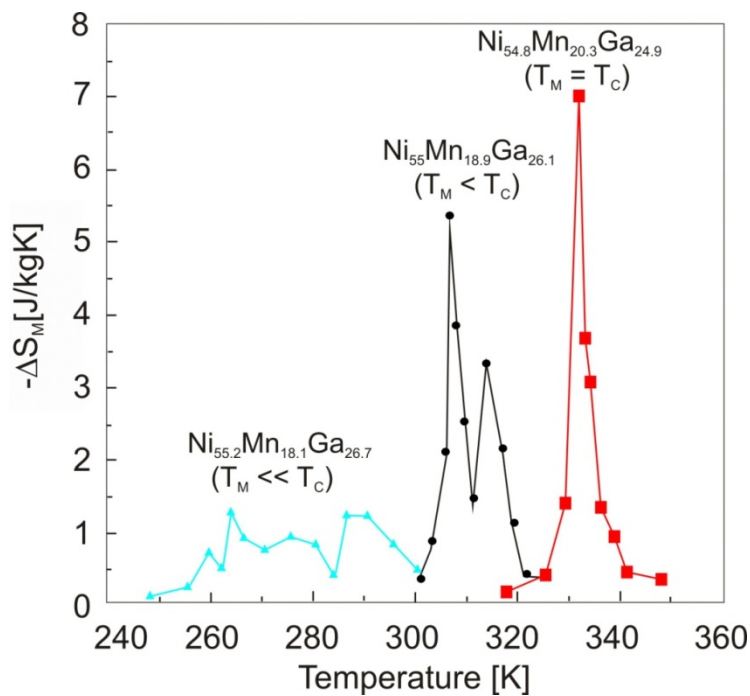


Figure 2.5.5: Magnetic entropy change of Ni-Mn-Ga samples with increasing Mn/Ga - ratio at their structural phase transformation in a magnetic field of  $1.2 \text{ T}$  (taken from [65]).

# CHAPTER 3 - EXPERIMENTAL TECHNIQUES

---

To determine the thermal, structural and magnetic properties of the produced samples, various established experimental techniques were used. This chapter will give only a short overview of these and can be studied in detail in several books and publications [66 - 72]. The stress – strain – experiments were performed with an especially designed device at the Boise State University [73, 74] (see section 3.7).

## 3.1 OPTICAL ANALYSIS

---

In order to visualize the martensite relief and the quality of the surface of the samples, light microscopy and scanning electron microscopy (SEM) were used.

With the light microscope a magnification of 100 times was possible, allowing visualization of the potential grain boundaries and pores in the micrometer range. The SEM made a magnification into the nm-range possible.

### 3.1.1 SCANNING ELECTRON MICROSCOPY

---

The SEM, used here, is a Philips XL 30 ESEM, which possesses a secondary electron detector and a backscattered electron detector. The electron beam is produced by a LaB<sub>6</sub> filament cathode and has an energy range from a few hundred eV up to 30 keV. For the Ni-Mn-Ga-Co samples a voltage of 20kV was used. The electron beam is focused by condenser lenses to a spot of 3 to 5 mm and can give a resolution down to 2 nm. This primary beam hits the sample surface, whereby the electrons are scattered either elastically from the atom cores or inelastically from the atom cores and electrons of the material. The first process results only in a change of the direction of the electrons but no change in energy. These back scattered electrons can leave the sample again and are determined by the detector system. The inelastic scattering can result in the emission of secondary electrons (SE) with a low energy and a small distance of operation. Therefore the SE do not contribute to the imaging of the surface. The teardrop like interaction volume of the primary beam extends from less than 100 nm to several μm, depending on the electron's landing energy, the atomic number of the specimen and the specimen's density.

## 3.2 ENERGY DISPERSIVE X-RAY SPECTROSCOPY

---

The SEM is connected with energy dispersive X-ray spectroscopy (EDX-S). This measurement method is used for the determination of the samples' composition.

Due to the interaction of the primary electron beam with the sample surface, electrons are inelastically scattered from atom cores or other electrons. Thereby, the primary electrons lose energy, which can interact with the electrons of the material and lead to the emission of inner shell electrons. The developed vacancy is filled up by an electron of a higher energy level. According to the potential model a difference between both energy levels of the electron shell exists. This energy difference is emitted in the form of a radiation quantum, characteristic for the element and shell (see Figure 3.2.1).

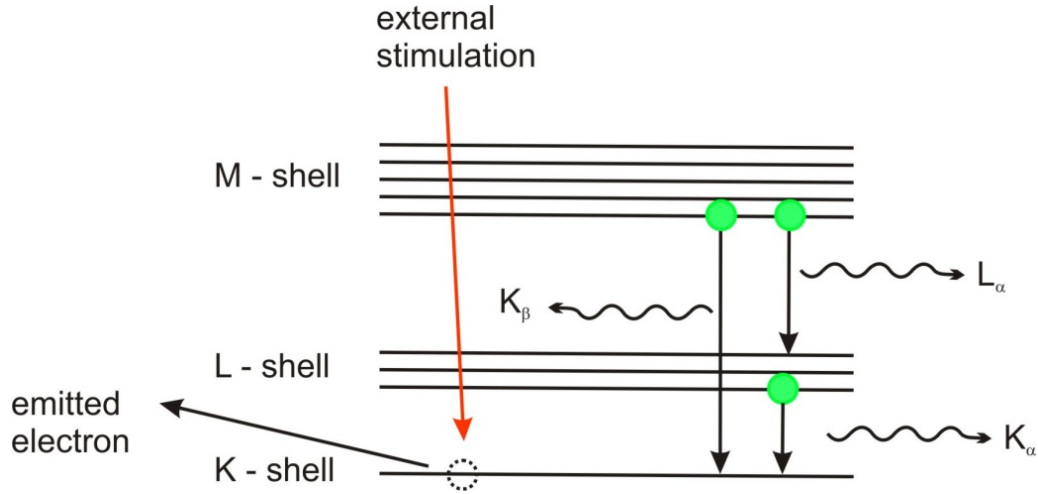


Figure 3.2.1: Principle of the characteristic X ray production by external stimulation for energy dispersive X-ray spectroscopy.

Characteristic X-ray radiation is used to determine the local composition of the sample. Therefore Moseley's law (equation 21) is used, which describes the relation between the nuclear charge of the atom ( $Z$ ) and the wavelength ( $\lambda$ ) and energy, respectively of the emitted radiation quantum:

$$\frac{1}{\lambda} = C(Z - \sigma)^2 \quad [21]$$

Where  $\sigma$  represents the screening constant, which depends on the shielding of the nuclear charge due to the electrons between the core and the observed emitted electron and therefore on the spectral line (for K lines,  $\sigma$  is equal to 1 and 7.4 for the more shielded L lines).  $C$  also depends on the spectral line and can be obtained by the following equation, taking into account the main quantum numbers of the initial  $n_1$  and final shell  $n_2$  as well as the Rydberg constant  $R_H$ :

$$C = R_H \left( \frac{1}{n_1^2} - \frac{1}{n_2^2} \right) \quad [22]$$

To increase the accuracy of the measurement, the spectrometer was calibrated, using a standard Ni-Mn-Ga-sample. The uncertainty in measurement lies around 1%.

---

## 3.3 DIFFERENTIAL SCANNING CALORIMETRY

---

The differential scanning calorimeter (DSC) has been used to determine the phase transformation temperatures of the samples. The measurement is based on the difference of the required amount of heat to increase the temperature of the sample and the reference sample. When the sample undergoes a physical transformation such as a phase transformation, more or less heat (depending whether it is an exothermic or endothermic phase transformation) has to flow from or to the sample being determined compared to the reference sample in order to maintain both at the same temperature.

The result of a measurement in the DSC is a curve of the heat flux versus the temperature or the time. For all samples a heating and cooling rate of 10K/min and 5K/min was used in a temperature range from 300K to 650K.

---

## 3.4 STRUCTURAL ANALYSIS

---

For the determination of the structure of single crystalline samples as well as powder samples, diffraction experiments were performed using X-rays and neutrons. This section describes some of the theoretical basics of the experimental techniques as well as the instruments used in this thesis to maintain the necessary information for cobalt alloyed Ni-Mn-Ga.

---

### 3.4.1 RECIPROCAL SPACE

---

Diffraction experiments are based on the coherent elastic scattering of a wave by the crystal. The space, where diffraction takes place is described by the reciprocal space. Similar to the basis vectors of the real space in a crystal  $\mathbf{a}$ ,  $\mathbf{b}$ ,  $\mathbf{c}$ , the reciprocal space is described by the translation vectors  $\mathbf{a}^*$ ,  $\mathbf{b}^*$ ,  $\mathbf{c}^*$ . In the case of an ideal crystal and an infinite lattice with the basis vectors  $\mathbf{a}$ ,  $\mathbf{b}$ ,  $\mathbf{c}$  diffraction intensity  $I(\mathbf{G})$  is only at the vectors

$$\mathbf{G} = h\mathbf{a}^* + k\mathbf{b}^* + l\mathbf{c}^*$$

[23]

Whereby  $h, k, l$  are the integer Miller indices. The peak found there is called a  $(hkl)$  reflection and each point  $hkl$  in a reciprocal lattice refers to a set of planes  $(hkl)$  in real space. The direction of the reciprocal lattice vector  $\mathbf{G}$  is normal to the  $(hkl)$  planes, while the length is reciprocal to the interplanar spacing  $d_{hkl}$ .

The basis vectors of the real space and reciprocal space satisfying the following conditions:

$$\mathbf{a}^* \cdot \mathbf{a} = \mathbf{b}^* \cdot \mathbf{b} = \mathbf{c}^* \cdot \mathbf{c} = 1 \text{ and } \mathbf{a}^* \cdot \mathbf{b} = \mathbf{a}^* \cdot \mathbf{c} = \mathbf{b}^* \cdot \mathbf{a} = \mathbf{b}^* \cdot \mathbf{c} = \mathbf{c}^* \cdot \mathbf{a} = \mathbf{c}^* \cdot \mathbf{b} = 0 \quad [24]$$

Furthermore both of these spaces are related in such a way, that the basis vectors of the reciprocal space can be calculated by

$$\mathbf{a}^* = 2\pi \frac{\mathbf{b} \times \mathbf{c}}{\mathbf{a} \cdot (\mathbf{b} \times \mathbf{c})}, \quad \mathbf{b}^* = 2\pi \frac{\mathbf{c} \times \mathbf{a}}{\mathbf{a} \cdot (\mathbf{c} \times \mathbf{a})} \quad \text{and} \quad \mathbf{c}^* = 2\pi \frac{\mathbf{a} \times \mathbf{b}}{\mathbf{a} \cdot (\mathbf{a} \times \mathbf{b})} \quad [25]$$

### 3.4.2 LAUE – EQUATION

When waves like x-rays or neutrons, are incident onto a single crystalline or polycrystalline structure they diffract, in more or less the same way a grating diffracts visible light. Based on this concept, Max Von Laue incorporated the three dimensions of real-crystal structures into a grating model, to create a mathematical framework for x-ray diffraction.

The diffraction of waves with a wavelength  $\lambda$  from a grating with a spacing  $d$  is described by following equation.

$$m\lambda = d(\sin\theta - \sin\theta_i) \quad [26]$$

Thereby  $\theta$  and  $\theta_i$  are the diffracted and incident angles with respect to the grating normal, while  $m$  is an integer and is the order of diffraction (zero for the straight through beam).

Max von Laue took the equation for grating diffraction [eq.26] and considered diffraction from a single row of point scattering centres, whereby each of the centres sits on a lattice point separated by the lattice parameter  $a$  (see Figure 3.4.1).

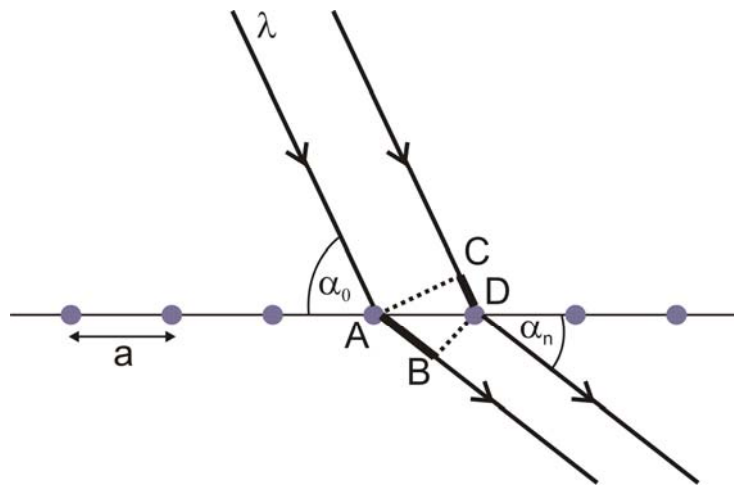


Figure 3.4.1: Diffraction from a grating with the repeatable distance  $a$  or a line of atoms

The path difference of rays scattering at points A and D is AB-CD. For constructive interference to occur, when the incoming rays are in phase, the path difference has to be equal to an integer multiple of the wavelength, which leads to the first Laue equation:

$$(AB - CD) = a(\cos \alpha_n - \cos \alpha_0) = n_x \lambda \quad [27]$$

With  $\alpha_n$  and  $\alpha_0$  defined as the angles between the diffracted and incident beams, respectively. However only one row of atoms is taken into account in eq. 27, which would give a scattering cone aligned along the atomic row and with the cone angle  $\alpha_n$ . The difference between the eqs. 26 and 27 has its origin from the angle taken for grating diffraction in eq. 26, which is taken between the incident or diffracted beam and the grating normal, whereas crystal diffraction deals with the angle between crystal planes (eq.27). Crystal diffraction also has to deal with three dimensions resulting in scattering from three-dimensional crystals and the scattering in specific directions in real space. Thereby the atomic arrangement in the y and z directions is taken to be equivalent to the x direction with scattering centers at lattice points separated by b and c in the respective directions. So eq. 27 can be adapted for these directions:

$$n_y \lambda = b(\cos \beta_n - \cos \beta_0) \quad [28]$$

$$n_z \lambda = c(\cos \gamma_n - \cos \gamma_0) \quad [29]$$

For a reflection to take place all three Laue equations have to be satisfied, meaning that the scattering is along the intersection of the three cones of diffraction. The three formulae can be restated in vector terms (Fig 3.4.2).

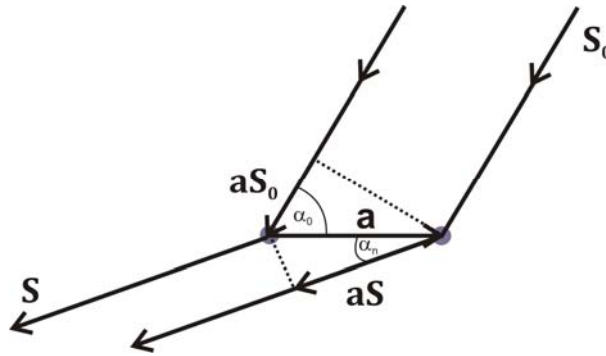


Figure 3.4.2: Vector notation of diffraction from a line of atoms in a particular direction

Depending on the direction, a, b and c become the respective unit cell vectors. Defining one unit vector parallel to the incoming rays  $S_0$  and one parallel to the scattered rays  $S$  results in some simple vector dot products, exemplified in following equations for the unit cell vector  $a$ :

$$aS = a \cos \alpha_n \quad [30]$$

$$aS_0 = a \cos \alpha_0 \quad [31]$$

$$a(\cos \alpha_n - \cos \alpha_0) = \mathbf{a}(\mathbf{S} - \mathbf{S}_0) = n_x \lambda \quad [32]$$

From a set of atoms separated by displacement vector  $\mathbf{r}$  and multiplying both sides by  $2\pi/\lambda$ , the three Laue equations condense down into one equation with the wavevectors  $\mathbf{k}$  and  $\mathbf{k}_0$ :

$$\mathbf{r}(\mathbf{k} - \mathbf{k}_0) = 2\pi n \quad [33]$$

The vector quantity  $\mathbf{k} - \mathbf{k}_0$  is known as the momentum transfer or Wavevector Transfer  $\mathbf{Q}$ , and for diffraction to occur this has to be equal to a reciprocal lattice vector  $\mathbf{G}$  (see subsection 3.4.4).

$$\mathbf{Q} = \mathbf{k} - \mathbf{k}_0 = \mathbf{G} \quad [34]$$

### 3.4.3 BRAGG FORMALISM

Considering that the crystal structure can be seen as planes of atoms with a certain distance  $d$  to each other, W.H. Bragg and L. Bragg [67] have shown that the intensity of an incident wave diffracted by the set of planes will be modulated by constructive or destructive interference. With atoms located on Bragg planes with the indices  $hkl$ , which are separated by  $d_{hkl}$ , the only surviving reflection results from constructive interference between waves reflected by a set of neighbouring planes. Hence, the difference in path length between waves from these neighbouring planes has to be an integral multiple of the wavelength  $\lambda$ . The condition for such a constructive interference is:

$$\begin{aligned} n\lambda &= d_{hkl} \sin \theta + d_{hkl} \sin \theta \\ &= 2d_{hkl} \sin \theta \end{aligned} \quad [35]$$

which is the Bragg equation, where  $n$  is an integer and  $\theta$  the angle between the Bragg plane and the incident and scattered beam respectively (see Figure 3.4.3), whereby the angle between the incident and scattered particle is  $2\theta$ .

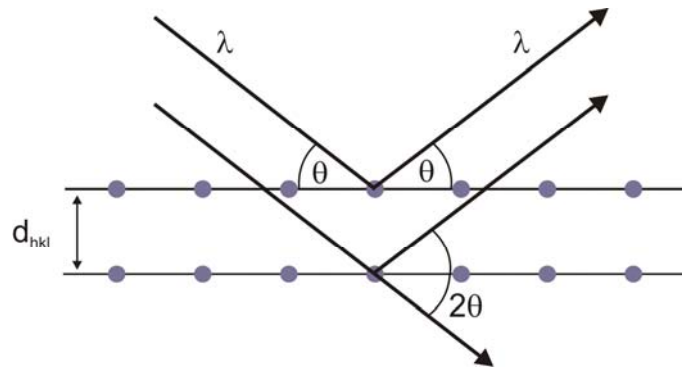


Figure 3.4.3: Origin of the Bragg equation: Schematic diagram of the scattering from parallel, neighbouring planes of atoms which are separated by a distance  $d$ . The incident and reflected waves have the wavelength  $\lambda$ .

### 3.4.4 EWALD SPHERE

To determine which lattice planes will give a constructive interference for a given wavelength, Ewald developed a sphere of reflections. This geometric construct is used in electron, X-ray and neutron crystallography. Considering a reciprocal lattice of a crystal, which has its origin at 000, a sphere can be drawn through the origin of the reciprocal lattice (see Figure 3.4.4). Thereby the radius of the sphere is equal to the wave vector  $\mathbf{k}_0 = 2\pi/\lambda$  of the incident beam.

If any of the reciprocal lattice points lies on the surface of this Ewald sphere, this point satisfies the Laue condition

$$\mathbf{Q} = \mathbf{G}$$

[34]

and a diffraction peak in the direction of the corresponding hkl reciprocal lattice point can be determined.

Using a monochromatic beam, only a few peaks satisfy Laue's condition and in the case of the structural analysis of a single crystal, a rotation of the crystal and therefore a rotation of the corresponding reciprocal lattice is commonly used to set the diffraction conditions of various hkl Bragg reflections.

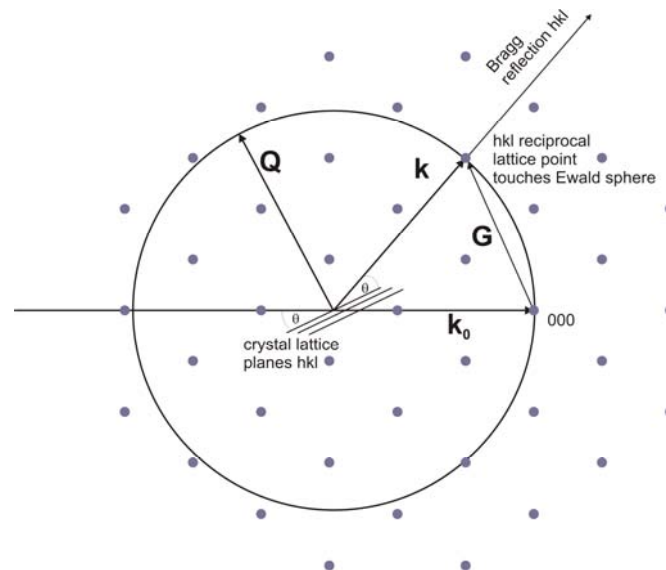


Figure 3.4.4: Ewald sphere construction in reciprocal space, showing the diffraction condition for the hkl reflection.

### 3.4.5 NEUTRON DIFFRACTION

Neutrons are suitable particles to study the nuclear and magnetic structures of materials. Since a neutron is a particle without a charge, it can penetrate material and, where applicable, the auxiliary facilities for the experiment. Therefore a neutron diffraction experiment is an excellent probe to perform non-destructive analysis of the structure of a bulk material. Furthermore, the neutrons interact with the nuclei of the material instead of the electron cloud, unlike x-rays, giving rise to the study of materials containing lighter elements like hydrogen.

Due to the focus on neutron diffraction, only elastic neutron scattering is treated in the following subsection, which implies, that the momentum transfer vector  $\mathbf{Q}$  is equal to the reciprocal lattice vector  $\mathbf{G}$  (see equation 34).

To determine the crystal structure of a material, it is necessary to analyse the amount of elastically scattered neutrons in a specific area of space  $dS$ , which is defined by the differential cross section  $d\sigma/d\Omega$ . Consider, that  $\varphi_0$  and  $\varphi_f$  are the incoming and final wave functions of the neutrons and  $d\Omega$  is the solid angle, where the scattering is determined, the differential scattering cross section is defined by following equation:

$$\begin{aligned} \frac{d\sigma}{d\Omega} &\equiv \frac{\text{number of neutrons scattered into the solid angle } d\Omega \text{ per second}}{\Phi \cdot d\Omega} \\ &= \frac{v|\varphi_f|^2 dS}{v|\varphi_0|^2 d\Omega} = \frac{|\varphi_f|^2}{|\varphi_0|^2} r^2 \end{aligned} \quad [36]$$

Where  $\Phi$  is the total flux of incident neutrons,  $v$  is the speed of the neutrons and

$$dS = r^2 d\Omega \quad [37]$$

Starting from the scattering of a neutron from one nucleus, the incoming neutron is described by a plane wave

$$\varphi_0 = e^{ik_0 r} \quad [38]$$

Due to the weak interaction of the neutrons with the material, the scattering can be treated according to the Born approximation [69], assuming, that the unperturbed incoming wave  $\varphi_0$  is scattered from  $r$ , neglecting the attenuation of  $\varphi_0$  on its path to the nucleus as well as multiple scattering. Therefore, the scattered neutron is described by a spherical wave, including the amplitude  $b$  as the scattering length of the nucleus:

$$\varphi_f = -b \frac{e^{ik_f r}}{r} \quad [39]$$

By combining the equations 36, 38 and 39 and assuming that  $|k_o|=|k_f|$  for elastic scattering, the differential neutron cross section for one nucleus can be written as

$$\frac{d\sigma}{d\Omega} = b^2 = \text{const} \quad [40]$$

However looking at the intensity of Bragg reflections of a system of  $n$  atoms of a monoatomic lattice, a structure factor  $F(\mathbf{G})$  has to be taken into account. Due to interference of the scattered neutrons with each other, the intensity of the Bragg peaks depend on the particular structure of the unit cell. The unit cell can be seen as a set of identical scatterers at the positions  $r_1$  to  $r_j$  within the cell, whereupon the amplitudes of two waves scattered at two different positions, differs by the factor  $e^{i\mathbf{G}(r_i-r_j)}$ . For an entire primitive cell, the absolute amplitude of a Bragg Peak contains the factor

$$F(\mathbf{G}) = \sum_{j=1}^n e^{i\mathbf{G} \cdot r_j} \quad [41]$$

If the unit cell consists of different elements, the structure factor changes to

$$F(\mathbf{G}) = \sum_{j=1}^n f_j(\mathbf{G}) e^{i\mathbf{G} \cdot r_j} \quad [42]$$

Where  $f_j(\mathbf{G})$  is determined by the internal structure of elements occupying the different positions from  $r_1$  to  $r_j$  in the unit cell. In case of neutron scattering this atomic form factor becomes

$$f_j(\mathbf{G}) = \int \varrho_r(\mathbf{r}) e^{-i\mathbf{G} \cdot \mathbf{r}} dV \quad [43]$$

With  $\varrho_j(\mathbf{r})$  as the scattering density, which is equal to the negative scattering length  $b$  by integration and neglecting the magnetic part.

$$f_j(\mathbf{G}) = -b_j \quad [44]$$

As it can be seen in the following equation, the nuclear structure factor  $F_{\text{nucl}}$  is the sum of the scattering of  $n$  atoms of the unit cell at the position  $r_j$ , taking into account the particular

characteristic nuclear scattering lengths  $b_j$  and a third Factor  $e^{-W_j}$ , known as the Debye – Waller – Factor [66],

$$F_{nucl}(\mathbf{G}) = F_{hkl} = \sum_j -b_j \cdot e^{i\mathbf{G}r_j} e^{-W_j} \quad [45]$$

This factor includes the mean square atomic displacement  $\overline{u_j^2}$ , accounting for the reduction in scattered amplitude due to thermal vibrations of the atoms:

$$W_j = \frac{1}{2} \mathbf{G}^2 \overline{u_j^2} \quad [46]$$

Neglecting the Debye – Waller – factor (possible for low temperature measurements), equation 45 can be written as

$$F_{hkl} = \sum_{j,\alpha} -b_j \cdot e^{2\pi i(h \cdot u_\alpha + k \cdot v_\alpha + l \cdot w_\alpha)} \quad [47]$$

Where h, k and l are the Miller indices of the atoms and  $u_\alpha, v_\alpha, w_\alpha$  are the coordinates of the atoms in units of the lattice constants and  $2\pi(hu_\alpha + kv_\alpha + lw_\alpha)$  describes the phase angle of the particular atom.

It can be seen, that the determination of the nuclear structure factor requires the measurement of the integrated intensity  $I_{hkl}$  of the Bragg reflection, as

$$I_{hkl} \propto |F_{hkl}|^2 \quad [48]$$

enabling the determination of the magnitude of  $|F_{hkl}|$  by the intensity of the hkl - reflection's intensities.

For this thesis, different diffractometers have been used to characterize single crystalline and powder samples of Ni-Mn-Ga-Co.

---

## THE HZB INSTRUMENTS E3 AND E7

---

The instruments E3 and E7 were used to determine the lattice parameters of single crystalline Ni-Mn-Ga and Ni-Mn-Ga-Co samples, by measuring the Bragg reflections of one (hk0) plane and using Bragg's law (eq. 35)

Both instruments, which are neutron two axes diffractometers, are actually designed for residual stress measurements, providing a high resolution in d spacing measurements. Therefore they can be also be used as single crystal diffractometers.

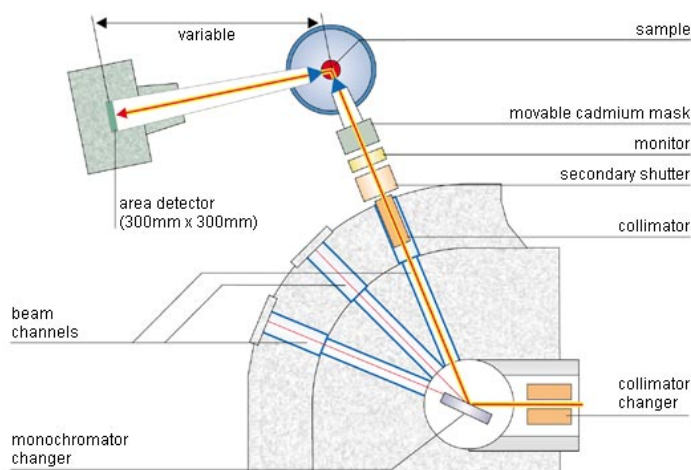


Figure 3.4.5: Schematic of the HZB Instrument E3

The instrument E3 (see Figure 3.4.5) provides a  $2\theta$  range from  $35^\circ$  to  $110^\circ$  and can be equipped with an Eulerian cradle or cryostat and furnace, respectively. The 2 dimensional 300mm x 300mm detector with a resolution of 256 x 256 pixels covers a diffraction range of approximately  $10^\circ$ . With the double focussing bended silicon monochromator, a monochromatic beam with a wavelength of  $1.486 \text{ \AA}$  [70], samples are probed. E7 covers the same diffraction range with a wavelength of  $1.8304 \text{ \AA}$  coming from a (110) copper monochromator and a 200mm x 200mm area detector with a resolution of 128 x 128 pixels.

Both instruments are equipped with a camera system to simplify the alignment of the sample on the transformation tables ( $x, y, z$  - direction) having two omega circles on top, allowing measurements of (hk0) planes of single crystalline samples by rotating the sample up to  $270^\circ$  for every particular  $2\theta$  range, the detector covers.

## THE ILL INSTRUMENTS D9 AND D10

The instruments D9 and D10 at the Institut Laue Langevin are four circle diffractometers, designed for single crystal diffraction (see Figure 3.4.6).

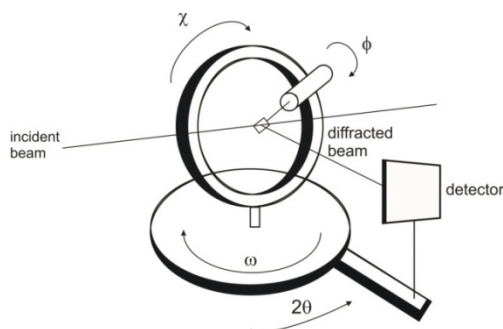


Figure 3.4.6: Schematic of a 4-circle diffractometer, depicting the 4 different angles used for the determination of structural parameters in single crystals.

A four circle diffractometer is a standard instrument, used for diffraction measurements on single crystals at constant wavelengths. This kind of instrument enables the determination of integrated intensities  $I_{hkl}$  of Bragg reflections by measuring the total intensity of each, while the crystal rotates through the reflections with a constant angular velocity.

The  $\chi$  - and  $\phi$  - circle of the instrument are realized by using an Eulerian cradle (see Figure 3.4.6). The sample is mounted on a goniometer, which is attached to the  $\phi$  - circle and rotates about the  $\chi$  - axis. These two connected circles rotate about the  $\omega$  - circle, which is vertical to them and coaxial with the fourth circle. The fourth circle is the  $2\theta$  axis and is independent from the others and rotates the detector in the horizontal plane. Therefore, the (hkl) – reflections of the mounted crystal are measured by bringing the particular diffraction vectors  $\mathbf{G}$  into the horizontal plane.

For the determination of the integrated intensities of a specific structure on a four circle diffractometer, the crystal has to be centred and aligned within the instrument by searching for Bragg reflections at low  $2\theta$  in order to define approximate values of the lattice parameters. All remaining reflections, which are possible for a specific structure can then be computed and measured. Thereby, the integrated intensity  $I_{hkl}$  is measured by turning the crystal through the  $\omega$  - axis, scanning the diffraction vector  $\mathbf{G}$  in small steps through the Ewald sphere and summing up the neutron counts of each step.

The hot neutron diffractometer D9 (see Figure 3.4.7), with a Cu (220) monochromator is used for accurate measurements of Bragg intensities up to very high momentum transfer. The resolution allows the detailed study of atomic disorder and atomic thermal motions. The wavelength of the neutrons is among the shortest available for a neutron instrument and has a continuous choice of wavelengths in the range 0.35 - 0.85 Å. For the performed measurements a wavelength of 0.85 Å was used. The instrument is equipped with a 2-D area detector which is particularly useful for rapid alignment and characterisation of samples and for studies of satellites and twinning. It covers  $8^\circ \times 8^\circ$  in  $32 \times 32$  pixels.

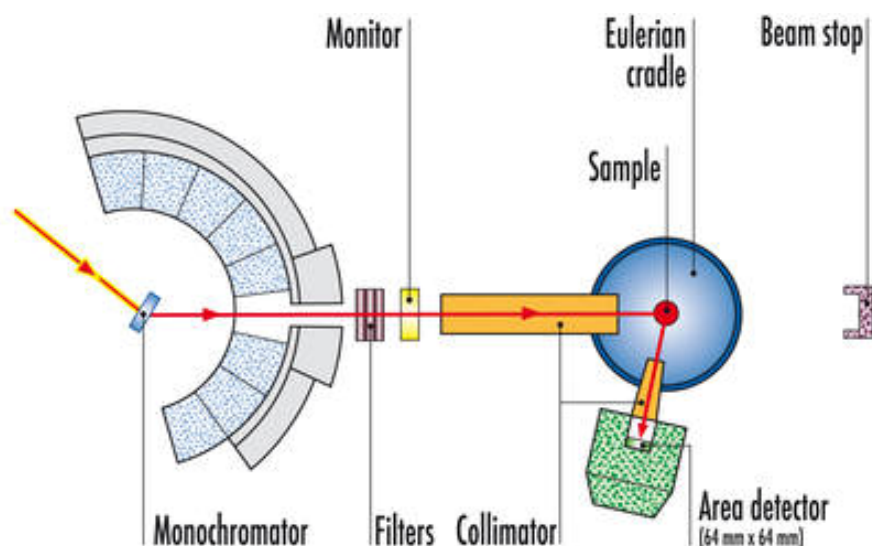


Figure 3.4.7: Schematic of the ILL instrument D9, a four circle diffractometer, which enables the measurement of various hkl –reflections of a sample and makes the determination of atomic positions and magnetic structures possible. Since D10 is also a four circle diffractometer, the principle is the same as that shown in this schematic.

The thermal neutron instrument D10 operates at a higher wavelength range between 1.1 Å and 3 Å using a (200) copper monochromator and between 1.8 Å and 6 Å using pyrolytic graphite, respectively. The Eulerian cradle of the instrument can be equipped either with a helium-flow cryostat allowing measurements from 1.6 K to 450 K, or 0.1 K to 10 K in dilution mode, or with a hot-air furnace enabling measurements of up to 1000 K. D10 provides two detectors in the diffraction configuration: one 80x80 mm<sup>2</sup> 2D detector for three-dimensional resolution in reciprocal space, and a single <sup>3</sup>He detector when the highest efficiency and lowest background are required.

Both instruments were used to determine the distribution of cobalt within the Ni-Mn-Ga unit cell in the high and low temperature phase. On D9 a wavelength of 0.83 Å was chosen, while on D10 the experiments were performed with a wavelength of 1.26 Å.

### 3.4.6 X-RAY DIFFRACTION

X-rays are electromagnetic radiation of wavelengths in the range of 1 Å, which is about the same size as an atom. They occur in the region of the electromagnetic spectrum between gamma-rays and ultraviolet. The discovery of X-rays in 1895 by K. Röntgen enabled the determination of crystalline structures at the atomic level.

While neutrons interact with the nucleus of the atom, X-rays are scattered on the electrons of the atoms. The depth of penetration of laboratory X-ray devices lies in the range of several millimetres, while the range for thermal neutrons (5-100meV) lies in the centimetre region. Furthermore the interaction with the electrons instead of the nuclei of the atoms leads to significant differences of the measured intensities. The atomic form factor (equation 43) has to take the expansion of the scattered object, the electron cloud into account.

$$f_j(\mathbf{Q}) = \int \rho_j(\mathbf{r}) e^{-i\mathbf{Q}\cdot\mathbf{r}} dV \quad [49]$$

Considering a spherical charge density  $\rho_j(r)$  distribution of the atom and neglecting the charge density between the atoms, the atomic form factor only depends on the momentum transfer  $\mathbf{Q}$  and leads to following equation when using spherical coordinates:

$$f_j(\mathbf{Q}) = \int_0^{R_j} dr \int_0^\pi d\vartheta \int_0^{2\pi} d\varphi \rho_j(r) r^2 \sin \vartheta e^{-iQr \cos \vartheta} = \int_0^{R_j} 4\pi r^2 \rho_j(r) \frac{\sin Qr}{Qr} dr \quad [50]$$

Assuming also scattering with  $\mathbf{Q} \rightarrow 0$ , only the scattering density has to be integrated, which results in the total number  $Z$  of the scattered atom's electrons.

$$f_j(\mathbf{Q} \rightarrow 0) = \int_0^{R_j} 4\pi r^2 \rho_j(r) dr = Z$$

[51]

As already seen in subsection 3.4.5, the scattering intensity is proportional to  $f^2$ . In contrast to the Q-independent scattering length  $b$  of the neutrons, the atomic form factor of the X-rays shows a Q-dependence and is proportional to  $Z^2$  for small angles.

In this thesis X-ray diffraction has been performed to probe powder samples of Ni-Mn-Ga-Co. In this case a BRUKER D8 Advance in Bragg-Bentano-Geometry and Cu- $K_\alpha$ -radiation with a wavelength of 1.5418 Å was used.

## 3.5 VIBRATING SAMPLE MAGNETOMETER

For determining the magnetic properties of materials, a vibrating sample magnetometer is a widely used instrument. This experimental technique was invented by Simon Foner in 1959 [75] and enables measurements of the magnetization of a material in a wide temperature range (from 2K up to 1000K) and magnetic field variation (from 0T up to 14T).

The measurement technique is based on Faraday's law, stating that an electromagnetic flux is generated in a coil, when a magnetic flux, linked to the coil, changes. The electromagnetic flux in a coil with  $n$  windings and a cross – sectional area  $a$  can be calculated by

$$E = -na \frac{dB}{dt}$$

[52]

Positioning this coil in a constant magnetic field  $H$ , the magnetic flux density  $B$  is given by the following equation (eq.53) and is described by equation 54 when a sample with a magnetization  $M$  is brought into the coil:

$$B = \mu_0 H$$

[53]

$$B = \mu_0 (H + M)$$

[54]

Hence the flux change is

$$\Delta B = \mu_0 M \quad [55]$$

By combining the two eqs. 48 and 51, it can be seen, that the output signal of the coil is proportional to the magnetization  $M$ , but independent of the applied magnetic field  $H$ :

$$Edt = -na\mu_0 M \quad [56]$$

If the sample is vibrated with sinusoidal motion within the suitable placed pick-up coils in a magnetic field  $H$  a sinusoidal electrical signal can be induced in these coils (see Figure 3.5.1). The signal has the same frequency of vibration and its amplitude will be proportional to the magnetic moment, amplitude, and relative position with respect to the pick-up coils system.

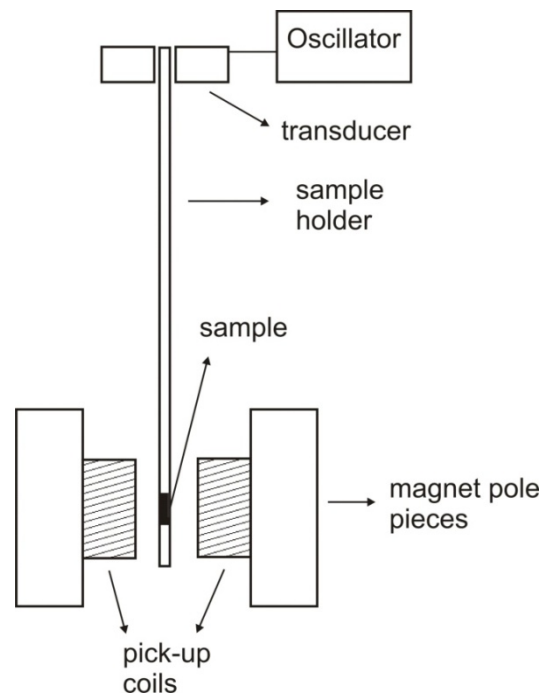


Figure 3.5.1: Schematic of the principle of a vibrating sample magnetometer.

## 3.6 STRESS-STRAIN - MEASUREMENTS

A determining factor for all MSM – alloys is the twinning stress of the material, since only a relatively low twinning stress can be overcome by a magnetic field (see section 2.3). For the determination of the stress – strain – behaviour of the Ni-Mn-Ga-Co – single crystalline samples, the static magneto-mechanical device (SMMT) at Boise State University, Idaho, USA, [73, 74] was used.

With the SMMT, it is possible to perform uniaxial compression experiments with and without an applied orthogonal magnetic field (see Figure 3.6.1).

Therefore the sample with two parallel surfaces is placed between two pressure pistons, which introduce the uniaxial compression. While the pistons, equipped with a 500N load cell (MTS Schaffhausen), load and unload the sample with a constant speed of  $2 \times 10^{-6} \text{m/s}$ , two quartz glass push rods transmit the displacement of the pistons surfaces and with it the induced strain of the sample to the extensometers (Heidenhain, Traunreut).

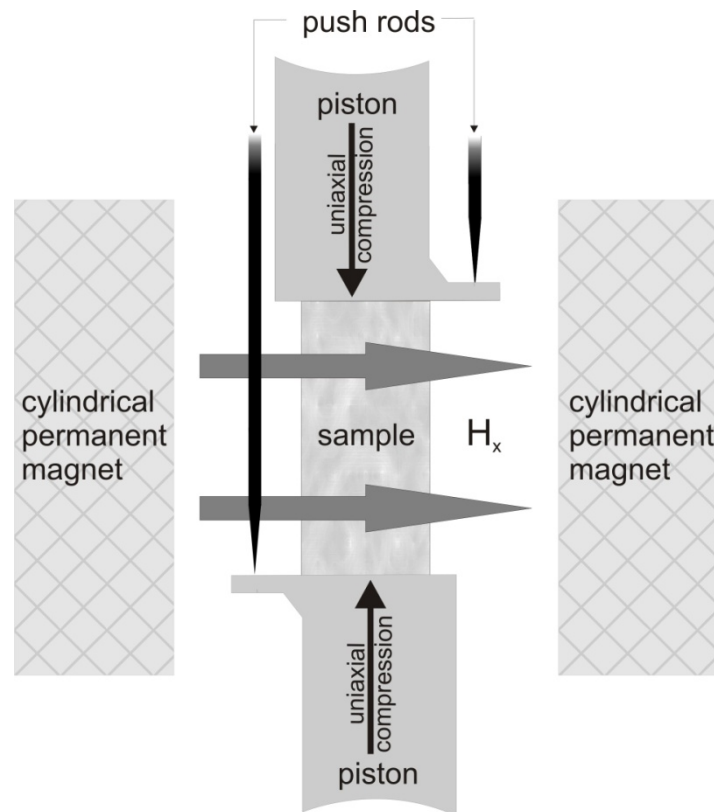


Figure 3.6.1: Setup of the stress – strain device at the Boise State University [73, 74]. Due to the non-magnetic pistons, push rods and extensometers used for the device, determination of the mechanical and magnetic field induced strain of a magnetoplastic material are possible.

The device is insensitive to magnetic fields, which enables accurate measurements of the magnetic field induced strain of the sample. The variable magnetic field with a maximum of 2 T is produced by a cylindrical permanent magnet (Magnetic Solutions, Dublin) with a field direction that can be rotated with the plane orthogonal to the mechanical compression direction.

The force resolution of the device is better than 0.5 N, which corresponds to an uncertainty of 0.1 MPa. The uncertainty in displacement is better than 10 nm. The applied magnetic field shows a better homogeneity than 1% for the field strength  $H$  at the position of the sample. Furthermore the deviation for the field direction is less than  $1^\circ$  for any arbitrary direction within the perpendicular plane to the loading direction. The resolution of the magnetic field is better than 0.1 mT.

# CHAPTER 4 – SAMPLE PREPARATION

---

## 4.1 WHY SINGLE CRYSTALLINE MATERIALS?

Magnetic Shape memory alloys are promising materials to substitute giant magnetostrictive systems and piezoelectrical ceramics in actuating devices due to their large actuation strains. Furthermore the actuation stress needed to induce the strain is much lower than in other well known actuator materials (see Figure 4.1.1) and can be induced magnetically, which enables the development of actuators with higher working frequencies than for example realizable in shape memory materials.

However large magnetically induced strains of 5 to 10 % in low magnetic fields of less than 500mT have been achieved only in single crystalline materials, while polycrystalline samples show a much smaller strain of approximately 0.1 to 1% [76, 77]. Due to their low twinning stress and relatively high working temperature, Ni-Mn-Ga alloys seem to have the most potential for applications in actuators and sensors.

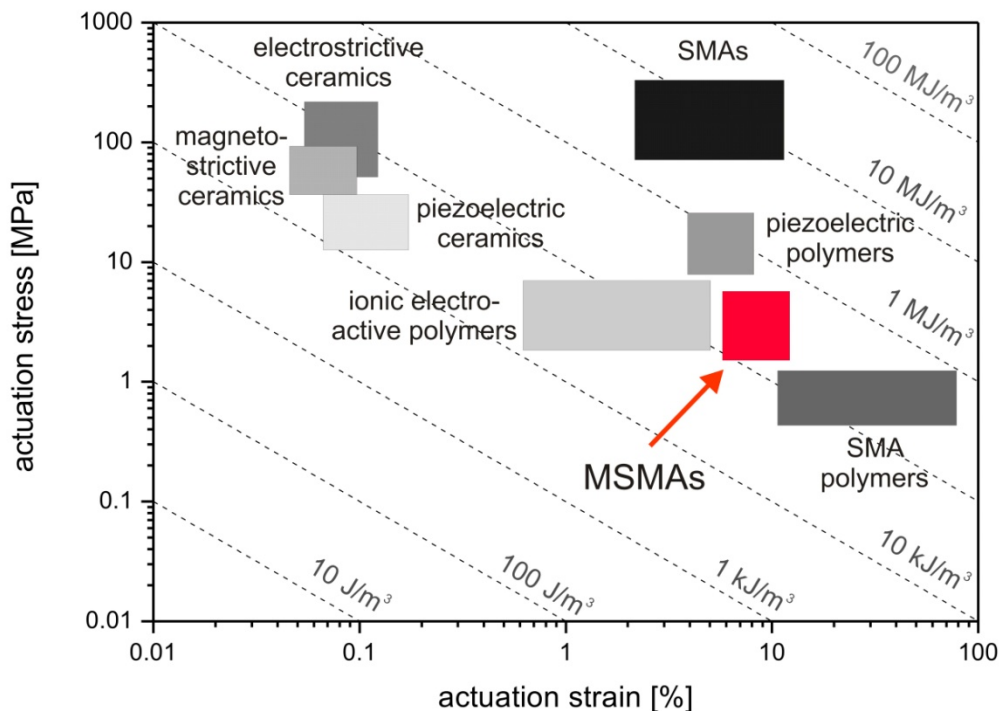


Figure 4.1.1: Typical ranges of actuating stress and strain of different actuator materials. [78] The dashed lines depict the work output of the materials, which is defined as the residual force times the residual way and is given here per volume. Therefore it is assumed, that the material is working under constant stress.

In order to improve the properties, like phase transformation temperatures and ductility, of Ni-Mn-Ga as an actuator material, different compositions of Ni-Mn-Ga were alloyed with different amounts of cobalt. Growing single crystals from these alloys involves overcoming several difficulties, like the high vapour pressure of the manganese, which can impede the production of high quality single crystalline samples and makes an application difficult. Therefore the

development of a new and reliable single crystal growth technique, avoiding those problems was necessary. Therefore a modified Bridgman technique has been developed successfully at the Helmholtz – Centre Berlin for Materials and Energy.

All samples produced for this thesis, were grown with this new Bridgman like technique called Slag remelting and Encapsulation (SLARE) – technique [79].

---

## 4.2 CRYSTAL GROWTH – TECHNIQUE

---

Crystal growth techniques can be classified roughly by the medium the crystal is grown from, like from a gaseous phase, liquid phase or from the melt. For detailed information about crystal growth techniques several books can be recommended (e.g. [80-82]).

Focussing on the growth techniques from the melt, the most common techniques are the Czochralski – technique [80], where a crystal seed is dipped into the melt, on which crystallization takes place and the Bridgman – technique [81], which will be briefly introduced in the following section.

---

### 4.2.1 BRIDGMAN – TECHNIQUE

---

The Bridgman technique is based on the movement of the solidification front of the material, by moving the crucible or the furnace during the crystal growth. The maximum temperature of the furnace has to be about 50 to 100K higher than the melting point of the material. In this temperature range, the crucible has to be placed for the homogenisation of the melt, before the kneeling can start. For the development of a crystal seed a temperature gradient in the furnace is necessary. This can be realised either by different distances from the heating systems to the crucible along the furnace or by using a two-zone furnace or a cooling system on the bottom of the furnace. By kneeling the crucible into the temperature range below the melting point a crystal seed is build and crystallisation starts on the tip of the crucible.

Due to the geometry, only a few, in the best case only one crystal seed is preferred and by kneeling the crucible further down, the seed grows further. Depending on the number of crystal seeds build during the process, a poly or single crystalline rod grows, limited only by the size of the crucible.

However the temperature gradient flattens out towards the crystal axis, since the heat dissipation in the melt becomes smaller from the walls to the centre of the crucible, which causes more defects towards the axis of the crystalline rod. Due to this phenomenon, the bigger the diameter of the crucible is, the more defects develop in the centre of the crystal, reducing the quality of the sample.

Depending on the material, a gaseous atmosphere during the growth process is necessary. Highly reactive materials have to grow in a noble gas atmosphere, to avoid the reaction of oxygen with the melt for example. Furthermore the gas pressure can avoid the loss of elements with a high vapour pressure during the growth process.

## 4.2.2 SLAG REMELTING AND ENCAPSULATION (SLARE) – TECHNIQUE

The Slag Remelting and Encapsulation technique is also based on the movement of the temperature gradient during the crystal growth. Like with the conventional Bridgman technique, the crucible with the melt inside is kneeled through a temperature gradient.

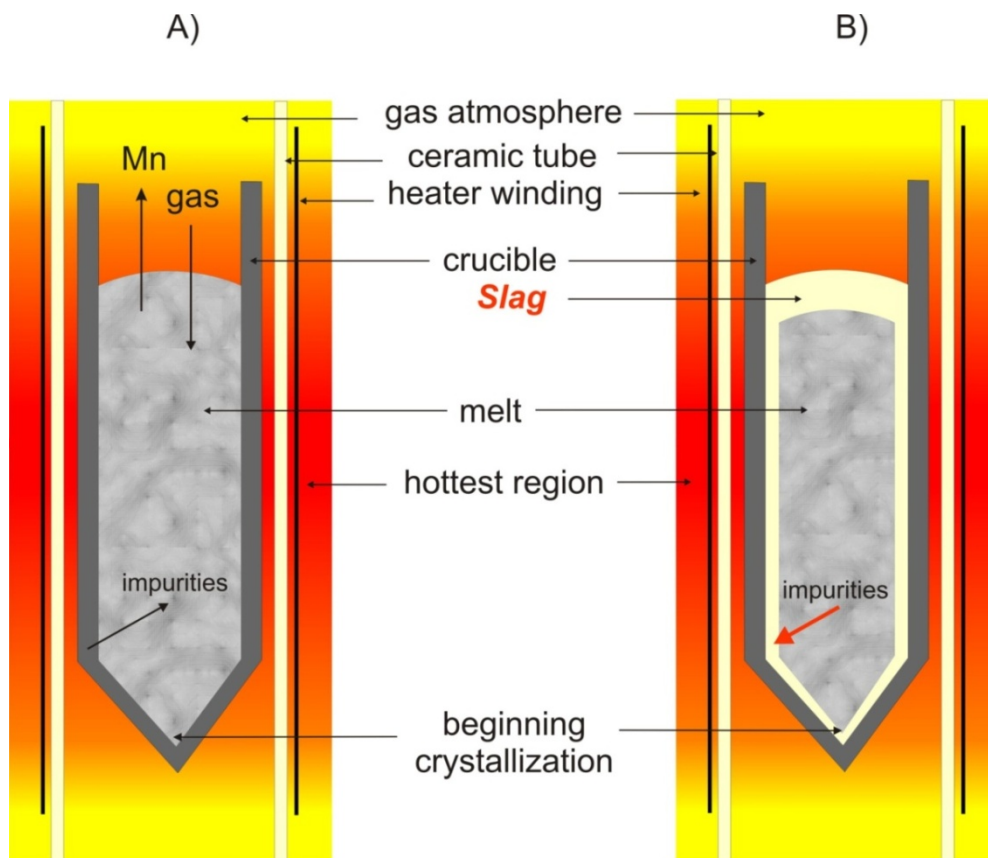


Figure 4.2.1: Principle of A) the Bridgman – and B) the SLARE – technique in comparison, depicting the disadvantages of the Bridgman – technique, like manganese loss, and inclusions of impurities and gas pores. This is avoided with the modified technique SLARE. Impurities are soluble in the Slag, which also impedes the loss of manganese and inclusions of gas pores in the crystalline material.

The crucial difference between the conventional Bridgman – technique and the SLARE – technique is the use of a slag (see Figure 4.2.1), adapted to the material system, which has to be grown.

Thereby the growth process starts by melting the metals, intermetallic compounds or alloys together with a slag building flux melting agent. The starting material can be a powder, pellets or even rods of the metals and alloys, respectively. However a powder has to be solidified before the melting.

The solidus of the slag building flux melting agent has to be lower than the melting point of the metals or the alloy and lower than the solidus of the grown crystal. During the melting process the components are heated up under an inert atmosphere and the slag builds a fluid covering on top of the metallic melt. This process impedes the uncontrolled loss of elements with a high vapour pressure and avoids the inclusion of gas pores in the metallic melt. The slag building flux melting agent has to be chemically inert against the used metals, however the slag has to show a high solubility for impurities in the metallic melt, which are mainly oxides und sulphides. Since the slag has to liquate from the metallic melt slowly, the density has to be smaller than that of the metallic melt, but still high enough to ensure a contact long enough to dissolve the impurities in the slag.

## 4.3 PREPARATION OF NI-MN-GA-CO – SINGLE CRYSTALS

---

To prepare single crystalline samples of Ni-Mn-Ga-Co, the phase diagram of this material class has to be known. Since Ni-Mn-Ga is a material studied intensively, many experiments have been performed to determine the solidus and liquidus point as well as the ordering temperature from the B2 to the L2<sub>1</sub> structure of different compositions.

Taking into account the change of melting point of Ni-Mn-Ga when keeping the nickel content constant while the manganese content is increasing and the gallium content decreases, respectively, it can be seen, that a higher content of manganese results in a decreasing solidification point from 1150°C in Ni<sub>50</sub>Mn<sub>50</sub> to 1035°C in Ni<sub>50</sub>Ga<sub>50</sub> (see Figure 4.3.1) [83,84]. Furthermore it has been determined, that the ordering temperature from the B2 to L2<sub>1</sub> structure has its maximum in the stoichiometric compound Ni<sub>50</sub>Mn<sub>25</sub>Ga<sub>25</sub> at 870°C and decreases to 500°C in Ni<sub>50</sub>Mn<sub>35</sub>Ga<sub>15</sub> and Ni<sub>50</sub>Mn<sub>15</sub>Ga<sub>35</sub> respectively [84].

Measuring the melting points of several Ni-Mn-Ga-Co samples (1 to 6 at-% cobalt), showed that the melting points and ordering temperatures are similar to the Ni-Mn-Ga samples with an equivalent Mn/Ga – ratio. In regard to these results, the used flux melting agent and the program for the furnace were configured before.

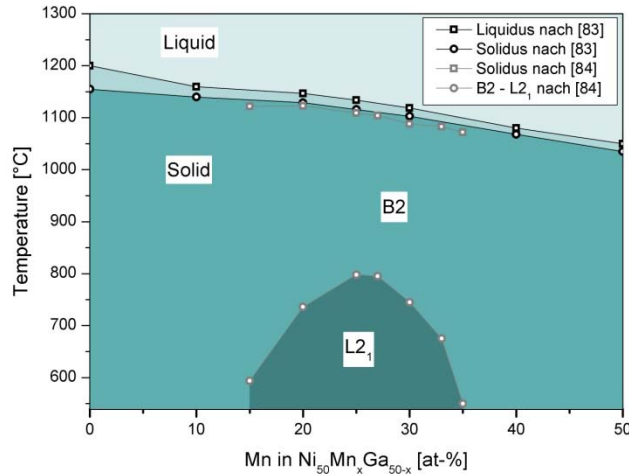


Figure 4.3.1: Phase diagram of  $\text{Ni}_{50}\text{Mn}_x\text{Ga}_{50-x}$ . The Solidus data (grey squares) and transformation temperatures from B2 to  $\text{L}_{21}$  (grey circles) structure taken from [84] have been determined by DTA and neutron diffraction. The solidus (black circles) and liquidus (black squares) data taken from [83] have been determined by thermal analysis in a graphite resistance heated furnace.

### 4.3.1 SLAG BUILDING FLUX MELTING AGENT

Nearly every molten metal dissolves hydrogen, oxygen and nitrogen if it is in contact with the atmosphere. The solubility of these elements decreases with the solidification of the metal. Thereby gas bubbles can form and become trapped in the solid metal. However, most of the oxygen and nitrogen precipitates as oxides and nitrides. Some metals can even react with the hydrogen. Introducing a slag into the growth process, isolates the metallic melt from the gas atmosphere and inhibits the transfer of the gas molecules into the metal. Furthermore the covering of the melt by the slag inhibits the loss of volatile elements, like the manganese in Ni-Mn-Ga and Ni-Mn-Ga-Co. Therefore the slag has to liquefy at lower temperature than the metal. Besides avoiding new impurities and inclusions during the crystal growth process, the slag also has to dissolve the oxides which Ni-Mn-Ga and Ni-Mn-Ga-Co already contains. These oxides have a lower density, than the pure metal and therefore rise to the surface of the molten metal. On the metal surface the impurities have to be absorbed into the slag. Halides are good flux melting agents, which slag the impurities from the melt surface and separate this layer from the metal, without reacting with the Ni-Mn-Ga – or Ni-Mn-Ga-Co – melt and the crucible.

The metallic alloys Ni-Mn-Ga and Ni-Mn-Ga-Co show a liquidus line above  $1050^\circ\text{C}$  (see Figure 4.3.1) and for a Mn/Ga - ratio of approximately 1.5 a liquidus temperature of  $1150^\circ\text{C}$ . While pure  $\text{CaF}_2$  with its melting point at  $1410^\circ\text{C}$  and pure  $\text{MgF}_2$  at  $1252^\circ\text{C}$  show a liquidus temperature which is too high for those metallic alloys, the mixture of both components shows an eutectic point at 44.4%  $\text{CaF}_2$  and 55.6%  $\text{MgF}_2$  where the melting point decreases to  $980^\circ\text{C}$  (see Figure 4.3.2). This lies more than  $100^\circ\text{C}$  below the solidus line of the alloys used in this project.

The transport of the impurities from the surface of the melt to the slag increases with a decreasing viscosity of the slag. Another advantage of a lower viscosity of the slag is a better

separation of the melt and the slag. By superheating above the liquidus temperature of the flux melting agent, the viscosity decreases.

In order to reach a higher temperature difference between the maximum furnace temperature and the liquidus temperature of the flux, the melting point was lowered by introducing  $\text{BaF}_2$  into the slag. As it can be seen in the ternary phase diagram (Figure 4.3.2), the mixture of all three fluorides ( $\text{CaF}_2$ ,  $\text{MgF}_2$  and  $\text{BaF}_2$ ) has a ternary eutectic at  $830^\circ\text{C}$ , 52 wt-%  $\text{BaF}_2$ , 29wt-%  $\text{MgF}_2$ , 19wt-%  $\text{CaF}_2$  and a second one at  $800^\circ\text{C}$ , 72 wt-%  $\text{BaF}_2$ , 14.5 wt-%  $\text{MgF}_2$  and 13.5wt-%  $\text{CaF}_2$ .

For the single crystal growth of Ni-Mn-Ga-Co rods two different slags were used. Three of the five successful grown crystals were grown with the binary eutectic  $\text{CaF}_2/\text{MgF}_2$  mixture, while the last two crystals were grown with the ternary slag (see Tab.4.3.1). Both slags were made out of  $\text{CaF}_2$  and  $\text{MgF}_2$  both with a purity of 99.99%. The ternary slag includes also  $\text{BaF}_2$  with the same purity degree. The powders were ball milled to ensure a contact best possible between the components. The amount of used slag depends on the weight of the metal to grow and lies between 5 to 10 wt-% of the starting alloy material.

In all growth processes  $\text{YO}_2$  – crucibles were used, which do not react with the slag. The slag was poured into the crucible and was covered by the Ni-Mn-Ga-Co bars.

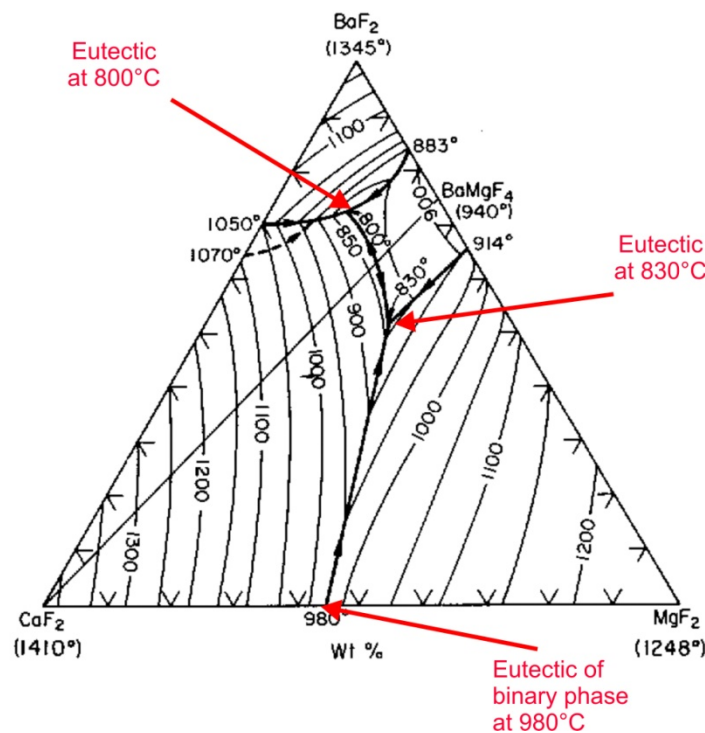


Figure 4.3.2: Ternary phase diagram of  $\text{CaF}_2$  and  $\text{MgF}_2$  and  $\text{BaF}_2$  showing two ternary eutectics at  $800^\circ\text{C}$  and  $830^\circ\text{C}$ . The third arrow shows the binary eutectic of  $\text{CaF}_2$  and  $\text{MgF}_2$  at  $980^\circ\text{C}$ . [85]

### 4.3.2 GROWTH PROCESS

---

The furnace used for the single crystal growth technique was build from HTM Reetz in Berlin. The temperature gradient, which is necessary, is realized by the heater of the furnace and the moving of the crucible through the furnace.

At the beginning, the crucible has to be positioned in an area with a small temperature gradient. Therefore, the middle of the crucible is positioned approximately 2 cm above the hottest region of the furnace. After the evacuation of the furnace chamber, the temperature is increased to 200°C. When the best possible vacuum is reached (approximately  $0.3 \cdot 10^{-3}$  bar), the material has to dry and outgas for 60 to 90 min at this temperature. Afterwards the temperature is increased to 1250°C at the tip of the crucible, whereby the maximum temperature in the furnace chamber is approximately 1360°C, to ensure the melting of the metallic alloy. As soon as the maximum temperature is reached, the chamber is filled with  $5 \cdot 10^{-3}$  bar H<sub>2</sub> to reduce the rest of the gaseous oxygen to gaseous H<sub>2</sub>O [86]. After 20 min, the chamber is filled with the inert gas Argon, until a pressure of 1 bar is reached. In this atmosphere, the crucible is kneeled to reach a high temperature gradient. The hottest region in the furnace chamber stays constant at a temperature of 1360°C, while the tip of crucible is lowered to the temperature region of 1110°C, which is still above the solidus temperature of the alloy. In this position, the chamber is evacuated again and subsequently filled with 1 bar of Argon and stays for 20 min. Afterwards the temperature is decreased with a cooling rate of 3°C/min, which is measured at the tip of the crucible. When the temperature of the middle of the crucible decreases below 980°C and 800°C respectively, the furnace is shut down and cools down slowly to room temperature, which takes approximately three days.

---

### 4.3.3 POSTGROWTH TREATMENT OF THE CRYSTALS

---

After the growth process, the solid slag is removed from the crystalline rod by sandblasting. To remove impurities from the surface of the crystal, the rod is electropolished in a mixture of methanol and nitric acid at 0°C.

Due to the SLARE – technique it is possible to grow single crystalline rods of approximately 8 cm in height and a diameter of 1.6 cm. The weight of these rods is about 110g. Even though no manganese is lost during the growth process; the high vapour pressure of this element causes a concentration gradient from the tip to the end of the crystal. The amount of manganese increases along the growth axis which results in a decreasing amount of gallium in the same direction. To increase the homogeneity and ordering in the manganese and gallium sublattices, the rods are annealed in a quartz tube. The first step is done at 1000°C for 72h in an Argon atmosphere. As it can be seen in Figure 4.3.1, the ordering temperature from a B2 structure to the L2<sub>1</sub> structure in Ni-Mn-Ga with a Mn/Ga - ratio of approximately 1.5 lies around 750°C. Ni-Mn-Ga-Co with the same Mn/Ga - ratio shows the ordering in the same temperature range. Therefore the temperature in the quartz tube is decreased to 700°C after the annealing for

homogeneity and stays at this temperature for 48h before it is cooled down to room temperature with 20°C/h.

After the annealing, the crystalline rods are orientated in the austenite phase along the [100] – and [010] – direction by X-Ray Laue diffraction (done by the MaTeck Company). Afterwards smaller samples (usually 6 x 5 x 4 mm in size) are cut out of the rod. To avoid external stress on the surface, the cutting is carried out by spark erosion. The spark erosion causes an oxide layer, mainly MnO<sub>2</sub>, on the surface of the rectangular samples. To remove this layer, they are electropolished again, using the same solution as for the rods.

#### 4.3.4 COMPOSITION OF THE NI-MN-GA-CO CRYSTALS

For this thesis five single crystalline rods were grown successfully. The composition was chosen with respect to the behaviour of Ni-Mn-Ga. From Ni-Mn-Ga-alloys it is well known that the composition has a big influence on the phase transformation temperatures as well as on the structural and, as a consequence also on the stress-strain behaviour (see section 2.5). Starting from Ni-Mn-Ga and substituting nickel by cobalt increases the Curie temperature while the martensite temperature decreases. By contrast, the replacement of manganese by cobalt results in a decrease of the Curie temperature but an increase of the martensite temperature [87].

The aim of this work was to increase the magnetic and structural phase transformation temperature, in order to find a material showing the magnetic shape memory effect within a bigger temperature range than Ni-Mn-Ga shows up to now. Therefore Ni<sub>2</sub>Mn<sub>25+x</sub>Ga<sub>25-x</sub> was alloyed with different amounts of cobalt, substituting nickel in all of the five successfully grown single crystalline rods to increase the Curie-temperature (see Table 4.3.1).

crystal rod	Ni [at-%]	Mn [at-%]	Ga [at-%]	Co [at-%]	Mn/Ga	e/a	slag
1	44.0	30.0	20.0	6.0	1.500	7.640	CaF <sub>2</sub> /MgF <sub>2</sub>
2	44.6	30.7	19.3	5.4	1.591	7.674	CaF <sub>2</sub> /MgF <sub>2</sub>
3	45.0	31.0	19.2	4.8	1.615	7.678	CaF <sub>2</sub> /MgF <sub>2</sub>
4	48.8	28.6	21.4	1.2	1.336	7.632	CaF <sub>2</sub> /MgF <sub>2</sub> /BaF <sub>2</sub>
5	49.2	28.4	21.6	0.8	1.315	7.628	CaF <sub>2</sub> /MgF <sub>2</sub> /BaF <sub>2</sub>

Table 4.3.1: Weighted composition of the single crystalline Ni-Mn-Ga-Co rods with the corresponding Mn/Ga – and e/a – ratio. The last column shows the slag which was used for the growth process

Besides the amount of cobalt, the starting composition was chosen by taking the e/a ratio in account. Since Ni-Mn-Ga with an e/a ratio higher than 7.7 has a non-modulated tetragonal structure with a twinning stress higher than the magneto stress and thus shows no MFIS [88], all crystal rods had an e/a ratio between 7.6 and 7.7. This lead to different manganese and gallium

amounts in the five crystals, depending on the amount of cobalt. In order to reach a high martensite temperature, the Mn/Ga was chosen as high as possible for the rods.

## 4.4 TRAINING OF SINGLE CRYSTALS

When single crystalline samples are cooled down from the austenite to the martensite phase the samples show a multivariant state (see section 2.2). The thermomechanical training of the sample leads to a singlevariant state of the sample. Furthermore the training can reduce the twinning stress within the samples, which decreases the necessary strength of the applied magnetic field to induce the strain.

For the training, a device has been constructed, which enables a simultaneous heating and applying of pressure (see Figure 4.4.1). Thermomechanical training starts with the heating of the sample into the austenitic state. Therefore the sample is put into the adapter piston. When the temperature is reached, a defined uniaxial pressure is applied by the pneumatic actuator, regulated by a nitrogen gas flow. The pressure is kept constant, while the sample is cooled down to the martensite state. Afterwards, the sample is turned by  $90^\circ$  and the training is done in that direction. The whole procedure is repeated until the sample shows the maximum strain, which is possible, considering eq. 4.

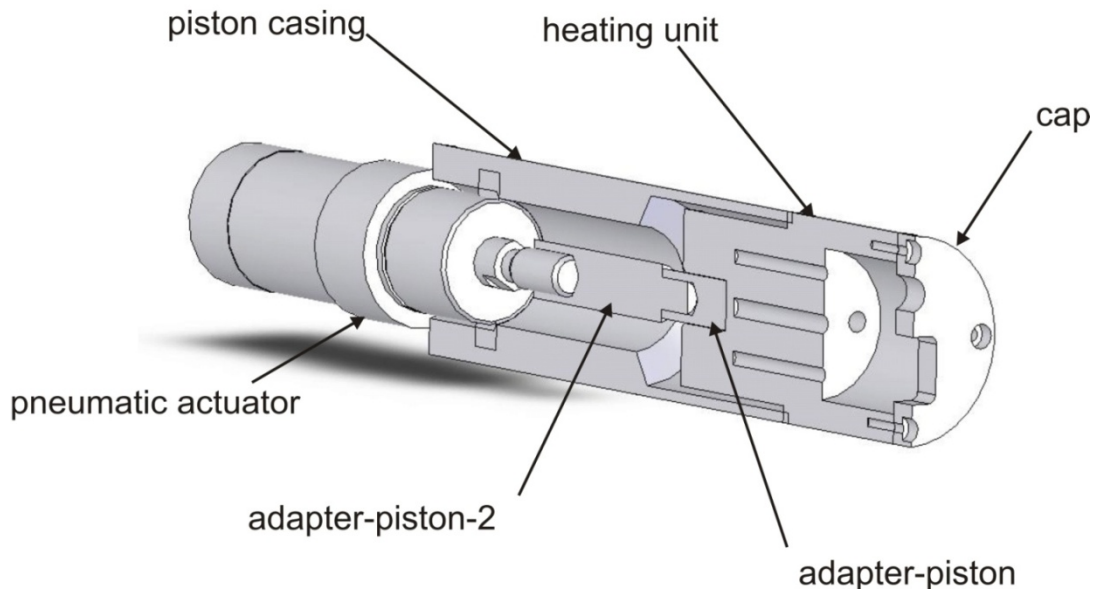


Figure 4.4.1: Schematic of the training device used for the thermomechanical training to reach a singlevariant sample and decrease the twinning stress.

# CHAPTER 5 – RESULTS

---

## 5.1 COMPOSITION OF THE SAMPLES

Due to the vapour pressure of manganese, a concentration gradient was expected in the rods (see section 4.2). Therefore the composition of the small samples (6 x 5 x 4 mm) cut out of the rods was determined by EDX-S. The mass of the single crystalline rods varied between 80 and 110 g. After the postgrowth annealing, the rods were electropolished in a solution of nitric acid and methanol to make the orientation by Laue and the subsequent spark eroding to parallelepipeds possible.

All rods were orientated along the [100] and [010] in the austenite state. The growth axis of the rods was in all cases either parallel to [100]<sub>Austenite</sub> or parallel to [110]<sub>Austenite</sub>. Depending on the crystallographic lattice orientation and the slightly varied mass, it was possible to cut samples out of 5 to 7 planes (see Figure 5.1.1). For all rods plane 1 is defined as the plane from the bottom (starting point of the crystallization) of the crystal, while the highest plane number is defined as the last plane taken from the top of the crystal.

In the first single crystalline rod (Figure 5.5.1 a) with the nominal composition Ni<sub>44.0</sub>Mn<sub>30.0</sub>Ga<sub>20.0</sub>Co<sub>6.0</sub> (all numbers are given in atom percent) the [110]<sub>Austenite</sub> was parallel to the growth direction. Samples from six planes were cut out. By determining the content of nickel, manganese, gallium and cobalt of the cut out samples, it is shown, that the content of nickel hardly changes and varies only about 0.6 at-% from 44.5 to 45.1 at-%. The same approximately constant distribution is measured for cobalt. Like for nickel, the content varies about 0.5 at-% from 6.0 to 6.5 at-%. In contrast, the content of manganese and gallium changes by about 1.5 at-% and 1 at-%, respectively. While the amount of manganese increases from 28.1 to 29.4 at-% with increasing plane number, the amount of gallium decreases from 20.8 to 19.8 at-% in the same direction.

Independent from the amount of cobalt alloyed to Ni-Mn-Ga and the varied nominal Mn/Ga - ratio, all rods show the same trend for the distribution of manganese and gallium. The third crystal rod with the nominal composition Ni<sub>45.0</sub>Mn<sub>31.0</sub>Ga<sub>19.2</sub>Co<sub>4.8</sub> shows a more significant increase of manganese of about 3 at-% from 27.8 to 30.8 at-% and a decrease of gallium from 20.8 to 19.1 at-% along the growth direction. This rod shows also the highest deviation in the measured nickel contents from 46.8 to 44.9 at-%, while cobalt distributes constantly over the whole volume of the rod (Max: 5.1 at-%, Min: 4.9 at-%).

However, such a high change in the amount of nickel was only determined in this third crystal rod. As pictured in Figure 5.5.1 and 5.5.2, crystal 1,2,4 and 5 show a nearly constant distribution of nickel with a deviation below 1 at-% within the volume.

Furthermore the distribution of the elements perpendicular to the growth axis of the crystal rods was measured. While crystal 1,3 and 4 were grown along the [110]<sub>Austenite</sub> axes, the crystal rods 2 and 5 grew along the [100]<sub>Austenite</sub>.

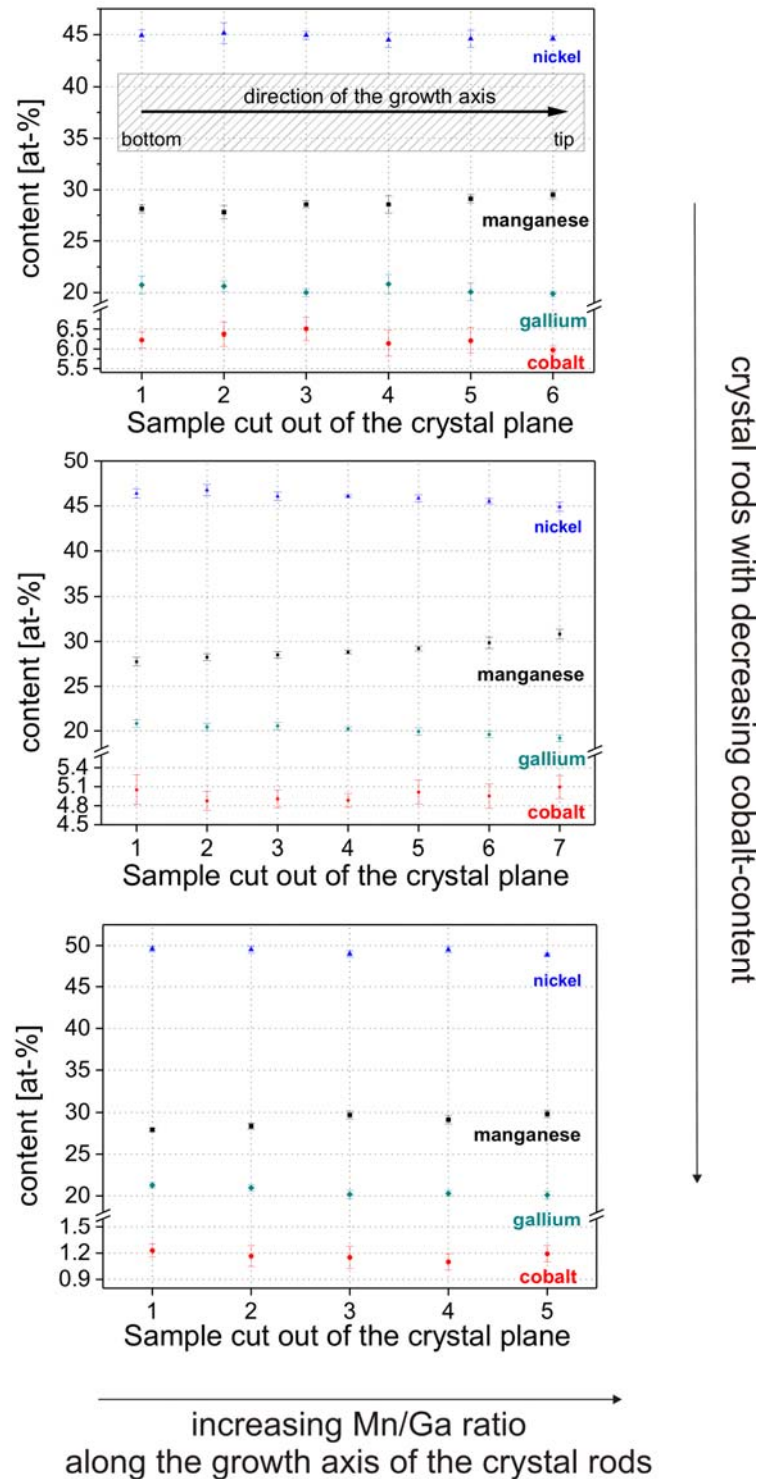


Figure 5.5.1: Composition of the samples cut out from different planes along the growth direction of the crystalline rods 1 (a), 3 (b) and 4 (c).

This enabled the measurement of several samples cut out of the same height of the rod, which is shown exemplarily for two planes of crystal 2 and 5 in Figure 5.5.2. Independent from the position in the rod (shown for the bottom and the top of a crystal rod in Figure 5.1.2), nickel, manganese gallium and cobalt distribute equally in this direction. The averaged deviation for all elements was not higher than 0.2 at-%.

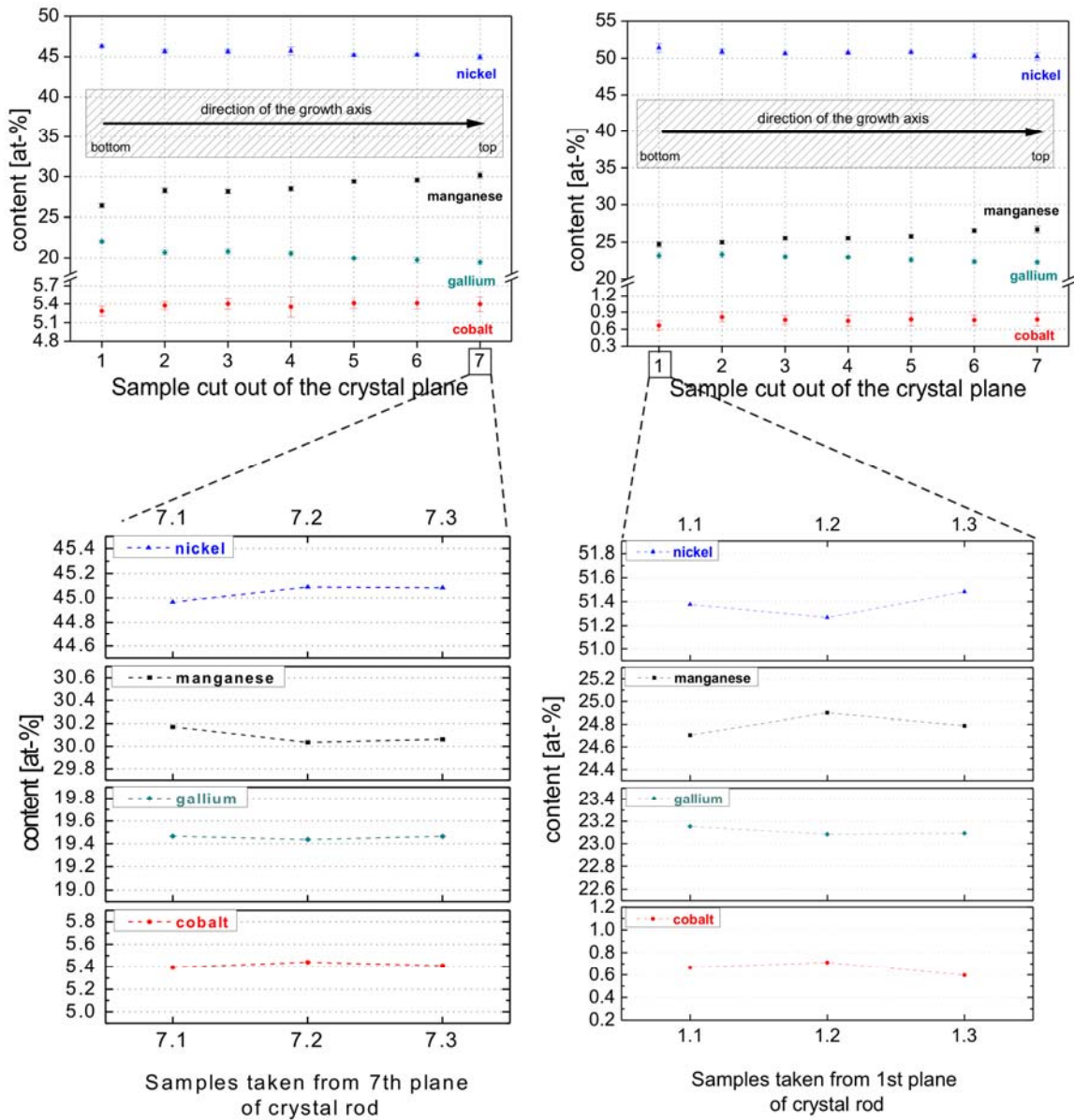


Figure 5.1.2: Composition of the cut out samples from the single crystalline rods 2 (a) rod 5 (b) along the growth direction and perpendicular to the growth direction for plane 6 in crystal rod 2 and for plane 1 in crystal rod 5.

## 5.2 PHASE TRANSFORMATION TEMPERATURES

The phase transformation temperatures of the parallelepipeds were determined by DSC. In order to eliminate possible stress within the samples, the samples were heated above the Curie-temperature with 10K/min before the martensite and Curie temperature as well as the melting points were verified. All temperatures depicted in the following section were determined by

heating and cooling the sample with 5K/min unless otherwise stated. Furthermore the magnetic and structural phase transformation from some samples was additionally measured using the PPMS.

## 5.2.1 STRUCTURAL AND MAGNETIC PHASE TRANSFORMATION

The structural phase transformation from the martensite to the austenite structure and vice versa, takes place over a certain temperature range and shows a hysteresis. As explained in detail in section 2.2, the martensite temperature  $T_M$  is calculated from the Martensite Start  $M_S$ , the Martensite Finish  $M_F$  and the Austenite Start  $A_S$  and Austenite Finish  $A_F$  temperature using eq. 2:

$$T_M = T_{eq} = \frac{(A_S + A_F)/2 + (M_S + M_F)/2}{2} \quad [2]$$

Also the magnetic phase transformation from the ferromagnetic to the paramagnetic state shows a small hysteresis and the transformation temperature  $T_C$  is calculated with following equation:

$$T_C = \frac{(T_{ferro-para} + T_{para-ferro})}{2} \quad [57]$$

Due to the fourth element cobalt, which has 9 valence electrons ( $4s^23d^7$ ), the equation to calculate the e/a ratio changes from equation 19 to following equation:

$$e/a = \frac{10 \cdot c^{Ni} + 9 \cdot c^{Co} + 7 \cdot c^{Mn} + 3 \cdot c^{Ga}}{c^{Ni} + c^{Co} + c^{Mn} + c^{Ga}} \quad [58]$$

### 5.2.1.1 CRYSTAL ROD NO.1 “Ni<sub>44.0</sub>Mn<sub>30.0</sub>Ga<sub>20.0</sub>Co<sub>6.0</sub>”

As shown in the previous section 5.1, the composition of samples cut out of the single crystalline rods deviate from the nominal composition depending on the position in the rod. Therefore the e/a – ratio as well as the Mn/Ga-ratio is different in every sample (see Table 5.2.1).

In this rod, the Mn/Ga – ratio varies from 1.30 up to 1.49 and the e/a ratio changes in the range of 7.62 to 7.66. The calculated martensite temperatures lie between 67.91 °C and 112.86 °C, while the Curie – temperature remains nearly constant at around 160 °C.

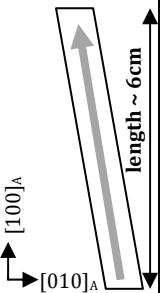
Rod – orientation Sample	Ni [at-%]	Mn [at-%]	Ga [at-%]	Co [at-%]	e/a	Mn/Ga	T <sub>M</sub> [°C]	T <sub>C</sub> [°C]
	1_1	45.28	27.53	21.20	5.99	7.63	73.37	159.92
	1_2	45.18	27.80	20.64	6.38	7.66	75.49	161.30
	1_3	44.90	28.12	20.75	6.23	7.64	67.91	161.77
	1_4	44.47	28.56	20.83	6.14	7.62	97.95	159.38
	1_5	44.93	28.57	20.00	6.50	7.68	92.04	159.64
	1_6	44.58	29.13	20.08	6.21	7.66	112.86	159.09
	1_7	44.62	29.52	19.88	5.98	7.66	105.14	159.04

Table 5.2.1: Composition and the resulting e/a and Mn/Ga – ratios for samples cut out of the single crystalline rod Nr. 1 with the nominal composition  $\text{Ni}_{44.0}\text{Mn}_{30.0}\text{Ga}_{20.0}\text{Co}_{6.0}$  and the corresponding martensite and Curie Temperatures. The grey arrow in the first column gives the growth direction of the crystal rod (black rectangle). The position of the sample numbers in the table gives the approximate position of the particular sample in this rod, sketched on the left side of the column.

By plotting the phase transformation temperatures of the parallelepipeds versus their Mn/Ga – ratios it becomes obvious, that with the increasing ratio, the martensite temperature increases significantly (see Figure 5.2.1 a). The increase of the Mn/Ga – ratio is accompanied by a slight decrease of the Ni-content. This results in a slight falling of Curie – temperature. The measurement of the start and finish temperatures of the austenite and martensite, respectively showed a relatively high temperature range within which the structural phase transformation takes place (maximum value: sample 1\_3  $|A_s - A_f| = 62$  °C; minimum value: sample 1\_3  $|M_s - M_f| = 13$  °C – see Figure 5.2.1b).

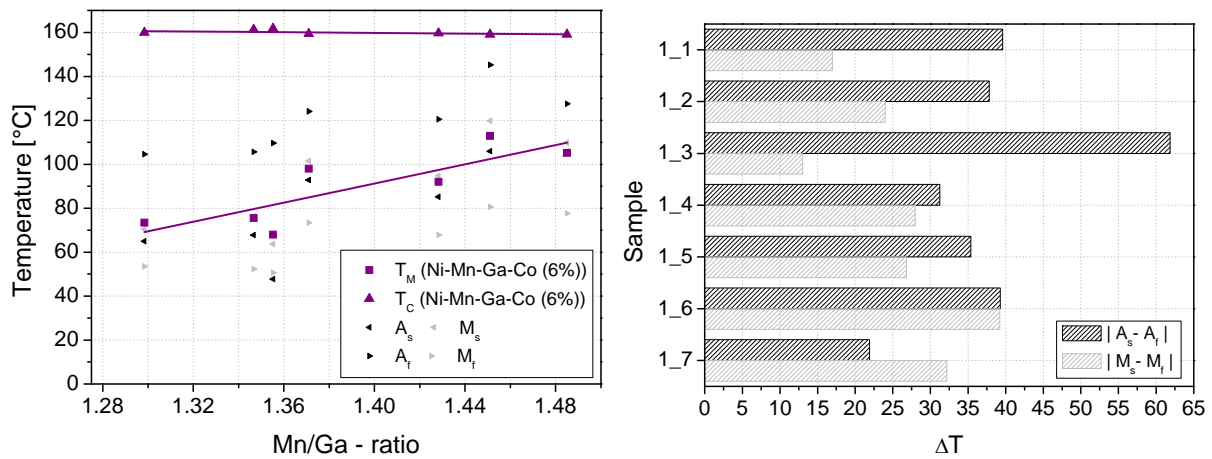


Figure 5.2.1: a) Structural ( $\blacksquare$ :  $T_M$  calculated by eq.2,  $\blacktriangleleft$ / $\blacktriangleright$ :  $A_s$  /  $M_s$  determined by DSC,  $\blacktriangleright$ / $\blacktriangleleft$ :  $A_f$  /  $M_f$  determined by DSC) and magnetic phase transformation temperature ( $\blacktriangle$ : calculated  $T_C$  by eq. 53) of samples cut out of single crystalline rod nr.1 versus their Mn/Ga – ratio. B) Temperature range of the phase transformation from the martensite to austenite structure and from the austenite to the martensite structure, respectively calculated from the start and finish temperatures determined by DSC.

Thereby the average range between  $M_s$  and  $M_f$  is approximately two thirds of the average range between  $A_s$  and  $A_f$ . However there was no relation found between composition of the samples and the determined temperature range.

By determining the phase transformation temperatures, the samples 1\_6 and 1\_7 show a splitting in the first order phase transformation (see for sample 1\_6 as an example Figure 5.2.2). The first structural phase transformation from the martensite to an intermartensite phase lies at  $105^\circ\text{C}$  and from the intermartensite to the austenite phase lies at  $119^\circ\text{C}$ .

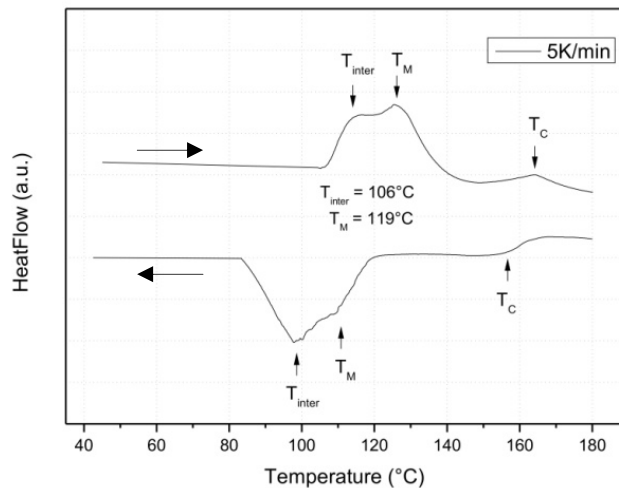


Figure 5.2.2: Thermogram of sample 1\_6 measured with a heating – and cooling rate of 5K/min.

### 5.2.1.2 CRYSTAL ROD NO.2 “ $\text{Ni}_{44.6}\text{Mn}_{30.7}\text{Ga}_{19.3}\text{Co}_{5.4}$ ”

Like in the first grown rod, the compositions and therefore  $e/a$  and  $\text{Mn}/\text{Ga}$  – ratios of the cut out samples differ from the nominal composition of the crystal rod (see Table 4). The  $\text{Mn}/\text{Ga}$  – ratio in this rod changes from 1.20 up to 1.55, while the  $e/a$  ratio differs only from 7.61 to 7.68.

The lowest martensite temperature of  $81.36^\circ\text{C}$  within this rod was determined in sample 2\_1 and the highest in sample 2\_6 with  $127.93^\circ\text{C}$ , which also shows the highest  $\text{Mn}/\text{Ga}$  – ratio. As verified for the samples of crystal rod no.1, the Curie temperature changes only slightly from  $153^\circ\text{C}$  to  $150^\circ\text{C}$  with the slightly decreasing Ni content.

Rod – orientation Sample	Ni [at-%]	Mn [at-%]	Ga [at-%]	Co [at-%]	e/a	Mn/Ga	T <sub>M</sub> [°C]	T <sub>C</sub> [°C]
2_1	46.27	26.43	22.02	5.28	7.61	1.20	81.36	154.30
2_2	45.64	28.16	20.80	5.40	7.65	1.35	86.45	153.85
2_3	45.66	28.28	20.68	5.38	7.65	1.37	82.03	154.85
2_4	45.68	28.48	20.52	5.31	7.66	1.39	93.00	153.85
2_5	45.22	29.40	19.97	5.41	7.67	1.47	112.73	152.85
2_6	45.26	29.57	19.76	5.41	7.67	1.50	110.63	153.85
2_7	44.97	30.17	19.47	5.40	7.68	1.55	127.93	149.85

Table 5.2.2: Composition and the resulting e/a and Mn/Ga – ratios for samples cut out of the single crystalline rod No. 2 with the nominal composition  $\text{Ni}_{44.6}\text{Mn}_{30.7}\text{Ga}_{19.3}\text{Co}_{5.4}$  and the corresponding martensite and Curie temperatures. The single crystalline rod had a length of approximately 6cm, whereas the first sample (2\_1) has been cut out 1cm away from the bottom of the crystal and the following samples from the planes above. The positions of the sample names in the second column indicate the positions in the rod (rectangular sketch in the first column), which grew along the [100] direction of the austenite phase (growth direction is marked by the grey arrow).

As illustrated in Figure 5.2.3 a, the martensite temperature increases about 45 °C from around 85°C to 130°C with the increasing Mn/Ga – ratio from 1.35 to 1.55 of the cut out samples. The samples show again a broader martensite to austenite transformation (except sample 2\_6) than the austenite to martensite transformation (see Figure 5.2.3 b), thereby the average temperature range is 41.5 °C from  $A_s$  to  $A_f$  and 31.7°C from  $M_s$  to  $M_f$ .

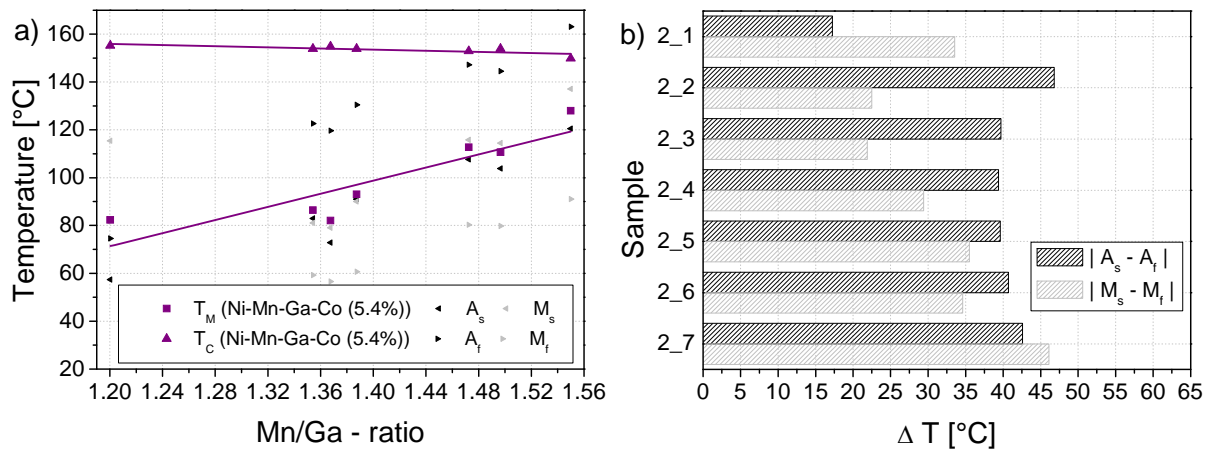


Figure 5.2.3: a) Structural ( $\blacksquare$ :  $T_M$  calculated by eq.2,  $\blacktriangleleft/\blacktriangleright$ :  $A_s / M_s$  determined by DSC,  $\blacktriangleright/\blacktriangleleft$ :  $A_f / M_f$  determined by DSC) and magnetic phase transformation temperature ( $\blacktriangle$ : calculated  $T_C$  by eq. 53) of samples cut out of single crystalline rod no.2 plotted against the corresponding Mn/Ga – ratio. B) Temperature range of the phase transformation from the martensite to austenite structure and vice versa respectively calculated from the start and finish temperatures determined by DSC.

In order to see whether the annealing for ordering is sufficient, the samples were sealed again in a quartz tube in an argon atmosphere and were annealed for another 10 days around the ordering temperature, which lies between 700°C and 750°C. Afterwards the phase transformation temperatures were determined by DSC again. It can be seen in Figure 5.2.4 a, that the structural phase transformation temperature was not affected significantly by the

additional annealing procedure. Only samples 2\_4 and 2\_6 show a small difference in  $T_M$ . Thereby the martensite temperature  $T_M$  decreases in sample 2\_4 from 112.7°C to 105.8°C, while  $T_M$  increases from 127.9°C to 138.0°C.

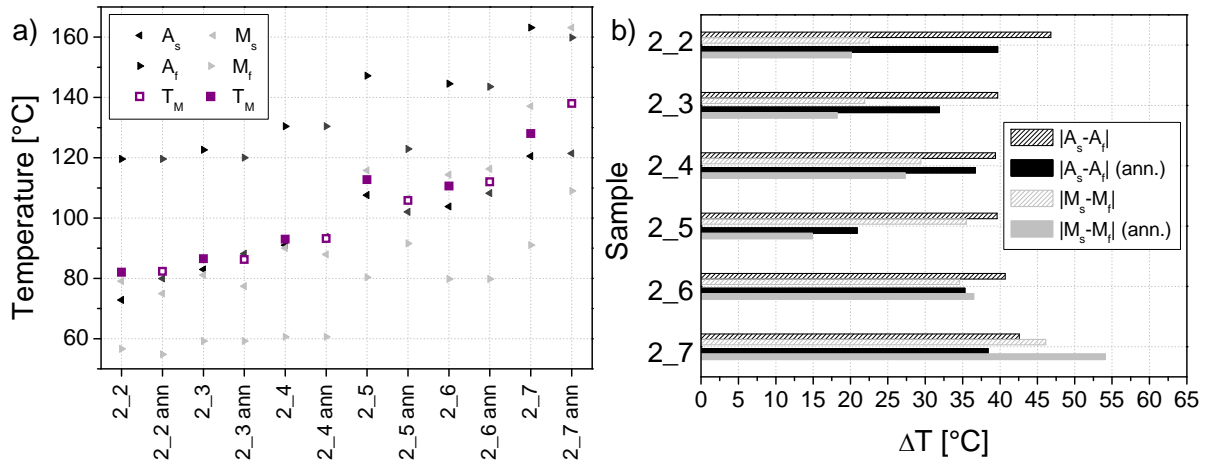


Figure 5.2.4: a) Structural phase transformation temperature of Ni-Mn-Ga with 5.4% Co before and after annealing. B) Broadness of phase transformation from the martensite to the austenite and vice versa respectively.

However, it was determined, that the second annealing has an influence on the broadness of the structural transformation. While the average temperature range from the martensite to the austenite structure decreases from 41.5°C to 33.8°C, the temperature range for the reverse transformation decreases from 31.7°C to 28.5°C (see Figure 5.2.4 b.)

### 5.2.1.3 CRYSTAL ROD NO.3 “Ni<sub>45.0</sub>Mn<sub>31.0</sub>Ga<sub>19.2</sub>Co<sub>4.8</sub>”

With the decreasing amount of Cobalt, the Curie – temperature  $T_C$  decreases from 160°C, in the single crystalline rod no.1 alloyed with 6 at-% cobalt, to approximately 140°C (see Table 5.2.3) within this rod alloyed with 4.8 at%.

As mentioned in section 5.1, the manganese and gallium content deviates significantly within this single crystalline rod. This results in a changing Mn/Ga – ratio from 1.33 up to 1.61. Like in the samples of the rod no.1 and 2 the martensite temperature increases with increasing Mn/Ga – ratio (see Figure 5.2.5 a). However the relation of the Mn/Ga – ratio and the martensite temperature shows a higher deviation from the general tendency than in the other single crystalline rods. The lowest martensite temperature of 80.25 was determined in sample 3\_2 with a Mn/Ga – ratio of 1.38, while sample 3\_3 with the same Mn/Ga – ratio has a martensite temperature of 105.99°C. Furthermore, the highest temperature of 146.19°C was determined in sample 3\_4 with a Mn/Ga – ratio of 1.43. The sample with the highest Mn/Ga – ratio of 1.61 has the structural phase transformation temperature at 99.80°C.

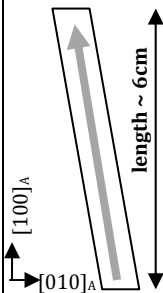
rod - orientation Sample	Ni [at-%]	Mn [at-%]	Ga [at-%]	Co [at-%]	e/a	Mn/Ga	T <sub>M</sub> [°C]	T <sub>C</sub> [°C]	
	3_1	46.39	27.76	20.81	4.88	7.66	1.33	82.89	143.69
	3_2	46.77	28.24	20.41	5.05	7.70	1.38	80.25	143.02
	3_3	46.08	28.51	20.53	4.91	7.66	1.38	105.99	143.77
	3_4	46.09	28.82	20.21	4.89	7.67	1.43	146.19	in T <sub>M</sub>
	3_5	45.86	29.21	19.92	5.01	7.68	1.47	119.99	140.26
	3_6	45.54	29.89	19.61	4.96	7.68	1.53	133.11	in T <sub>M</sub>
	3_7	44.91	30.82	19.18	5.09	7.68	1.61	101.10	141.10

Table 5.2.3: Composition and the resulting e/a and Mn/Ga – ratios for samples cut out of the single crystalline rod no. 3 with the nominal composition  $\text{Ni}_{45.0}\text{Mn}_{31.0}\text{Ga}_{19.2}\text{Co}_{4.8}$  and the corresponding martensite and Curie temperatures. As with the single crystalline rod no 1, this rod grew along the 110 direction (marked by the grey arrow in the first column), whereas the samples were cut out of the annealed part in the middle which had a length of approximately 6cm. The positions of the sample names in column 2 give the position of the samples in the rod (indicated by the black rectangle in the first column).

The broadness of the phase transformation is similar to the temperature ranges measured in the samples from the rod no.1 and 2. With an average range of 32.5°C from the austenite to the martensite is four fifths of the average range of 40.7°C from the martensite to the austenite phase (see Figure 5.2.5 b for detailed temperature ranges of the samples cut out of the rod).

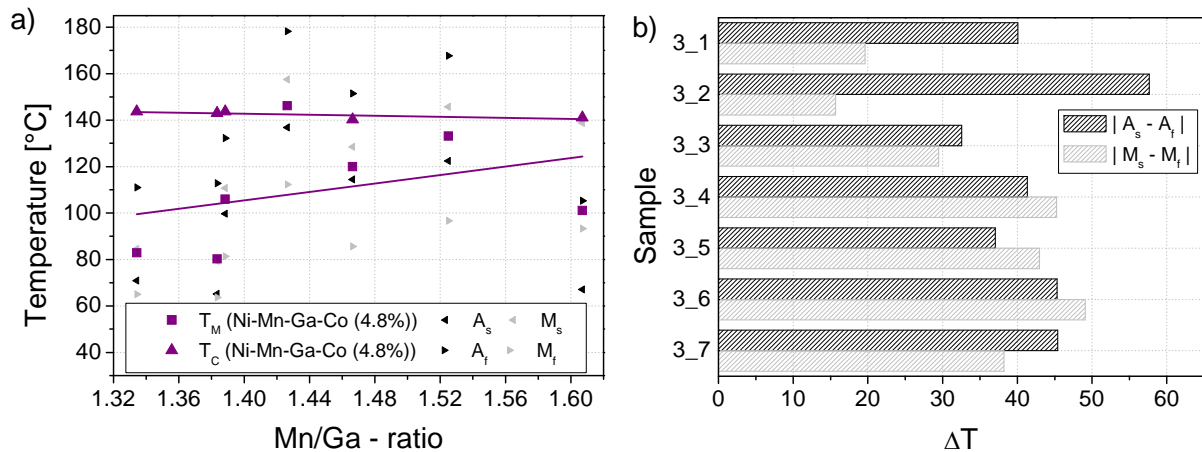


Figure 5.2.5: a) Structural (■: T<sub>M</sub> calculated by eq.2, ◀/◁: A<sub>s</sub> / M<sub>s</sub> determined by DSC, ▶/▷: A<sub>f</sub> / M<sub>f</sub> determined by DSC) and magnetic phase transformation temperature (▲: calculated T<sub>C</sub>) of samples cut out of single crystalline rod no. 3 versus their Mn/Ga – ratio. B) Temperature interval, where the structural transformation from the martensite to austenite phase and vice versa, respectively takes place.

### 5.2.1.4 CRYSTAL ROD NO.4 “Ni<sub>48.8</sub>Mn<sub>28.6</sub>Ga<sub>21.4</sub>Co<sub>1.2</sub>” AND NO.5 “Ni<sub>49.2</sub>Mn<sub>28.4</sub>Ga<sub>21.62</sub>Co<sub>0.8</sub>”

The crystal rods no.4 and no.5 were alloyed with much less cobalt. Instead of 5 to 6 at-% of cobalt only 1.2 and 0.8 at-% were used. This results in a significant decrease of the Curie-temperature from 140°C in crystal rod no.3 to around 100°C in the fourth and fifth rod (see Table 5.2.4 and 5.2.5 as well as Figure 5.2.6).

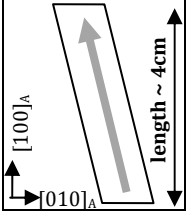
rod - orientation Sample	Ni [at-%]	Mn [at-%]	Ga [at-%]	Co [at-%]	e/a	Mn/Ga	T <sub>M</sub> [°C]	T <sub>C</sub> [°C]	
	4_1	49.58	27.92	21.27	1.23	7.66	1.31	83.39	98.89
	4_2	49.51	28.36	20.95	1.17	7.67	1.35	86.18	101.41
	4_3	49.50	29.13	20.28	1.10	7.70	1.44	95.20	in T <sub>M</sub>
	4_4	49.00	29.69	20.17	1.15	7.69	1.47	103.70	in T <sub>M</sub>
	4_5	48.90	29.83	20.09	1.19	7.69	1.48	104.38	in T <sub>M</sub>

Table 5.2.4: Composition and the resulting e/a and Mn/Ga – ratios for samples cut out of the single crystalline rod No. 4 with the nominal composition Ni<sub>44.8</sub>Mn<sub>28.6</sub>Ga<sub>21.4</sub>Co<sub>1.2</sub> and a length of approximately 4cm. The sample 4\_1 and 4\_5 have been cut out 2cm below and above the top and the end of the crystalline rod respectively. The growth direction is given by the grey arrow in the schematic. Furthermore the corresponding martensite and Curie temperatures, determined by DSC with a heating rate of 5K/min are listed.

Within the fourth crystal rod, which grew in the [110]<sub>A</sub> like the rods no. 1 and 3, the martensite temperature and the Curie temperature T<sub>C</sub> become equal. Sample 4\_1 (Mn/Ga = 1.31) and 4\_2 (Mn/Ga = 1.35) have separated phase transformation temperatures, whereby the martensite temperatures are 83.83°C and 86.18°C, respectively. The increasing Mn/Ga – ratio leads to a structural phase transformation temperature from 95.20°C for sample 4\_3 up to 104.38°C in sample 4\_5. Due to the broadness of the phase transformation, the magnetic phase transformation lies within the structural transformation and cannot be resolved by DSC.

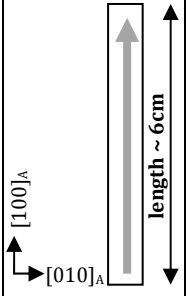
Sample	Ni [at-%]	Mn [at-%]	Ga [at-%]	Co [at-%]	e/a	Mn/Ga	T <sub>M</sub> [°C]	T <sub>C</sub> [°C]	
	5_1	51.38	24.70	23.15	0.67	7.62	1.07	50.24	100.11
	5_2	50.89	24.99	23.30	0.81	7.61	1.07	50.76	101.41
	5_3	50.69	25.54	23.01	0.76	7.62	1.11	54.16	102.53
	5_4	50.77	25.53	22.95	0.75	7.62	1.11	53.39	100.22
	5_5	50.84	25.77	22.62	0.77	7.63	1.14	56.56	102.81
	5_6	50.35	26.55	22.35	0.76	7.63	1.19	57.82	101.56
	5_7	50.25	26.70	22.28	0.77	7.63	1.20	64.81	103.88

Table 5.2.5: Composition and the resulting e/a and Mn/Ga – ratios for samples cut out of the single crystalline rod No. 4 with the nominal composition Ni<sub>49.2</sub>Mn<sub>28.4</sub>Ga<sub>21.6</sub>Co<sub>0.8</sub> and the corresponding martensite and Curie temperatures. Like rod no. 2 this rod grew along the [100] direction of the austenite phase (indicated by the grey arrow in the sketch). The samples were cut out of the middle part, which had a length of approximately 6cm.

With the changing Mn/Ga – ratio in crystal rod no.5 to lower values, the martensite temperature is lower than the Curie temperature again. While the Curie temperature stays approximately constant at 100°C, the martensite temperature increases from 50.24°C in sample 5\_1 to 64.81°C in sample 5\_7.

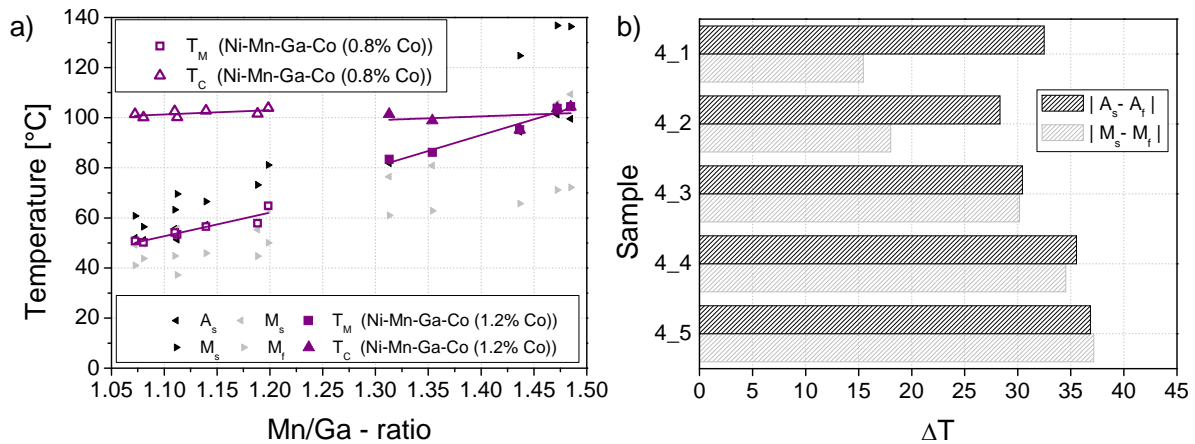


Figure 5.2.6: a) Structural ( $\blacksquare$ :  $T_M$  calculated by eq.2,  $\blacktriangleleft/\triangleleft$ :  $A_s / M_s$  determined by DSC,  $\blacktriangleright/\triangleright$ :  $A_f / M_f$  determined by DSC) and magnetic phase transformation temperature ( $\blacktriangle$ : calculated  $T_C$ ) of samples cut out of single crystalline rod nr.4 and 5 versus their Mn/Ga – ratio. B) Temperature range of the phase transformation of crystal rod no.4 from the martensite to austenite structure and vice versa respectively calculated from the start and finish temperatures determined by DSC.

## 5.3 STRUCTURAL PROPERTIES

The structural properties of the various samples were determined by neutron and X-ray – diffraction. The different experimental techniques are explained in detail in section 3. The programs used for the analysis of the data from the instruments E3 and E7 were TVTueb [89] and PeakFit [90]. For the ILL data the programs LAMP [91], FULLPROF [92] and Matlab [93] were used.

### 5.3.1 NEUTRON DIFFRACTION

To determine the structure of the single crystalline samples cut out of crystal rod no.1, the HZB neutron diffractometers E3 and E7 with the wavelengths 1.486Å and 1.804Å, respectively were used. The samples were pre-orientated by Laue-diffraction and their diffraction patterns were obtained by rotating the samples about 180° around two axes perpendicular to the (hk0) and (h0l) diffraction planes.

### 5.3.1.1 CRYSTAL ROD NO.1 “Ni<sub>44.0</sub>Mn<sub>30.0</sub>Ga<sub>20.0</sub>Co<sub>6.0</sub>”

Diffraction patterns of five samples of this rod were determined, whereby the samples were chosen from different positions of the rod and therefore showed a changing Mn/Ga – ratio (see Table 5.3.1). For the single crystalline samples 1\_3 and 1\_4 a tetragonal structure with two short axes ( $a = b$ ) and one long  $c$  – axis was verified at room temperature in the martensite phase. The samples 1\_6 and 1\_7 showed an orthorhombic martensite structure ( $a \neq b \neq c$ ) at room temperature. For sample 1\_5 a small deviation between  $a$  and  $b$  was measured. However the difference lies in the error bars of the measurements, therefore the martensite structure is assumed to be tetragonal, like the samples 1\_3 and 1\_4.

Sample	Mn/Ga	a [Å]	b [Å]	c [Å]	V [Å <sup>3</sup> ]
1_3	1.36	5.50	5.50	6.49	196.32
1_4	1.37	5.54	5.54	6.48	198.88
1_5	1.43	5.50	5.49	6.54	197.48
1_6	1.45	5.49	5.43	6.56	195.56
1_7	1.49	5.48	5.43	6.58	195.80

Table 5.3.1: Mn/Ga – ratio and the determined cell parameter and volumes of the cut out 6 x 5 x 4 mm Ni-Mn-Ga-Co – samples of the single crystalline rod no.1, showing the highest Cobalt content and a Mn/Ga – ratio varying from 1.36 to 1.49, on the HZB-Instruments E3 and E7.

As depicted in Figure 5.3.1, it was determined, that the samples cut out of the top of the rod (starting from sample 1\_3) show a longer  $a$  and  $b$  axis than the samples cut out from the bottom of the single crystalline rod (ending with sample 1\_7). The shortest axis  $a$  decreases from 5.50 Å in sample 1\_3 to 5.43 Å in sample 1\_7. The  $b$ -axis shows the same but less distinctive trend and decreases from 5.5 Å in the tetragonal sample down to 5.48 Å in the orthorhombic samples 1\_6 and 1\_7. Comparing the  $c$ -axis of the samples an inverse trend can be observed. From 6.49 Å determined in sample 1\_3 the length of the  $c$ -axis increases to 6.58 Å in sample 1\_7.

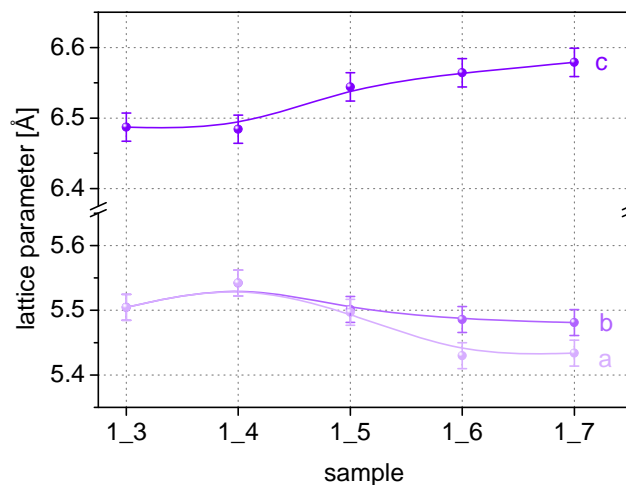
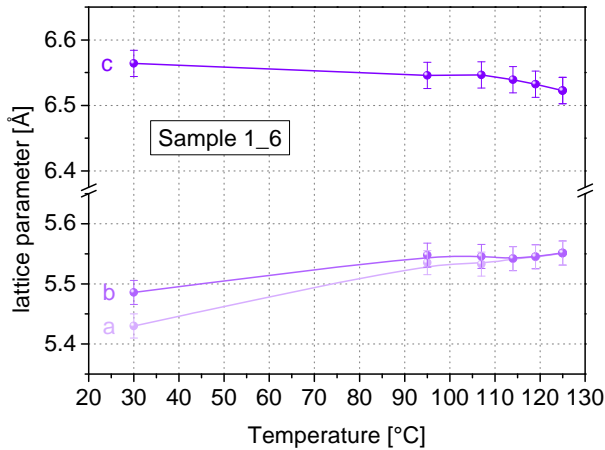


Figure 5.3.1: Lattice parameters of five samples cut out from different positions of the single crystalline rod No.1 with the weighted composition Ni<sub>44.0</sub>Mn<sub>30.0</sub>Ga<sub>20.0</sub>Co<sub>6.0</sub>, whereby the Mn/Ga – ratio of the samples increases from sample 1\_3 to 1\_7

In order to prove the preliminary assumption of an intermartensite phase in sample 1\_6 and 1\_7, made due to the splitting of the structural phase transformation temperature seen in the DSC-measurements (see subsection 5.1.1), diffraction patterns of sample 1\_6 were obtained at different temperatures (see Figure 5.3.2). It can be seen, that the orthorhombic structure measured at room temperature has a longer c – axis (6.56 Å) than at 125°C (6.52 Å), while the a – and b – axis (5.43Å and 5.49Å, respectively) increase in length at 107°C (5.53Å and 5.55Å) before they become equal at 114°C (a = b = 5.54Å). At 135°C the structure transforms from the tetragonal structure to the austenite cubic structure (see Table 5.3.2).



T [°C]	a [Å]	b [Å]	c [Å]
30	5.43	5.49	6.56
95	5.53	5.55	6.55
107	5.53	5.55	6.55
114	5.54	5.54	6.54
119	5.54	5.55	6.53
125	5.55	5.55	6.52
135	6.00	6.00	6.00

Figure 5.3.2: temperature dependent measurement of the lattice parameters of sample 1\_6 from room temperature to 125°C.

Table 5.3.2: lattice parameters of sample 1\_6 for different temperatures

### 5.3.1.2 CRYSTAL ROD NO.2 “Ni<sub>44.6</sub>Mn<sub>30.7</sub>Ga<sub>19.3</sub>Co<sub>5.4</sub>”

Three samples from the single crystalline rod no.2 were taken for the structural analysis by neutron diffraction. The measurements were the same as for the samples of the previous rod, whereby sample 2\_1 and 2\_2 showed a much lower Mn/Ga – ratio than sample 2\_6, which was taken from the opposite side of the rod (see Tab. 14).

Sample	Mn/Ga	a [Å]	b [Å]	c [Å]	V [Å <sup>3</sup> ]
2_1	1.35	5.50	5.50	6.52	197.23
2_2	1.37	5.49	5.49	6.54	197.12
2_6	1.55	5.48	5.48	6.57	197.30

Table 5.3.3: Mn/Ga – ratio and the determined cell parameter and volumes of the cut out 6 x 5 x 4 mm Ni-Mn-Ga-Co – samples 2\_1, 2\_2 and 2\_6 of the single crystalline rod no.2, showing a big difference in the Mn/Ga – ratio from 1.20 in sample 2\_1 to 1.50 in sample 2\_6. The tetragonal structures were determined at the HZB-Instruments E3 and E7 and analysed by TVTueb and PeakFit.

All samples show a tetragonal martensite structure at room temperature with two short axes a and b and a long c axis. As it can be seen in Figure 5.3.3, the a and b axes slightly decrease from 5.50Å to 5.48Å with increasing Mn/Ga – ratio. However the change of the position, where the samples have been cut out and therefore Mn/Ga – ratio, shows a more significant influence on the length of the c axis, which increases from 6.52Å to 6.57Å with the increasing Mn/Ga – ratio.

The unit cell volume seems to be unaffected from the changing composition in that range and was calculated to lie at approximately  $197\text{\AA}^3$ .

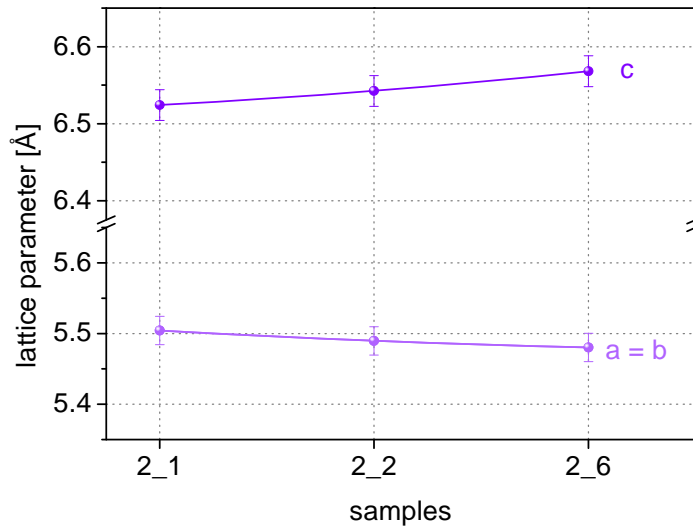


Figure 5.3.3: Lattice parameters of three samples cut out from different positions of the single crystalline rod no.2 with the weighted composition  $\text{Ni}_{44.6}\text{Mn}_{30.7}\text{Ga}_{19.3}\text{Co}_{5.4}$ , whereby the Mn/Ga – ratio of the samples increases from sample 2\_1 to 2\_6.

### 5.3.1.3 CRYSTAL ROD NO.3 “ $\text{Ni}_{45.0}\text{Mn}_{31.0}\text{Ga}_{19.2}\text{Co}_{4.8}$ ”

The samples from crystal rod no.3 show a changing Mn/Ga – ratio from 1.33 to 1.53. Like from the rods before samples from different positions were taken to determine a possible influence of the composition on the structure by single crystal neutron diffraction on the HZB-instruments E3 and E7. Furthermore sample 3\_2 was taken to analyse the distribution of cobalt in the sublattices of Ni-Mn-Ga at the ILL-instrument D9.

Sample	Mn/Ga	a [Å]	b [Å]	c [Å]	V [Å <sup>3</sup> ]
3_1	1.33	5.51	5.51	6.50	197.34
3_2	1.38	5.49	5.49	6.40	192.90
3_5	1.47	5.46	5.46	6.53	194.67
3_6	1.53	5.48	5.84	6.58	210.58

Table 5.3.4: Mn/Ga – ratio and the determined cell parameter and volumes of the cut out 6 x 5 x 4 mm Ni-Mn-Ga-Co – samples of the single crystalline rod no.3 on the HZB-Instruments E3 and E7, showing a change in structure from the tetragonal to the orthorhombic non modulated structure in the sample with the highest Mn/Ga – ratio of 1.53.

As it is depicted in Figure 5.3.4, sample 3\_1, 3\_2 and 3\_3 show a tetragonal non modulated structure in the martensite phase. Also the samples of this rod show the tendency of an increasing c – axis when determining the structure of the samples from the top to the bottom and therefore from a lower to a higher Mn/Ga-ratio, while the a – and b – axis of the tetragonal

martensites decreases in length (see also Tab.5.3.4). The sample with the highest determined Mn/Ga – ratio of this rod shows an orthorhombic non modulated structure, whereby the a – and b – axis show a much higher difference in length ( $a = 5.48\text{\AA}$ ,  $b = 5.84\text{\AA}$ ) than the samples 1\_6 and 1\_7 (see subsection 5.3.1.1).

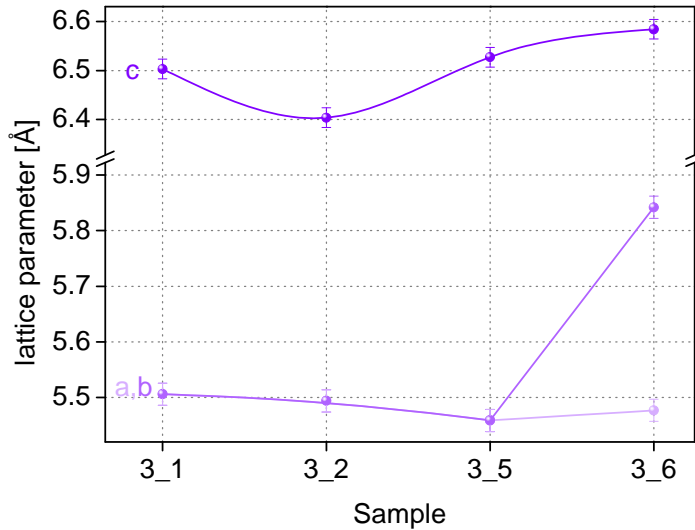


Figure 5.3.4: Lattice parameters of four samples cut out from different positions of the single crystalline rod No.3 with the weighted composition  $\text{Ni}_{45.0}\text{Mn}_{31.0}\text{Ga}_{19.2}\text{Co}_{4.8}$ , whereby the Mn/Ga – ratio of the samples increases from sample 3\_1 to 3\_6.

### 5.3.1.3.1 DISTRIBUTION OF MN AND CO IN MN-EXCESS NI-MN-GA-CO

In order to verify the distribution of cobalt in the sublattices of Ni-Mn-Ga the single crystalline sample 3\_6 ( $\text{Ni}_{46.77}\text{Mn}_{28.24}\text{Ga}_{20.41}\text{Co}_{5.05}$ ) was measured on the ILL-instrument D9 in the austenite state at 415K with a wavelength of  $0.833\text{\AA}$ . Considering a cubic structure with the lattice parameters  $a = b = c = 5.77\text{\AA}$  and the symmetry Fm-3m, like in Ni-Mn-Ga, the intensity of 767 reflections from  $-10 \leq h \leq 10$ ,  $-10 \leq k \leq 10$  and  $-10 \leq l \leq 0$  was measured.

The subsequent integration of the peaks using Matlab provided a list of the intensity and the squared structurefactor of the measured reflections, respectively. Due to the analysis with FullProf (see Appendix B), the most likely distribution of the atoms was evaluated, by comparing the theoretically calculated squared structure factors for a specific distribution with the squared structure factors determined by the experiment (see Figure 5.3.5).

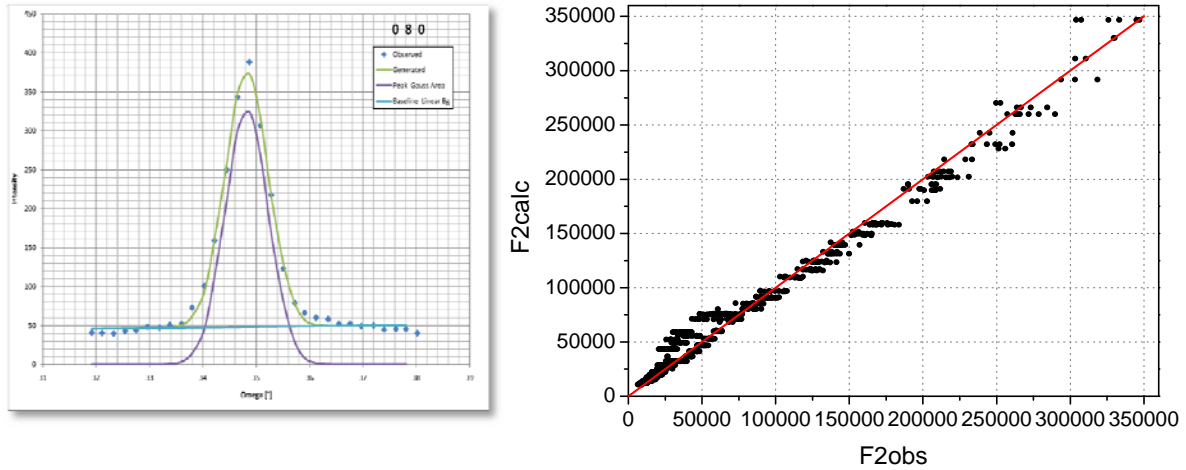


Figure 5.3.5: After the integration of the 767 reflections (one example is shown here for the 080 reflection), the determined squared structure factors were compared with the theoretically calculated structure factors for different distributions of the atoms in the sublattices of a Fm-3m structure to find the best correspondence between the two values (best result shown on the right side).

With an RF – factor of 4.52 the system with cobalt partly located on the manganese – and on the nickel – places (see Table 5.3.5) is the most likely scenario found by the analysis, while the manganese excess is located on the free gallium positions.

Element	x	y	z	occupation
Ni	$\frac{1}{4}$	$\frac{1}{4}$	$\frac{1}{4}$	1.85
Co1	$\frac{1}{4}$	$\frac{1}{4}$	$\frac{1}{4}$	0.15
Mn1	$\frac{1}{2}$	$\frac{1}{2}$	$\frac{1}{2}$	0.97
Co2	$\frac{1}{2}$	$\frac{1}{2}$	$\frac{1}{2}$	0.03
Ga	0	0	0	0.80
Mn2	0	0	0	0.20

Table 5.3.5: Distributions of nickel, manganese, gallium and cobalt on the positions of the austenitic Ni-Mn-Ga (Fm-3m) structure for sample 3\_6.

#### 5.3.1.4 CRYSTAL ROD NO.4 “Ni<sub>48.8</sub>Mn<sub>28.6</sub>Ga<sub>21.4</sub>Co<sub>1.2</sub>”

From this single crystalline rod four samples were taken to determine the structure of the martensite phase with a changing Mn/Ga – ratio between 1.31 and 1.48. For the measurements the HZB – instruments E3 and E7 were used performing the same experiments as for the samples discussed before.

All the samples showed a tetragonal non modulated structure at room temperature. As it is shown in Figure 5.3.6, the a and b axis decrease with the increasing Mn/Ga – ratio by trend, while the c axis increases.

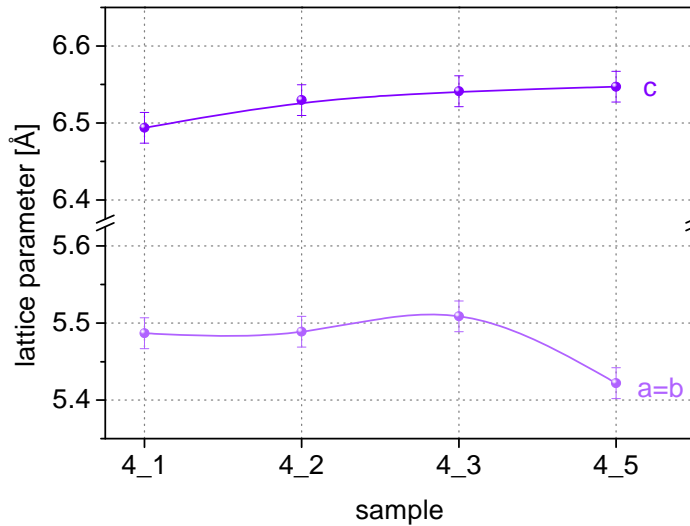


Figure 5.3.6: Lattice parameters of three samples cut out from different positions of the single crystalline rod No.3 with the weighted composition  $\text{Ni}_{48.8}\text{Mn}_{28.6}\text{Ga}_{21.4}\text{Co}_{1.2}$ , whereby the Mn/Ga – ratio of the samples increases from sample 4\_1 to 4\_5.

As it is tabulated in Table 5.3.6, the volume of the unit cell does not show a distinctive trend with the changing Mn/Ga – ratio and varies between  $192.42$  and  $198.56\text{\AA}^3$ .

sample	Mn/Ga	a [Å]	b [Å]	c [Å]	V [Å <sup>3</sup> ]
4_1	1.31	5.49	5.49	6.49	195.61
4_2	1.35	5.49	5.49	6.53	196.81
4_3	1.44	5.51	5.51	6.54	198.56
4_5	1.48	5.42	5.42	6.55	192.42

Table 5.3.6: Mn/Ga – ratio and the determined cell parameter and volumes of the cut out  $6 \times 5 \times 4$  mm Ni-Mn-Ga-Co – samples of the single crystalline rod no.4. All measurements were performed on the HZB-Instruments E3 and E7.

### 5.3.1.5 CRYSTAL ROD NO.5 “ $\text{Ni}_{49.2}\text{Mn}_{28.4}\text{Ga}_{21.6}\text{Co}_{0.8}$ ”

The martensite structures of the samples cut out of the single crystalline rod no.5 were determined on the diffractometer E3. By applying an uniaxial stress along one crystal axis, the samples showed one main variant.

All samples showed a tetragonal 5M structure (see Figure 5.3.7) at room temperature, whereby the lattice parameters changed slightly along the growth axis of the rod (see Table 5.3.7).

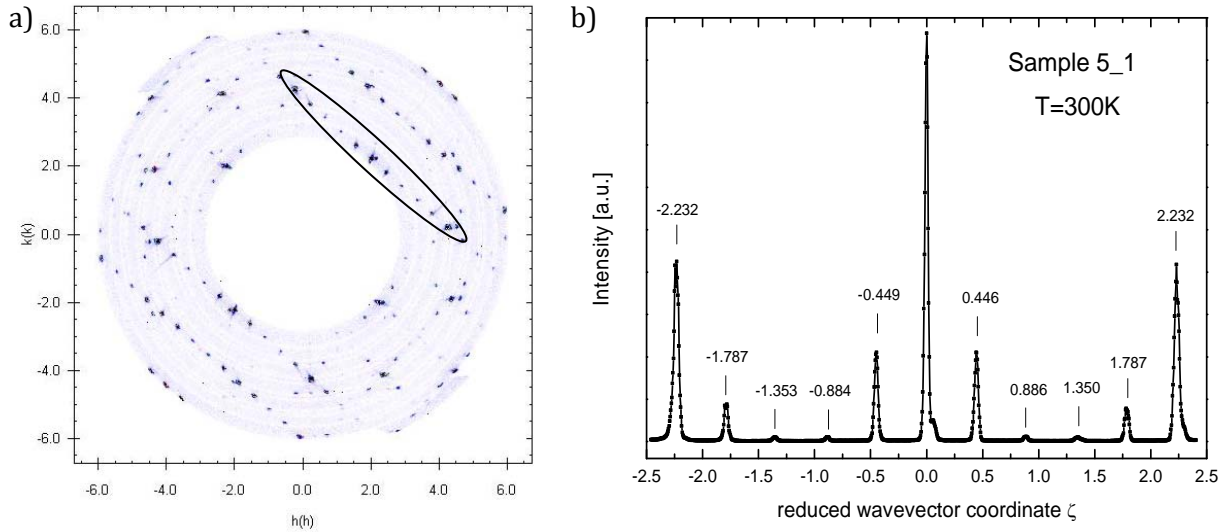


Figure 5.3.7: a)  $hk0$ -plane of the tetragonal modulated structure, shown exemplarily of sample 5\_1, in the martensite phase at room temperature. b) Modulation peaks of sample 5\_1 measured at HZB – instrument E3

With increasing Mn/Ga – ratio, the long lattice parameters  $a$  and  $b$  slightly increase from  $5.934\text{\AA}$  in sample 5\_1 to  $5.986\text{\AA}$  in sample 5\_7, while the length of the short axis  $c$  decreases from  $5.588\text{\AA}$  in sample 5\_1 to  $5.576\text{\AA}$  determined in sample 5\_7 (see Figure 5.3.8). Altogether the volume of the unitcell increases from  $195.78\text{\AA}^3$  for sample 5\_1 to  $199.80\text{\AA}^3$  for sample 5\_7.

Sample	Mn/Ga	$a$ [ $\text{\AA}$ ]	$b$ [ $\text{\AA}$ ]	$c$ [ $\text{\AA}$ ]	$V$ [ $\text{\AA}^3$ ]
5_1	1.07	5.934	5.934	5.588	195.78
5_2	1.07	5.953	5.953	5.578	197.99
5_3	1.11	5.953	5.953	5.576	197.57
5_4	1.11	5.953	5.953	5.576	197.57
5_5	1.14	5.953	5.953	5.576	197.57
5_6	1.19	5.953	5.953	5.580	197.74
5_7	1.20	5.986	5.986	5.576	199.80

Table 5.3.7: Mn/Ga – ratio and the determined cell parameter and volumes of the cut out  $6 \times 5 \times 4$  mm Ni-Cio-Mn-Ga – samples of the single crystalline rod no.5

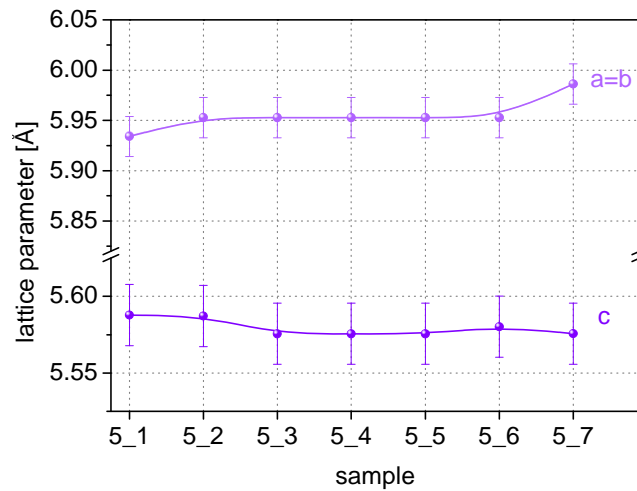


Figure 5.3.8: Lattice parameters of samples cut out from different positions of the single crystalline rod No.5 with the weighted composition  $\text{Ni}_{48.8}\text{Mn}_{28.6}\text{Ga}_{21.4}\text{Co}_{0.8}$ , whereby the Mn/Ga – ratio of the samples increases from sample 6\_1 to 6\_7, which all show a tetragonal modulated (5M) martensite structure at room temperature.

### 5.3.2 X-RAY DIFFRACTION

For the X-ray diffraction experiments several single crystalline samples were pulverised by ballmilling them into an approximately homogeneous powder. Therefore a closed marble ball mill, was taken to minimize the risk of impurities. To pulverize the samples with the dimensions of approximately 4 x 5 x 6 mm the ball mill needed about 45min.

The powder samples were measured with a BRUKER D8 Advance in Bragg-Brentano-Geometry and  $\text{Cu-K}\alpha$ -radiation (1.5406 Å) in a  $2\theta$  range between 30 and 100°.

Independent from the amount of cobalt or the Mn/Ga – ratio all samples treated with the ball mill showed a structure different from the martensite structure determined in the single crystalline samples by neutron diffraction. Instead of a tetragonal or orthorhombic structure, a disordered fcc – structure [94, 95] with the lattice parameters  $a = b = c = (3.66 \pm 0.2) \text{ \AA}$  (see Figure 5.3.9) and a mixture of the structures, respectively was verified at room temperature.

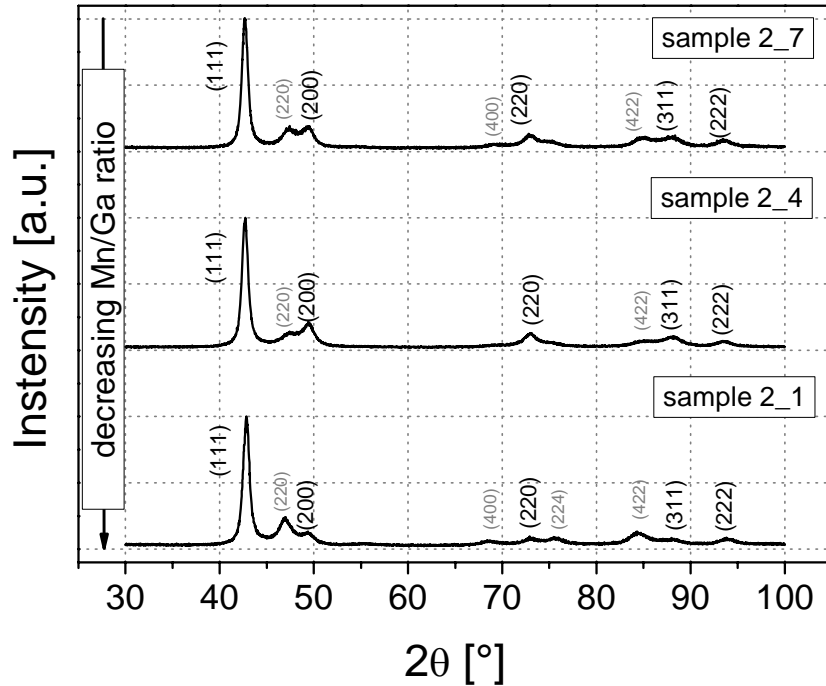


Figure 5.3.9: X-Ray powder diffraction patterns of sample 2\_1, 2\_4 and 2\_7. The black Miller indices, labelled in bold, belong to the disordered fcc structure, while the grey smaller indices belong to the tetragonal non modulated structures of the samples.

Taking a closer look at the calculated lattice parameters of sample 2\_1, 2\_4 and 2\_7 taken the powder sample data, it can be seen, that they differ significantly from the lattice parameters obtained from the single crystal experiments with neutron diffraction even though they show the same trend of a decreasing  $a$  and  $b$  axis with the increasing Mn/Ga – ratio and a increasing  $c$  axis in the same direction. As it is tabulated in the following Table 5.3.8, the  $a$  and  $b$  axis of the powder sample is much smaller than of the single crystalline samples, whereby the long  $c$  axis shows the opposite behaviour.

Sample	fcc – disordered in powder sample			martensite structure in powder sample			martensite structure in single crystalline sample		
	a	b	c	a	b	c	a	b	c
2_1	3.65	3.65	3.65	5.47	5.47	6.55	5.50	5.50	6.52
2_4	3.66	3.66	3.66	5.42	5.42	6.59	5.49	5.49	6.54
2_7	3.67	3.67	3.67	5.42	5.42	6.65	5.48	5.48	6.57
3_1	3.66	3.66	3.66	only fcc disordered			5.51	5.51	6.50
3_3	3.65	3.65	3.65	5.47	5.47	6.57	no measurement		
3_7	3.67	3.67	3.67	not possible to analyse			no measurement		

Table 5.3.8: The structures and lattice parameters, respectively, determined in the powder samples after ball milling single crystalline specimens of the crystal rod no. 2 and 3 by x-ray diffraction and the lattice parameters of the single crystalline material determined by neutron diffraction.

To identify if the stress induced structure can be changed to the stress free martensite structure found in the single crystalline material, the powder samples 3\_1, 3\_3 and 3\_7 were annealed at 600°C in an argon flow for 45min. As it can be seen in Figure 5.3.10, the annealing procedure led to a structural change of sample 3\_7 to an orthorhombic martensite structure with the lattice parameters  $a = 5.49\text{\AA}$ ,  $b = 5.87\text{\AA}$  and  $c = 6.22\text{\AA}$ .

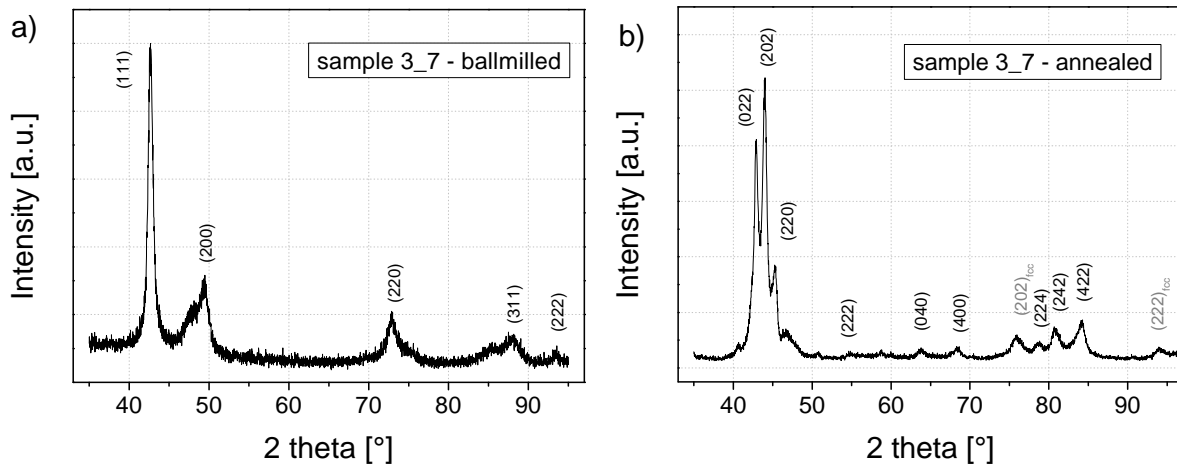


Figure 5.3.10: X-ray diffraction pattern of the powder sample 3\_7 a) after the ball milling showing the fcc disordered structure and b) after the annealing procedure at 600°C for 45min under argon flow, showing a mixture of the orthorhombic martensite phase (black subscripts) and the still partly existing fcc disordered phase (grey subscripted).

However the annealing procedure did not transform the whole sample successfully, so that a part of the sample still showed the stress induced fcc – structure (see grey subscripted peaks in Figure 5.3.10 b).

Samples 3\_1 and 3\_3 showed no structural phase transformation (depicted exemplarily for sample 3\_1 in Figure 5.3.11) to a stress free martensite phase after this treatment and were still in the fcc – disordered phase with the lattice parameters  $a = b = c = 3.66\text{\AA}$  (red curve).

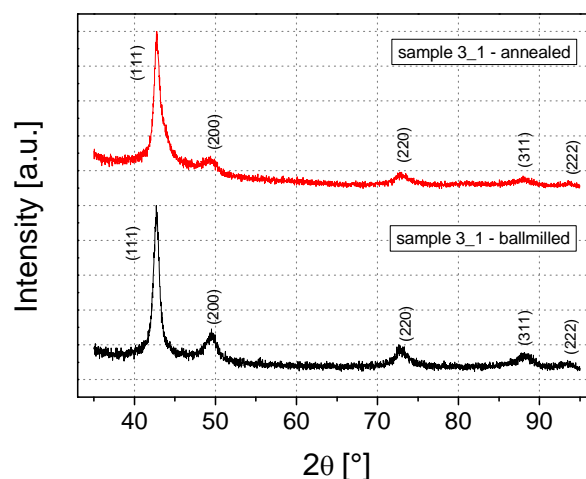


Figure 5.3.11: X-ray diffraction patterns of sample 3\_1 before (black curve) and after (red curve) the annealing procedure at 600°C for 45min under argon flow showing the fcc disordered structure independent from the treatment.

## 5.4 MECHANICAL PROPERTIES

The mechanical properties measured for the Ni-Mn-Ga-Co – samples are the twinning stress and the mechanical induced strain of the specimen of different composition and structure (see subsection 1 to 3) by using the testing device described in section 3.5. To determine a possible favoured training and the highest possible strain as well as lowest possible twinning stress of the samples, the compression tests were performed with two different loading sequences with two cycles each. In order to apply an uniaxial pressure high enough to reach the single variant state, several samples were cut to smaller specimen. For samples showing a twinning stress lower than the magneto stress, the magnetic field induced strain was also measured.

### 5.4.1 CRYSTAL ROD NO.1 “Ni<sub>44.0</sub>Mn<sub>30.0</sub>Ga<sub>20.0</sub>Co<sub>6.0</sub>”

From the first single crystalline rod with the nominal composition Ni<sub>44.0</sub>Mn<sub>30.0</sub>Ga<sub>20.0</sub>Co<sub>6.0</sub> the stress – strain – behaviour of the three samples 1\_1, 1\_4, 1\_5 and 1\_7 has been measured by applying a uniaxial mechanical stress on the samples.

The sample with the smallest Mn/Ga – ratio 1\_1 was cut to a small cuboid with the dimensions  $x = 2.550\text{mm}$ ,  $y = 1.671\text{mm}$  and  $z = 1.052\text{mm}$ . The dimensions were measured before and after each loading with a micrometer (see Figure 5.4.1).

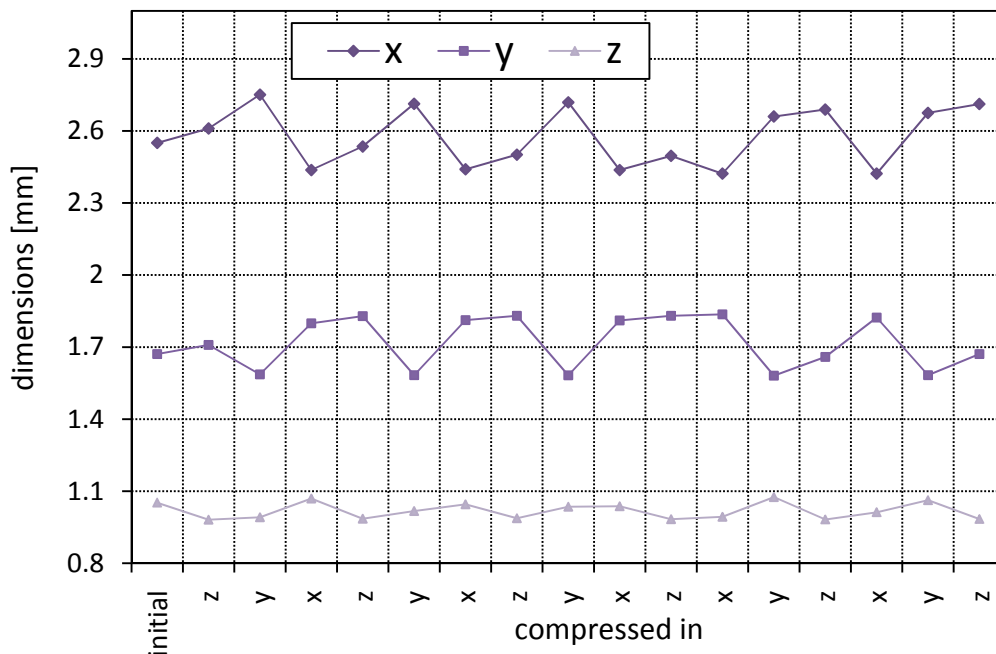


Figure 5.4.1: The change of the dimensions of the sample 1\_1 when applying uniaxial pressure along different axes. After three “loading cycles” the loading sequence was changed from  $z \rightarrow y \rightarrow x$  to  $z \rightarrow x \rightarrow y$ .

The first uniaxial pressure was applied along the shortest axis, z, which resulted in an increase in the other two dimensions (see Figure 5.4.2). Afterwards the samples were compressed along the y-direction, followed by the compression of the longest axis, x. Both compressions showed a change of all three dimensions. In the y-direction, the uniaxial pressure led to a mechanical induced strain of 7.75%, whereby the x – and z – direction changed about 5.13% and 1.01%, respectively (see Figure 5.4.2). The compression in the x – direction showed similar results with a mechanical induced strain of 12.88% and a change of 11.84% and 7.30% along the y – and z – direction. The loading cycle, the compression along all three axes with the sequence z → y → x, was repeated twice, before the sequence was changed to z → x → y for the last two loading cycles.

Thereby the mechanical induced strain in the y – direction increased up to 16.13% and was repeatedly measured independently from the loading sequence. The same behaviour was determined for the other two axes. The maximum strain reached in the x – direction was 12.88% and stayed at approximately the same value, when the measurement was repeated. The z – direction showed the smallest mechanical induced strain with its maximum at 9.47%.

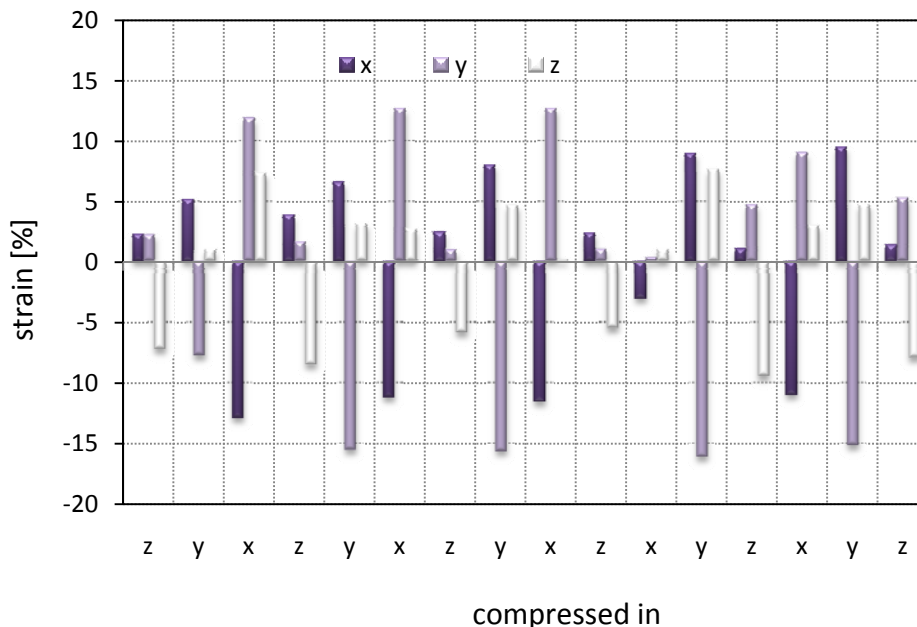


Figure 5.4.2: The change of the length of the axes in percentages according to the previous length at any one time.

In all directions the mechanical stress was increased constantly from 0 Mpa up to 110 Mpa to determine the twinning stress which has to be overcome to reach the maximum mechanically induced strain. Independent from the loading sequence the determined stress plateaus were not very distinctive for all three directions (see Figure 5.4.3). In the z – direction, the stress had to be increased constantly up to  $25\text{Mpa} \pm 6\text{Mpa}$  to reach a strain of 8%. Afterwards the slope of the curve increases and results in an additional strain of less than 2% only. In order to reach a mechanical strain of 13% - 14% in the y – direction, a stress of 40Mpa to 50Mpa was necessary. The x – direction shows a similar behaviour like the z – direction when applying the uniaxial pressure. Up to a mechanically stress induced strain of 8%, a constant increase of the stress from 12Mpa to 25Mpa was determined, while the required stress increases to 75Mpa to reach an additional strain of 2%.

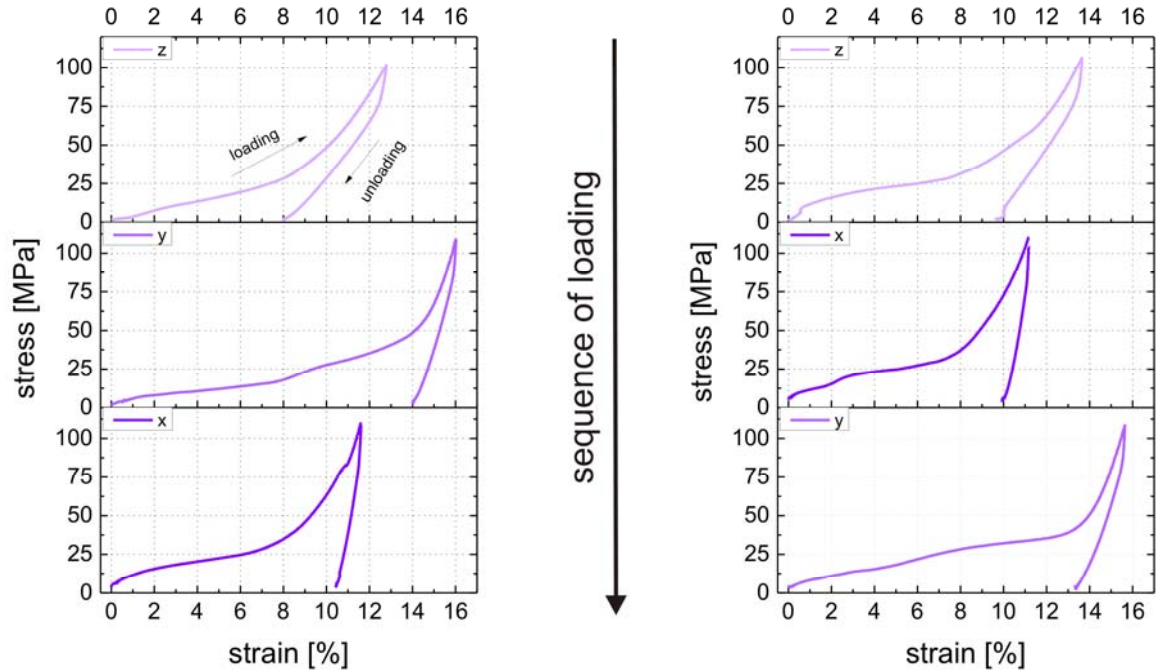


Figure 5.4.3: The stress – strain – behaviour of sample 1\_1 as a function of the loading sequence, which is changing from  $z \rightarrow y \rightarrow x$  (left diagram) to  $z \rightarrow x \rightarrow y$  (right diagram).

Sample 1\_4 ( $\text{Ni}_{44.47}\text{Mn}_{28.56}\text{Ga}_{20.83}\text{Co}_{6.14}$ ) with the initial dimensions  $x = 2.054$  mm,  $y = 2.084$  mm and  $z = 2.867$  mm was first compressed in the longest direction. Thereby the sequence of loading  $z \rightarrow y \rightarrow x$  was repeated three times and then changed to  $z \rightarrow x \rightarrow y$ . Already from the change of the dimensions (see Figure 5.4.4) it can be seen, that only the  $x$  and  $z$  direction show a significant length change. The uniaxial stress in  $x$ - or  $z$ - direction results in a mechanically induced strain of 14.6% to 15.4% in  $x$ -direction and of 14.1% to 14.9% in  $z$ -direction and an equivalent positive strain in  $z$ - and  $x$ -direction respectively (see Figure 5.4.4 right diagram).

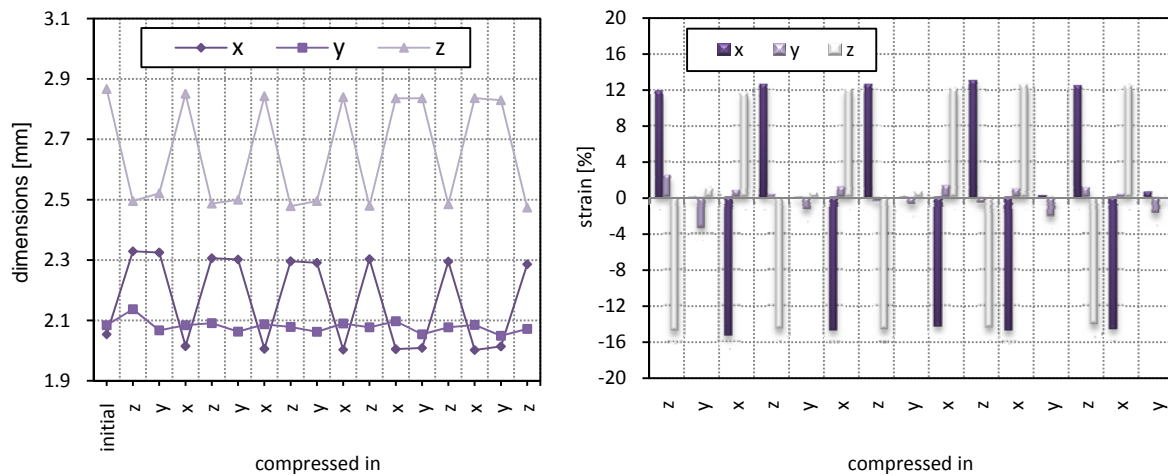


Figure 5.4.4: Change of the dimensions of the sample by applying a uniaxial pressure along one direction given as the  $x$ -axis (left diagram). Mechanical stress induced strain of all three dimensions referring to the previous state (right diagram).

The maximum positive strain in x – direction varies between 11.9% and 13% and shows similar values to the maximum positive strain determined in z – direction (11.6% - 12.6%). Independent from the loading sequence, the uniaxial pressure in y – direction does not result in a significant shape change. The highest mechanical induced strain determined is 3.4% only, whereby the x- and z – direction show nearly no strain.

Like in the previous sample 1\_1, the stress – strain – behaviour of sample 1\_4 was measured by increasing constantly the uniaxial pressure to 110Mpa and determining the induced strain. Independent from the sequence of loading, the same stress is required to reach comparable strain values in the z – and x – direction (see Figure 5.4.5). By applying a stress of 25Mpa, a strain of approximately 8% can be reached, while for an additional 5% strain a uniaxial pressure of 75Mpa is needed. To reach the maximum determined strain in x – direction a mechanical stress of 50Mpa has to be applied. As it can be seen in Figure 5.4.5, the twinning stress in the y – direction cannot be overcome until 80Mpa. Furthermore it was determined that the twinning stress is not reduced by repeated compressions as well as the reachable strain does not increase significantly due to more loading cycles.

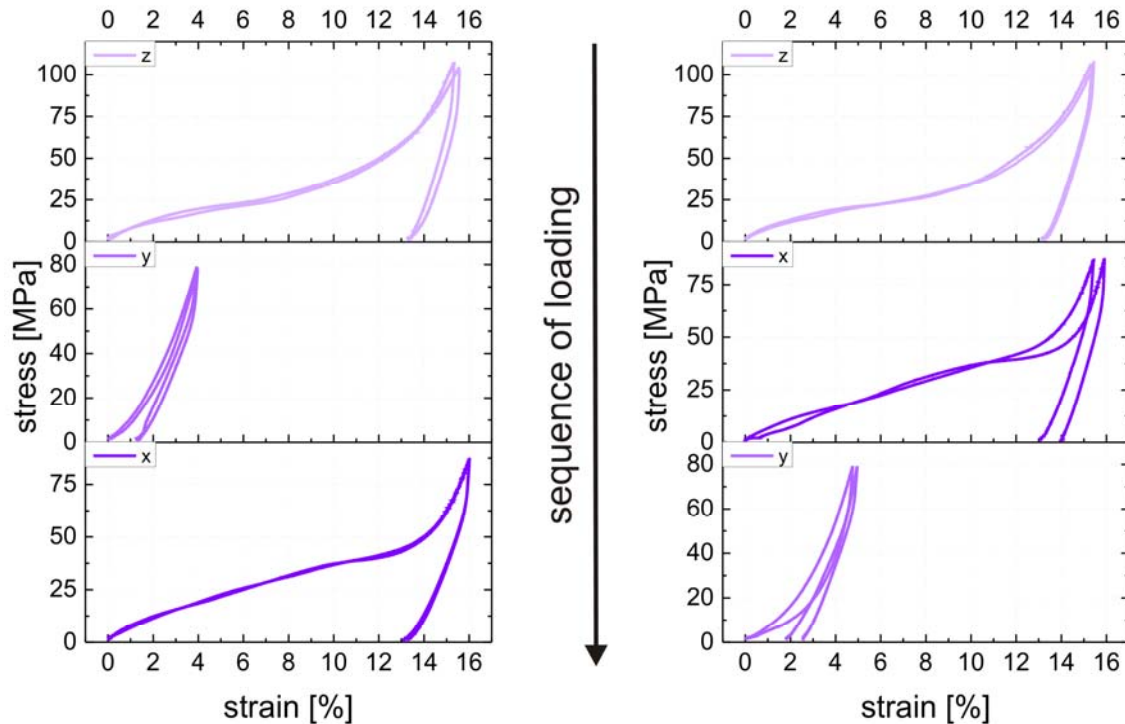


Figure 5.4.5: The stress – strain – behaviour of sample 1\_4 ( $\text{Ni}_{44.47}\text{Mn}_{28.56}\text{Ga}_{20.83}\text{Co}_{6.14}$ ) of all three axes for two loading cycles with the sequence  $z \rightarrow y \rightarrow x$  and  $z \rightarrow x \rightarrow y$ , respectively.

Sample 1\_5 with the composition  $\text{Ni}_{44.93}\text{Mn}_{28.57}\text{Ga}_{20.00}\text{Co}_{6.50}$  and the dimensions  $x = 2.497$  mm,  $y = 2.604$  mm and  $z = 1.291$  mm showed first a change of all three dimensions when applying the uniaxial pressure in the z – direction (see Figure 5.4.6). The subsequent compression in the y – direction resulted in a length decrease of 8.67% in y and an increase of 6.20% in x, while the z-direction stayed nearly constant. With the third loading (in x – direction) the maximum negative change of 17.01% in this direction was reached. Independent from the loading sequence which

was changed in the same way like in the other samples (from  $z \rightarrow y \rightarrow x$  to  $z \rightarrow x \rightarrow y$ ), the compression along the x - axis resulted in similar values for the dimension of x. However the resulting increase of the y - and z - length changed from nearly equal change of 12.08% and 10.25%, respectively to 12.54% and 3.02%. When changing the sequence of loading it was observed, that the first compression along the x - axis results in a very small change of 1.6% in the length of x but increases to normal values in the second cycle already.

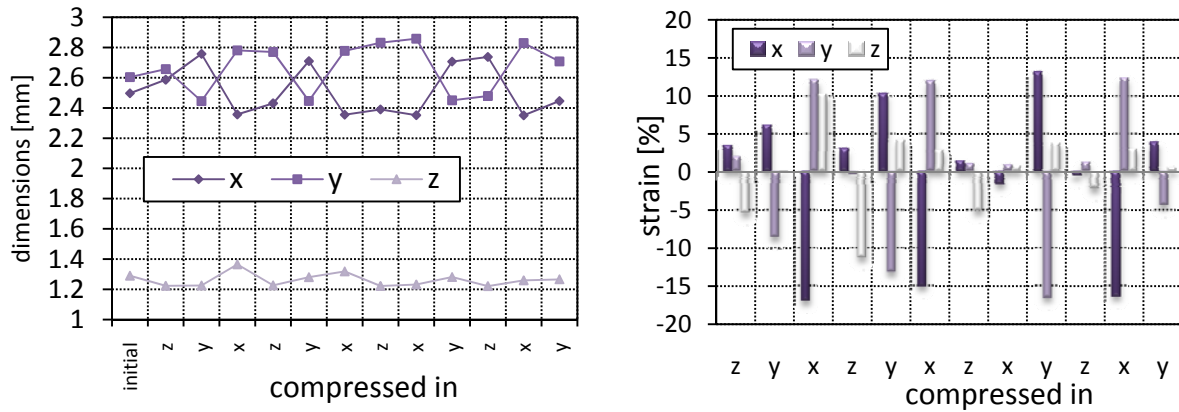


Figure 5.4.6: Change of the dimensions of the sample 1\_5 after each deformation step in mm (left diagram) and in percentage referring to the dimensions measured before the compression (right diagram).

The measurement of the twinning stress showed the stress plateau for the compression along the z - direction at approximately 25 Mpa, resulting in a strain of 11% and vanishes in the following loading cycles, while the strain decreases to 4% even with an applied stress of 75Mpa (see Figure 5.4.7).

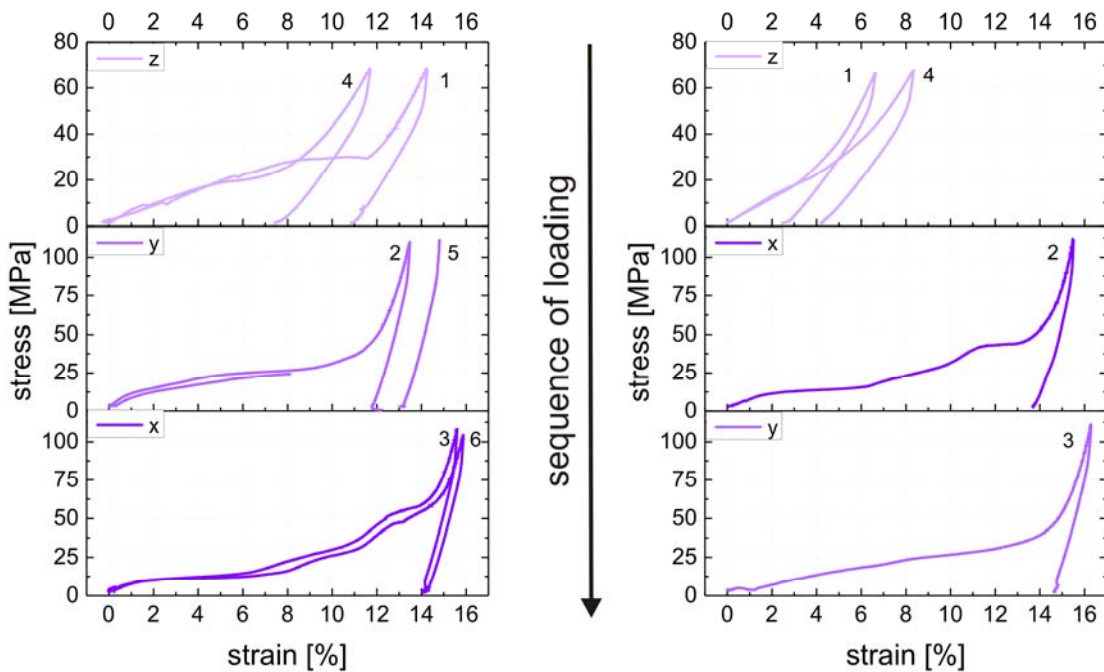


Figure 5.4.7: The stress - strain - behaviour of sample 1\_5 ( $\text{Ni}_{44.93}\text{Mn}_{28.57}\text{Ga}_{20.00}\text{Co}_{6.50}$ ) of all three axes for two loading cycles with the sequence  $z \rightarrow y \rightarrow x$  (left diagram) and  $z \rightarrow x \rightarrow y$  (right diagram), respectively.

Furthermore it was determined, that the twinning stress in the x – direction has to be overcome stepwise, whereby the first stress plateau lies around 12 Mpa, increasing to 43Mpa as with the last stress plateau. The determined stress plateau for the y – direction is very distinctive and lies around 25Mpa independent from the loading sequence.

The sample 1\_7 with the highest Mn/Ga – ratio ( $\text{Ni}_{44.62}\text{Mn}_{29.52}\text{Ga}_{19.88}\text{Co}_{5.98}$ ) shows the same stress – strain – behaviour like sample 1\_4. Only two directions (here x and y) show a mechanical stress induced strain, while the third direction, z stays nearly constant (see Figure 5.4.8) independent from the loading sequence. Thereby the change in the x – and y – direction are nearly equal around 16%. When changing the sequence of loading from  $z \rightarrow y \rightarrow x$  to  $z \rightarrow x \rightarrow y$  it was determined, that the first compression in x resulted in nearly no shape change but recovered like in sample 1\_5 in the subsequent loading cycle.

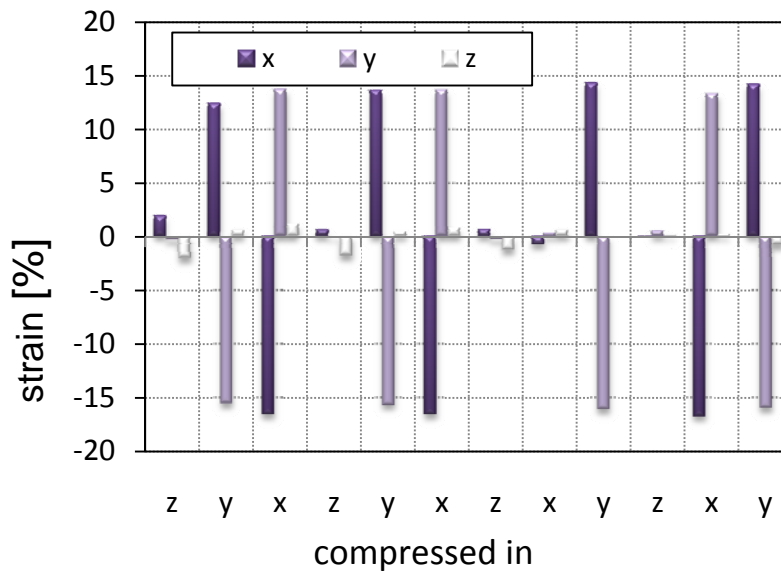


Figure 5.4.8: The change of the length of the axes in percentages according to the previous length at any one time of sample 1\_7 ( $\text{Ni}_{44.62}\text{Mn}_{29.52}\text{Ga}_{19.88}\text{Co}_{5.98}$ )

Also the twinning stress in the x – and y- directions are similar to each other. Both show a very distinctive stress plateau around 15Mpa, which is slightly lower than in sample 1\_4. Independent from the sequence of loading, a strain of approximately 13% can be reached when applying a stress of 25Mpa, which is nearly the maximum strain, determined in that sample. The compression in the z – direction does not overcome the twinning stress even with a uniaxial compression of 100Mpa (see Figure 5.4.9). Furthermore it was determined that a repeated loading cycle does not reduce the force needed to overcome the twinning stress or increase the reachable strain.

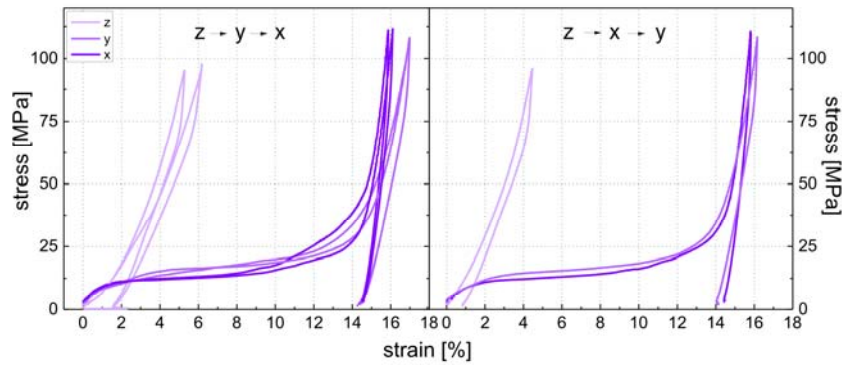


Figure 5.4.9: The stress- strain – behaviour in all three axes of sample 1\_7 for different loading sequences (z →y→x – left diagram, z →x→y – right diagram)

### STRESS – STRAIN – VALUES

As it can be seen already from the depicted stress-strain – curves of the samples of the single crystalline rod no.1, the shape of the determined curves as well as the behaviour, when a uniaxial mechanical stress is applied with different sequences and the twinning stress measured for low and high strains differ significantly from each other. While some show a stepwise increase of the twinning stress (e.g. sample 1\_5) others show a peak in the twinning stress before reaching the maximum strain. In order to make a comparison of the samples easier, the averaged twinning stress  $\sigma_{TW}$  (see Figure 5.4.10) from 0.2% strain ( $\epsilon=0.2\%$ ) to 95% of the maximum strain,  $\epsilon_{95}$  was calculated [96]. Furthermore the difference between the stresses needed to induce 0.2% strain in the sample and  $\epsilon_{95}$  was calculated,  $\Delta\sigma$  and is listed in the following tables below (Table 5.4.1-5.4.5). A detailed description of the mechanical stress induced strain curves for the samples of the single crystalline rods no.2 to 5 is attached in Appendix C, while a short summary of the results will be given in the following subsections.

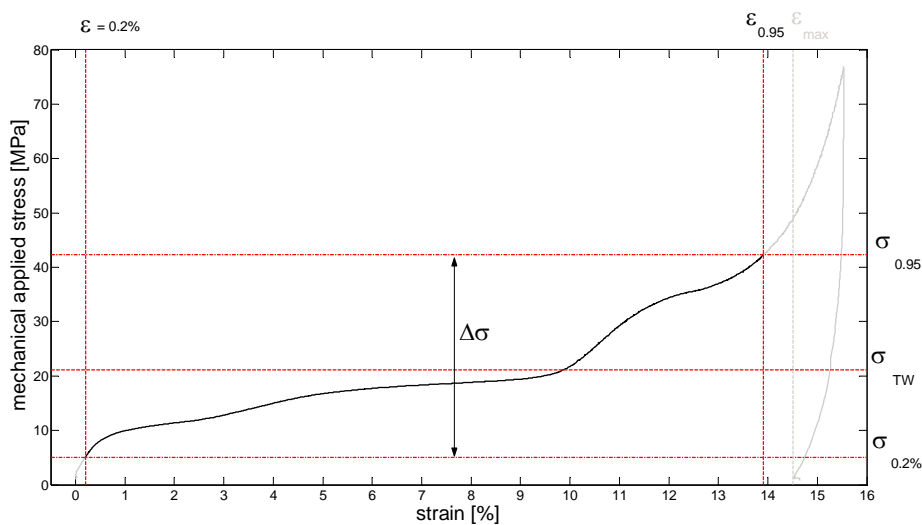


Figure 5.4.10: Schematic of the determination of the different key values (maximum twinning strain  $\epsilon_{max}$ , twinning stress  $\sigma_{0.95}$  and  $\sigma_{0.2\%}$ , averaged twinning stress  $\sigma_{TW}$ , and twinning stress interval  $\Delta\sigma$ ) of the stress – strain – behaviour.

Sample	Cycle No.	Compression direction	max. Strain $\epsilon_{max}$ [%]	95% of $\epsilon_{max}$ $\epsilon_{95}$ [%]	$\sigma_{TW}$ [Mpa]	$\Delta\sigma$ ( $0.2\% \leq \epsilon \leq \epsilon_{95}$ ) [Mpa]
1_1	1	z	7.61	7.23	16.35	24.3
		y	13.4	12.73	15.8	37.5
		x	10.33	9.81	25.04	58.9
	2	z	7.99	7.59	9.377	23.9
		y	14	13.30	16.27	39.2
		x	10.44	9.92	24.25	55.7
	3	z	4.83	4.59	12.45	16.6
		x	missing data points			
		y	13.86	13.17	18.31	32.6
	4	z	9.67	9.19	15.61	36.5
		x	9.93	9.43	26.76	52.9
		y	13.38	12.71	21.47	33
		z	9.73	9.24	13.29	24
	1_4	1	z	13.38	12.71	25.65
y			1.39	1.32	6.6	10.4
x			13.31	12.64	24.6	40.3
2		z	13.29	12.63	24.92	49.3
		y	1.25	1.19	7.45	10.5
		x	13.07	12.42	24.14	37.8
3		z	13.24	12.58	24.37	49.8
		x	14.02	13.32	19.82	40.3
		y	2.54	2.41	6.03	11.06
4		z	13.14	12.48	25.68	51.4
		x	13.04	12.39	22.96	40.5
		y	1.78	1.69	6.87	10.78
		z	13.18	12.52	23.49	46.2
1_5		1	z	10.86	10.32	17.36
	y		11.81	11.22	22.46	33.3
	x		14.01	13.31	23.64	50.2
	2	z	7.36	6.99	12.71	19.53
		y	13.16	12.50	missing data points	
		x	14.07	13.37	18.51	45.2
	3	z	6.63	6.30	8.447	22.03
		x	1.82	1.73	11.79	16.8
		y	14.52	13.79	20.68	32.2
	4	z	6.33	6.01	10.39	27.8
		y	2.29	2.18	15.41	26.5
	5	z	2.42	2.30	7.72	11.17
		x	13.7	13.02	20.29	40.07
		y	14.62	13.89	19.66	34.5
z		4.19	3.98	12.04	19.78	
1_7	1	z	1.56	1.48	3.853	9.7
		y	14.25	13.54	16.32	26
		x	14.53	13.80	15.15	31.9
	2	z	1.56	1.48	6.473	9.2
		y	14.41	13.69	15.97	22.8
		x	14.52	13.79	13.08	20.9
	3	z	2.03	1.93	3.862	8.9
		x	1.08	1.03	11.3	12.8
		y	14.28	13.57	15.11	24.9

Sample	Cycle No.	Compression direction	max. Strain $\epsilon_{\max}$ [%]	95% of $\epsilon_{\max}$ $\epsilon_{95}$ [%]	$\sigma_{TW}$ [Mpa]	$\Delta\sigma$ (0.2% $\leq \epsilon \leq \epsilon_{95}$ ) [Mpa]
1.7	4	z	0.81	0.77	6.644	7.2
		x	14.43	13.71	13.67	23.7
		y	14.06	13.36	16.06	23.6
		z	0.62	0.59	4.547	3.6

Table 5.4.1: The maximum strain, the averaged twinning stress in the interval 0.2% to  $\epsilon_{95}$  and the difference of the applied mechanical stress at 0.2% strain and  $\epsilon_{95}$  for all determined samples of the single crystalline rod no 1. The grey shaded cells show one sequence of loading, the white cells the subsequent loading sequence.

### 5.4.2 CRYSTAL ROD NO.2 “Ni<sub>44.6</sub>Mn<sub>30.7</sub>Ga<sub>19.3</sub>Co<sub>5.4</sub>”

From crystal rod No. 2 the stress – strain – behaviour of three samples two from the bottom (2\_1 and 2\_2) and one from the top (2\_6) were determined in the same way like the samples from crystal rod No.1 and are summarized in the following table (Table 5.4.2).

Sample	Cycle No.	Compression direction	max. Strain $\epsilon_{\max}$ [%]	95% of $\epsilon_{\max}$ $\epsilon_{95}$ [%]	$\sigma_{TW}$ [Mpa]	$\Delta\sigma$ (0.2% $\leq \epsilon \leq \epsilon_{95}$ ) [Mpa]	
2_1	1	y	1.62	1.54	14	31.1	
		x	14.8	14.06	17.4	31.27	
	2	z	13.7	13.02	15.36	22.3	
		y	0.82	0.78	12.22	22.9	
	3	x	14.19	13.48	14.94	21.57	
		z	13.51	12.83	14.99	23.5	
	4	y	0.67	0.64	11.92	15.1	
		x	13.74	13.05	14.8	21.18	
		z	13.84	13.15	14.61	21.4	
	2_2	1	x	14.02	13.32	14.25	19.41
			y	0.48	0.46	6.556	5.9
			z	14.17	13.46	21.29	36.7
2		y	1.63	1.55	11.47	20.6	
		x	14.57	13.84	20.9	36.37	
		z	14.2	13.49	20.3	30.8	
3		y	0.803	0.76	7.19	21.9	
		x	14.47	13.75	21.19	31.57	
		z	14.31	13.59	19.81	28.3	
4		x	14.07	13.37	20.14	26.18	
		y	0.419	0.40	17.41	9.9	
		z	13.75	13.06	21.48	31.4	
2_6		1	x	14.09	13.39	20.97	28.73
			y	0.39	0.37	20.01	11.2
			z	13.46	12.787	42.17	62.6
		2	y	4.98	4.731	31.64	63.2
			x	13.09	12.4355	39.58	60.39
			z	12.07	11.4665	41.06	55.8

Sample	Cycle No.	Compression direction	max. Strain $\epsilon_{\max}$ [%]	95% of $\epsilon_{\max}$ $\epsilon_{95}$ [%]	$\sigma_{TW}$ [Mpa]	$\Delta\sigma$ ( $0.2\% \leq \epsilon \leq \epsilon_{95}$ ) [Mpa]
2.6	2	y	3.89	3.6955	30.22	66.8
		x	12.56	11.932	42.78	60.39
	3	z	12.1	11.495	38.45	56.7
		x	9.81	9.3195	36.38	50.88
		y	2.57	2.4415	29.66	58.1
	4	z	10.65	10.1175	35.05	55.5
		x	10.32	9.804	39.4	51.08
		y	2.53	2.4035	17.15	47.5

Table 5.4.2: Stress – strain – values of the samples cut out from the bottom (sample 2\_1 and 2\_2) and from the top (sample 2\_6) of the single crystalline rod No.2. The grey shaded cells show the results for compression test with the sequence z – y – x, the white cells in the table the results for the compression sequence z – x – y.

While the maximum strain reached by uniaxial compression and the twinning stress are very similar for the samples (about 15 Mpa to 20 Mpa) from the bottom of the rod, the sample 2\_6 of the top shows a twinning stress approximately double as high as the latter samples. Sample 2\_1 and 2\_2 show a strain of around 14% in the x – and z – direction and only a small strain of less than 0.9% in z – direction, which was independent from the loading sequence. In contrast, sample 2\_6 shows a smaller strain of 10 to 13% in the z – and x – direction, while the strain determined along the y – direction is much higher with 2 to 5%.

### 5.4.3 CRYSTAL ROD NO.3 “Ni<sub>45.0</sub>Mn<sub>31.0</sub>Ga<sub>19.2</sub>Co<sub>4.8</sub>”

From the crystal rod no.3 two samples, 3\_1 and 3\_6, have been taken to evaluate the stress strain measurements, whereby sample 3\_1 is cut out from the bottom of the rod and sample 3\_6 from the top of the rod (see table 5.4.3).

Sample	Cycle No.	Compression direction	max. Strain $\epsilon_{\max}$ [%]	95% of $\epsilon_{\max}$ $\epsilon_{95}$ [%]	$\sigma_{TW}$ [Mpa]	$\Delta\sigma$ ( $0.2\% \leq \epsilon \leq \epsilon_{95}$ ) [Mpa]
3_1	1	z	5.34	5.073	15.49	15.87
		y	13.06	12.407	14.1	26.34
		x	4.34	4.123	8.215	12.96
	2	z	5.94	5.643	29.07	28.06
		y	13.17	12.5115	13.03	28.09
3_6	1	x	16.54	15.713	28.31	25.1
		y	7.22	6.859	86.54	71.8
		z	0.09	0.0855	strain too small to determine	
	2	x	16.27	15.4565	30.51	17.2
		y	6.95	6.6025	76.27	65.1
		z	0	0	strain too small to determine	
	3	x	16.74	15.903	29.02	25

Sample	Cycle No.	Compression direction	max. Strain $\epsilon_{\max}$ [%]	95% of $\epsilon_{\max}$ $\epsilon_{95}$ [%]	$\sigma_{TW}$ [Mpa]	$\Delta\sigma$ ( $0.2\% \leq \epsilon \leq \epsilon_{95}$ ) [Mpa]
3_6	3	z	9.79	9.3005	55.38	27.8
		y	0.15	0.1425	strain too small to determine	
	4	x	16.78	15.941	28.94	22.1
		z	10.27	9.7565	51.5	52.9
		y	0.69	0.6555	21.17	24.7

Table 5.4.3: Results of the compression test performed on sample 3\_1 and 3\_6, giving the strain  $\epsilon_{\max}$ , and  $\epsilon_{95}$  and the averaged twinning stress  $\sigma_{TW}$  and the difference  $\Delta\sigma$ .

It can be seen from table 5.4.3, that the twinning stress in sample 3\_1 lies in the range (between 8 and 30 MPA, depending on the compression direction) of the samples measured in the samples before. Also the maximum strain determined in the sample is as large as measured in previous samples. However sample 3\_6 shows a different behaviour. While for the x – direction the twinning stress and the strain stay constant with approximately 30 Mpa and 17% strain, the results for the other two directions highly depend on the loading sequence. For the sequence x – y – z, the z – direction shows no strain and the y – direction a strain of approximately 7% and a twinning stress of 86.54 Mpa decreasing about 10 Mpa in the second cycle. Changing the sequence to x – z – y, leads to an opposite behaviour. While a compression in the y – direction does not result in a strain, the z – direction shows a strain of approximately 10% and a twinning stress of about 30 Mpa.

#### 5.4.4 CRYSTAL ROD NO.4 “Ni<sub>48.8</sub>Mn<sub>28.6</sub>Ga<sub>21.4</sub>Co<sub>1.2</sub>”

From the beginning, the samples from crystal rod no.4 showed a shape change in two directions only. Hence the compression test were performed along the y – and x – direction, while the z – axis was not compressed. The three tested samples (4\_1 and 4\_2 from the bottom and 4\_4 from the middle part of the rod), show a very similar twinning stress of around 8 Mpa and a strain of  $13.5 \pm 0.5\%$  in y – direction and a slightly larger strain  $16 \pm 1.5\%$  in x – direction. The repeated compression did not result in a significant reduction of the twinning stress and an increase of the determined strain, respectively (see Table 5.4.4).

Sample	compression direction	max. Strain $\epsilon_{\max}$ [%]	95% of $\epsilon_{\max}$ $\epsilon_{95}$ [%]	$\sigma_{TW}$ [Mpa]	$\Delta\sigma$ ( $0.2\% \leq \epsilon \leq \epsilon_{95}$ ) [Mpa]
4_1	y	13.66	12.977	8.29	7.39
	x	14.88	14.136	8.542	10.04
	y	13.49	12.8155	8.25	8.03
	x	16.8	15.96	8.363	11.19
	y	13.82	13.129	8.114	9.27
4_2	y	13.37	12.7015	8.644	7.41
	x	17.44	16.568	8.379	11.61
	y	13.47	12.7965	7.958	7.7

Sample	compression direction	max. Strain $\epsilon_{\max}$ [%]	95% of $\epsilon_{\max}$ $\epsilon_{95}$ [%]	$\sigma_{TW}$ [Mpa]	$\Delta\sigma$ ( $0.2\% \leq \epsilon \leq \epsilon_{95}$ ) [Mpa]
4_2	x	16	15.2	8.385	9.03
	y	13.4	12.73	7.979	7.62
4_4	y	13.72	13.034	8.591	8.22
	x	16.56	15.732	8.787	11.86
	y	13.56	12.882	8.069	8.44
	x	15.68	14.896	8.81	11.74
	y	14.01	13.3095	8.319	8.48

Table 5.4.4: Determined stress – strain behaviour of the samples 4\_1, 4\_2 and 4\_4 cut out of the single crystalline rod no.2 with the nominal composition  $\text{Ni}_{48.8}\text{Mn}_{28.6}\text{Ga}_{21.4}\text{Co}_{1.2}$ .

### 5.4.5 CRYSTAL ROD NO.5 “ $\text{Ni}_{49.2}\text{Mn}_{28.4}\text{Ga}_{21.6}\text{Co}_{0.8}$ ”

The smallest twinning stress was determined in the samples from the single crystalline rod no.2. The four samples 5\_1, 5\_3, 5\_4 and 5\_6 were compressed along the z – direction and showed a twinning stress of 1.2 Mpa to 2.5 Mpa. The maximum strain measured in those samples varies between 4.7 and 5.3% (see detailed results in table 5.4.5).

Sample	compression direction	max. Strain $\epsilon_{\max}$ [%]	95% of $\epsilon_{\max}$ $\epsilon_{95}$ [%]	$\sigma_{TW}$ [Mpa]	$\Delta\sigma$ ( $0.2\% \leq \epsilon \leq \epsilon_{95}$ ) [Mpa]
5_1	z	5.2	4.94	1.209	2.035
5_3	z	5.31	5.0445	2.171	2.621
5_4	z	4.72	4.484	1.575	2.78
5_6	z	5.33	5.0635	2.549	3.451

Table 5.4.5: Results of the compression tests performed uniaxially in x – direction of the specimen 5\_1, 5\_3, 5\_4 and 5\_6.

Due to the low twinning stress, all samples of this rod (5\_1 to 5\_7) were tested in a magnetic field without prestress at room temperature to verify the magnetic shape memory effect. Therefore the applied magnetic field was increased constantly from 0 mT to 700 mT. As it can be seen in Figure 5.4.11, all samples show a magnetic field induced strain.

In the samples 1, 2, 3, 4 and 6 a strain was induced above a magnetic field of approximately 300 mT, while for the samples 5 and 7 a higher magnetic field of more than 400 mT is needed to induce the strain. The maximum strain determined with 700 mT in sample 5\_1 was 4.5% decreasing in sample 5\_2 to 4% and in sample 5\_3 to 3.5%. Sample 5\_4 shows again a maximum strain of 4% and 5\_6 of only 3%. Sample 5\_5 seems to show its stress plateau at 700 mT and above, which could not be verified due to the limitation in the testing device described in section 3. However a strain of 2.75% was determined in the maximum field. Sample 5\_7 shows the smallest magnetic field induced strain in this rod with 1.75%.

In summary the tendency is observed, that the twinning stress increases from the bottom to the top of the rod, resulting in a decrease of the measured magnetic field induced strain (see also table 5.4.6).

Sample	max. Strain $\epsilon_{\max}$ [%]	95% of $\epsilon_{\max}$ $\epsilon_{95}$ [%]	aver. H [mT]	$\Delta H$ ( $0.2\% \leq \epsilon \leq \epsilon_{95}$ ) [mT]
5_1	4.47	4.2465	410	342.3
5_2	4.05	3.8475	379.4	235.9
5_3	3.82	3.629	444.7	421.2
5_4	4.15	3.9425	434.3	224.8
5_5	2.71	2.5745	587.7	245.3
5_6	3.04	2.888	361	280.5
5_7	1.76	1.672	374.3	184.41

Table 5.4.6: The maximum strain, the averaged magnetic field, which has to be applied in the interval 0.2% strain to  $\epsilon_{95}$  (calculated as the averaged twinning stress  $\sigma_{TW}$ ) and the difference  $\Delta H$  of the applied magnetic field at  $\epsilon_{0.02}$  and  $\epsilon_{95}$  for sample 5\_1 to 5\_7 of rod no. 5.

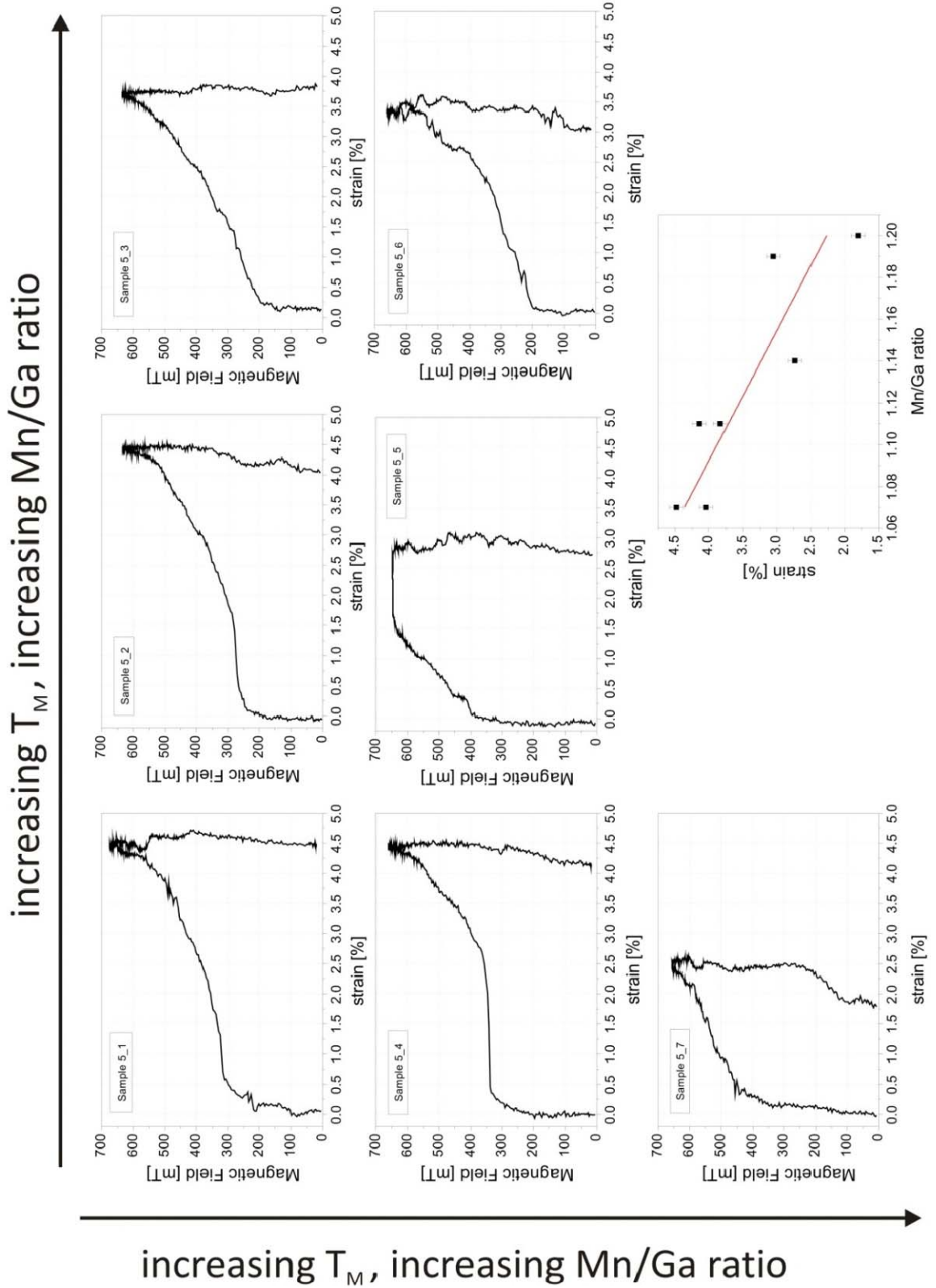


Figure 5.4.11: Stress – strain – behaviour of sample 2 to 7 of rod no.5 by applying a magnetic field which is constantly increasing for the measurements from 0 mT to max. 700 mT.

## 5.5 MAGNETIC PROPERTIES

To figure out the influence of cobalt on the magnetic properties of Ni-Mn-Ga, three samples with the highest cobalt content of approximately 6 at-% and different Mn/Ga – ratios and 2 samples of the single crystalline rod no.2 with 5.4% cobalt (see Table 5.5.1) were examined in the PPMS under varying conditions.

For the measurements, samples of the single crystalline rod no.1 and 2 were taken and cut into smaller pieces with a mass of less than 100mg.

Sample	Ni [at-%]	Mn [at-%]	Ga [at-%]	Co [at-%]	Mn/Ga	T <sub>M</sub> [°C]	T <sub>C</sub> [°C]
rod no.1							
A	44.62	29.52	19.88	5.98	1.48	105.1	159.38
B	44.50	28.54	20.72	6.24	1.38	98.6	155.55
rod no.2							
C	45.08	30.06	19.46	5.41	1.54	143.2	in T <sub>M</sub>
D	45.85	28.26	20.52	5.37	1.38	104.3	153.88
E	46.27	26.43	22.03	5.27	1.20	91.1	154.3

Table 5.5.1: The composition and Mn/Ga – ratio as well as the structural and magnetic phase transformation temperatures determined by DSC of the samples taken for PPMS measurements.

The structural and magnetic phase transformation temperatures were extracted by graphical analysis as it is shown exemplarily for the Austenite start –, Austenite finish – and Curie temperature in Figure 5.5.1 A. To extract the Curie – temperature T<sub>C</sub> and the paramagnetic Curie temperature θ, the molar susceptibility χ<sub>mol</sub> was calculated by the following equation:

$$\chi_{mol} = \frac{\chi}{n} = \frac{\chi[emu/Oe]}{(m[g]/M[g/mol])} = \frac{M[emu] * M[g/mol]}{H[Oe] * m[g]} \quad [59]$$

By plotting 1/χ<sub>mol</sub> versus the temperature, the paramagnetic Curie temperature θ can be determined by a Curie – Weiss – fit depicted exemplarily for sample B in Figure 61B due to following equations:

$$\chi_{mol} = \frac{C}{T - \theta} \Rightarrow \frac{1}{\chi_{mol}} = \frac{T}{C} - \frac{\theta}{C} \quad [60]$$

with  $C$  as the Curie constant.  $1/\chi_{\text{mol}}$  can be fitted to a straight line  $y=mx+b$ , and therefore  $\theta$  can be easily extracted by  $\theta=-b/m$ .

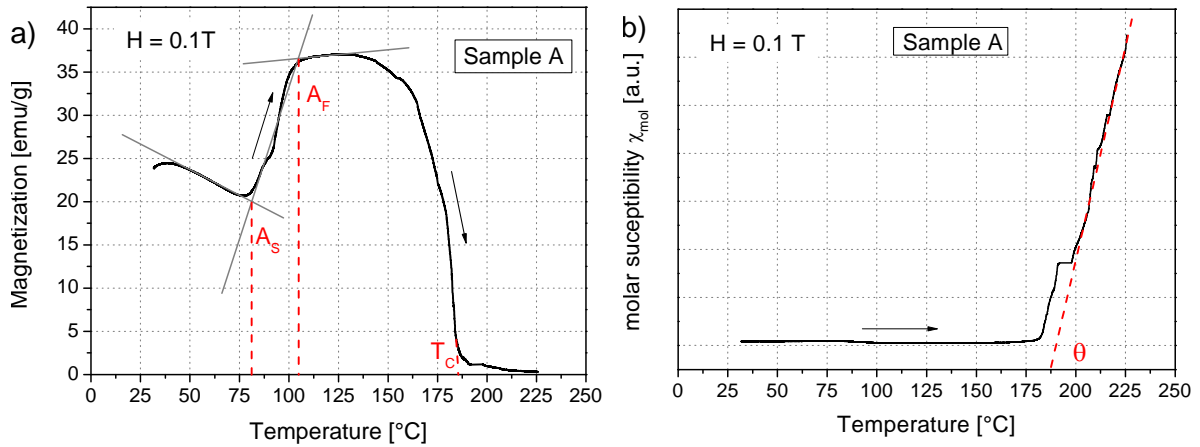


Figure 5.5.1: a) Magnetization  $M$  versus Temperature for a magnetic field of 0.1T showing the Zero field cooled (ZFC) curve of sample A for the determination of the Austenite start ( $A_S$ ) – Austenite finish ( $A_F$ ) – and the Curie temperature of the ferromagnetic phase ( $T_C$ ) b) Plot of the molar susceptibility  $\chi_{\text{mol}}$  versus the temperature for the Curie Weiss fit (red line) to extract the Curie temperature of the paramagnetic phase ( $\theta$ ).

### 5.5.1 M vs T - MEASUREMENTS

To determine the influence of the magnetic field on the phase transformation temperatures, the samples were measured in the multivariant state from 300K to at least 500K by applying a magnetic field of 0.1T, 1T and 5T, respectively. Therefore the samples were heated up above their Curie – Temperature (determined by DSC) without magnetic field and were cooled down to 300K before applying a magnetic field. Afterwards, the temperature was increased to the particular maximum temperature, whereby the magnetic moment was measured. The curves plotted from these data-sets will be titled as the so called “Zero field cooled – curve” (ZFC). The subsequent cooling under a magnetic field leads to the so called “Field cooled – curve” (FC), which is followed by the “Field heated – curve” (FH), whereby the temperature was increased again to its maximum.

As it can be seen in Figure 5.5.2, sample A, with the highest cobalt – content and a Mn/Ga - ratio of 1.49 shows a slight decrease of the magnetization with increasing temperature in the ferromagnetic martensite independent from the applied magnetic field. However the maximum magnetization increases from approximately 38 emu/g in an external field of 0.1T to 63 emu/g in  $H_{\text{ext}} = 1\text{T}$  and 70 emu/g in the external magnetic field of 5T. When reaching the Austenite Start Temperature  $A_s$  a significant increase of the magnetization  $M$  at the phase transformation from the ferromagnetic martensite to the ferromagnetic austenite ( $A_F$ ) was determined before it decreases towards zero at the Curie – Temperature.

While the sample shows an approximately constant magnetization in the ferromagnetic austenite (from 103 °C to 162 °C – ZFC, from 150°C to 80°C – FC and 100°C to 155°C – FH) in an external magnetic field of 0.1T (plateaus in the black curve of Figure 5.5.2), the magnetization in the ferromagnetic austenite decreases nearly linearly in the higher magnetic fields. Comparing the ZFC – and FH – curves of the sample it can be seen, that there is no significant difference in the magnetization and that the structural phase transformation temperatures are hardly affected by the cooling under magnetic field (see Table 5.5.2).

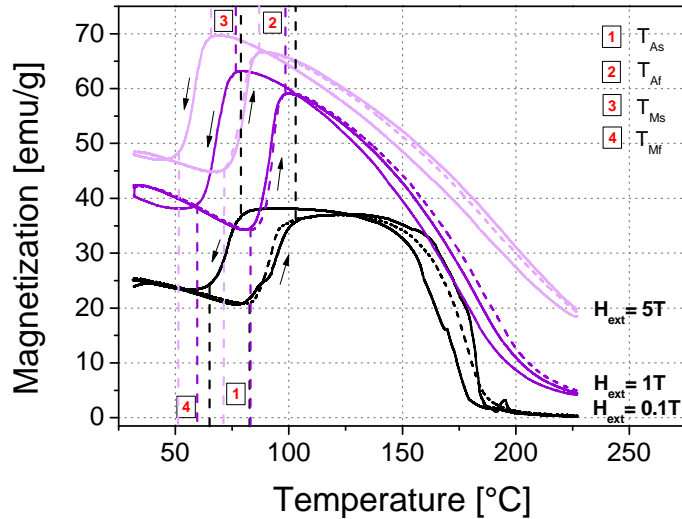


Figure 5.5.2: The magnetization of sample A in a magnetic field of 0.1T (black curve), 1T (dark green curve) and 5T (light green curve). The continuous line from low to high temperature (marked with the black arrows) shows the ZFC – curve, the dotted line displays the FH – curve. The continuous line from high to low temperature (also marked with arrows) is plotted from the FC – data.

However a significant influence of the magnetic on the phase transformation temperatures was determined. With increasing the external magnetic field from 1T to 5T a shift of  $A_S$ ,  $A_F$ ,  $M_S$  and  $M_F$  of about 10°C towards lower temperature was observed. Calculating the martensite temperature  $T_M$  using eq.2

$$T_M = T_{eq} = \frac{(A_S + A_F)/2 + (M_S + M_F)/2}{2} \quad [2]$$

whereas  $A_S$  and  $A_F$  are taken from the ZFC – data, it has been calculated, that a magnetic field of 1T shifts the structural phase transformation of this sample 1\_7 by about 1.4°C when taking the data from 1T and 5T.

$H_{\text{ext}}$ [T]	$A_S$ - ZFC [°C]	$A_F$ - ZFC [°C]	$A_S$ - FH [°C]	$A_F$ - FH [°C]	$M_S$ - FC [°C]	$M_F$ - FC [°C]	$T_M^*$ [°C]
0 (DCS)	92.9	124.0	-	-	101.5	73.5	105.14
0.1	82.5	103.5	82.5	96.9	79.3	64.6	82.5
1	82.6	99.2	85.4	99.2	76.9	59.6	79.6
5	71.2	87.3	71.2	87.2	86.2	50.7	73.9

\* For the calculation of  $T_M$  the Austenite start and Austenite Finish temperatures from the ZFC - curve were taken.

Table: 5.5.2 The calculated structural phase transformation temperature of sample A. The data for the calculation of  $T_M$  were taken from the ZFC - and FC - measurements.

By performing the same measurements on sample B with comparable cobalt content as the previously discussed sample A but a smaller Mn/Ga - ratio of 1.36, a similar behaviour was determined. Due to the smaller Mn/Ga - ratio, the structural phase transformation is much lower than in the previous sample, however also this sample shows a slight decrease of the magnetization with increasing temperature in the ferromagnetic martensite (see black and dark green curve in Figure 5.5.3) and a significant increase in the magnetization within a small temperature interval of approximately 10°C, where the transformation from the martensite to the austenite takes place. In the small magnetic field of 0.1T the sample shows a plateau like behaviour, where the magnetization of the ferromagnetic austenite decreases only slightly with increasing temperature, before the magnetic phase transformation from the ferro- to the paramagnetic state is reached. As already observed in sample A, the plateau vanishes in higher magnetic fields and the structural phase transformation shifts to lower temperatures (see Table 5.5.3).

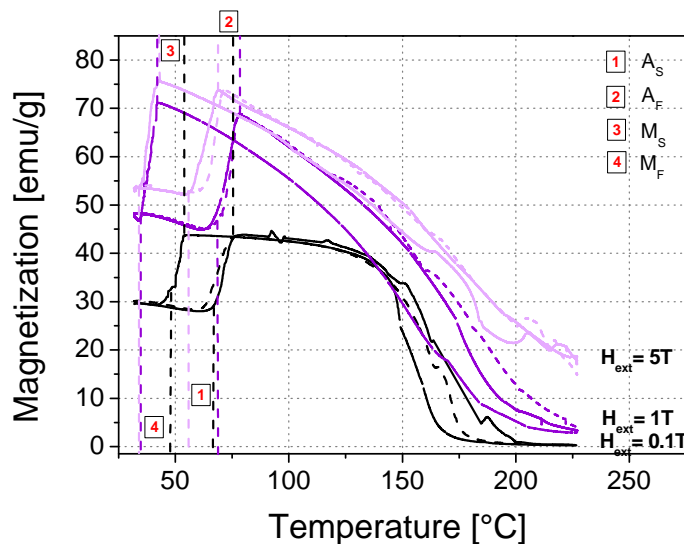


Figure 5.5.3: The magnetization of sample B in a magnetic field of 0.1T (black curve), 1T (dark green curve) and 5T (light green curve). The continuous line from low to high temperature (marked with the black arrows) shows the ZFC - curve, the dotted line displays the FH - curve. The continuous line from high to low temperature (also marked with arrows) is plotted from the FC - data.

Comparing the magnetization in the different magnetic fields with the data from sample A, it can be observed that the maximum magnetization of sample B is higher than in sample A with the higher Mn/Ga – ratio. While the previous sample shows 38 emu/g in 0.1T, 63 emu/g in 1T and 70 emu/g in 5T, sample B shows maximum values of 44 emu/g, 68 emu/g and 75 emu/g, respectively.

$H_{ext}$ [T]	$A_S - ZFC$ [°C]	$A_F - ZFC$ [°C]	$A_S - FH$ [°C]	$A_F - FH$ [°C]	$M_S - FC$ [°C]	$M_F - FC$ [°C]	$T_M^*$ [°C]
0 (DSC)	97.8	124.2			99.7	72.5	98.6
0.1	66.9	75.2	62.5	75.2	54.2	47.9	61.1
1	68.0	78.5	65.1	76.8	42.3	34.8	55.9
5	55.9	68.8	60.8	71.0	42.6	34.0	50.3

\* For the calculation of  $T_M$  the Austenite start and Austenite Finish temperatures from the ZFC - curve were taken.

Table 5.5.3 Structural phase transformation temperatures of sample in different magnetic fields determined by PPMS, whereby  $T_M$  is calculated by eq. 2

In order to see the influence of cobalt on the magnetization at the structural phase transformation temperature, the samples C, D and E were examined in the same way as samples A and B.

Sample C with a cobalt content of 5.4 at-% and a high Mn content and therefore a high Mn/Ga - ratio of 1.55 shows a much higher structural phase transformation temperature of 152.9°C due to the high ratio. The plateau in the magnetization determined in the previous samples at 0.1T was not measured in this sample and the maximum magnetization is much lower in all applied magnetic fields.

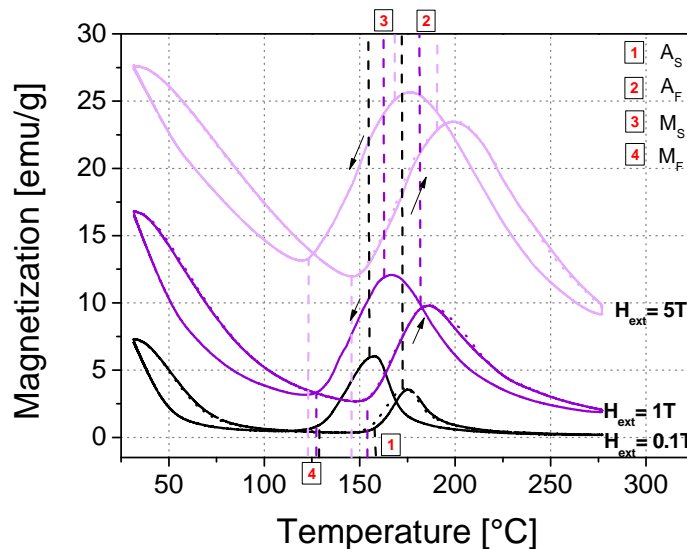


Figure 5.5.4: The magnetization of sample C in a magnetic field of 0.1T (black curve), 1T (dark green curve) and 5T (light green curve). The continuous line from low to high temperature (marked with the black arrows) shows the ZFC - curve, the dotted line displays the FH - curve. The continuous line from high to low temperature (also marked with arrows) is plotted from the FC - data.

As it can be seen in Figure 5.5.4, the maxima of the magnetization were determined at room temperature (7.26 emu/g at 0.1T, 16.79 emu/g at 1T and 27.60 emu/g at 5T). From the starting point of the measurements at 32°C, the magnetization decreases significantly until the structural phase transformation starts. As in the previous samples A and B, the magnetization increases up to the point of the transformation to the ferromagnetic austenite is reached.

Furthermore it was determined, that the broadness of the structural phase transformation increases in higher magnetic fields. Even though the Austenite Start and the Martensite finish temperature shifts to lower temperatures by applying higher magnetic fields, the averaged martensite temperature  $T_M$  increases to about 4°C with the increase of the applied magnetic field from 0.1T to 5T (see Table 5.5.4).

$H_{ext}$ [T]	$A_S$ - ZFC [°C]	$A_F$ - ZFC [°C]	$A_S$ - FH [°C]	$A_F$ - FH [°C]	$M_S$ - FC [°C]	$M_F$ - FC [°C]	$T_M^*$ [°C]
0 (DSC)	133.3	178.7			150.2	110.5	143.2
0.1	157.9	172.7	155.4	170.8	154.7	128.4	152.9
1	154.0	181.9	154.0	181.9	163.1	127.0	156.5
5	145.8	190.5	145.8	190.5	168.2	123.3	157.0

\* For the calculation of  $T_M$  the Austenite start and Austenite Finish temperatures from the ZFC - curve were taken.

Table 5.5.4: The structural phase transformation temperatures of sample C extracted by the ZFC -, FH - and FC - measurements in different magnetic fields.

The samples D and E with a similar cobalt content as the previous sample but with a lower Mn/Ga - ratio show a decrease of the martensite phase transformation temperature with an increasing magnetic field from 0.1T to 5T (see Table 5.5.5 and exemplarily for sample D in Figure 5.5.5). In contrast to samples A and B, which show a bigger difference between the structural and the magnetic phase transformation temperature, no distinctive plateau after the Austenite finish - and Martensite start - temperature, respectively, was determined.

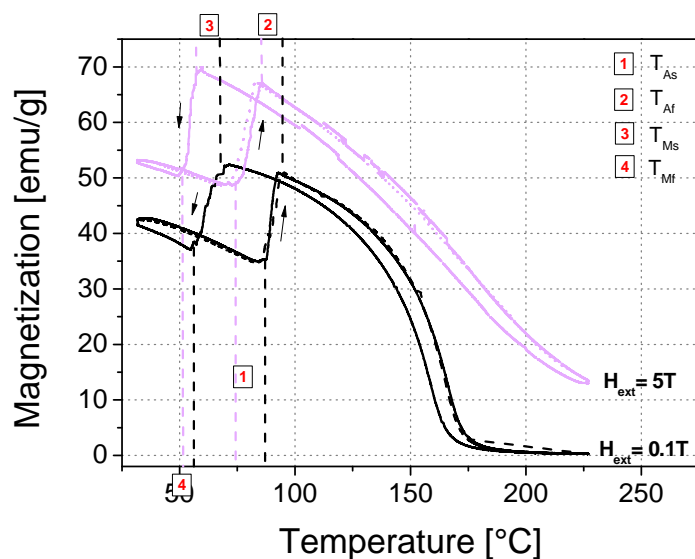


Figure 5.5.5: The Zero field cooled - and Field cooled - and Field heated - curves of sample D in a magnetic field of 0.1T (black graphs) and 5T (green graphs) with changing temperature.

$H_{ext}$ [T]	$A_S - ZFC$ [°C]	$A_F - ZFC$ [°C]	$A_S - FH$ [°C]	$A_F - FH$ [°C]	$M_S - FC$ [°C]	$M_F - FC$ [°C]	$T_M^*$ [°C]
Sample D							
0 (DSC)	105.5	133.5			103.6	74.4	104.3
0.1	113.0	134.4	110.7	127.3	110.2	85.4	110.75
1	108.8	127.3	105.1	123.1	105.1	81.7	105.7
5	92.2	118.5	92.2	118.5	74.3	50.5	83.9
Sample E							
0 (DSC)	83.2	115.2			73.3	53.7	81.1
0.1	86.9	94.8	86.9	93.0	67.3	56.2	76.2
1	84.5	92.2	86.7	94.2	67.3	55.0	74.8
5	74.2	86.1	72.3	83.0	57.3	51.6	67.3

\* For the calculation of  $T_M$  the Austenite start and Austenite Finish temperatures from the ZFC - curve were taken.

Table 5.5.5: The Austenite start and Austenite finish temperatures extracted from the ZFC - and FH - measurements as well as the Martensite start - and Martensite finish - temperature and the calculated martensite temperature  $T_M$ .

The Curie temperatures of the ferromagnetic and paramagnetic phase of the samples were determined by the magnetization curves measured in a 0.1T field. As it can be seen in Table 5.5.6, the paramagnetic Curie temperature is always higher than the ferromagnetic Curie temperature which shows, that the system is slightly frustrated, which can be explained due to the Mn excess in the samples and therefore the direct Mn-Mn- interaction which is of the Rudermann-Kittel-Kasuya-Yosida (RKKY) - type.

Sample	Ni [at-%]	Mn/Ga	$T_C$ (ZFC) [°C]	$T_C$ (FH) [°C]	$T_C$ [°C]	$\theta$ (ZFC) [°C]	$\theta$ (FH) [°C]
A	44.62	1.48	186.7	168.2	177.5	188.2	168.6
B	44.50	1.38	185.2	180.2	181.3	187.3	181.3
C	45.08	1.54	192.7	175.8	184.3	198.5	173.9
D	45.85	1.38	196.5	191.9	194.2	200.7	176.9
E	46.27	1.20	175.5	167.6	171.6	176.5	186.8

Table 5.5.6: The Curie temperatures of the ferromagnetic phase taken from the ZFC - and FH - measurements and the calculated averaged Curie temperature  $T_C$  as well as the Curie temperatures  $\theta$  of the paramagnetic phase taken from the same measurements.

## 5.5.2 M VS H - MEASUREMENTS

To work out the entropy change in the sample during the structural phase transformation, the magnetization of the sample was measured in a continuously increasing magnetic field from 0T to at least 10T in equidistant temperature steps below, during and above the martensite transformation. Thereby it was observed, that the magnetization in samples A and B from the single crystalline rod no.1 and D and E from the single crystalline rod no.2 increases with increasing magnetic field and increasing temperature at the structural phase transformation, which confirms the magnetization measurements in constant magnetic fields and increasing temperature. When the temperature for the martensite transformation was reached in high magnetic fields of more than 9T, samples B and D show a maximum magnetization of more than 76 emu/g and 63 emu/g, respectively, before it decreases at higher temperatures to 75 emu/g and 61 emu/g at the highest magnetic field.

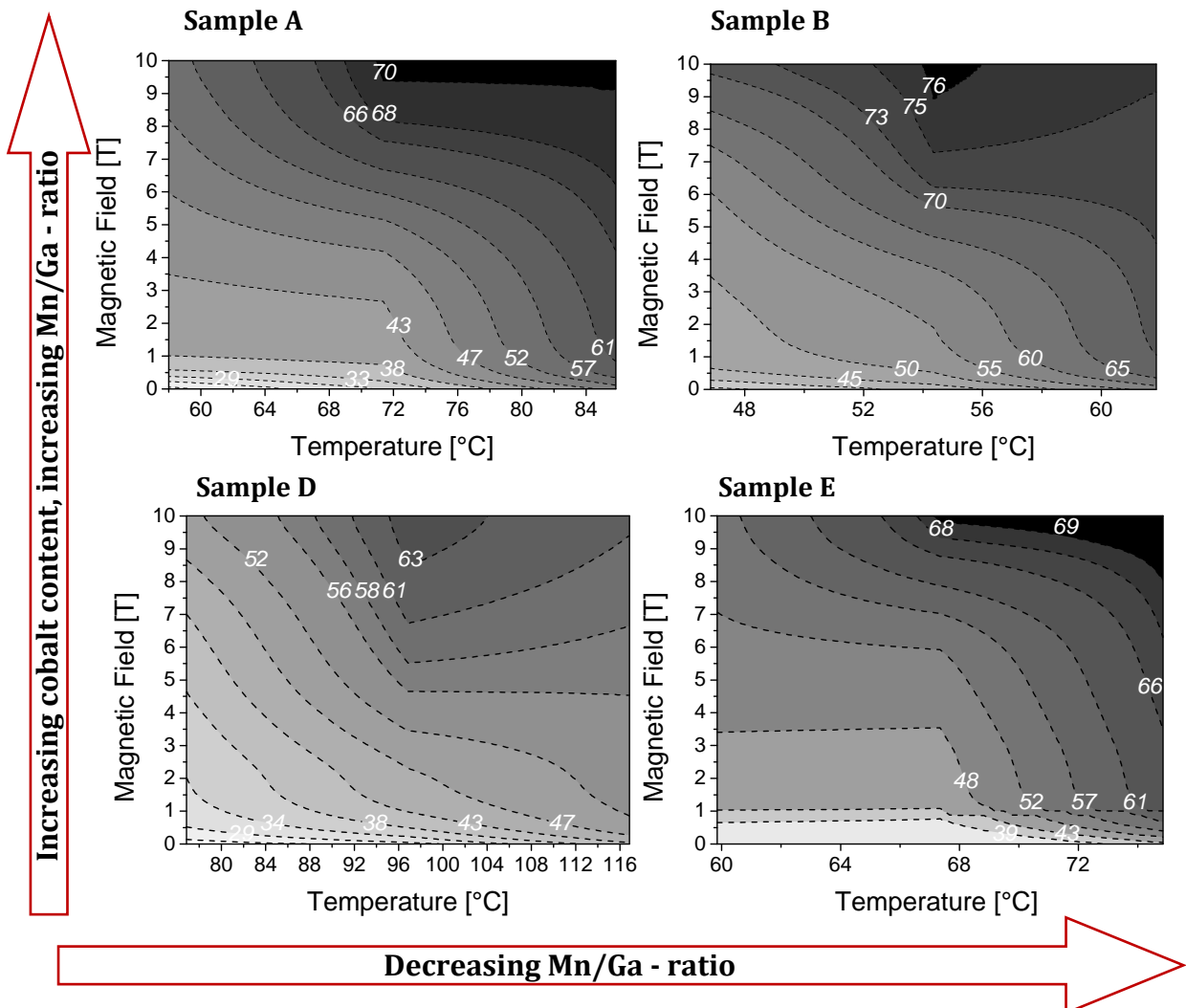


Figure 5.5.6: Contour diagrams of the magnetization  $M$  versus magnetic field  $H$  measurements for increasing temperature in  $2^\circ\text{C}$  steps of samples A, B, D, E. The dotted lines divide areas of magnetization whereas the limits are labeled in the diagrams.

Due to the influence of the magnetic field, which shifts the martensite transformation towards lower temperatures, the highest magnetization appears at 10T several degrees before the transformation would have taken place in lower magnetic fields (see Figure 5.5.6). While the magnetization in samples B and D increases continuously over the temperature steps, an abrupt change towards higher values was measured in samples A and E, whereby sample E, with the lowest Mn/Ga - ratio (1.20) and amount of cobalt (5.17 at-%) shows the more significant change within the temperature interval of the structural phase transformation (66°C to 70°C).

In contrast to the four samples shown above, sample C with a high Mn/Ga - ratio of 1.54 and a cobalt content comparable to samples D and E shows a decrease of the maximum magnetization with increasing temperature steps before the structural phase transformation (see Figure 5.5.7), before it shows the vice versa behaviour after the transformation at 130°C. Furthermore, the magnetization is much lower than in samples A, B, D and E. At the structural phase transformation, which is very close to the magnetic phase transformation, the sample showed a magnetization below 24emu/g, which is approximately one third of the samples discussed above.

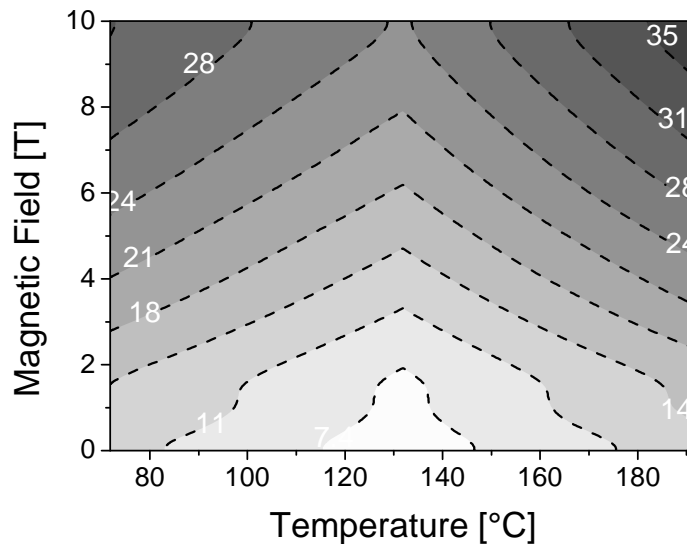


Figure 5.5.7: Contour diagram of sample C build from the data of the magnetization measured with increasing magnetic field  $H$  for several temperature steps around the structural phase transformation temperature. The dotted lines are labelled with the magnetization values reached at these points within the sample.

### 5.5.3 MAGNETOCALORIC EFFECT

As described in subsection 2.4, the magnetic entropy change  $\Delta S$  of a sample and therefore the magnetocaloric properties of a sample can be calculated by the data taken from the magnetization measurements in changing magnetic fields for various temperature steps. For the

calculation of the entropy change over the structural phase transformation, the magnetization data measured with increasing magnetic field were taken from the samples A to E. Using eq. 11

$$\Delta S_m(T, \Delta H) = - \int_{H_1}^{H_2} \left( \frac{\partial M(T, H)}{\partial T} \right)_H dH \quad [11]$$

the size of the magnetocaloric effect at the martensite temperature has been calculated for the five samples.

The analysis of the data showed, that the magnetocaloric effect is strongly influenced by the cobalt content and the Mn/Ga - ratio of the samples. However, independent of the composition, the four samples A, B, D and E show a positive magnetic entropy change in a magnetic field by passing the particular structural phase transformation temperatures (see Figure 5.5.8).

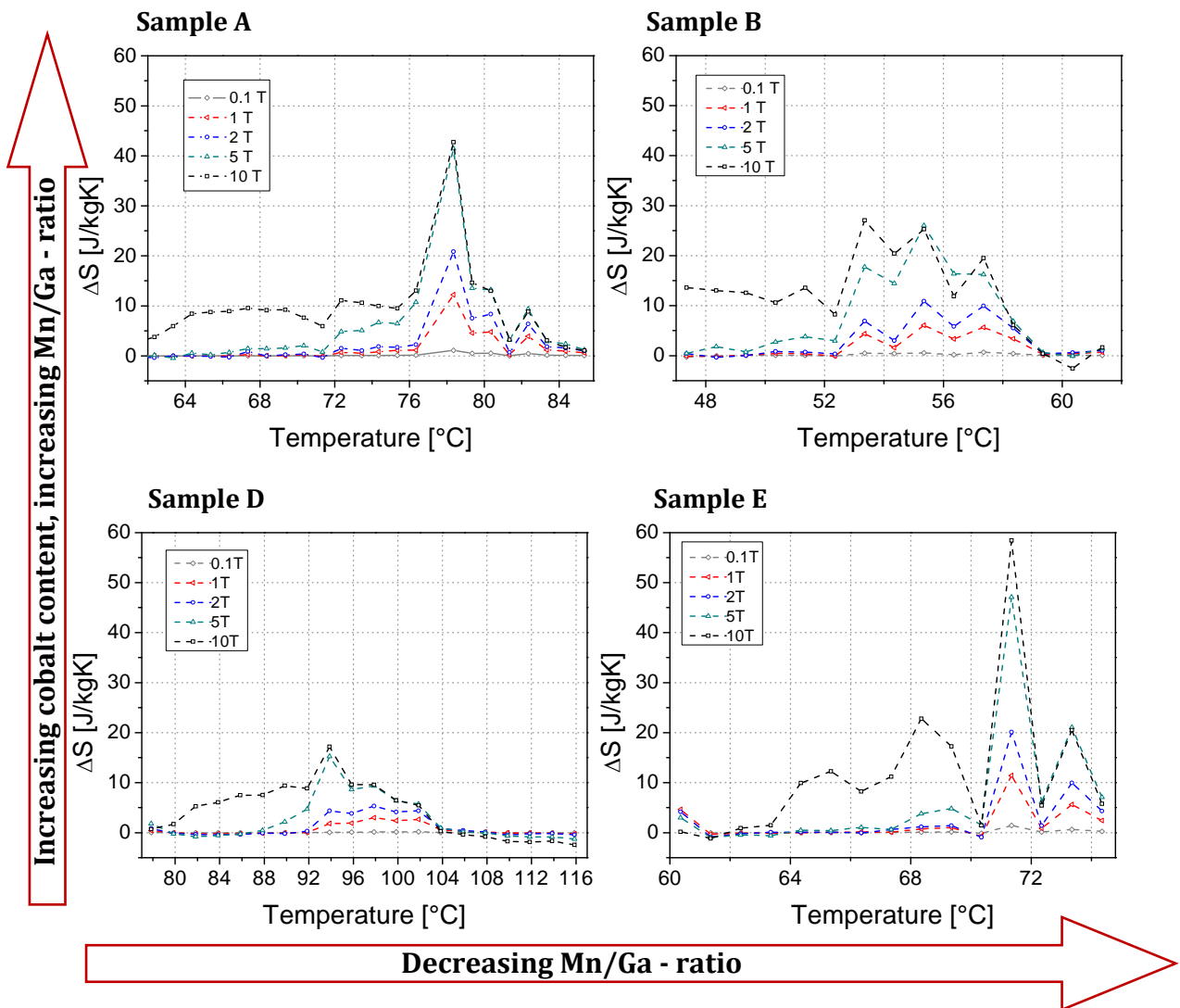


Figure 5.5.8: The magnetic Entropy change  $\Delta S_M$  with increasing temperature passing the particular structural phase transformation temperature of samples A and B, cut out from single crystalline rod no.1 and of samples D and E cut out from rod no.2 which has a lower cobalt amount. All samples show similar magnetization and samples B and D the same Mn/Ga - ratio, while sample A has a much higher Mn/Ga - ratio of 1.48 than sample E with 1.20. The dotted lines are a guide to the eye.

While the change of the magnetic entropy differs significantly in a field of 1T compared to an applied magnetic of 5T,  $\Delta S_M$  reaches the maximum in these four samples almost at the magnetic field of 5T and does not show a relevant increase when applying a magnetic field of 10T (e.g. Sample B shows a maximum  $\Delta S_M$  of 6 J/kgK, which is increasing to approximately 26 J/kgK in an applied magnetic field of 5T and remains more or less constant when increasing the field up to 10T (27 J/kg/K)).

Comparing the maximum values of the samples A and B, with approximately 6 at-% of cobalt, an increase of the magnetic entropy change from 27 J/kgK to 42.7 J/kgK (both in a magnetic field of 10T) was observed with increasing Mn/Ga – ratio from 1.38 (Sample B) to 1.48 (Sample A). Sample D, which shows the same Mn/Ga – ratio as sample A but a smaller content of cobalt, shows a smaller  $\Delta S_M$  of 17.2 J/kgK. For sample E, with a similar cobalt content as sample D and the smallest Mn/Ga – ratio of the four samples, the biggest change of the magnetic entropy was calculated, which lies with a maximum of 58.4 J/kgK three times higher than in sample D.

By extracting the magnetocaloric properties from the magnetization data measured from sample C a much smaller effect was observed. This sample, which shows already a much lower magnetization than the four samples A, B, D and E and a magnetic phase transformation in the structural phase transformation has its maximum positive entropy change above the phase transformation point and reaches only a value of about 3.7 J/kgK in an applied magnetic field of 10T (see Figure 5.5.9).

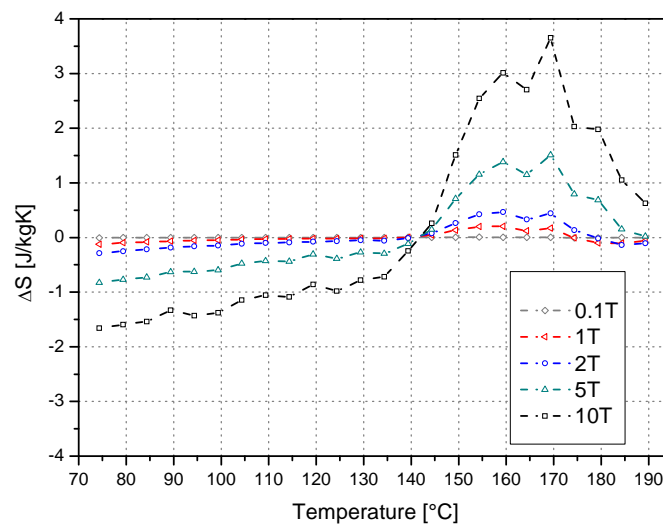


Figure 5.5.9: Change of the magnetic entropy  $\Delta S_M$  of sample C with increasing temperature passing the structural and magnetic phase transformation in different magnetic fields.



# CHAPTER 6 – DISCUSSION

---

## 6.1 INFLUENCE OF COBALT ON PHASE TRANSFORMATION TEMPERATURES

It is well known, that the structural and magnetic transformation temperatures of Ni-Mn-Ga are influenced by the composition. To determine the influence, the transformation temperatures are compared with respect to the Mn/Ga - ratio and the e/a ratio, respectively of the specimens. Due to the alloying with a fourth element, cobalt, the changing amount of cobalt has to be taken into account besides the two other values.

### 6.1.1 STRUCTURAL PHASE TRANSFORMATION TEMPERATURES

By comparing the structural phase transformation temperatures of the samples characterized in the previous chapter, an influence of the fourth element becomes obvious and will be discussed in this subsection.

The linear fitting of the martensite transformation temperatures of samples with approximately 6 at-% and 5.4 at-%, respectively and increasing Mn/Ga - ratio shows the expected increase due to higher amount of manganese in the samples (see Figure 6.1.1). Thereby the difference in the phase transformation temperature is not significant between samples with 6 at-% of cobalt and 5.4 at-% of cobalt and comparable Mn/Ga - ratio (1.27 – 1.55) as it can be seen by the linear fits of the two data sets in Figure 6.1.1 a

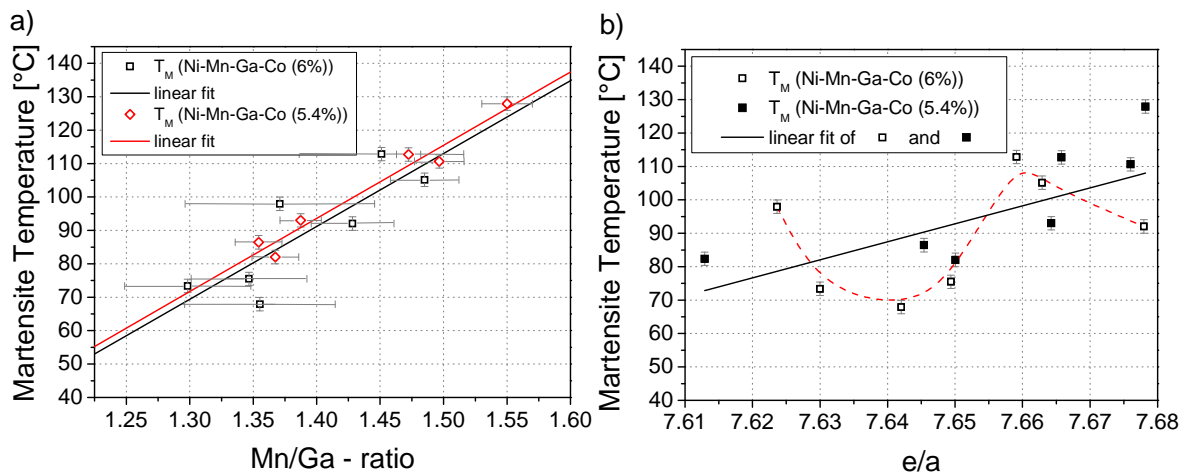


Figure 6.1.1: a) The martensite transformation temperatures of rod no.1 (black data points and black linear fit) and 2 (red data points and red linear fit) with increasing Mn/Ga - ratio and their linear fits (black line for the data of rod no. 1, red line for the data points of rod no.2). b) Martensite temperature of the samples cut out of rod no.1 (open squares) and 2 (full squares) plotted against their e/a ratio. The black line is the linear fit of all data points in the diagram. The red dotted line is a guide to the eye of the data taken from the sample rod no.1 with the weighted composition  $\text{Ni}_{44.0}\text{Mn}_{30.0}\text{Ga}_{20.0}\text{Co}_{6.0}$ .

Due to the fact, that the structural phase transformation temperatures of rod no.1 and 2 are very similar to each other, when comparing them by the Mn/Ga - ratio of the samples, the influence of the e/a ratio on the martensite temperature was determined for the samples of both rods simultaneously (see Figure 6.6.1 b). It can be seen, that the transformation temperature shows

the tendency to increase with the increase of the e/a ratio. However the linear fit shows a high deviation from the data points. That can be explained by the uncertainty in the measurements of the composition by EDX. Even though the EDX was calibrated, a standard – deviation for every single measured element arises from the measurements. The absolute error for the Mn/Ga - ratio and e/a are calculated with following eqs. [55] and [56] using Gaussian error propagation [97] (equation [54])

$$\Delta y = \sqrt{\left(\left|\frac{\partial y}{\partial x_1}\right| * \Delta x_1\right)^2 + \left(\left|\frac{\partial y}{\partial x_2}\right| * \Delta x_2\right)^2 + \dots}$$

[61]

$$\Delta\left(\frac{Mn}{Ga}\right) = \sqrt{\left(\frac{\sigma_{Mn}}{c_{Mn}}\right)^2 + \left(\frac{\sigma_{Ga}}{c_{Ga}}\right)^2}$$

[62]

$$\Delta\left(\frac{e}{a}\right) = \sqrt{(0.1 * \sigma_{Ni})^2 + (0.07 * \sigma_{Mn})^2 + (0.03 * \sigma_{Ga})^2 + (0.09 * \sigma_{Co})^2}$$

[63]

Thereby  $\sigma$  is the standard deviation of the particular element content and  $c$  the averaged content, which leads to following values for rod no.1 (see Table 6.6.1)

By taking exemplarily the samples from single crystal rod no. 1, it can be seen, that the absolute errors of e/a become very big, the more elements are involved. The uncertainty of the e/a ratio lies around 1%, which cannot be included in the graphs, since the error bars would be bigger than the scale used.

Ni [at-%]	$\sigma$ (Ni) [at-%]	Mn [at-%]	$\sigma$ (Mn) [at-%]	Ga [at-%]	$\sigma$ (Ga) [at-%]	Co [at-%]	$\sigma$ (Co) [at-%]	Mn/Ga	$\Delta$ (Mn /Ga)	e/a	$\Delta$ (e/a)
45.28	0.637	27.53	0.728	21.20	0.586	5.99	0.402	1.30	0.050	7.63	0.091
45.18	1.006	27.80	0.647	20.64	0.505	6.38	0.303	1.35	0.046	7.66	0.115
44.90	0.559	28.12	0.421	20.75	0.854	6.23	0.198	1.36	0.059	7.64	0.071
44.47	0.700	28.56	0.358	20.83	0.938	6.14	0.329	1.37	0.075	7.62	0.102
44.93	0.398	28.57	0.874	20.00	0.382	6.50	0.293	1.43	0.033	7.68	0.055
44.58	0.829	29.13	0.426	20.08	0.847	6.21	0.324	1.45	0.065	7.66	0.096
44.62	0.231	29.52	0.356	19.88	0.271	5.98	0.099	1.49	0.027	7.66	0.036

Table 6.1.1: The composition of the samples cut out of crystal rod no.1 with the standard deviation  $\sigma$  of nickel, manganese, gallium and cobalt and the resulting absolute errors for the Mn/Ga – ratio and e/a – ratio.

Even though the standard deviation of the EDX – measurements leads to an uncertainty of 1% in the calculated e/a ratios of the samples, the error can be seen as a systematic error, since the compositions were measured with the same device under same conditions, such as voltage, vacuum, distance between sample and detector. Additionally the samples of one rod were determined one after the other, which guaranteed the use of one cathode for the measurements.

Hence the eventual shift of the martensite temperature dependent on the  $e/a$  ratio can be discussed at least for the samples within every single rod itself.

The samples of the single crystalline rod no.1 ( $\text{Ni}_{44.0}\text{Mn}_{30.0}\text{Ga}_{20.0}\text{Co}_{6.0}$ ) show the increase of the martensite temperature up to a  $e/a$  ratio of approximately 7.66 before the structural phase transformation point starts to decrease again (see red dotted line in Figure 6.1.1 B), while the samples of rod no.2 with a little lower amount of cobalt shows a increase of martensite temperature up to the highest  $e/a$  ratio calculated for this rod of 7.68.

The increase of the structural phase transformation temperature with increasing  $e/a$  ratio puts forward an argument for a stabilization of the non modulated tetragonal phase [98]. In the single crystalline rod no.1, two martensite temperatures were determined, whereby the samples with the higher Mn/Ga – and  $e/a$  ratio (7.66) show a non modulated orthorhombic structure in the martensite phase. This structural change can explain the subsequent decrease from  $e/a = 7.66$  onwards, where the cubic austenite phase becomes more stable than the low temperature martensite phase. This agrees also with the behaviour of the samples cut out from crystal rod no.2 with 5.4 at-% cobalt. Compared to the sample of the first rod, all specimens show a non modulated tetragonal martensite structure which becomes more stable with increasing  $e/a$  ratio.

Comparing the martensite temperatures of rod no.1 and 3, where the cobalt content differs about 1.2 at-%, the difference becomes more significant. As it can be seen in Figure 6.1.2, the martensite temperature of the samples with the lower cobalt content of approximately 4.8 at-% is generally higher in the comparable Mn/Ga – ratio range than of the samples cut out from single crystal rod no.3.

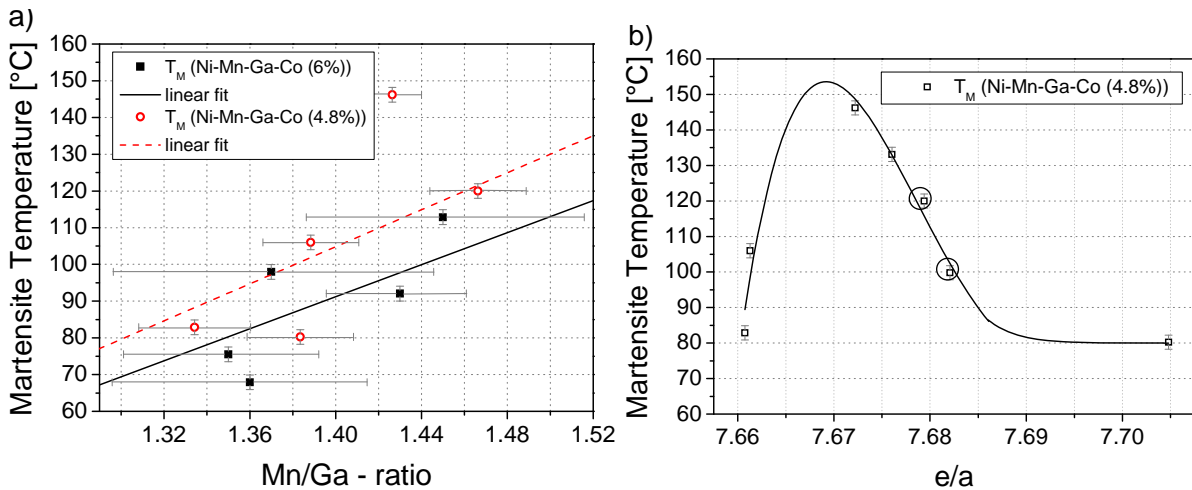


Figure 6.1.2: a) The martensite transformation temperatures of rod no.1 (full black data points and linear fit) and 3 (open red data points and (dashed line) linear fit) with increasing Mn/Ga - ratio and their fits. b) Martensite temperatures of the samples cut out of rod no.3 with non modulated tetragonal martensite and non modulated orthorhombic martensite structure (indicated by circles around the datapoints).

This shows, that the cobalt reduces the structural phase transformation temperature, the higher the amount of this element in the samples is, which strengthens the argument for the cobalt atoms sitting in the manganese sublattice of the unit cell. Otherwise no influence on the structural phase transformation can be determined. The distribution of cobalt atoms in the manganese places was confirmed by the single crystal diffraction measurements of sample 3\_2

on the four circle diffractometer D9 (see subsection 5.4) where it could be shown, that approximately 80% of the alloyed cobalt sits at the manganese positions in the cubic austenite structure and therefore also in the martensite structure.

Although all samples plotted in Figure 6.1.2 show a non modulated tetragonal martensite (except the circled datapoints, showing a non modulated orthorhombic and undetermined structure, respectively), the martensite temperature decreases after a certain e/a ratio. This implies, that the stability of the martensite phase increases only up to a certain point, which seems to be also dependent on the amount of cobalt in the samples, before the opposite behaviour starts. The amount of cobalt in the third rod is approximately 1.2 at-% lower than in the first single crystalline rod and 0.6at-% compared to the second. Furthermore the samples show a broader e/a ratio range than the samples cut out from the second rod. These two aspects can explain, why the negative slope in single crystalline rod no.2 was not determined, since the highest e/a ratio measured is 7.68, while the significant decrease of the martensite temperature in crystal rod no.3 already starts at approximately e/a=1.67 and can be traced up to an e/a ratio of 7.70.

Comparing the martensite temperature of samples with a relatively high amount of cobalt (in Figure 6.1.3 samples from single crystalline rod no.2 with 5.4 at-% Co were plotted) and samples with the lowest cobalt amount of 1.2 at-% and 0.8 at-%, respectively, it can be seen, that their structural phase transformation shift to lower temperatures and is approximately 8°C lower for samples with 1.2at-% than for samples with 5.4 at-% in the high Mn/Ga range above 1.45 and becomes similar (~2°C) for samples with a Mn/Ga - ratio below 1.15. The linear fit from the samples of the fifth single crystalline rod with the lowest cobalt content indicates, that even with higher Mn/Ga - ratio (above 1.45) the structural phase transformation temperature would lie below the fourth rod samples' and approximately 20°C below the samples from rod no.2 with 5.4 at-%.

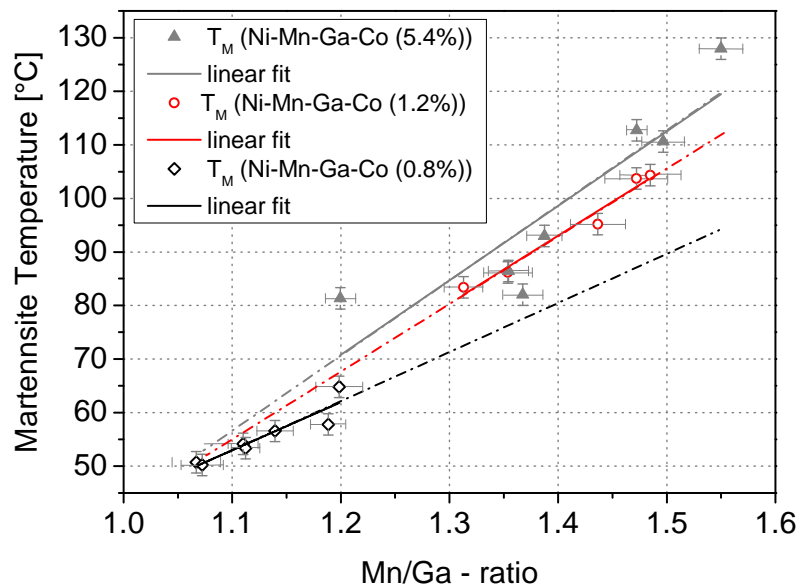


Figure 6.1.3: The martensite transformation temperatures of rod no.2 (grey data points and black linear fit) compared to samples taken from the single crystalline rods 4 and 5 with low cobalt amount of 1.2 at-% (red data points and red linear fit) and 0.8 at-% (black data points and black linear fit) with increasing Mn/Ga - ratio. Due to the huge difference in the Mn/Ga - ratio of rod no.5 to rod no. 2 and 4, the linear fits were extended to make a comparison easier. This is indicated by the dotted lines.

The comparison of the martensite temperatures of samples with significant different cobalt content and equal Mn/Ga - ratio shows that the addition of cobalt up to approximately 5 at-% results in a general increase of stability of the martensite phase. However the further increase of the amount of cobalt seems to lead to a new instability of the martensite phase, which can be determined by the shift of martensite temperature back to lower temperatures in the same Mn/Ga - ratio.

As with the samples of rod no.1 and 3 ( $\text{Ni}_{44.0}\text{Mn}_{30.0}\text{Ga}_{20.0}\text{Co}_{6.0}$  and  $\text{Ni}_{45.0}\text{Mn}_{31.0}\text{Ga}_{19.2}\text{Co}_{4.8}$ ) the specimens of rod no.4 and 5 ( $\text{Ni}_{48.8}\text{Mn}_{28.6}\text{Ga}_{21.4}\text{Co}_{1.2}$  and  $\text{Ni}_{49.2}\text{Mn}_{28.4}\text{Ga}_{21.6}\text{Co}_{0.8}$ ) show an initial increase of the structural phase transformation temperature with increasing e/a ratio. In rod no.4, from an e/a ratio greater than 6.66 and up to 7.685, the martensite temperature increases about 20°C from 84°C to 104°C and decreases again with higher e/a ratio (see Figure 6.1.4 A). Although the gap between the e/a ratios of the rod no.5 samples' is rather large (from 7.635 to 7.685), the same relation between the martensite temperature and e/a ratio can be verified (depicted in Figure 6.1.4 B).

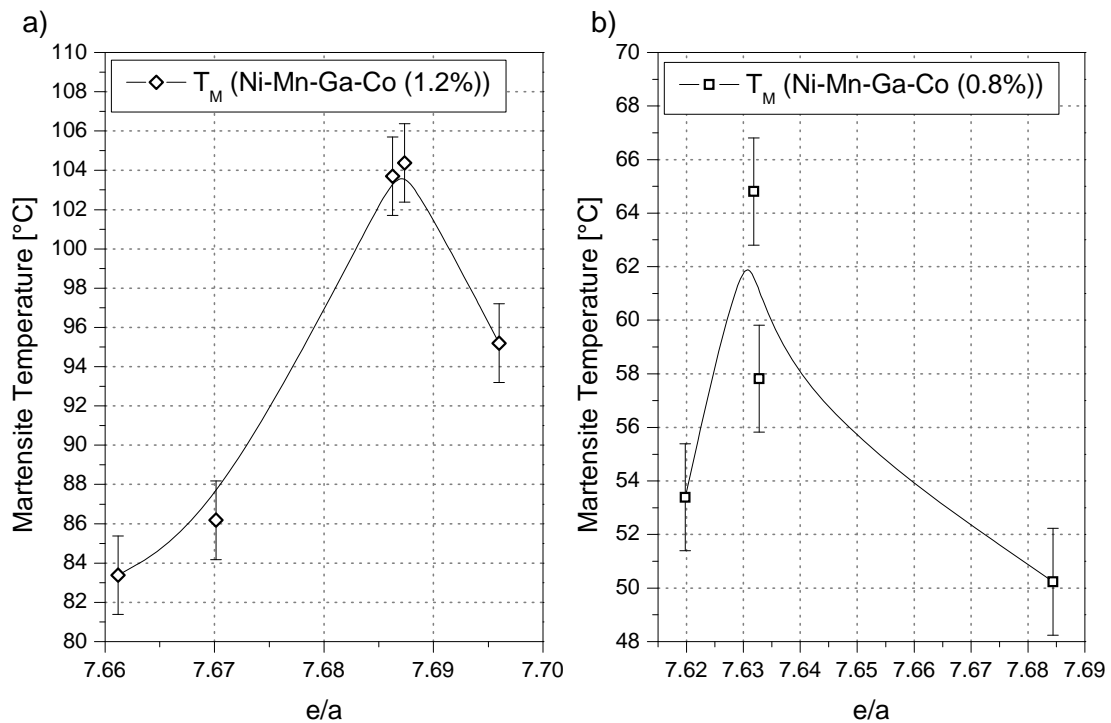


Figure 6.1.4: Structural phase transformation temperatures of samples cut out of single crystalline rod 4 and 5 with the weighted compositions  $\text{Ni}_{48.8}\text{Mn}_{28.6}\text{Ga}_{21.4}\text{Co}_{1.2}$  and  $\text{Ni}_{49.2}\text{Mn}_{28.4}\text{Ga}_{21.6}\text{Co}_{0.8}$  plotted against their e/a ratios, showing the initial increase and subsequent decrease of the temperature with increasing e/a ratio.

Independent from the amount of alloyed to Ni-Mn-Ga, it was shown, that an increasing e/a ratio results in an initial stabilization of the martensite phase and a subsequent destabilization when overcoming a particular e/a ratio. Furthermore it was shown, that the destabilization is independent from the martensite structure, since the decrease in martensite temperature was observed for non modulated orthorhombic (rod no.1), non modulated tetragonal (rod no.3 and 4), as well as for modulated tetragonal phases. Due to the uncertainties discussed before, it cannot be determined, if the inflexion point of the martensite temperature lies at the same point

for all cobalt amounts and therefore it is not possible to define the absolute value for the inflexion point.

Finally the comparison of Ni-Mn-Ga and Co-alloyed Ni-Mn-Ga shows once more the significant influence of the fourth element. As it can be seen in Figure 6.1.5, the structural phase transformation temperature of unalloyed Ni-Mn-Ga (green area) is far below the martensite temperatures measured for Co-alloyed Ni-Mn-Ga (red area). In the Mn/Ga - ratio range from 1.3 to 1.65 they differ by about 20°C minimum, which shows, that the low temperature phase of Ni-Mn-Ga-Co seems to be more stable than that of Ni-Mn-Ga. Taking into account, that the instability of the Ni-Mn-Ga martensite is due to the modulated structure of the samples taken for this plot, it also shows a lower structural phase transformation temperature [100] compared to the Ni-Mn-Ga-Co samples showing the same martensite structure (see Figure 6.1.5 B). Already the addition of 0.8 at-% of cobalt results in the stabilization of the modulated structure above 60°C at a low Mn/Ga - ratio of 1.2.

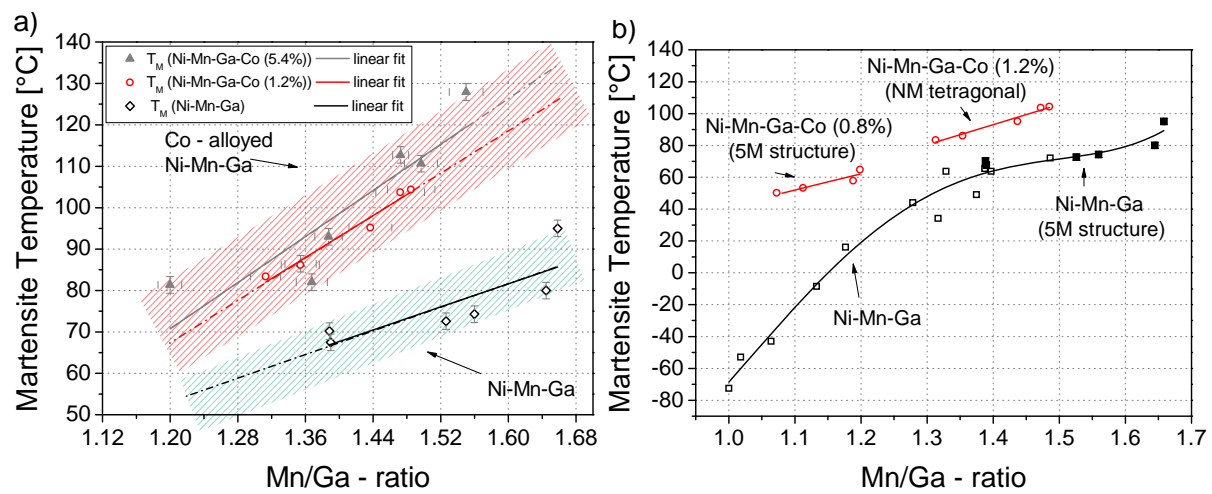


Figure 6.1.5: a) Comparison of the martensite temperature of high and low cobalt alloyed Ni-Mn-Ga (rod no.2:  $\text{Ni}_{44.6}\text{Mn}_{30.7}\text{Ga}_{19.3}\text{Co}_{5.4}$  and rod no.4:  $\text{Ni}_{48.8}\text{Mn}_{28.6}\text{Ga}_{21.4}\text{Co}_{1.2}$ ) and pure Ni-Mn-Ga [54] in the Mn/Ga - ratio range from 1.20 to 1.65. The red shaded area depicts the area of structural phase transformation temperatures found for Ni-Mn-Ga-Co, the green area the Ni-Mn-Ga samples' to clarify the difference. b) Comparison of martensite temperature of Ni-Mn-Ga-Co with non modulated and modulated martensite structure (red open circles) and Ni-Mn-Ga - samples close to the stoichiometric system [99] as well as Ni-Mn-Ga with modulated martensite structure (full black squares) [54].

## 6.1.2 MAGNETIC PHASE TRANSFORMATION TEMPERATURES

The addition of cobalt to the Ni-Mn-Ga has also a tremendous influence on the magnetic phase transformation from the ferro- to the paramagnetic state. According to the distribution of cobalt atoms in the Ni-Mn-Ga lattice, approximately 20% are placed on the nickel site, responsible for the stabilization of the ferromagnetic phase. It could be verified, that the increase of the amount of cobalt in the samples leads to a significant increase of the Curie temperature. As it is depicted in Figure 6.1.6, the highest Curie temperatures were determined in samples with 6 at-% cobalt and increases noticeably by reducing the amount only about 0.6 at-% (samples with 5.4 at-%

cobalt) from approximately 160°C to 155°C. For samples with 1.2 at-% less cobalt the magnetic phase transformation decreases even down to 145°C. Furthermore it was determined that the amount of manganese has also an effect on the Curie temperature. The increase of the manganese counteracts with the cobalt and results in a destabilization of the ferromagnetic phase and therefore a lower Curie temperature.

By determining the behaviour of the magnetic phase transformation temperature of Co-alloyed Ni-Mn-Ga dependent on the e/a ratios of the samples, the same tendency was observed. With the increase of the cobalt amount, the Curie temperature increases significantly, as it is depicted exemplarily in Figure 6.1.6 B for rod no.1, 2 and 3 with 6 at-%, 5.4 at-% and 4.8 at-%, respectively. With constant amount of cobalt but increasing e/a ratio, the Curie temperature decreases slightly over a broad range from 7.61 to 7.70.

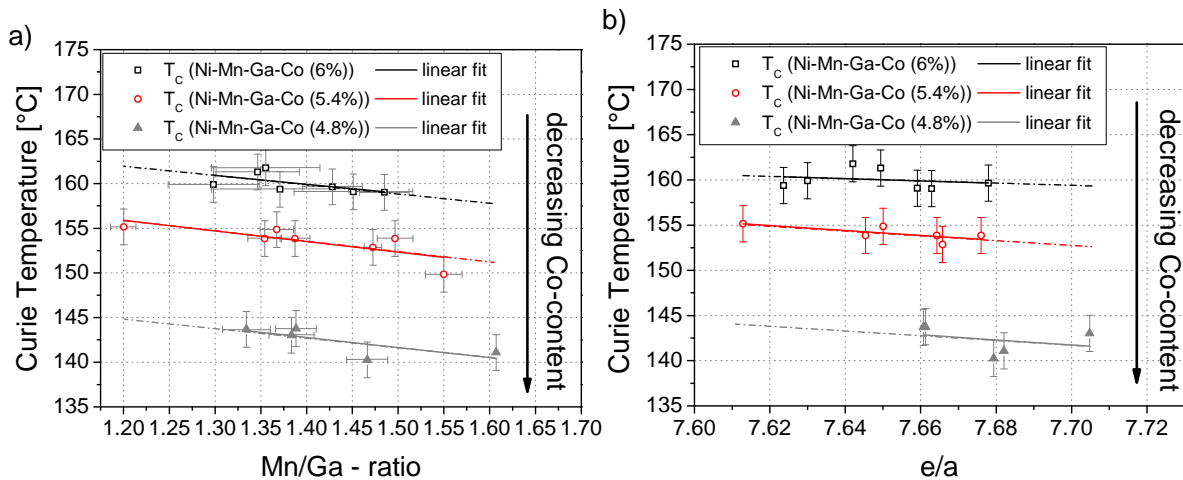


Figure 6.1.6: Curie temperature plotted against the Mn/Ga - ratio (a) and e/a ratio (b) of samples cut out of the single crystalline rods no.1 ( $\text{Ni}_{44.0}\text{Mn}_{30.0}\text{Ga}_{20.0}\text{Co}_{6.0}$ ),  $\square$ , rod no.2 ( $\text{Ni}_{44.6}\text{Mn}_{30.7}\text{Ga}_{19.3}\text{Co}_{5.4}$ ),  $\circ$ , and rod no.3 ( $\text{Ni}_{45.0}\text{Mn}_{31.0}\text{Ga}_{19.2}\text{Co}_{4.8}$ ),  $\blacktriangle$ . The lines with corresponding colours are the linear fits of the Curie temperatures to simplify the comparison of the data over the whole Mn/Ga - and e/a - ratio range.

As expected, the further reduction led to a significant decrease of the Curie temperatures, as it can be seen in Figure 6.1.7. The samples cut out of the rods no. 4 and 5 (1.2 at-% Co and 0.8 at-% Co) have very similar Curie temperatures independent from the Mn/Ga - ratio of about 100°C. Furthermore it was observed, that the amount cobalt in these samples hardly influences the magnetic phase transformation temperature when compared to Ni-Mn-Ga, which shows similar transformations.

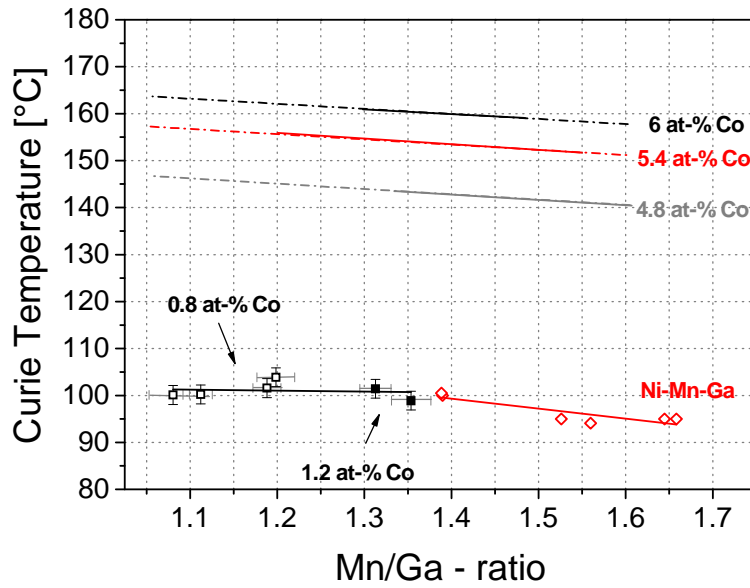


Figure 6.1.7: Curie temperatures of the samples cut out of the single crystalline rods no.4 and 5 with the low cobalt amounts 1.2 at-% ■ and 0.8 at-% □, respectively. Versus their Mn/Ga - ratio. For comparison, the Curie temperatures of Ni-Mn-Ga [54] ◇, and the linear fits of the samples with higher amount of cobalt (4.8 to 6 at-%) are inserted in the graph.

## 6.2 STRUCTURAL PARAMETERS OF NI-MN-GA-CO OF DIFFERENT COMPOSITIONS

Many publications about structural properties of Ni-Mn-Ga with different compositions showed, that the amount of manganese has a significant influence not only on the phase transformation temperatures but also on the martensite structure of this system [100-102]. As it became obvious in the previous subsection 6.1, the addition of cobalt to Ni-Mn-Ga affects the structural as well as the magnetic phase transformation temperature. In order to determine the potential influence of cobalt and manganese in the Ni-Mn-Ga-Co system several single crystalline samples were analysed in their martensite phases (see subsection 5.3.1), whose results will be discussed in the following subsection.

### 6.2.1 INFLUENCE OF COBALT AND MANGANESE

As it was shown in subsection 5.3.1 three different structures were determined in the martensite phase of Ni-Mn-Ga-Co. Two of them, the non modulated tetragonal and the modulated tetragonal structure, are well known from the Ni-Mn-Ga system [100, 101], while the third one, a non modulated orthorhombic structure, has not been determined in Ni-Mn-Ga up to now. Taking a general look on the summarized results of the single crystal diffraction measurements performed for this thesis and plotted in Figure 6.2.1, it can be seen, that all analysed samples, apart from the samples cut out of rod no.5 ( $\text{Ni}_{49.2}\text{Mn}_{28.4}\text{Ga}_{21.6}\text{Co}_{0.8}$ ) show a non modulated

martensite structure. Furthermore it can be seen that with an increasing sample number within the particular rods, and therefore with increasing Mn/Ga - ratio, the long axis of the unit cell elongates about  $0.1\text{\AA}$ , while the short axis shows the tendency to decrease about the same value in same direction.

Furthermore it can be shown, that the maximum values of the long axes and the minimum of the short axes, respectively of the rods 1 to 4 differs only by about  $0.05\text{\AA}$  to each other. This would imply that the amount of cobalt does not affect the unit cell parameters of the martensite temperature. To confirm this assumption, the lattice parameters of the samples with a non modulated tetragonal martensite structure were taken and plotted against their Mn/Ga - ratios, to verify if samples with different cobalt contents but similar Mn/Ga - ratio show a difference in the lengths determined.

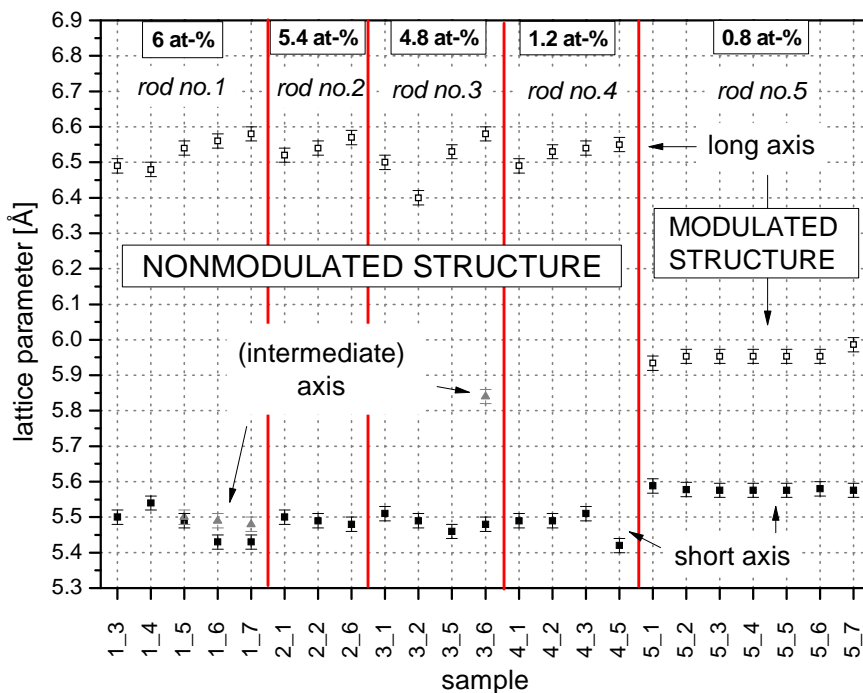


Figure 6.2.1: The unit cell parameters of the analysed samples of all five single crystalline rods with decreasing Co-content, each given in the order cut out from the bottom to the top of the respective rods. The squares on the top of the graphic contain the weighted content of cobalt in the rods.

As it is depicted in Figure 6.2.2, all cell parameters fit approximately to a linear increase of the long axis and decrease of the short axis, with the increase of the manganese content and independent from the amount of cobalt in the samples. This shows that cobalt has no measurable influence on the non modulated martensite structure, while the influence of a changing Mn/Ga - ratio becomes clear. However, the unit cell volume varies only between  $192\text{\AA}^3$  to  $200\text{\AA}^3$ , whereby no tendency could be determined.

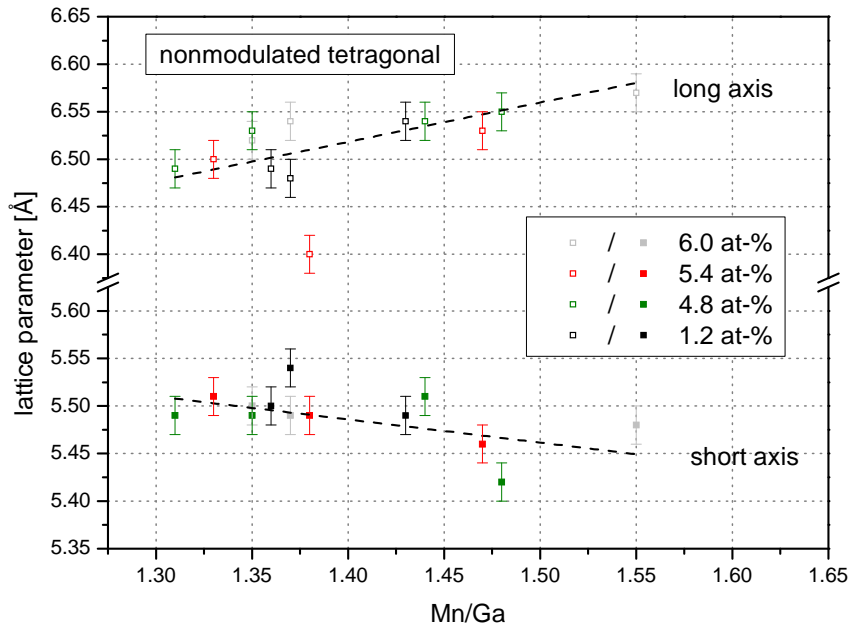


Figure 6.2.2: Unit cell parameters of the non modulated tetragonal martensites of Ni-Mn-Ga-Co samples plotted against their Mn/Ga - ratios.

Nevertheless another potential influence of cobalt was observed in samples of single crystalline rod no.1 with the weighted composition  $\text{Ni}_{44.0}\text{Mn}_{30.0}\text{Ga}_{20.0}\text{Co}_{6.0}$  and rod no.3, whereas Ni-Mn-Ga was alloyed with 4.8 at-% cobalt (see Figure 6.2.1). In both rods samples with a high Mn/Ga - ratio showed a non modulated orthorhombic martensite structure, which does not exist in Ni-Mn-Ga. Thereby for the samples 1\_5, 1\_6 and 1\_7, the difference between the short and intermediate axis is with approximately 1% rather small, while the difference in sample 3\_6 is more than 6%. All three samples of rod no.1, with the Mn/Ga - ratios 1.43, 1.45 and 1.49, respectively show an intermartensite phase transformation to the non modulated tetragonal structure before transforming to the cubic austenite state. In contrast sample 3\_6 with a lower Co content but an even higher Mn/Ga - ratio of 1.53 stays in the orthorhombic structure in the martensite phase and is therefore more stable than the orthorhombic structure found in the samples of rod no.1.

However the most significant influence of cobalt is the suppression of a modulated martensite structure, when going to a higher Mn/Ga - ratio. It became evident here, that in a Mn/Ga - ratio range between 1.2 and 1.7 the addition of 6 at-% of cobalt leads to a non modulated martensite, which does not change with decreasing the cobalt content down to 1.2%. Only at a lower Mn/Ga - ratio between 1.05 and 1.20 a modulated tetragonal structure was found, which shows similar lattice parameters and therefore cell volumes such as Ni-Mn-Ga having the same martensite structure [88].

## 6.2.2 INFLUENCE OF BALLMILLING

It was shown in subsection 5.3.2, that the ballmilling of a single crystalline samples, which was carried out for samples with 2 different cobalt contents and varying Mn/Ga - ratio, changes the

martensite structure to a stress induced disordered fcc structure. The lattice parameters of this structure, determined for the 6 samples, which were grinded are equal to the ones found for Ni-Mn-Ga powder produced in the same way. With a deviation of  $0.1\text{\AA}$  all samples showed the same lattice constants of  $3.67\text{\AA}$  and therefore no influence of the stoichiometry on this structure.

It was also shown, that the subsequent annealing of the powders results in a stress release and the retransformation to the initial martensite structure, which can be seen exemplarily by comparing the structural parameters of the bulk sample 3\_6 ( $\text{Ni}_{45.54}\text{Mn}_{29.89}\text{Ga}_{19.61}\text{Co}_{4.96}$ ) and the annealed powder sample 3\_7 ( $\text{Ni}_{44.91}\text{Mn}_{30.82}\text{Ga}_{19.18}\text{Co}_{5.09}$ ). As discussed in the previous subsection sample 3\_6 with a high Mn/Ga - ratio of 1.53 shows a non modulated orthorhombic martensite structure (see Figure 6.2.3) with  $a=6.62\text{\AA}$ ,  $b=5.84\text{\AA}$  and  $c=5.48\text{\AA}$ . For the neighbouring sample 3\_7 a higher Mn/Ga - ratio of 1.61 was determined and therefore the same martensite structure can be assumed. As expected, the analysis of the powder diffraction pattern showed, that the annealing of the powder sample leads to the retransformation, whereas the sample the sample has a non modulated orthorhombic structure with the cell parameters  $a=6.22\text{\AA}$ ,  $b=5.87\text{\AA}$  and  $c=5.49\text{\AA}$ .

The same retransformation was found in samples with initially non modulated tetragonal structure (sample 2\_4 and 2\_7), which show similar cell parameters as that found in the bulk material, which confirms the result.

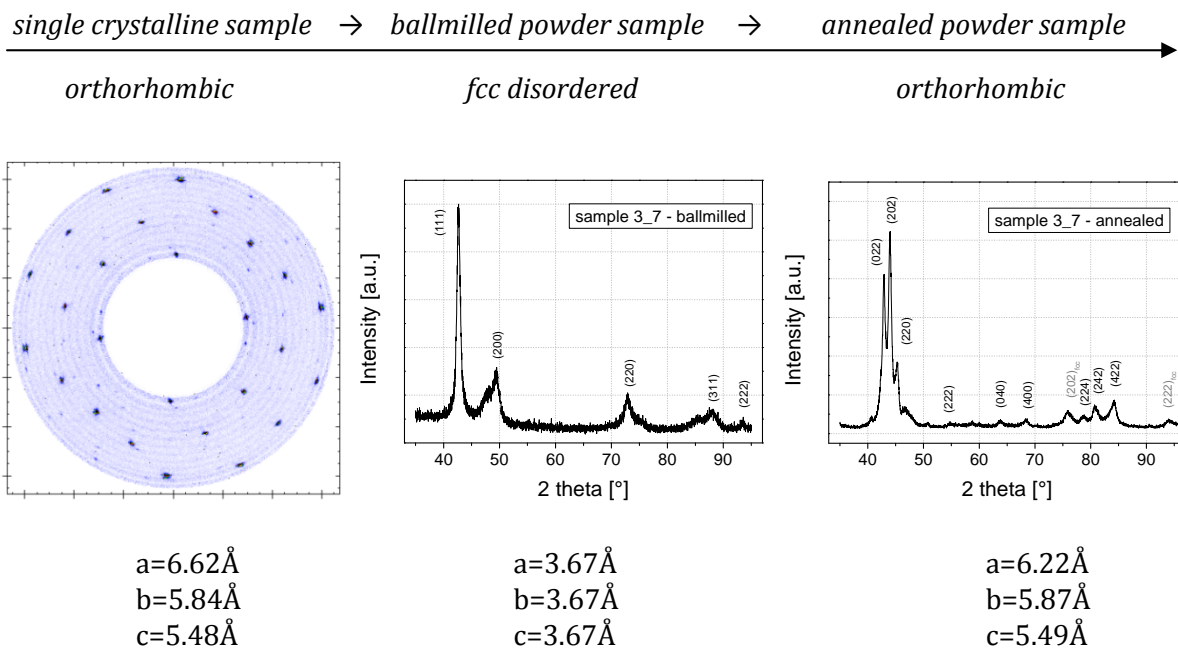


Figure 6.2.3: Comparison of the different structures determined in bulk material (h0l - plane on the left side), ballmilled powder sample (diffraction pattern in the middle) and the subsequent annealed powder sample (diffraction pattern on the right side of the graphic)

## 6.3 STRESS AND STRAIN BEHAVIOUR

From the results in subsection 5.4 it can be seen, that the stress-strain behaviour of the Ni-Mn-Ga-Co samples is quite different, not only in the stress needed for reaching the maximum possible strain but also in the designation of plateaus. In order to sort all the results presented, the first following subsection will give an overview over all samples measured and focus on general aspects of the results, before going into details.

### 6.3.1 GENERAL ASPECTS

For ferromagnetic shape memory alloys the key value is the twinning stress  $\sigma_{TW}$  of the specimen. Only with a small  $\sigma_{TW}$ , below approximately 2MPa [103], the crystal can be deformed by a magnetic field. It is well known from Ni-Mn-Ga that only specimens with modulated (either 10 or 7M) martensite structures have a twinning stress low enough to show the magnetic shape memory effect [104].

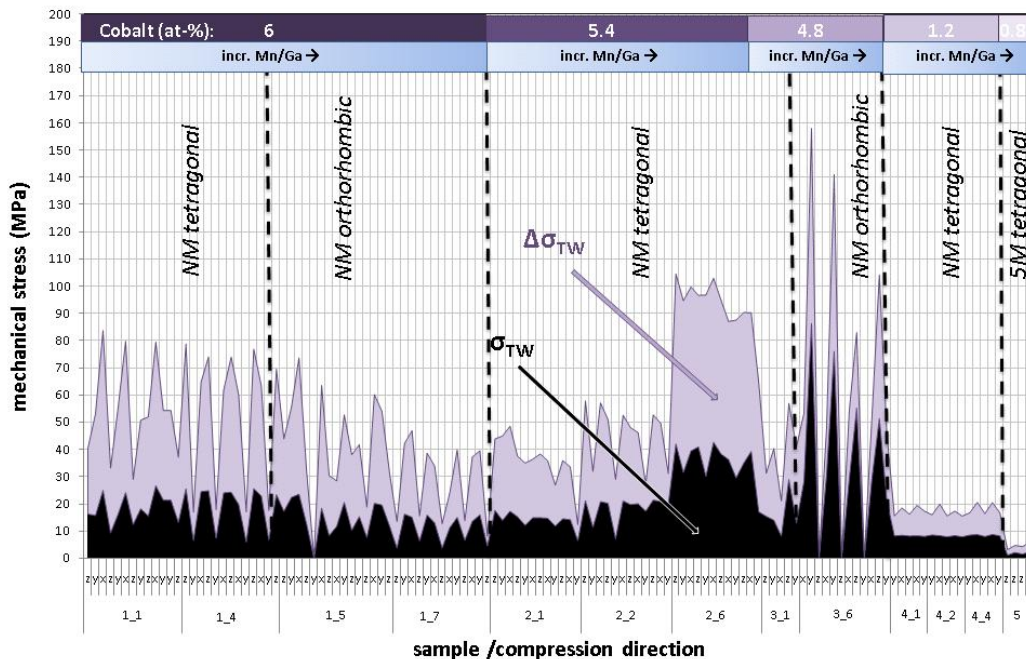


Figure 6.3.1: Overview of the twinning stresses  $\sigma_{TW}$  (black graph) of all measured Ni-Mn-Ga-Co samples with given martensite structure, amount of cobalt and in the order of increasing Mn/Ga - ratio. Furthermore the difference between the twinning stress needed to reach 0.2% of strain and 95% of the maximum strain  $\Delta\sigma_{TW}$  is given (violet graph). The dotted lines indicate the change of the martensite structure, which is labelled as well.

As it can be seen in Figure 6.3.1, Co – alloyed Ni-Mn-Ga shows the same behaviour. All samples with a non modulated structure show a  $\sigma_{TW}$  above 10MPa and only the samples of rod no.5 with 0.8 at-% cobalt have a twinning stress low enough for the deformation by magnetic field.

In the field of non modulated martensite structures, the diagram shows that samples with a 1.2 at-% of cobalt (rod no.4) show the lowest twinning stress, which does not change significantly with increasing Mn/Ga - ratio. The highest twinning stress above 50 MPa was measured in sample 3\_6, with 4.8 at-% cobalt, a high Mn/Ga - ratio of 1.53 and the non modulated orthorhombic martensite structure. In contrast the samples of rod no.1, which also have a non modulated orthorhombic structure, however with a much smaller difference between the a and b axis (see subsection 6.2.1), show a lower twinning stress of about 15 to 20 MPa, which is slightly lower than the twinning stresses determined for the non modulated tetragonal samples in this rod (sample 1\_1 and 1\_2), lying in the range of 18 to 25 MPa. The highest twinning stress in a non modulated tetragonal sample was found in rod no.2, where the stress needed to reach the maximum strain overcomes 30 MPa. Beside this exception, the twinning stress in non modulated tetragonal martensites seems to decrease with decreasing amount of cobalt in the samples. As a consequence, the difference between the stress needed to reach 0.2% strain and 95% of the maximum strain  $\Delta\sigma_{TW}$  shows the same tendencies as observed for  $\sigma_{TW}$ . The difference  $\Delta\sigma_{TW}$  determined for the Ni-Mn-Ga-Co specimen is at least double as high and up to three times higher as the twinning stress, which is the averaged value of  $\sigma_{TW}$ . That implies that small strains can be reached by applying a much lower stress than necessary for 95% of the maximum strain. This can be explained by the stress – strain curves depicted in subsection 5.4 and Appendix C for Ni-Mn-Ga-Co with different compositions, where it was shown, that by inducing the strain mechanically the stress plateau, which is usually very distinctive up to a certain strain is replaced by a rising stress needed to reach the high strain, before reaching the point of plastic deformation.

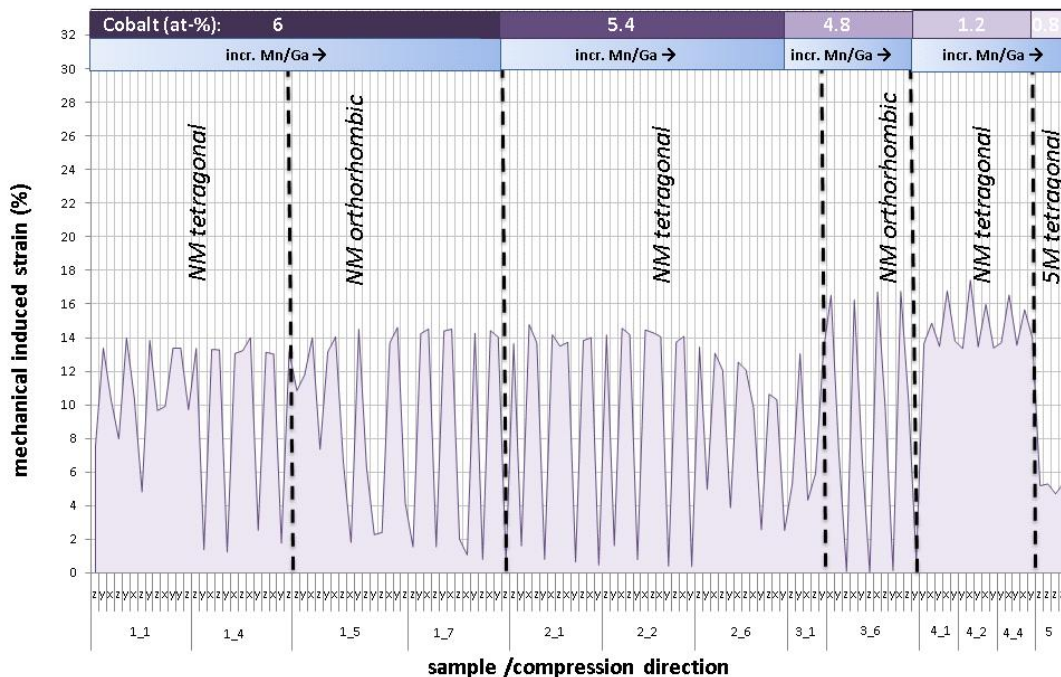


Figure 6.3.2: The maximum mechanically stress induced strain of all determined Ni-Mn-Ga-Co samples with decreasing Co – content from the left to the right of the diagram and increasing Mn/Ga - ratio within the rods. The dotted lines, which not necessarily fit to different amounts of cobalt, show the changing of martensite structure (also labelled in the diagram).

The maximum mechanical induced strain determined in the single crystalline samples increases slightly from about 14% to more than 16% in non modulated tetragonal specimen with

decreasing cobalt content, but seems to be not affected by changing the Mn/Ga - ratio (see Figure 6.3.2). An exception is again sample 2\_6 with 5.4 at-% cobalt, with a strain of less than 14% even decreasing by repeating the measurements. This can be explained by the stress needed to reach the strain. As already mentioned in the previous paragraph, which is significantly higher than for the other non modulated tetragonal samples. This could be caused by defects for example, which leads to a much higher blocking stress and prohibits a higher strain. Like the non modulated tetragonal samples of rod no.4 with 1.2 at-% cobalt, the non modulated orthorhombic sample 3\_6 with 4.8 at-% cobalt shows a strain of more 16% , while the samples 1\_5 and 1\_7 show only a slightly higher strain of about 14.5% than the non modulated tetragonal samples of the same rod with 6 at-% cobalt. The strain measured in the samples with the lowest Co - content of 0.8 at-% and the modulated tetragonal structure corresponds with approximately 5.5% to the expected value, measured for Ni-Mn-Ga single crystals with comparable lattice parameters and is close to the theoretical maximum strain based on the determined  $c/a$  ratio.

As it can be seen in Figure 6.3.3 and discussed in the previous subsection 6.2, the maximum theoretical strain  $\epsilon_0$  calculated from the measured lattice parameters of the samples increases within the rods with increasing Mn/Ga - ratio. The theoretical strain was calculated by the ratio of short over long axis. For the samples of rod no. 1 and 2 with 6 at-% and 5.4 at-% cobalt the measured maximum strain  $\epsilon_{\max}$  is up to 2% smaller than  $\epsilon_0$  and lies about 4% below  $\epsilon_0$  for sample 2\_6, the sample with the high twinning stress. The highest strain observed here was determined in the non modulated samples of rod no.4 with a cobalt content of 1.2 at-%, showing similar values to the maximum theoretical strain  $\epsilon_0$ . Also the non modulated orthorhombic sample 3\_6 shows a theoretical and the measured maximum strain equal to each other.

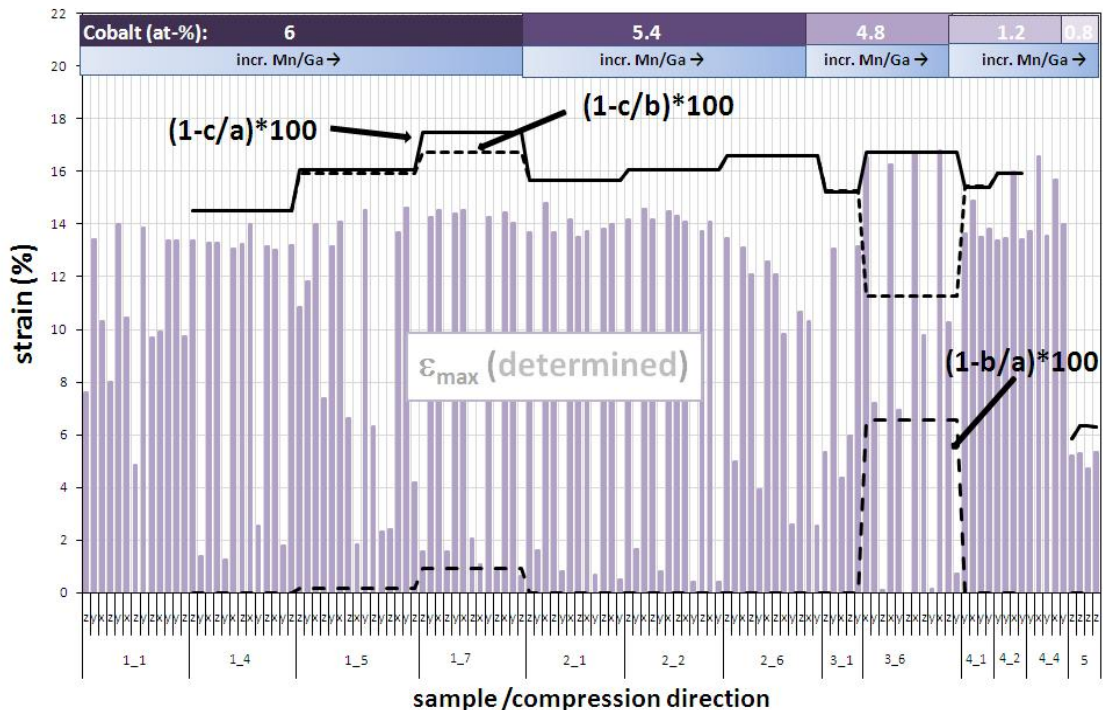


Figure 6.3.3 The maximum determined strain  $\epsilon_{\max}$  (violet bars) for all samples and different compression directions compared to the maximum theoretical strains  $\epsilon_0$  for all three directions (indicated by the black lines) calculated from the lattice parameter determined by neutron diffraction.

Taking a closer look on the diagram 6.3.1 and 6.3.3, it can be seen, that the determined twinning stress and the induced strain change significantly with the changing compression direction. To explain this behaviour, the measurements have to be analysed not only with regards to the structure and lattice parameters but also to the change of the samples in all three dimensions for the particular compression directions and the sequence of the deformation experiments.

---

## 6.3.2 TWINNING MECHANISM IN NON MODULATED TETRAGONAL SAMPLES

---

As discussed in the previous subsection, the theoretical maximum strain  $\varepsilon_0$  is in most of the samples showing a non modulated tetragonal martensite structure higher than the determined maximum strain  $\varepsilon_{\max}$ . However the samples taken from rod no. 4, with the weighted composition  $\text{Ni}_{48.8}\text{Mn}_{28.6}\text{Ga}_{21.4}\text{Co}_{1.2}$  show a  $\varepsilon_{\max}$  which is very similar to  $\varepsilon_0$ . Thus it can be considered, that the single variant state is reached in the compression experiments and the samples can be taken as a model for the twinning mechanism in the samples with that structure.

---

### 6.3.2.1 MACROSCOPIC SHAPE CHANGE IN TWO DIRECTIONS

---

In subsection 5.4.4 it was shown, that the samples of rod no.4 show a change in all three dimensions when applying a uniaxial pressure on the multivariant specimen. The initial fraction of martensite variants to each direction of the sample should be about 1/3, since the cooling from the austenite to the martensite phase causes a twinning, whereas the variants distribute equally. During the first compression the variants with the long axis  $c$  along the direction of the uniaxial pressure (here the  $z$  – direction) disappear and transform to the two other variants with the short  $a$  and  $b$  axis aligned to the compression direction and a two variant martensite state is reached. The second compression towards a direction perpendicular to the first (here the  $y$  – direction) results in an elongation towards the third direction ( $x$  – direction) only, since only variants with the  $c$  – axis in the deformation direction are affected [107]. The strain reached due to the second compression is approximately half of the maximum strain  $\varepsilon_{\max}$ , which is ideally equal to  $\varepsilon_0$  if no defects and blocking twins inhibit the formation of the two-variant and in consequence of the single variant state. The subsequent compression of the now (nearly) single variant specimen creates the maximum strain, which is possible to induce with the given stress, and the elongation towards the previous compression direction (here the  $y$  – direction). Again, the initial compression direction is not affected by the uniaxial pressure. However the twinning stress, which has to be overcome to switch from one single variant state to the other is with at least 8MPa (measured in sample 4\_1 and 4\_4) in a non modulated tetragonal martensite still too high for a magnetic field induced strain response.

As the samples of rod no.4 sample 1\_4 ( $\text{Ni}_{44.47}\text{Mn}_{28.56}\text{Ga}_{20.83}\text{Co}_{6.14}$ ) shows the shape change in only two dimensions after the initial transformation from a multivariant to a nearly single variant

state. With this sample it can be shown, that even the change of the sequence of compression directions will not change the trained twinning mechanism. It is not possible to “reinduce” the third variant by a mechanical stress. The same behaviour was found in sample 2\_1 and 2\_2.

However samples with the same martensite structure (1\_1, 2\_6 and 3\_1) showed the change of all three dimensions even after repeated compressions.

---

### 6.3.2.2 MACROSCOPIC SHAPE CHANGE IN THREE DIRECTIONS

---

The samples 1\_1, 2\_6 and 3\_1, which show a shape change in all three directions due to a uniaxial compression, seem to have “blocking twins”, impeding a complete single variant state. Figure 6.3.3 shows that the theoretical strain  $\epsilon_0$  determined for sample 2\_6 and 3\_1 is about 4% higher than the maximum strain reached in the deformation experiments. It can be seen in all samples, that the strain induced in one direction matches with the sum of the caused elongation in the other two directions, whereas one direction is shows a bigger elongation than the second (see exemplarily Figure 5.4.2 for sample 1\_1) Therefore the repeated compression of up to 120 and 50MPa, respectively, induces a strain in all three directions, due to the presence of more than one variant. For a single variant state a much higher mechanical stress would have been necessary, not reachable with the test device.

---

## 6.3.3 TWINNING MECHANISM IN NON MODULATED ORTHORHOMBIC SAMPLES

---

As for the tetragonal samples, the twinning mechanism for the orthorhombic samples will be discussed for the specimen showing a good agreement between the theoretical and the experimentally reached strain first. In contrast to the samples with a tetragonal non modulated structure, the orthorhombic sample shows a change of all three dimensions by uniaxial compression. In case of this structure, the results of sample 3\_6, also with the highest difference in the short axes, will be discussed in the next section.

---

### 6.3.3.1 MACROSCOPIC SHAPE CHANGE IN THREE DIRECTIONS

---

Comparing the results of the deformation experiments of the orthorhombic sample 3\_6 with the neutron diffraction results reveals interesting correlations between macroscopic shape change and unit cell orientations as well as the twinning mechanisms that are responsible for the macroscopic change. Figure 5.4.15 depicts the switch of the sample between two shape states, I and II. In state I, the sample is extended along the  $x$  direction and compressed along the  $y$  and  $z$

directions. In state II, the sample is compressed along the  $x$  direction and extended along the  $y$  and  $z$  directions (see section 5.4.3).

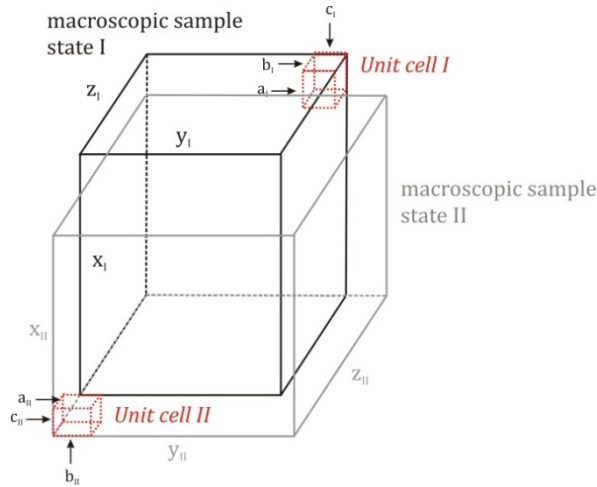


Figure 6.3.4: The macroscopic shape states I and II and the corresponding unit cells of the sample.

As in all deformation experiments the sequence of loading directions was changed during the compression tests. It was shown that the order of deformation sequences does not affect the result. Independent on loading history, the sample assumed shape state I when compressed along the  $y$  or  $z$  direction, while a compression along the  $x$  direction, resulted in state II. Furthermore, by comparing the theoretical strains (determined by the quotient of the shorter and longer axes) with the maximum strains reached due to the compression  $\epsilon_i$  ( $i = x, y, z$ ) measured in the  $x, y,$  and  $z$  directions, it turns out that these values match almost perfectly (see Table 6.3.1).

	Expanded State [mm]	Compressed State [mm]	Compr./Exp.	Strain $\epsilon_i$ [%]	Unit Cell Parameter		Parameter Ratios	
					[Å]	[Å]	[-]	[-]
x	1.60	1.33	0.83	17	a	c	c/a	1-c/a
					6.62	5.48	0.83	<b>0.17</b>
y	1.53	1.41	0.93	7	b	c	c/b	1-c/b
					5.84	5.48	0.938	<b>0.062</b>
z	1.65	1.49	0.90	10	a	b	b/a	1-b/a
					6.62	5.84	0.882	<b>0.118</b>

Table 6.3.1 Comparison of the experimentally determined strains  $\epsilon_i$  ( $i = x, y, z$ ) and theoretical strains  $1 - c/a, 1 - b/a,$  and  $1 - c/b$  for sample 3\_6

These results imply two preferred microscopic orientation states, more precisely two orientations of the unit cell. Each microscopic orientation state corresponds to a macroscopic shape state. For the microscopic orientation state I, the crystallographic directions are parallel to the coordinate axes:  $a // x, b // z,$  and  $c // y$ . For orientation state II, the orientation relationship is  $a // z, b // y,$  and  $c // x$ . The crystallographic directions  $a, b, c$  permute cyclically during one uniaxial deformation experiment. Figure 6.3.4 shows a schematic of the macroscopic sample shape and the corresponding orientation of the unit cell for both states. A cyclic permutation of the crystallographic axes cannot be accommodated by a single twinning event since for  $ac$  twinning, the crystallographic  $a$  and  $c$  directions interchange while the  $b$  direction remains

constant. Equally for ab and bc twinning, the c and a directions remain constant, respectively. Cyclic permutation of the crystallographic axes may be achieved when two twinning modes occur successively. Consider, for example, ab twinning followed by bc twinning as shown in Figure 6.3.5. During the first twinning event (ab twinning in this case), a is mapped onto b and vice versa b onto a from state I (index I) to the intermediate state (index i). During the second twinning event (bc twinning), b is mapped onto c and c onto b from the intermediate state to state II (index II). Thus, the combined twinning sequence results in a permutation of the crystallographic axes, i.e. a is mapped onto b, c onto a, and b onto c, which corresponds to the transformation from state I to state II.

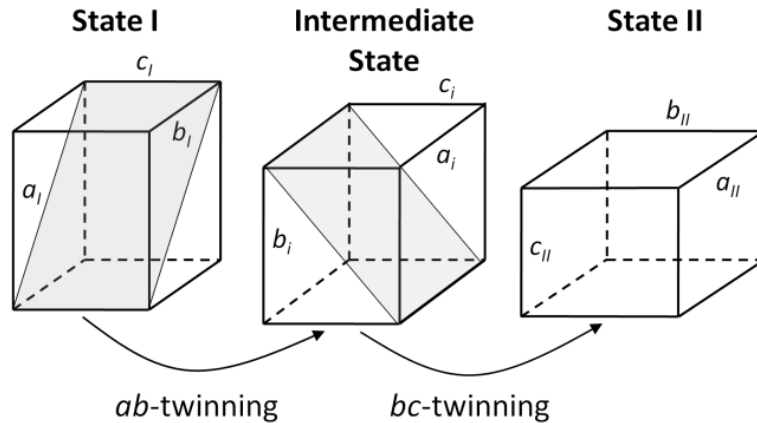


Figure 6.3.5 Example of one double twinning mode: ab twinning followed by bc twinning, whereas the grey planes indicate twin planes of the particular twinning event. For ab twinning, the a and b axes are interchanged while the c axis stays constant. For the subsequent bc twinning event, the b and c axes interchange while the a axes stays constant. As a result of double twinning, the crystallographic axes permute cyclically.

The sense of the permutation is reversed when reversing the twinning sequence, i.e. when the first event is bc twinning and the second event is ab twinning. The sense of the permutation is also reversed when ab twinning is followed by ac twinning (compared to ab twinning followed by bc twinning). Thus, the six possible twinning sequences yield two permutations as listed in the following Table 6.3.2.

first twinning mode	second twinning mode	Permutation of crystallographic axes
<i>ac</i>	<i>bc</i>	$a \rightarrow c, c \rightarrow b, b \rightarrow a$
<i>bc</i>	<i>ab</i>	
<i>ab</i>	<i>ac</i>	
<i>ac</i>	<i>ab</i>	$a \rightarrow b, b \rightarrow c, c \rightarrow a$
<i>ab</i>	<i>bc</i>	
<i>bc</i>	<i>ac</i>	

Table 6.3.2 Twinning sequences and corresponding permutation of crystallographic axes of the non modulated orthorhombic sample 3\_6

The crystallographic theory of such combined twinning was given by A. G. Crocker [108] who termed this mechanism ‘double twinning’. Crocker applied his theory to twinning phenomena in

hexagonal metals. The regularity of the stress-strain curves indicates that the two twinning events occur simultaneously, which results in a cyclic permutation of all three crystallographic axes by one uniaxial compression.

It is currently not clear what causes double twinning in orthorhombic Ni-Mn-Ga-Co. This is different from previous results obtained with deformation experiments with a  $\text{Ni}_{50}\text{Mn}_{29.4}\text{Ga}_{20.6}$  (single crystal with 7M structure) [109]. In that case, two different twinning modes are active in strict sequence, i.e. ab twinning produced the first 3.3% strain followed by bc twinning which leads to a total strain of 6.6%. It might be possible that chemical and/or structural order of the Ni-Mn-Ga-Co crystal couples the two twinning events. If order is (partially) destroyed during twinning (a mechanism which is called ‘pseudo twinning’ [110, 111]), it might be restored during the second twinning mode. The disordered intermediate state would have a higher energy. The increased energy would trigger the second twinning event. In the presence of structural order (i.e. lattice modulation as present in 5M and 7M martensite [112-114]), only special twinning systems restore the order without requiring shuffle [115].

---

### 6.3.4 TWINNING MECHANISM IN MODULATED TETRAGONAL SAMPLES

---

It was shown in subsection 5.4, only the samples with the modulated tetragonal structure show a twinning stress low enough to induce a strain by applying a magnetic field. With the same 10M structure with similar lattice parameters like that determined in Ni-Mn-Ga, in a certain Mn/Ga - ratio range [115], the twinning stress  $\sigma_{\text{TW}}$  lies below 2MPa initially. All mechanically tested samples showed approximately the strain, which is theoretically possible, calculated from the c/a ratio determined by the neutron diffraction results (see Figure 6.3.3). Like in other magnetic shape memory single crystals, the specimens elongate only in one direction when compressed uniaxially [116], consequently showing a change in two directions only. Therefore the detwinning (reaching the single variant state) follows the mechanism of the twinning mechanism explained in the theoretical section 2.3, causing the strain due to the alignment of the magnetic moments parallel to the applied magnetic field and the so induced growth of the variant with the long axis along the same direction by the simultaneous decrease of the size of the other variants existing in the sample. However, the twinning stress  $\sigma_{\text{TW}}$  and the difference  $\Delta\sigma$  increases by the increase of the Mn – content (see Figure 6.3.6 a). The difference between the stress needed to reach 0.2% strain and 95% of the maximum strain  $\Delta\sigma$  lies for three of the four samples higher than the 2MPa, which implies (and can be seen in Figure 5.4.18 for sample 5\_1, 5\_3, 5\_4 and 5\_6), that the strain increases for higher strains to a value, too high to be overcome by a magnetic field. Therefore the magnetic field induced strain  $\varepsilon$  determined in a magnetic field up to 700mT decreases in the same direction of the Mn/Ga - ratio (see Figure 6.3.6 b), as  $\sigma_{\text{TW}}$  and  $\Delta\sigma$  increase, since the single variant state cannot be reached in this magnetic field.

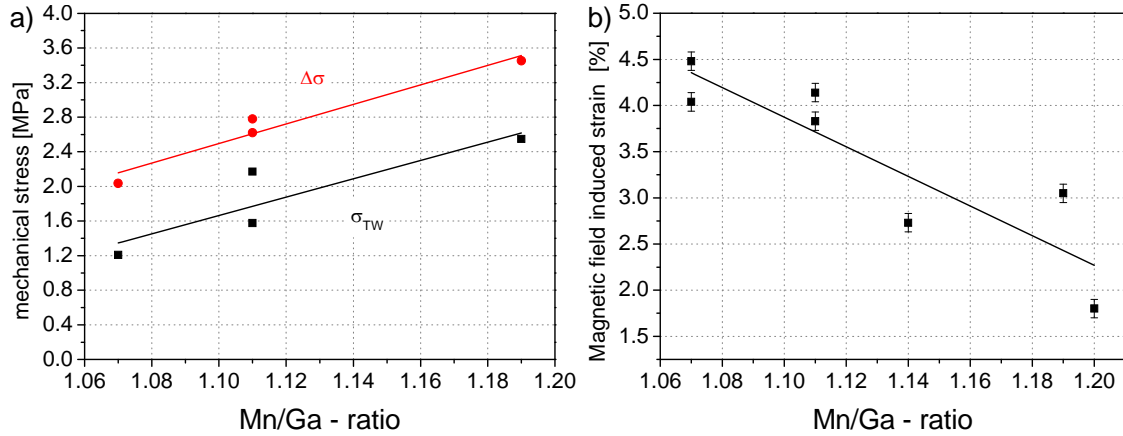


Figure 6.3.6: a) The twinning stress  $\sigma_{TW}$  (black data points) and the difference between the stress needed to reach 0.2% strain and 95% of the maximum experimentally determined strain  $\Delta\sigma$  (red data points) of sample 5\_1, 5\_3, 5\_4 and 5\_5 as a function of their particular Mn/Ga - ratio. The black and red lines in the graph show the linear fitted trend. b) The magnetic field induced strain of all samples from the single crystalline rod no.5 (sample 5\_1 to 5\_7) plotted versus their Mn/Ga - ratio and linear fitted (red line in the graph)

## 6.4 MAGNETIC PROPERTIES

From the results in subsection 5.5 it can be seen, that the structural and magnetic phase transformation temperatures  $T_M$  and  $T_C$  of Ni-Mn-Ga-Co samples are influenced by the application of a magnetic field. As seen already without a magnetic field, the samples with the higher cobalt content of 6 at-% (see filled squares in Figure 6.4.1) show a higher martensite temperature than the samples with 5.4 at-% Co and comparable Mn/Ga - ratio.

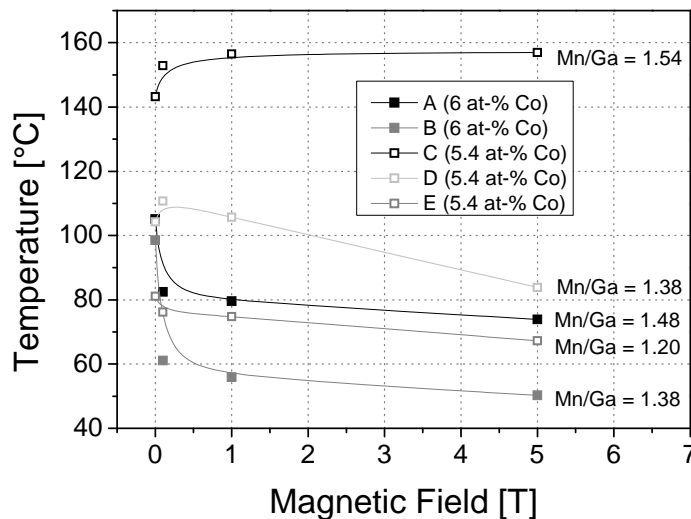


Figure 6.4.1 The martensite temperature  $T_M$  plotted versus the magnetic field. The data points labelled with filled squares stay for the samples with approximately 6 at-% cobalt (Mn/Ga - ratio is given next to the curves), data points with open squares are the data points for samples with approximately 5.4 at-%.

In contrast to Ni-Mn-Ga (see Figure 6.4.2) a significant increase of the magnetization was observed during the structural phase transformation from the ferromagnetic martensite to the ferromagnetic austenite for the samples A, B, D and E.

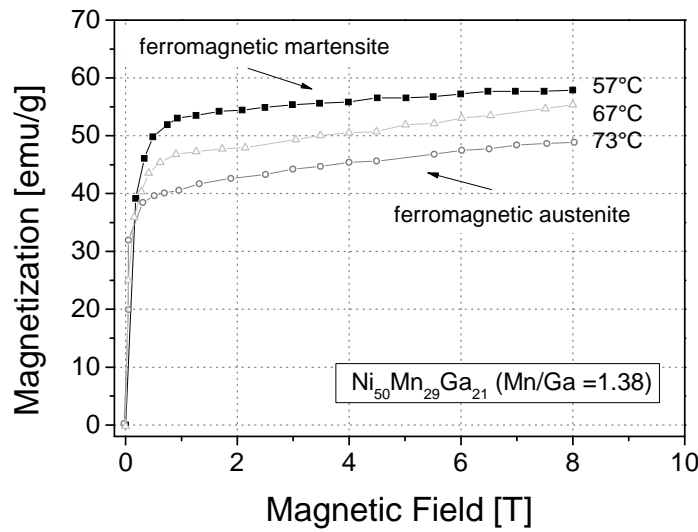


Figure 6.4.2: The isothermal magnetization curves of  $\text{Ni}_{50}\text{Mn}_{29}\text{Ga}_{21}$  ( $\text{Mn}/\text{Ga} = 1.38$ ) in an increasing magnetic field up to 8 T for three different temperatures around the martensite phase transformation [116].

By applying a magnetic field the phase with the higher magnetization is favoured and the phase with the lower magnetization destabilizes, resulting in a shift of the structural phase transformation temperature. Besides sample C all samples show a decrease of the martensite temperature with increasing magnetic field, which all have a lower magnetization in the martensite phase. In contrast sample C, with the highest Mn/Ga - ratio, shows an increase of the martensite temperature with increasing magnetic field. Since the structural and magnetic phase transformation temperature are very close to each other, the austenite phase shows a lower magnetization than the martensite phase (see Figure 5.5.4), due to that the martensite phase becomes more stable in a magnetic field. Furthermore the magnetic field stabilizes the ferromagnetic phase, which results in an increase of the Curie temperature for all samples.

The sudden increase of magnetization during the structural phase transformation even at high magnetic field in samples B and E is so high, that the entropy change determined in these samples is comparable to the entropy change in Ni-Mn-Ga samples, which show the giant magnetocaloric effect. However, Ni-Mn-Ga shows a sudden decrease in magnetization during the structural phase transformation temperature [61]. The saturation magnetization of Ni-Mn-Ga and Ni-Mn-Ga-Co (alloyed with maximum 6 at-% cobalt) is higher in Ni-Mn-Ga with a comparable Mn/Ga - ratio of 1.38 and a non modulated tetragonal structure, which shows, that cobalt reduces the magnetic moment of the sample (see Figure 6.4.3). Since the magnetization decreases slowly towards the Curie temperature the difference of the saturation magnetization would be even larger due to the Curie temperature of about 100°C in the  $\text{Ni}_{50.0}\text{Mn}_{28.9}\text{Ga}_{21.1}$  sample and 155°C in sample B. However sample B is in the austenite state at this temperature, whereby the values cannot be compared with each other anymore.

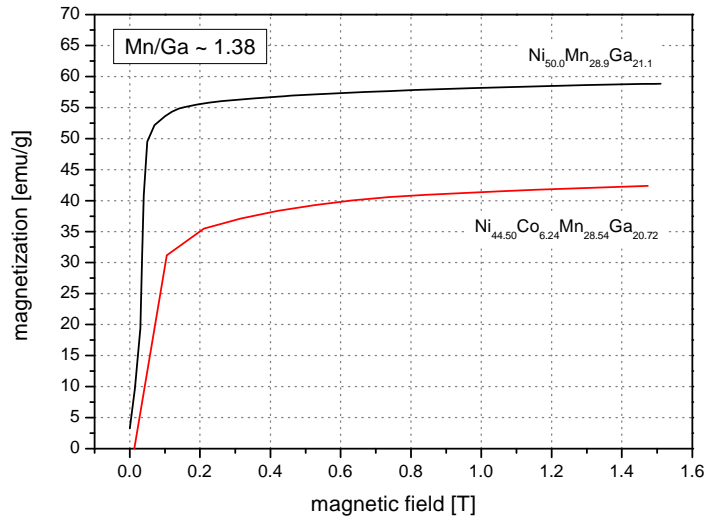


Figure 6.4.3 Saturation magnetization of Ni-Mn-Ga (black curve) and Co – alloyed Ni-Mn-Ga (red curve) with similar Mn/Ga measured at room temperature.

In Figure 6.4.4 a it can be seen, that the value of the entropy change  $\Delta S$  decreases with the Mn/Ga - ratio within the samples taken from rod no.2 containing 5.4 at-% cobalt. However, the samples of rod no.1 seem to show the opposite behaviour. This implies, that the comparison of  $\Delta S$  cannot be done only by the Mn/Ga - ratio but has to take the cobalt content into account as well. That can be verified by comparing sample B and D, which show the same Mn/Ga - ratio, but different Co – content. By applying a magnetic field, the sample with the 6 at-% of cobalt shows a much higher entropy change than the sample with the lower content of 5.4 at-% (see Figure 6.4.4 a).

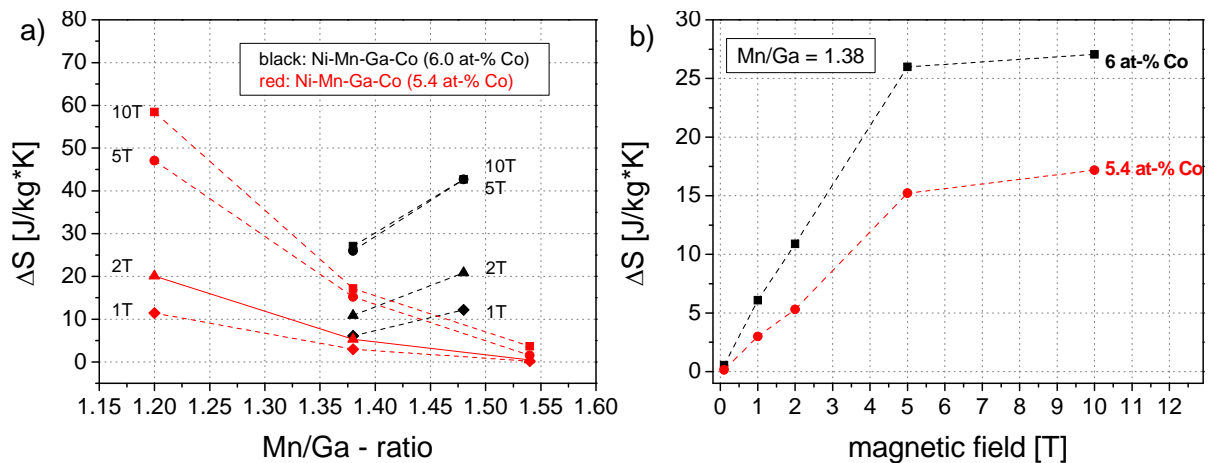


Figure 6.4.4: a) The determined entropy change  $\Delta S$  with a changing Mn/Ga - ratio for samples cut out from rod no.1 (sample A and B – black data points) and from rod no.2 (sample C, D and E – red data point). b) Comparison of the entropy change of two samples with the same Mn/Ga - ratio but different Co content with increasing magnetic field.

Due to the dependence of the martensite temperature and Curie temperature on the Mn/Ga - ratio as well as the cobalt content, the better comparison of the entropy change is done by the temperature difference between the structural and magnetic phase transformation within the samples, as depicted in Figure 6.4.5.

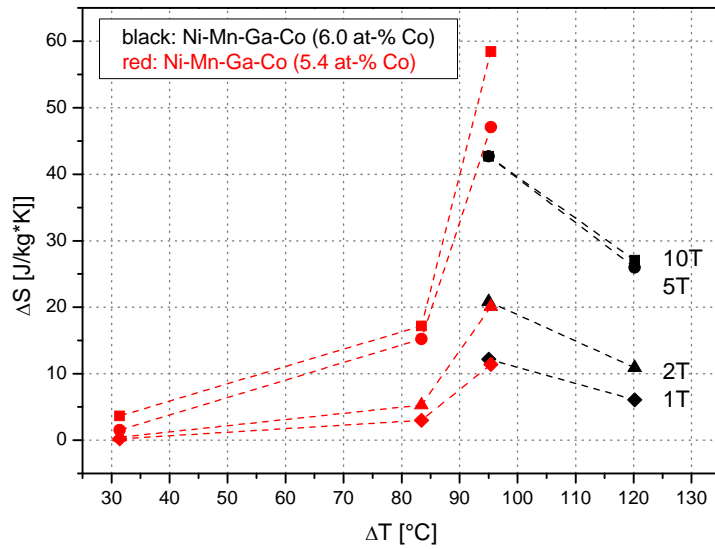


Figure 6.4.5 The entropy change  $\Delta S$  versus the temperature difference between the structural and magnetic phase transformation temperature  $T_M$  and  $T_C$  for samples of the first and second single crystalline rod with 6 (black data points) and 5.4 at-% (red data points) cobalt, respectively. The measurements were performed in different magnetic fields.

It becomes apparent, that the increasing difference between these two temperatures causes first an increase in the entropy change at the structural phase transformation. Samples with equal differences in the temperatures show a similar  $\Delta S$  at the martensite transformation. A further increase of the temperature interval results in a decrease of the entropy change again, which implies a nonlinear behaviour but a maximum for a certain composition.

# CHAPTER 7 – CONCLUSIONS AND PERSPECTIVES

---

With this work it is shown, that by using the single crystal growth technique SLARE, it is possible to grow single crystalline rods of Ni-Mn-Ga-Co with different compositions of about 120g, without the disadvantages of the Bridgman technique, such as uncontrolled loss of elements with a high vapour pressure or the unwanted inclusion of impurities (like oxides or sulphides) as well as gas pores. During the growth process a new slag has been developed to improve the quality of the single crystals and increase the probability of growing single crystals by suppressing the formation of multiple crystal seeds.

The results presented here show that the alloying of Ni-Mn-Ga with cobalt affects the thermal, magnetic and structural and therefore mechanical properties remarkably.

It was determined that by substituting nickel by cobalt, the cobalt atoms distribute itself mainly in the nickel places and partly in the manganese sublattice, which results in a significant influence of the magnetic and the structural phase transformation temperature. Both phase transformations have been shifted to higher temperatures successfully, compared to Ni-Mn-Ga within the same Mn/Ga - ratio range.

By alloying Ni-Mn-Ga with cobalt in the range of 1.2 at-% up to 6 at-%, it was shown, that the cobalt seems to impede a modulation in the martensite structure within the Mn/Ga range of 1.2 to 1.6, where non modulated phases have been determined only. Thereby a non modulated orthorhombic structure was identified, which has not yet been found in Ni-Mn-Ga. The additional decrease of the Mn/Ga - ratio below 1.2, leads to samples with a modulated tetragonal (5M) structure in the martensite phase.

Since the stress – strain behaviour of magnetic shape memory is known to be highly dependent from the structure in the martensite phase and the composition of the specimen, detailed measurements on samples with all three samples and changing composition have been performed and presented here.

Samples with a non modulated tetragonal structure, which is well known from the Ni-Mn-Ga system, have a twinning stress, which is too high to be overcome by a magnetic field. However, it was determined that the twinning stress decreases with the decreasing amount of cobalt in the samples.

The non modulated orthorhombic martensite, an unknown structure in Ni-Mn-Ga, shows also a twinning stress too high to induce the strain magnetically. An interesting point of this structure is the different twinning mechanism found by uniaxial compression. This mechanism is known as “double twinning”, which exists in a modified way, called “pseudo-double-twinning” in hexagonal cobalt and in orthorhombic modulated martensite of Ni-Mn-Ga.

As mentioned before, Ni-Mn-Ga-Co with a small amount of cobalt and a low Mn/Ga - ratio have a modulated tetragonal (5M) martensite structure. These specimen show a twinning stress comparable to Ni-Mn-Ga with the same martensite structure and therefore the magnetic shape memory effect. The temperature range within the strain of up to 6% can be induced by the magnetic field in these samples is comparable to the highest temperature range found in Ni-Mn-Ga samples.

A big advantage of the addition of cobalt is the increase of the ductility and hence the lifetime of the samples, which makes the material more attractive for the use in actuators for example. In

Figure 7.1, it can be seen, that the material, with the modulated tetragonal structure shows a training-effect, due to repeated magnetomechanical cycling in a rotating magnetic field of 0.97 T.

In  $\text{Ni}_{50.69}\text{Mn}_{25.54}\text{Ga}_{23.01}\text{Co}_{0.76}$  (sample 5\_3 in Figure 7.1), the theoretical maximum strain, calculated by ratio of the lattice parameter  $c$  and  $a$ , was reached after 4000 cycles, starting from a magnetic field induced strain of below 2.5% increasing to 6%. Also  $\text{Ni}_{51.38}\text{Mn}_{27.70}\text{Ga}_{23.15}\text{Co}_{0.67}$  (sample 5\_1 in Figure 7.1) shows an increase of the magnetic field induced by the increasing number of magnetomechanical cycles. In both samples no cracks have been developed during the test.

These results make Ni-Mn-Ga-Co with a low Mn/Ga - ratio to a very promising magnetic shape memory material.

However further long term measurements for the fatigue behaviour of the specimens have to be performed, which was not possible due to the flaking of the glued sample from the sample holder.

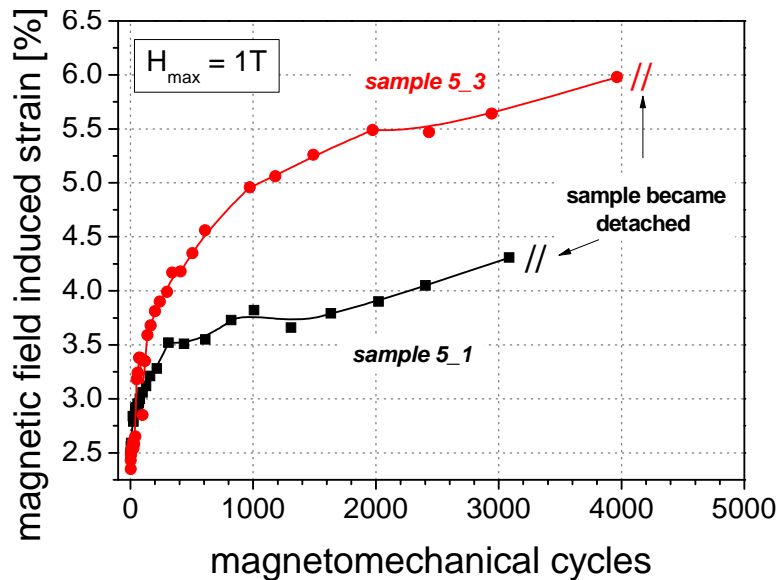


Figure 7.1: Magnetomechanical measurements in a rotating 1T field, determine the magnetic field induced strain, whereas the strain plotted here, shows the difference measured, when the long axis of the samples aligns 90° perpendicular to the magnetic field and parallel to the field.

The problems of gluing Ni-Mn-Ga-Co samples on a sample holder also occurred for the installation of the sample in the PPMS, reducing the number of successfully completed measurements. However, the samples examined verified the strong influence of cobalt on the magnetic properties of the martensite and austenite phase of the alloy.

While Ni-Mn-Ga shows a higher magnetization in the martensite state than in the austenite state in magnetic fields above 0.1T, the addition of cobalt inverts the behaviour, with a higher magnetization in the austenite phase. The change of magnetization at the structural phase transformation in the Ni-Mn-Ga-Co specimens occurs as with Ni-Mn-Ga within a small

temperature interval, resulting in a giant inverse magnetocaloric effect, with a positive entropy change from the low to the high temperature phase.

This makes the material a potential candidate for cooling applications in the temperature region of about 100°C. However, the dependence of the Mn – and Co – content in the samples on the (inverse) magnetocaloric effect, has to be investigated by more measurements of samples with changing stoichiometry, to verify the maximum possible entropy change. By measurements of the adiabatic temperature change at the particular structural phase transformation temperature the capability for industrial application has to be verified.

# ACKNOWLEDGEMENT

---

This thesis would not have been possible without the kind support and encouragement of many people I would like to thank in these final lines. First of all I am indebted to my thesis advisor Prof. Dr. Winfried Petry at the physics department of the TU München for many inspiring discussions, suggestions and comments concerning my work.

I owe the Helmholtz Centre Berlin a debt of gratitude for the outstanding experimental environment and for the opportunity to participate in various conferences and workshops. Speaking of financial support, I would like to mention the Deutsche Forschungsgesellschaft (DFG) giving me the possibility to work in the research project SPP1239. Therefore special thanks go to Dr. Rainer Schneider.

I have been fortunate to get the possibility to work with Dr. Robert Wimpory, who offered me an outstanding support during my experiments and the writing of my thesis and who became a very good friend. I am glad, that Dr. Markus Chmielus joined the research project, who always had time for fruitful discussions and gave the opportunity of new experiments. Sincere thanks are extended to Arno Mecklenburg who introduced me to the research field and showed me how much fun science can provide. Furthermore I would like to thank my friends and colleagues Dr. Markus Strobl, Dr. Ewout Kemner, Dr. Evgeny Moskvina, Dr. Nadir Aliouane and Felix Groitl, raising a creative and enjoyable atmosphere at work and beyond.

I want to especially thank my best friend Thomas Hügler for supporting me mentally as nobody else has been able to. Special thanks also go to Dirk Broßwick for his never fading encouragement.

Nothing would have been possible without my parents and my sister, who have always been there for me.

# BIBLIOGRAPHY

---

- [1] F. Heusler, *Verh. Dtsch. Phys. Ges.* **5**, 219, (1903)
- [2] A.J. Bradley, J.W. Rodgers, *Proc. R. Soc. London Ser. A*, **144**, 340, (1934)
- [3] N.W. Ashcroft, N.D. Mermin, *Solid State Physics*, Cengage Learning Services, (1976)
- [4] R. Kainuma, N. Satoh, X. J. Liu, I. Ohnuma, K. Ishida, *Journal of Alloys and Compounds*, **266**, 191, (1998)
- [5] G.B. Johnston, E.O. Hall, *J. Phys. Chem. Solids* **29**, 193, (1968)
- [6] M. Acet, E. Duman, E.F. Wassermann, Ll. Manosa, A. Planes, *J. Appl. Phys.*, **92**, 3867, (2002)
- [7] X. Moya, L. Mañosa, A. Planes, T. Krenke, M. Acet, V.O. Garlea, T.A. Lograsso, D.L. Schlagel, J.L. Zaretsky, *Phys. Rev. B*, **73**, 064303, (2006)
- [8] H. Wada, Y. Tanabe, *Appl. Phys. Lett.*, **79**, 3302, (2001)
- [9] A.A. Cherechukin, T. Tagaki, M. Matsumoto, V.D. Buchel'nikov, *Phys. Lett A*, **326**, 146, (2004)
- [10] S. Stadler, M. Khan, J. Mitchell, N. Ali, A. M. Gomes, I. Dubenko, A. Y. Takeuchi, A. P. Guimaraes, *Appl. Phys. Lett.*, **88**, 192511 (2006)
- [11] D.A. Porter, K.E. Easterling, *Phase transformations in metals and alloys*, (1992)
- [12] B. W. Batterman, C. S. Barrett, *Phys. Rev.*, **145**, 296, (1966)
- [13] B. K. Chakrabarti, B. P. Barua, S. K. Sinha, *Physica Status Solidi b*, **86**, K55, (1978)
- [14] G. M. Wolten, *J. Am. Ceram. Soc.*, **46**, 418, (1963)
- [15] P.M. Kelly and L.R. Rose, *Prog Mater Sci*, **47**, 463, (2002)
- [16] P.J. Webster, *The magnetic and chemical structure of the Heusler alloys*, thesis, Sheffield University, (1968)
- [17] A. Planes, L. Mañosa, A. Saxena, *Magnetism and structure in functional materials*, Materials Science, Springer, (2005)
- [18] W. Pfeiler, *Alloy physics*, Wiley-VCH, (2007)
- [19] K. Otsuka, C. M. Wayman, *martensite transformation: thermodynamic aspects*, in *Shape Memory Materials*, Cambridge University Press (1998)
- [20] Y. Aydogdu, A. Aydogdu, O. Adiguzel, *Journal of Materials Processing Technology*, **123**, 498, (2002)

- [21] L. Zhang, C. Xie, J. Wu, *Materials Science and Engineering A* **438–440**, 905, (2006)
- [22] K. Otsuka, T. Kakeshita, *Science and technology of shape-memory alloys: New developments, MRS Bulletin* (2002).
- [23] A. Falvo, F. Furgiuele, C. Maletta, *Smart Mater. Struct.*, **16**, 771, (2007)
- [24] A. Sozinov, A. A. Likhachev, N. Lanska and K. Ullakko, *Appl. Phys. Lett.*, **80**, 1746, (2002)
- [25] C. R. Rathod, B. Clausen, M. A. M. Bourke, R. Vaidyanathan, *Appl. Phys. Lett.* **88**, 201919, (2006)
- [26] H.H. Liebermann, C.D. Graham Jr., *Acta Metallurgica*, **25**, 715, (1977)
- [27] V.A. Chernenko, V.A. Lvov, S. Besseghini, Y. Murakami, *Scripta Materialia*, **55**, 307, (2006)
- [28] O. Heczko, L. Straka, *J. Appl. Phys.*, **94**, 7139, (2003)
- [29] O. Heczko, L. Straka, N. Lanska, K. Ullakko, J. Enkovaara, *J. Appl. Phys.*, **91**, 8228, (2002)
- [30] G. Liu, J. Chen, Y. Cui, Z. Liu, M. Zhang, G. Wu, E. Brück, F.R. de Boer, F. Meng, Y. Li, J. Qu, *Solid State Communications* **130**, 687, (2004)
- [31] E. Warburg, *Ann. Phys.*, **249**, 141, (1881)
- [32] P. Debye, *Ann. Phys.*, **386**, 1154, (1926)
- [33] W. F. Giaque, *J. Am. Chem. Soc.*, **49**, 1864, (1927)
- [34] V. K. Pecharsky, K. A. Gschneidner, Jr., *Appl. Phys. Lett.*, **70**, 3299, (1997)
- [35] E. Brück, O. Tegus, D.T.C. Thanh, K.H.J. Buschow, *Journal of Magnetism and Magnetic Materials*, **310**, 2793, (2007)
- [36] V. Franco, K. R. Pirota, V. M. Prida, A. M. J. C. Neto, A. Conde, M. Knobel, B. Hernando, M. Vazquez, *Phys. Rev. B*, **77**, 104434, (2008)
- [37] J.S. Lee, *phys. Stat. Sol. (b)*, **241**, 1765, (2004)
- [38] V. K. Pecharsky, K. A. Gschneidner, Jr., *J. Appl. Phys.*, **86**, 6317, (1999)
- [39] P.J. Webster, K.R.A. Ziebeck, *Philos Mag B*, **49**, 295, (1984)
- [40] K.Ullakko, J.K. Huang, C. Kantner, R.C. O’Handley, V.V. Kokorin, *Appl. Phys. Lett.*, **69**, 1966, (1996)
- [41] V.A. Chernenko, V.V. Kokorin, *Proc. Int. Conf. on Martensitic Transformations (ICOMAT-92)*, Monterey Institute for Advanced Studies, Monterey, CA, 1205, (1993)
- [42] W. H. Wang, G. H. Wu, J. L. Chen, C. H. Yu, S. X. Gao, W. S. Zhan, Z. Wang, Z. Y. Gao, Y. F. Zheng, L. C. Zhao, *Appl. Phys. Lett.*, **77**, 3245, (2000)
- [43] X. Jin, M. Marioni, D. Bono, S. M. Allen, R. C. O’Handley, *J. Appl. Phys.*, **91**, 8222, (2002)

- [44] V. A. Chernenko, E. Cesari, V. V. Kokorin, I. N. Vitenko, *Scr. Metall. Mater.*, **33**, 1239, (1995)
- [45] V. A. Chernenko, *Scr. Mater.* **40**, 523, (1999)
- [46] S. J. Murray, M. Farinelli, C. Kantner, J. K. Huang, S. M. Allen, R. C. O'Handley, *J. Appl. Phys.*, **83**, 7297, (1998)
- [47] A. N. Vasil'ev, A. D. Bozhko, V. V. Khovailo, I. E. Dikshtein, V. G. Shavrov, C. D. Buchelnikov, M. Matsumoto, S. Suzuki, T. Takagi, and J. Tani, *Phys. Rev. B*, **59**, 1113, (1999)
- [48] K. Ullakko, Y. Ezer, A. Sozinov, G. Kimmel, P. Yakovenko, and V. K. Lindroos, *Scr. Mater.*, **44**, 475, (2001)
- [49] M. Richard, J. Feuchtwanger, D. Schlagel, T. Lograsso, S.M. Allen, R.C. O'Handley, *Scr. Mater.*, **54**, 1797, (2006)
- [50] S. J. Murray, M. Marioni, S. M. Allen, R. C. O'Handley, T. A. Lograsso *Appl. Phys. Lett.*, **77**, 886, (2000)
- [51] P. J. Brown, J. Crangle, T. Kanomata, M. Matsumoto, K.-U. Neumann, B. Ouladdiaf, K. R. A. Ziebeck, *J. Phys.: Condens. Matter*, **14**, 10159, (2002)
- [52] J. Pons, V.A. Chernenko, R. Santamarta, E. Cesari, *Acta Mater.*, **48**, 3027, (2000)
- [53] A. Sozinov, A.A. Likhachev, N. Lanska and K. Ullakko, *Appl. Phys. Lett.*, **80**, 1746, (2002)
- [54] K. Rolfs, A. Mecklenburg, J.M. Guldbakke, R.C. Wimpory, A. Raatz, J. Hesselbach, R. Schneider, *JMMM*, **321**, 1063, (2008)
- [55] C. Bechtold, A. Gerber, M. Wuttig, E. Quandt, *Scr. Mater.*, **58**, 1359, (2008)
- [56] L. Righi, F. Albertini, E. Villa, A. Paoluzi, G. Calestani, V. Chernenko, S. Besseghini, C. Ritter, F. Passaretti, *Acta Mater.*, **56**, 4529, (2008)
- [57] L. Straka, O. Heczko, K. Ullakko, *JMMM*, **227-276**, 2049, (2003)
- [58] S. Banik, P. K. Mukhopadhyay, A. M. Awasthi, S. R. Barman, *Advanced Materials Research*, **52**, 109, (2008)
- [59] A. Sozinov, A.A. Likhachev, N. Lanska, O. Söderberg, K. Koho, K. Ullakko, V.K. Lindroos, *J. Phys. IV France*, **115**, 121, (2004)
- [60] V. A. Chernenko, C. Seguí, E. Cesari, J. Pons, V. V. Kokorin, *Phys. Rev. B*, **57**, 2659, (1998)
- [61] T. Ohba, N. M., K. Fukuda, T. Fukuda, T. Kakeshita, K. Kato, *Smart Mater. Struct.*, **14**, S197, (2005)
- [62] C. Jiang, Y. Muhammad, L. Deng, W. Wu, H. Xu, *Acta Mater.*, **52**, 2779, (2004)
- [63] F. Hu, B.-G. Shen, J.-R. Sun, G.-H. Wu, *Phys. Rev. B*, **64**, 132412, (2001)
- [64] A.A. Cherechukin, T. Takagi, M. Matsumoto, V.D. Buchel'nikov, *Phys Lett. A*, **326**, 146, (2004)

- [65] B. Ingale, R. Gopalan, M. Manivel Raja, V. Chandrasekaran, S. Ram, *J. Appl. Phys.*, **102**, 013906, (2007)
- [66] Günther Höhne, W. Hemminger, H.-J. Flammersheim, *Differential scanning calorimetry, 2<sup>nd</sup> Edition*, Springer Verlag, (2003)
- [67] W.L. Bragg, *Proceedings of the Cambridge Philosophical Society*, **17**, 43, (1913)
- [68] G.L. Squires, *Introduction to the theory of thermal neutron scattering*, Cambridge University Press, (1996)
- [69] T. Springer, K. Sturm, U. Buchenau, *Streumethoden zur Untersuchung kondensierter Materie*, Vorlesungsmanuskripte, Forschungszentrum Jülich GmbH, (1996)
- [70] R.C. Wimpory, P. Mikula, J. Saroun, T. Poeste, J. Li, M. Hofmann, R. Schneider, *Neutron News*, **19 (1)**, 16, (2008)
- [71] B. D. Cullity, C. D. Graham, *Introduction to Magnetic Materials*, Wiley, (2009)
- [72] D. Jiles, *Introduction to magnetism and magnetic materials*, CRC Press, (1998)
- [73] P. Müllner, V.A. Chernenko, G. Kostorz, *Scripta Materialia* **49**, 129, (2003)
- [74] P. Müllner, V.A. Chernenko, G. Kostorz, *Journal of Magnetism and Magnetic Materials* **267**, 325, (2003)
- [75] S. Foner, *Rev. Sci. Instrum.* **30**, 548, (1959)
- [76] N. Scheerbaum, O. Heczko, J. Liu, D. Hinz, L. Schultz, O. Gutfleisch, *New J. Phys.*, **10**, 073002, (2008)
- [77] O. Söderberg, Y. Ge, N. Glavatska, O. Heczko, K. Ullakko, V.K. Lindroos, *J. Phys. IV France*, **11**, 287, (2001)
- [78] D. C. Lagoudas, *Shape Memory Alloys: Modeling and Engineering Applications*, Springer Verlag, (2008)
- [79] A. Mecklenburg, S. Fiechter, H.-P. Nabein, R. Schneider, DE102004018664A1 (2005)
- [80] P. Haasen, *Physikalische Metallkunde*, Springer Verlag, (1984)
- [81] K.-Th. Wilke, *Kristallzüchtung*, VEB Deutscher Verlag der Wissenschaften, (1973)
- [82] F. Rosenberger, *Fundamentals of Crystal Growth I*, Springer Verlag, (1981)
- [83] D.L. Schlagel, Y.L. Wu, W. Zhang, T.A. Lograsso *Journal of Alloys and Compounds*, **312**, 77, (2000)
- [84] R. W. Overholser, M. Wuttig, D. A. Neumann, *Scripta Materialia*, **40**, 1095, (1999)
- [85] M. Rolin, M. Clausier, *Rev. Int. Hautes Temp. Refract.*, **4 [1]**, 47, (1967)
- [86] C. Bodsworth, *The Extraction and Refining of Metals*, CRC Press, (1994)

- [87] V. Sa´nchez-Alarcos J.I. Pe´rez-Landaza´bal, V. Recarte, C. Go´mez-Polo, J.A. Rodr´ıguez-Velamaza´n, *Acta Mater.* **56**, 5370, (2008)
- [88] N. Lanska, O. Söderberg, A. Sozinov, Y. Ge, K. Ullakko, V.K. Lindroos, *J. Appl. Phys.*, **95**, 8074, (2004).
- [89] [http://www.helmholtzberlin.de/media/media/oea/web/pr\\_webseite/druckschriften/infos/neutr\\_scat\\_instrum.pdf](http://www.helmholtzberlin.de/media/media/oea/web/pr_webseite/druckschriften/infos/neutr_scat_instrum.pdf) (last visit June 2010)
- [90] <http://www.sigmaplot.com/products/peakfit/peakfit.php> (last visit June 2010)
- [91] <http://www.ill.eu/instruments-support/computing-for-science/cs-software/all-software/lamp/> (last visit June 2010)
- [92] <http://www.ill.eu/sites/fullprof/> (last visit June 2010)
- [93] <http://www.mathworks.com/products/matlab/> (last visit June 2010)
- [94] Y. D. Wang, Y. Ren, Z. H. Nie, D. M. Liu, L. Zuo, H. Choo, H. Li, P. K. Liaw, J. Q. Yan, R. J. McQueeney, J. W. Richardson, A. Huq, *J. Appl. Phys.* **101**, 063530, (2007)
- [95] B. Tian a, F. Chen a, Y. Liu a,b, Y.F. Zheng, *Intermetallics* **16**, 1279, (2008)
- [96] M. Chmielus, K. Rolfs, R. Wimpory, W. Reimers, P. Müllner, R. Schneider, *Acta Mat.* **58**, 3952, (2010)
- [97] <http://de.wikipedia.org/wiki/Fehlerfortpflanzung> (last visit June 2010)
- [98] V.A. Chernenko, *Scripta Mat.* **40**, 523, (1999)
- [99] P. Entel, V. D. Buchelnikov, M. E. Gruner, A. Hucht, V. V. Khovailo, S. K. Nayak, A. T. Zayak, *Materials Science Forum*, **583**, 21, (2008)
- [100] V.V. Khovaylo, V.D. Buchelnikov, R. Kainuma, V.V. Koledov, M. Ohtsuka, V. G. Shavrov, T. Takagi, S. V. Taskaev, and A. N. Vasiliev, *Phys. Rev. B* **72**, 224408, (2005)
- [101] G. D. Liu, J. L. Chen, Z. H. Liu, X. F. Dai, G. H. Wu, B. Zhang, and X. X. Zhang, *Appl. Phys. Lett.* **87**, 262504 (2005).
- [102] C. Jiang, Y. Muhammad, L. Deng, W. Wu, and H. Xu, *Acta Mater.* **52**, 2779 (2004).
- [103] A.A. Likhachev, K. Ullakko, *Physics Letters A* **275**, 142, (2000)
- [104] A. Sozinov, A. A. Likhachev, K. Ullakko, *Smart Structures and Materials 2001: Active Materials: Behavior and Mechanics*, **4333**, 189, (2001)
- [105] A. Sozinov, A.A. Likhachev, N. Lanska, O. Söderberg, K. Koho, K. Ullakko, V.K. Lindroos, *J. Phys. IV France* **115**, 121, (2004)
- [106] P. Müllner, *Z. Metallkd.* **97**, 205, (2006)
- [107] G. Kosterz, P. Müllner, *Z. Metallkd.* **96**, 703, (2005)

- [108] A. G. Crocker, *Phil. Mag. Ser. 8*, **7**, 1901, (1962)
- [109] P. Müllner, V. A. Chernenko, G. Kostorz, *J. Appl. Phys.* **95**, 1531, (2004)
- [110] F. Laves, *Die Naturwissenschaften* **39**, 546, (1952)
- [111] S. S. Yang, D.-H. Hou, J. Shyue, R. Wheeler, H. L. Fraser, *Mater. Res. Soc. Proc.* **364**, 1359, (1995)
- [112] V. V. Martynov, V. V. Kokorin, *J. Phys. III France* **2**, 739, (1992)
- [113] J. Pons, V. A. Chernenko, R. Santamarta, E. Cesari, *Acta Mater.* **48**, 3027, (2000)
- [114] J. Pons, R. Santamarta, V. A. Chernenko, E. Cesari, *Mater. Sci. Eng. A* **438**, 931, (2006)
- [115] J. W. Christian, S. Mahajan, *Prog. Mater. Sci.* **39**, 1, (1995)
- [116] X. Zhou, H. Kunkel, G. Williams, S. Zhang, X. Desheng, *JMMM*, **305**, 372, (2006)

# APPENDIX A

---

For the neutron diffraction experiments at the HZB – instruments E3 and E7 uncertainties have to be taken into account, when determining the lattice parameters of the different samples. The offset of the  $2\theta$  of the instruments lies below  $0.1^\circ$  and has to be summed with the fitting error, which lies below  $0.003^\circ$ . The third uncertainties is the deviation in the wavelength, which is not more than  $0.001\text{\AA}$ .

For a conservative calculation of the uncertainty in the lattice parameters, the uncertainty in  $d$  will be calculated with following absolute errors:

- $2\theta$  - offset:  $0.1^\circ$
- Fitting error:  $0.01^\circ$
- Deviation in wavelength:  $0.001\text{\AA}$

Since  $d$  is calculated with the Bragg – equation:

$$n\lambda = 2d\sin\theta$$

The absolute error of  $d$  can be calculated as:

$$\Delta d = \left| \frac{-n\lambda\cos\theta}{2\sin^2\theta} \right| \Delta\theta + \frac{\Delta\lambda}{2\sin\theta}$$

Since the lattice parameter is calculated from the indices  $h00$  and  $0k0$  by following equation:

$$\frac{1}{d^2} = \frac{h^2}{a^2} \quad , \quad \frac{1}{d^2} = \frac{k^2}{b^2} \quad \text{and} \quad \frac{1}{d^2} = \frac{l^2}{c^2}, \text{ respectively,}$$

The relative error in  $d$  is equal to the relative error of the lattice parameters:

$$\delta d = \frac{\Delta d}{d} = \delta a (b, c)$$

As we have seen from the measurements, the lattice parameters vary from  $5.45\text{\AA}$  to  $6.00\text{\AA}$ . The  $2\theta$  range of the measurements lain between  $40^\circ$  and  $100^\circ$ . By calculating the absolute error of the minimum and maximum lattice parameters measured here, it can be seen, that the uncertainty is never bigger than  $0.02\text{\AA}$  (see Tab.) and becomes even smaller with increasing  $2\theta$ . Therefore the value of the error bars in the graphs with structural properties (see subsection 5.3) is  $0.02\text{\AA}$ .

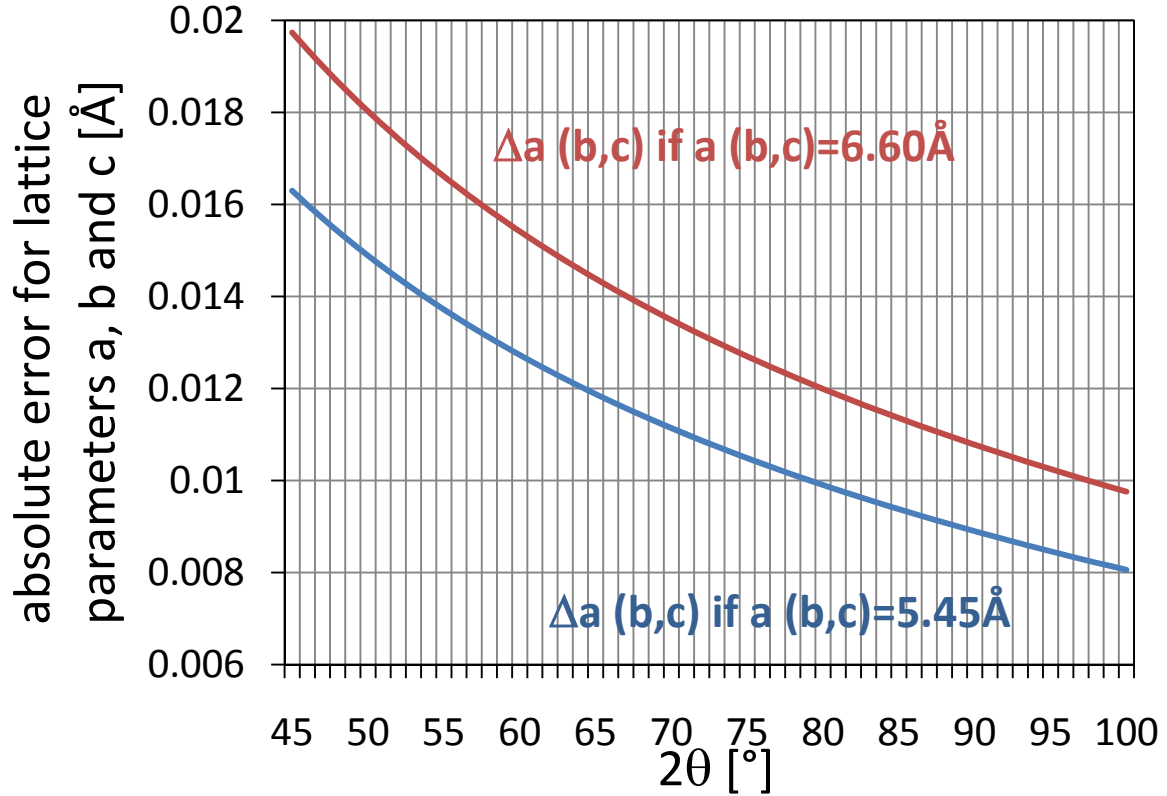


Figure A.1: Absolute uncertainty in dependence of the  $2\theta$  value of the analysed Bragg peak for the approximate maximum and minimum length of lattice parameter determined in the here presented results (see subsection 5.3)

$2\theta$	$d$	$\Delta d(\theta)$	$\Delta d(\lambda)$	$\delta d$	$\Delta d$ for $a=5.45 \text{ \AA}$	$\Delta d$ for $a=6.60 \text{ \AA}$
45	1.941553	0.0045	0.001307	0.00299	0.016298	0.019737
46	1.901563	0.0043	0.00128	0.002934	0.015992	0.019367
47	1.863327	0.004114	0.001254	0.002881	0.015699	0.019012
48	1.826735	0.003939	0.001229	0.002829	0.015418	0.018671
49	1.791686	0.003774	0.001206	0.002779	0.015147	0.018344
50	1.758088	0.003619	0.001183	0.002732	0.014887	0.018028
51	1.725856	0.003473	0.001161	0.002685	0.014636	0.017724
52	1.694911	0.003336	0.001141	0.002641	0.014394	0.017431
53	1.665181	0.003206	0.001121	0.002598	0.014161	0.017149
54	1.636598	0.003083	0.001101	0.002557	0.013935	0.016876
55	1.609101	0.002967	0.001083	0.002517	0.013717	0.016612
56	1.58263	0.002857	0.001065	0.002478	0.013507	0.016357
57	1.557134	0.002753	0.001048	0.002441	0.013303	0.01611
58	1.53256	0.002654	0.001031	0.002405	0.013106	0.015871
59	1.508864	0.00256	0.001015	0.00237	0.012914	0.015639
60	1.486	0.002471	0.001	0.002336	0.012729	0.015415
61	1.463929	0.002386	0.000985	0.002303	0.012549	0.015197
62	1.442612	0.002305	0.000971	0.002271	0.012374	0.014986
63	1.422013	0.002228	0.000957	0.002239	0.012205	0.01478

Appendix A

2 $\theta$	d	$\Delta d$ ( $\theta$ )	$\Delta d$ ( $\lambda$ )	$\delta d$	$\Delta d$ for a=5.45Å	$\Delta d$ for a=6.60Å
64	1.4021	0.002154	0.000944	0.002209	0.01204	0.01458
65	1.382841	0.002084	0.000931	0.00218	0.01188	0.014386
66	1.364206	0.002017	0.000918	0.002151	0.011724	0.014197
67	1.346168	0.001952	0.000906	0.002123	0.011572	0.014013
68	1.328701	0.001891	0.000894	0.002096	0.011424	0.013834
69	1.311779	0.001832	0.000883	0.00207	0.01128	0.01366
70	1.295381	0.001776	0.000872	0.002044	0.011139	0.01349
71	1.279484	0.001722	0.000861	0.002019	0.011002	0.013324
72	1.264067	0.00167	0.000851	0.001994	0.010868	0.013162
73	1.249112	0.00162	0.000841	0.00197	0.010738	0.013003
74	1.234599	0.001573	0.000831	0.001947	0.01061	0.012849
75	1.220511	0.001527	0.000821	0.001924	0.010486	0.012698
76	1.206832	0.001483	0.000812	0.001902	0.010364	0.012551
77	1.193546	0.00144	0.000803	0.00188	0.010245	0.012406
78	1.180639	0.0014	0.000795	0.001858	0.010128	0.012265
79	1.168095	0.00136	0.000786	0.001837	0.010014	0.012127
80	1.155903	0.001322	0.000778	0.001817	0.009902	0.011992
81	1.144048	0.001286	0.00077	0.001797	0.009793	0.011859
82	1.13252	0.001251	0.000762	0.001777	0.009686	0.01173
83	1.121306	0.001217	0.000755	0.001758	0.009581	0.011602
84	1.110396	0.001184	0.000747	0.001739	0.009478	0.011478
85	1.099779	0.001152	0.00074	0.001721	0.009377	0.011355
86	1.089445	0.001121	0.000733	0.001702	0.009278	0.011235
87	1.079386	0.001092	0.000726	0.001685	0.009181	0.011118
88	1.069591	0.001063	0.00072	0.001667	0.009085	0.011002
89	1.060052	0.001035	0.000713	0.00165	0.008991	0.010889
90	1.050761	0.001009	0.000707	0.001633	0.008899	0.010777
91	1.04171	0.000983	0.000701	0.001616	0.008809	0.010667
92	1.032892	0.000957	0.000695	0.0016	0.00872	0.01056
93	1.024299	0.000933	0.000689	0.001584	0.008632	0.010454
94	1.015924	0.000909	0.000684	0.001568	0.008546	0.010349
95	1.007762	0.000886	0.000678	0.001553	0.008461	0.010247
96	0.999805	0.000864	0.000673	0.001537	0.008378	0.010146
97	0.992048	0.000843	0.000668	0.001522	0.008296	0.010047
98	0.984485	0.000822	0.000663	0.001507	0.008215	0.009949
99	0.97711	0.000801	0.000658	0.001493	0.008136	0.009853
100	0.969918	0.000781	0.000653	0.001478	0.008057	0.009758

Table A1: Uncertainties  $\Delta d$  for two lattice parameters (approximately shortest and longest determined in the samples) in the 2 $\theta$  range of 40 to 100°, according to the range, from which Bragg peaks were used for analysis.

# APPENDIX B

---

For the determination of the nuclear structure of the austenite phase of Ni-Mn-Ga-Co, it was assumed to have a Fm-3m structure and therefore 776 Bragg reflections have been measured in the four circle diffractometer D9, fulfilling the symmetry rules of the structure. The collected Bragg intensities have to be integrated and corrected, to allow for the set up of a model for the crystal structure and to refine the corresponding atomic parameters by comparing the measured and calculated structure factors.

The integrated intensities  $I_{obs}$  have to be corrected for the Lorentz factor  $L$ , which takes into account that different lattice planes remain for different times in reflection position during a scan through the reciprocal lattice. The Lorentz factor can be calculated by

$$L = (\sin 2\theta)^{-1},$$

which has to be inserted into the calculation for the square of the structure factor  $F_{obs}^2$

$$I_{obs} = SL|F_{obs}|^2 = S(\sin 2\theta)^{-1}|F_{obs}|^2.$$

The overall scale factor  $S$  depends on the particular instrumental set up, the incident flux and some universal constants. Furthermore extinction – and absorption factors have to be included.

The integrated and corrected Bragg intensities were used for the refinement of the crystal structure, which is based on the least square method, whereas the following equation has to be minimized:

$$\sum_{hkl} \omega (F_{obs}^2 - F_{cal}^2)^2 = \min.$$

Thereby  $F_{cal}$  is the calculated structure factor for the Bragg reflections, while  $\omega = 1/\sigma$  takes the standard deviation of the observed reflections into account.

The structure factor for the  $N$ th Bragg reflection is calculated by

$$F_N(\tau) = \sum_j \bar{b}_j e^{i\tau d_j} e^{-W_j},$$

With  $d_j = (x_j, y_j, z_j)$  as the positions of the  $j$ th atom in the unit cell and  $b_j$  as the coherent scattering length. The term  $e^{-W_j}$  is the Debye – Waller factor, describing the displacement of the  $j$ th atom due to thermal fluctuations about the equilibrium position. In the case of an isotropic displacement  $W_j$  can be expressed with following equation:

$$W_j = b_j \sin^2(\theta/\lambda).$$

As it can be seen, the calculated structure factor  $F_{cal}$  depends on  $(d_j, b_j)$  in a complicated and nonlinear fashion. For the determination and refinement of the structural parameters, the measured structure factors  $F_{obs}$  and an iterative method have to be used to find the minimum of

equation. Therefore it is important to find suitable starting parameters, which lie in the vicinity of the final ones.

To indicate the accuracy of the assumed structural model, agreement factors are given for each refinement, whereas the most common ones are:

$$R_F = \frac{\sum_{hkl} ||F_{obs}| - |F_{cal}||}{\sum_{hkl} |F_{obs}|}$$

$$R_F^2 = \frac{\sum_{hkl} |F_{obs}^2 - F_{cal}^2|}{\sum_{hkl} |F_{obs}^2|}$$

$$R_{\omega F}^2 = \sqrt{\frac{\sum_{hkl} \omega (F_{obs}^2 - F_{cal}^2)^2}{\sum_{hkl} \omega (F_{obs}^2)^2}}$$

The first factor  $R_F$  depends on the differences of the calculated and observed structure factors and gives the relative deviation between the values. Since the quantity observed in an experiment is actually the squared structure factor,  $R_F^2$  can be taken. The third factor  $R_{\omega F}^2$  takes the precision of the measured parameters into account and is therefore another helpful quantity. Even though the most often given factor in publications is  $R_F$ , all three values are given on this thesis.

# APPENDIX C

The following subsections give the detailed description of the mechanical stress – strain – strain behaviour, determined for the samples cut out from the single crystalline rods no.2 to no.5.

## CRYSTAL ROD NO.2 “Ni<sub>44.6</sub>Mn<sub>30.7</sub>Ga<sub>19.3</sub>Co<sub>5.4</sub>”

From crystal rod No. 2 the stress – strain – behaviour of three samples two from the bottom (2\_1 and 2\_2) and one from the top (2\_6) were determined in the same way like the samples from crystal rod No.1.

The samples from the bottom of the rod showed the same behaviour like the samples 1\_4 and 1\_7. The uniaxial pressure along the x – and z – direction, respectively resulted in an increase of the other axis, while the length in y- direction hardly changed. Thereby a maximum mechanical stress induced strain of 13.69% in x – and of 13.22% in the z – direction was measured (see Figure C1 for sample 2\_1). Furthermore it was verified, that the compression along the y – axes does not lead to a significant change of the samples dimensions independent from the sequence of loading.

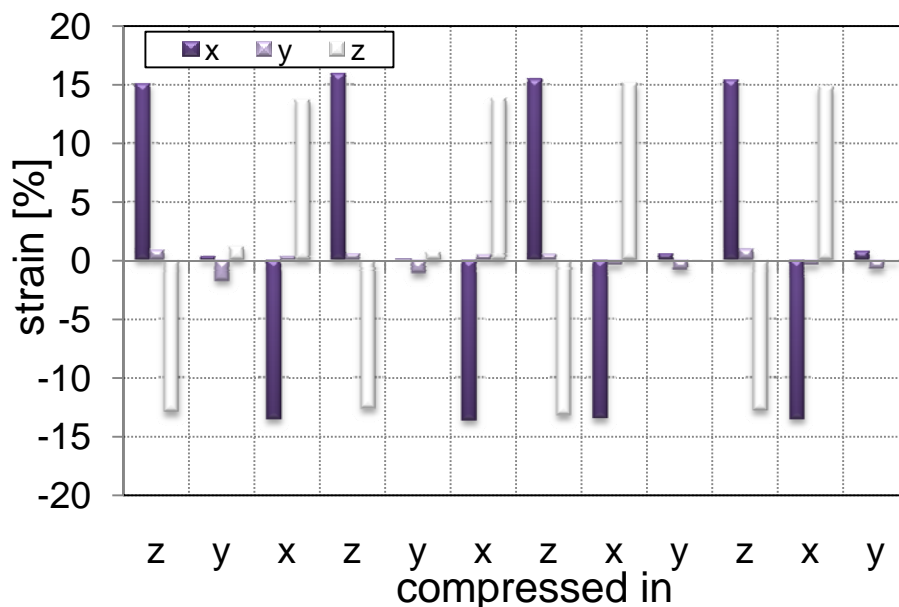


Figure C1: The change of the length of the axes in percentages according to the previous length at any one time of sample cut out of plane one of crystal rod No.2.

Also the twinning stress of the samples is similar to each other. However the mechanical stresses needed to overcome the twinning stresses increase with the Mn/Ga - ratio. In the z – direction, the samples show an increase of the stress up to 30 MPa (sample 2\_1) and 45 MPa (sample 2\_2)

to reach the maximum strain of 14%, before the slope increases and do not result in any plastic deformation anymore (see Figure C2). In x - direction the samples show a stepwise stress plateau. Whereby the first plateau lies at around 12 MPa and 18 MPa and increase to 22 MPa and 32 MPa in the second plateau, respectively. The maximum strain in these samples was determined by applying a stress of 32 MPa and 45 MPa.

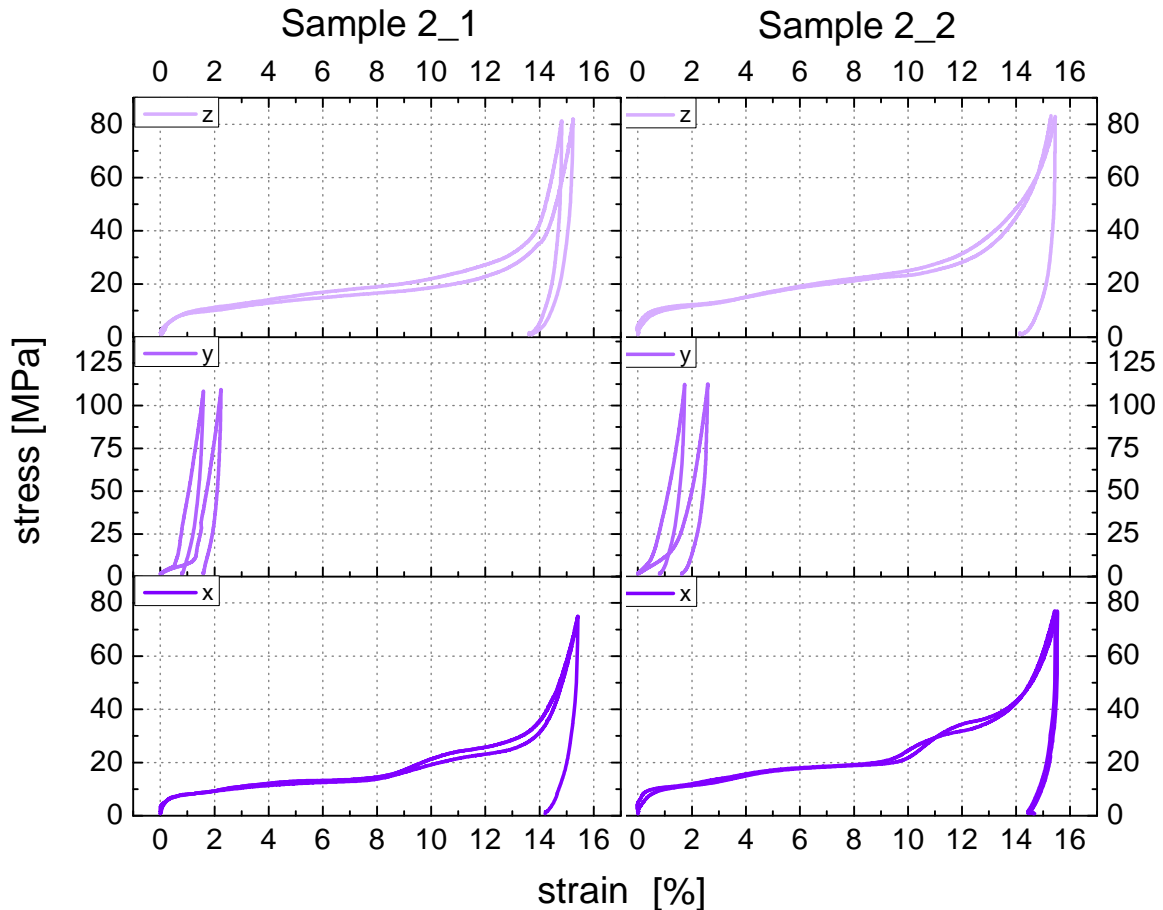


Figure C2: The stress - strain -behaviour of two samples from the bottom of the crystal, whereby sample 2\_1 has a slightly lower Mn/Ga - ratio (1.35) than sample 2\_2 (1.37). The diagram shows response to the uniaxial pressure in all three directions.

The sample with the highest Mn/Ga - ratio in this rod (sample 2\_6) shows much higher twinning stresses which have to be overcome to induce the strain. As depicted in Figure C3, the sample shows no stress plateau in the z - direction. The stress increases constantly to the maximum of 90MPa, whereby a strain between 12% and 13% is reached. Furthermore it was determined, that a stress of at least 30MPa is required to induce any plastic deformation in this direction of the sample. The x - direction still shows the stepwise stress - strain - behaviour like already measured in sample 2\_1 and 2\_2. However the plateaus have more or less vanished. Only one small plateau was measured, which lies around 40MPa and 50MPa. Before and after this, the stress increases constantly up to 70MPa, whereby a strain of 10% to 13% was determined. Compared to the samples 2\_1 and 2\_2, sample 2\_6 shows a mechanical stress induced strain in the third direction. However a stress of 120MPa is needed to induce a strain of maximum 5%, which was only reached once and decreased to 2% in the last measurement.

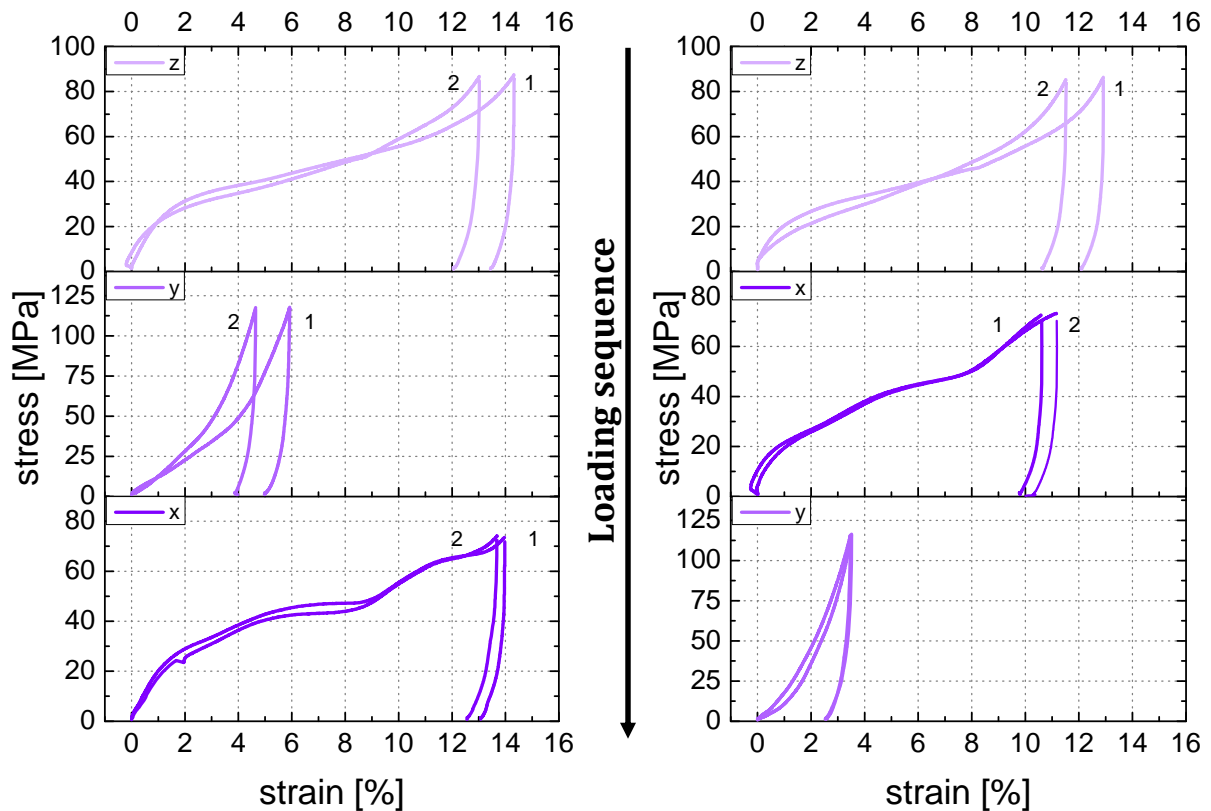


Figure C3: The stress – strain – behaviour of sample 2\_6 ( $\text{Ni}_{44.93}\text{Mn}_{28.57}\text{Ga}_{20.00}\text{Co}_{6.50}$ ) of all three axes for two loading cycles with the sequence  $z \rightarrow y \rightarrow x$  and  $z \rightarrow x \rightarrow y$ , respectively.

### CRYSTAL ROD NO.3 “ $\text{Ni}_{45.0}\text{Mn}_{31.0}\text{Ga}_{19.2}\text{Co}_{4.8}$ ”

In crystal rod No.3 two different responses to the deformation experiments were determined. The sample 3\_1 with the lowest Mn/Ga - ratio in this rod was cut down to a cuboid with the dimension  $x = 2.381$  mm,  $y = 4.254$  mm and  $z = 4.765$  mm, before analyzed to enable a higher stress application. The sample was compressed uniaxially first in z direction before compressed in the y - and x - direction. The experiment was repeated in the same sequence. The specimen shows a similar behaviour to the samples measured from the rods No.1 and 2. However the sample shows an initial stress peak of 31.7 MPa before it decreases to 15.7 MPa, when compressed in the z - direction and reaches a strain of 5.35% (see Figure C4, curve z1). In the second loading cycle, the stress needed to induce a strain increases to 40.9 MPa before decreasing to 32.7 MPa. Therefore the mechanical induced strain increases to 5.94%. The compression in the y - direction results in a strain of 13.1%. In this direction no stress plateau was determined. To reach the maximum strain, a stress of approximately 35.5 MPa has to be applied, which does not change in the second loading cycle (Figure C4, curve y1 and y2). The deformation in the x - direction results in a strain of 3.8%, by applying a stress of approximately 15 MPa before reaching the maximum strain of 4.3% by the uniaxial compression with 25 MPa.

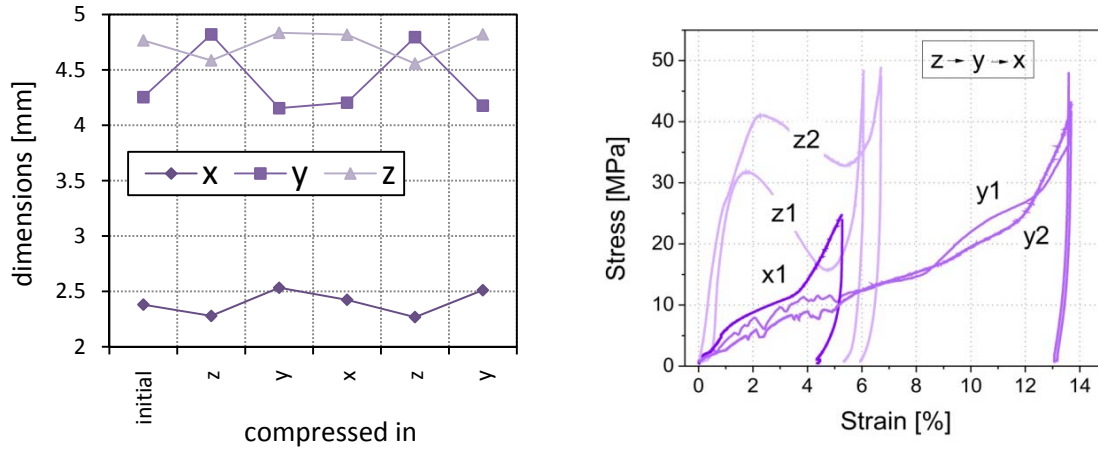


Figure C4: Stress – Strain curves of sample 3\_1 with the uniaxial compression along z and subsequently y and x.

To apply a mechanical stress high enough to overcome the twinning stress in the second determined sample 3\_6, the specimen was cut to smaller size with edges of length  $x = 1.6$  mm,  $y = 1.4$  mm, and  $z = 1.5$  mm. Sample 3\_6 was initially loaded in the x direction (see deformation curve x in Figure C5 A), followed by deformation along the y direction (curve y in Figure C5 A), then in the z direction (curve z in Figure C5 A), and again was repeated with the same sequence (see deformation curves in Figure C5 B).

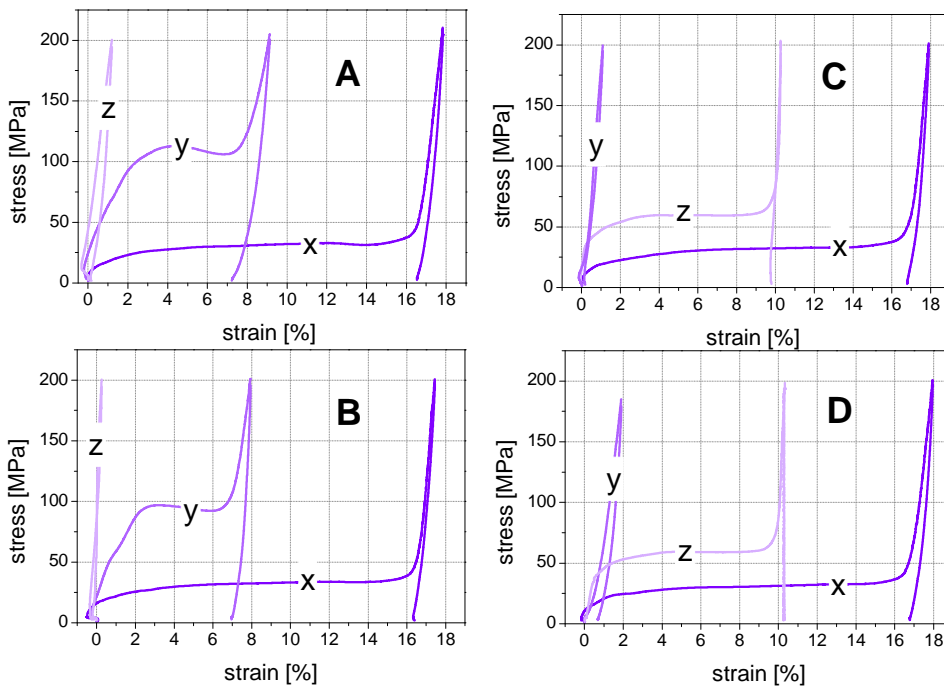


Figure C5: Stress – strain – behaviour of sample 3\_6, whereby the sequence of loading  $x \rightarrow y \rightarrow z$  was repeated twice (A and B) and then was changed to  $x \rightarrow z \rightarrow y$  (C and D).

Altogether, 12 deformation experiments were carried out where the sequence of loading directions varied such that loading in a given direction (example in the x direction) was

preceded at least once by loading in each of the other two directions (i.e. in the  $y$  and then  $z$  directions).

Independent of the loading direction of the preceding experiment, the plastic strain upon loading in the  $x$  – direction was between 16 and 17% (Figure C5, curve  $x$  in A, B, C and D). Upon subsequent loading in the  $y$  direction (Figure C5 A and B, curve  $y$ ) and in the  $z$  direction (Figure C5 C and D, curve  $z$ ) respectively, a strain of 6.8% and 9.5% plastic strain was measured while the following loading in the third direction ( $y$  or  $z$ ) did not result in any plastic deformation (curves  $z$  in Figure C5 A and B and curves  $y$  in Figure C5 C and D). Figure C6 lists the final sample size in all directions after each deformation experiment.

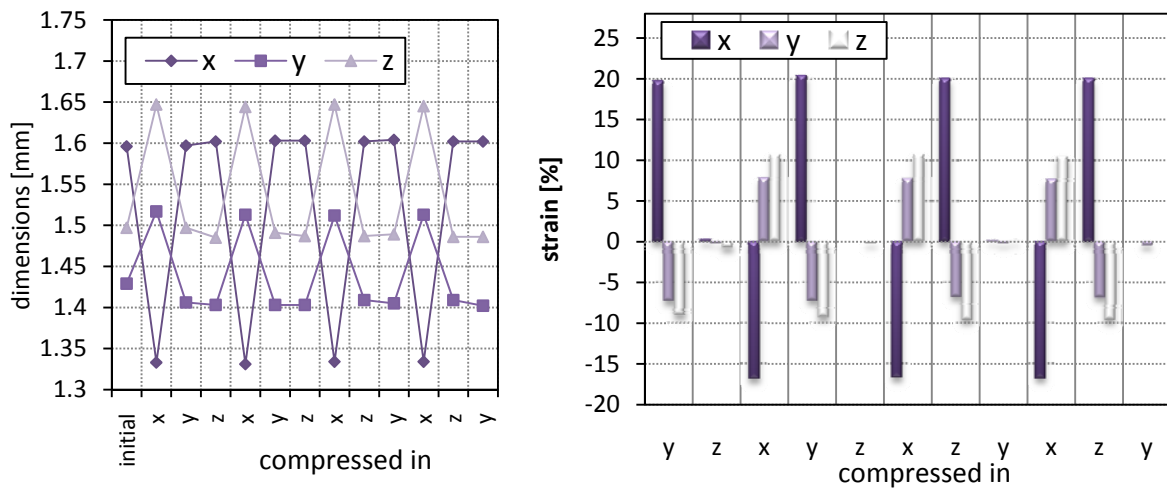


Figure C6: Change of the dimensions of the sample after each deformation step in mm (left diagram) and in percentage referring to the dimensions measured before the compression (right diagram) of sample 3\_6.

While the sample was deformed in compression repeatedly in all three directions, at the end of each of the twelve deformation experiments, only two sample shapes were found. These two shapes are referred to as “shape states” I and II. For shape state I:  $x_I = 1.60 \pm 0.01$  mm,  $y_I = 1.41 \pm 0.02$  mm,  $z_I = 1.44 \pm 0.01$  mm. For shape state II:  $x_{II} = 1.33 \pm 0.01$  mm,  $y_{II} = 1.52 \pm 0.01$  mm,  $z_{II} = 1.64 \pm 0.01$  mm. The sample exists in two distinct “shape states”. Independent of the preceding loading direction, the sample is in shape state I after loading in the  $y$  and  $z$  directions, while due to loading in the  $x$  direction the sample reaches another state (shape state II). For every loading in the  $x$  direction the twinning stress is approximately 30 MPa, for loading in the  $z$  direction the twinning stress is 60 MPa, and for loading in the  $y$  direction the twinning stress decreases from 110 MPa (Figure C5 A, curve  $y$ ) in the first loading cycle to 95 MPa (Figure C5 B, curve  $y$ ) in the second loading cycle. The stress strain curves for loading in the  $x$  direction fall nearly on top of each other. The stress strain curves for loading in the  $y$  direction after loading in the  $x$  direction are also similar.

## CRYSTAL ROD NO.4 “ $\text{Ni}_{48.8}\text{Mn}_{28.6}\text{Ga}_{21.4}\text{Co}_{1.2}$ ”

The samples 4\_1, 4\_2 and 4\_4, which show an increasing Mn/Ga - ratio, show the same stress – strain – behaviour like most of the samples of crystal rod No. 1, 2 and 3 (e.g. sample 1\_, 2\_ and

3\_). The uniaxial compression along the x – and y – direction result in an increase in the y – and x – direction respectively (see sample 4\_1 as an example in Figure C7). Both compressions do not result in a length change of the z – direction.

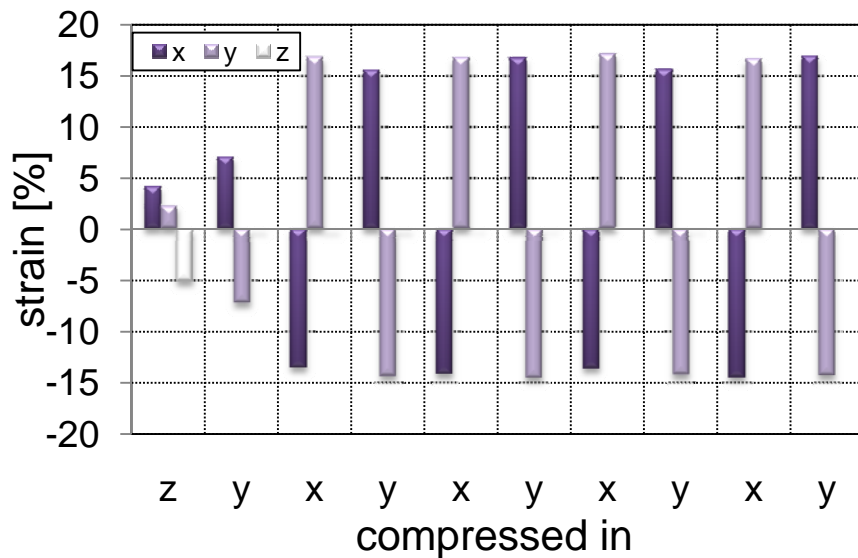


Figure C7: The change of the length of the axes in percentages according to the previous length at any one time of sample cut out of sample 4\_1 of crystal rod No.4.

The twinning stress which has to be overcome is similar for all samples in this rod. As depicted in Figure C8, the samples show a distinctive stress plateau with an averaged stress plateau of around 10MPa to around 8MPa for the x – and y – direction, which is not significantly changing with the increasing Mn/Ga - ratio of the measured samples. Sample 4\_1, 4\_2 and 4\_4 show a reproducible mechanical induced strain between 13% and 14% in the y – direction. In the x – direction the samples show a maximum strain between 15% and 17%, whereby the strain decreases slightly (approximately 1%) in the second cycle.

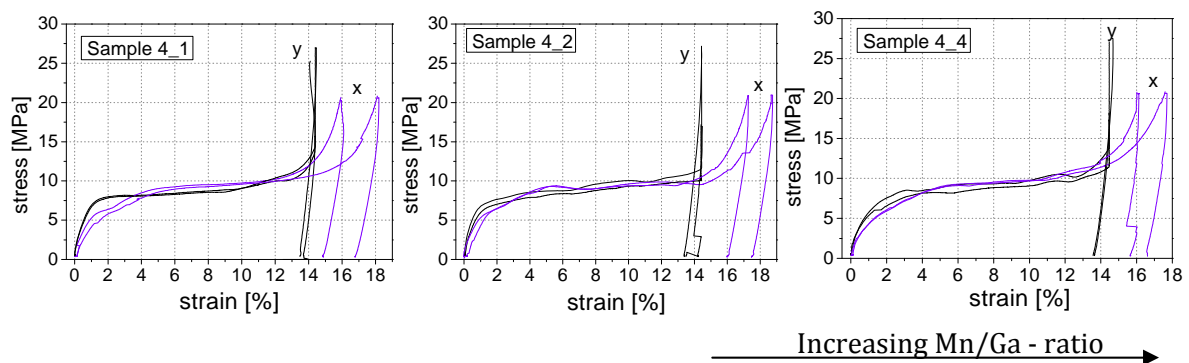


Figure C8: Stress – strain – behaviour of sample 4\_1, 4\_2 and 4\_4 with increasing Mn/Ga - ratio.

## CRYSTAL ROD NO.5 “Ni<sub>49.2</sub>Mn<sub>28.4</sub>Ga<sub>21.6</sub>Co<sub>0.8</sub>”

Four specimens of this rod were compressed mechanically in the same testing device as with the samples of the previous rods. Thereby in all these samples (5\_1, 5\_3, 5\_4 and 5\_6) a twinning stress of around 2MPa was determined. Sample 5\_1 shows a distinctive stress plateau with a twinning stress below 2MPa up to a strain of 4.10% (see Figure C9) and reaches the maximum strain by applying a uniaxial pressure of 3.22MPa. With the increasing Mn/Ga - ratio the samples, the stress which has to be overcome slightly increases, whereby a stress of 4.52MPa and 3.88MPa, respectively has to be applied to reach the maximum strain (5.31% and 4.72%) in the samples 5\_3 and 5\_4. The sample 5\_6 shows a strain of 2.1% when applying a stress of 2MPa and reaches the maximum strain of 5.33% with a uniaxial compression with 5.14MPa.

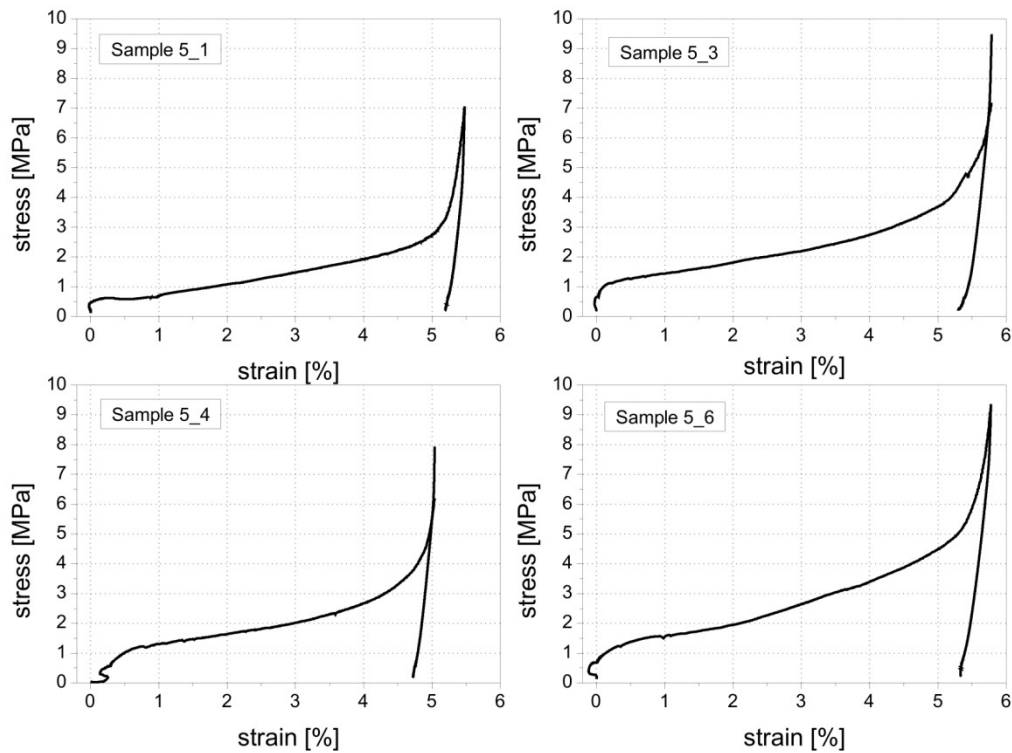


Figure C9: Stress - Strain - curves of sample 5\_1, 5\_3, 5\_4 and 5\_6 determined by applying uniaxial pressure onto the samples.



# ERKLÄRUNG

---

Hiermit versichere ich, dass ich die vorliegende Arbeit selbstständig verfasst und keine anderen als die angegebenen Quellen und Hilfsmittel benutzt habe.

München, den